



**Manchester
Metropolitan
University**

[Newton-Mann, Chloe Rebecca](#) (2019) Finite Element Modelling of Snowboard Wrist Protectors. Doctoral thesis (PhD), Manchester Metropolitan University.

Downloaded from: <http://e-space.mmu.ac.uk/625433/>

Usage rights: Creative Commons: Attribution-Noncommercial-No Derivative Works 4.0

Please cite the published version

<https://e-space.mmu.ac.uk>

FINITE ELEMENT MODELLING OF SNOWBOARD WRIST PROTECTORS

C R NEWTON-MANN

PhD 2019

FINITE ELEMENT MODELLING OF SNOWBOARD WRIST PROTECTORS

CHLOE REBECCA NEWTON-MANN

A thesis submitted in partial fulfilment of the
requirements of the Manchester Metropolitan
University for the degree of Doctor of Philosophy.

Department of Engineering, Manchester
Metropolitan University

2019

Abstract

Snowboarding has a higher injury risk than alpine skiing, with the upper extremities being the most common site for injuries. Wrist protectors are recommended to reduce injury risk by limiting wrist hyperextension and impact forces. There are different wrist protector designs but there is currently no recognised standardisation, with little consensus as to which are most effective. While experimental protocols are useful for analysing current products, they are limited when assessing the effect of design changes and predicting the performance of future protector concepts. The aim of this project was to develop finite element models to assess the impact performance of snowboard wrist protectors, whilst fitted to a surrogate.

Two wrist protectors were chosen for modelling, both with palmar and dorsal splints and padding in the palmar region, with one classified as short and the other a long protector (based on splint length). The component materials within the protectors were characterised and impact tested. Using the measured material properties, finite element models replicating these impact tests were developed and compared to the experiment for validation. These models were developed into full protectors fitted to a wrist surrogate under impact. To validate the full protector models, experimental testing was conducted using a modified version of the pendulum impact rig developed by Adams (2018) across a range of energies (10 to 50 J). The validated models were then used to explore the effect of changing components (e.g. splint length, material) on impact performance, in order to enhance the understanding of wrist protector design.

The research highlighted clear differences in the properties of wrist protector components from the same size/brand, re-iterating the need for standardisation. The palmar splint was found to have the largest influence on impact force and the dorsal splint on wrist angle, in agreement with the literature. Model outputs showed peak force and maximum wrist angle to decrease as splint length or stiffness (thickness or material) increased. Future work could develop the model into a tool for improving wrist protectors as well as to predict whether new designs would meet the requirements of the new ISO standard (once published).

Outputs from this Thesis

Conference Proceedings

Newton-Mann, C., Driscoll, H., Winwood, K., Hamilton, N. and Allen, T., 2017, April. Identification of protective elements and materials of snowboard wrist protectors. 22nd International Congress of Snow Sports Trauma and Safety – Innsbruck, Austria – This abstract was presented based on the work of Chapter 2 and 3 of this thesis

Newton-Mann, C., Winwood, K., Driscoll, H., Hamilton, N. and Allen, T., 2018, February. Finite element model of an impact on a palmar pad from a snowboard wrist protector. In Multidisciplinary Digital Publishing Institute Proceedings (Vol. 2, No. 6, p. 314). 12th Engineering of Sport Conference (ISEA) – Brisbane, Australia. – This paper was presented based on the work of Chapter 4 and 5 of this thesis

Newton-Mann, C., Hamilton, N., Winwood, K., Driscoll, H. and Allen, T., 2019, April. Comparison of a Finite Element Model for Snowboard Wrist Protectors against an Impact Test. 23rd International Congress of Snow Sports Trauma and Safety – Squaw Valley, California. – Winner of the Sachiko Yahashi Award and \$1,000_{USD} for the best young researcher at the conference – This abstract was presented based on the work of Chapter 6, 7 and 8 of this thesis

Invited Talks

- July 2019 – Simulations in Sports Applications – TU Chemnitz, Germany
- 6th February 2018 – “Snowboarding Wrist Protection for Beginners to Elite Athletes”, Ansys Sports Webinar series, online.
- October 2017 - Simulations in Sports Applications - Engineering Design Show, Ricoh Arena, Coventry - Ansys

Acknowledgements

Muhammed Ali the great boxer once said: “It isn’t the mountains ahead to climb that wear you out; it’s the pebble in your shoe”. When you are trying to achieve something, you can get lost thinking about the mountain that is ahead of you, however, it is the small problems that can defeat you mentally. The mountains can be conquered with persistence. I think this quote is very true of my PhD project, there were many ups and downs but I have lots of people to thank for helping me get rid of the pebbles and climb the PhD mountain.

Firstly, I would like to thank my supervisory team; Dr Thomas Allen, Dr Keith Winwood, Dr Heather Driscoll and Nick Hamilton for their continual support and guidance throughout the PhD. I am also very grateful to the technical staff, especially Mike Green, Stephen Moyle and Bob Bamford, with help using material testing machines and developing rigs.

Thank you to my fellow E0.33 and E3.24 PhD students, for the everyday support they have given me including tubs of hummus, biscuit supplies and coffee. They also provided great help with feedback on my project, kept me fit with lunchtime workouts, gave me a shoulder to cry on when needed and always provided very good banter.

Finally, I would like to thank my family, friends and my fiancé, Finnian, for providing endless support throughout the project, without whom I would not have completed it. I would like to dedicate this piece of work in loving memory of my two grandmothers and great uncle, Robyn, Rosemary and Michael who passed away during the first year of my PhD, they inspired me to take on this project and I hope I have made them all proud.

Contents

Abstract.....	i
Outputs from this Thesis	ii
Conference Proceedings	ii
Invited Talks	ii
Acknowledgements.....	III
Contents	IV
List of Figures	X
List of Tables.....	XVII
1 Introduction.....	1
1.1 Motivation for the Research	1
1.2 Aim and Objectives.....	2
1.3 Thesis Structure.....	2
2 Literature Review	5
2.1 Introduction	5
2.2 Snowboarding.....	6
2.2.1 Injury Rates	6
2.2.2 Mechanisms of Wrist Injuries	6
2.2.3 Injury Criteria.....	7
2.3 Protective Mechanisms.....	11
2.3.1 Wrist Protectors.....	12
2.3.2 Wrist Protector Design	13
2.3.3 Usage Rates of Snowboard Wrist Protectors	17
2.4 Experimental Testing	17
2.4.1 Testing of PPE	17
2.4.2 Testing of Snowboard Wrist Protectors	19
2.4.3 Draft Standard for Snowboard Wrist Protectors (ISO/DIS 20320).....	23
2.5 FE Modelling.....	23

2.5.1	FE Process.....	24
2.5.2	Geometric Model.....	32
2.5.3	Material Characterisation and Modelling.....	32
2.5.4	Validation.....	34
2.5.5	FE Studies in Snowboarding.....	35
2.6	Summary.....	37
3	Wrist Protector Selection & Material Characterisation.....	39
3.1	Introduction.....	39
3.2	Protector Selection.....	40
3.2.1	Selection Criteria.....	42
3.2.2	Selected Protectors.....	43
3.3	Material Identification.....	44
3.3.1	Fourier Transform Infrared Spectroscopy (FT-IR).....	46
3.4	Material Characterisation.....	48
3.4.1	Methodology.....	48
3.4.2	Results.....	55
3.4.3	Discussion.....	61
3.5	Chapter Summary.....	62
4	Experimental Impact Testing of Wrist Protector Components.....	63
4.1	Introduction.....	63
4.2	Methodology.....	64
4.3	Results.....	69
4.3.1	Individual Component Impacts.....	69
4.3.2	Full Palmar Impacts.....	73
4.3.3	Median Component Impacts at a Range of Energies.....	75
4.4	Discussion.....	76
4.5	Chapter Summary.....	78
5	FE Modelling of Wrist Protector Components Under Impact.....	79

5.1	Introduction	79
5.2	Material Models	80
5.2.1	Linear Elastic Models	80
5.2.2	Hyperelastic Models	81
5.2.3	Viscoelastic Models	85
5.3	FE Model Methodology	88
5.4	Results	92
5.4.1	FE of Individual Components	93
5.4.2	FE of Full Palmar Impact	95
5.5	Discussion	97
5.6	Chapter Summary	100
6	Impact Testing of Wrist Protectors	101
6.1	Introduction	101
6.2	Impact Rig Development	101
6.2.1	Impact Velocities from the Literature	104
6.3	Impact Testing of Two Wrist Protector Designs - Methods	106
6.3.1	Pre Testing	106
6.3.2	Impact Testing	106
6.3.3	Post-Processing	109
6.4	Impact Testing of Two Wrist Protector Designs - Results	113
6.4.1	Polychloroprene Degradation	113
6.4.2	Example Impact Traces	113
6.4.3	Bare Hand vs. Protector	118
6.4.4	Untested vs. Tested Protector	119
6.5	Discussion	123
6.6	Chapter Summary	125
7	FE Model of Wrist Protectors Under Impact	126
7.1	Introduction	126

7.2	Polychloroprene	127
7.2.1	Material Characterisation - Methods.....	127
7.2.2	Impact Testing – Methods	128
7.2.3	Material Characterisation – Results and Discussion	129
7.2.4	Impact testing – Results and Discussion.....	130
7.2.5	FE Model of Polychloroprene Impact – Methods.....	131
7.2.6	FE model of Polychloroprene Impact – Results and Discussion	133
7.3	FE Modelling of Full protector – Methodology.....	134
7.3.1	Geometry Creation	134
7.3.2	Material Models	137
7.3.3	Boundary Conditions	139
7.3.4	Mesh	142
7.3.5	Post-Processing	144
7.4	Results.....	144
7.4.1	Pilot Results Informing Methods.....	144
7.4.2	Bare Hand	148
7.4.3	Example Comparison of the Model and Experimental Impact.....	149
7.4.4	Model and Experiment Comparison – Temporal Force and Temporal Wrist Angle Traces	152
7.4.5	Model and Experiment Comparison - Force vs. Wrist Angle	155
7.4.6	Comparative Overview	158
7.4.7	Sensitivity of the Model	158
7.5	Discussion	160
7.6	Chapter Summary.....	162
8	FE Model Design Case Study	163
8.1	Introduction	163
8.2	Methodology	163
8.3	Results.....	167
8.3.1	Changes in Splint Length	167

8.3.2	Changes in splint material	170
8.3.3	Changes in Splint Thickness	174
8.3.4	Summary of Results	175
8.4	Discussion	179
8.5	Chapter Summary.....	181
9	Conclusions and Future Research	182
9.1	Introduction	182
9.2	Summary of Research – Findings, Limitations, Novelty and Future Work 183	
9.2.1	Objective 1	183
9.2.2	Objective 2	184
9.2.3	Objective 3	186
9.2.4	Objective 4	188
9.3	Overall Conclusions.....	190
	References.....	191
10	Appendices	209
10.A	ISO/DIS 20320 Bend Test Surrogate Engineering Drawing	209
10.B	Monthly Stock Check of Wrist Protectors in the UK.....	210
10.C	FT-IR Traces for Wrist Protector Components	212
10.D	Statistical Analysis.....	216
10.D.1	Chapter 3	216
10.D.2	Chapter 4	221
10.D.3	Chapter 6	229
10.D.4	Chapter 7	234
10.D.5	Chapter 8	236
10.E	Experimental Testing.....	241
10.E.1	Instrumentation Calibration	241
10.E.2	Impact Rig Validation & Calculations	241
10.E.3	Material Data Sheets	243

10.E.4	Rigid and Dynamic Model Calculations.....	243
10.E.5	Loading Rate.....	246
10.E.6	Comparison of Data to Adams (2018).....	247
10.F	Material Models	248
10.G	Mesh Convergence Studies.....	251
10.G.1	Individual Component Impacts.....	251
10.G.2	Bare Hand Impact	253

List of Figures

Figure 1-1 Schematic diagram indicating the content of each chapter within the overall project.....	3
Figure 2-1 Prevention of sports injuries sequence	5
Figure 2-2 Distal forearm fracture caused by a wrist impact (Michel et al., 2013)...	7
Figure 2-3 Example of experimental setups.....	10
Figure 2-4 Suggested falling techniques for Snowboarding to minimise wrist injuries.. ..	12
Figure 2-5 Identified protective elements of two different protectors.....	16
Figure 2-6 Schematic showing a typical impact test set up for a sports PPE safety standard (Payne, 2015)	18
Figure 2-7 Example setup of the two tests in EN 14120.	19
Figure 2-8 Surrogate designs that were compared by Adams et al. (2018).	21
Figure 2-9 Impact rig developed by Adams (2018).	22
Figure 2-10 Flowchart of the FE modelling process.....	25
Figure 2-11 THUMS model of a male 50th percentile developed by Toyota.	32
Figure 2-12 Example of previous FE studies of snowboard wrist protectors.....	36
Figure 2-13 Senner et al. (2019) modelling process.	37
Figure 3-1 Schematic diagram indicating where this chapter fits within the overall project.	40
Figure 3-2 Flowchart of the inclusion criteria used to select the wrist protectors to model.	42
Figure 3-3 Components of the short protector chosen for modelling.	45
Figure 3-4 Components of the long protector chosen for modelling.....	45
Figure 3-5 Example FT-IR trace.....	46
Figure 3-6 Example (a) set up for obtaining samples for material characterisation and a (b) compression and (c) tensile sample.	50
Figure 3-7 Example modifications to splints that were trialled to create a tensile sample	52
Figure 3-8 Three point bend test setup of the two protector splints.	53
Figure 3-9 Mean stress vs. strain plot for an example compression sample, at 3 strain rates.	56
Figure 3-10 Stress vs. strain response for compression samples.....	57
Figure 3-11 Mean stress vs. strain plots for five tensile samples at 0.2 s ⁻¹	58

Figure 3-12 Shear modulus vs. time plots obtained from stress relaxation testing.	59
Figure 3-13 Mean force vs. deflection plots for three point bend testing of splint samples.	60
Figure 4-1 Schematic diagram indicating where this chapter fits within the overall project.	63
Figure 4-2 (a) Isometric and (b) top view of the bespoke drop tower rig used for impact testing of individual components.	65
Figure 4-3 Example of components being impacted.	66
Figure 4-4 Example data obtained from the oscilloscope.	68
Figure 4-5 Example of how maximum deformation was measured in Phantom® CineViewer.	69
Figure 4-6 Mean temporal force traces for five samples of the short protector (a) pad, (b) pad + shell and (c) supporting foam.	70
Figure 4-7 An example mean temporal force trace for the short protector supporting foam impact and corresponding high-speed camera images at 1 ms intervals, highlighting that the sample does not become fully engaged until ~2 ms.	70
Figure 4-8 Mean temporal force traces for five samples of the long protector (a) D3O® and (b) supporting foam.	72
Figure 4-9 Mean temporal force traces for all five samples of combined palmar components.	74
Figure 4-10 Mean temporal force traces for the short protector components and long protector components at a range of energies.	75
Figure 5-1 Schematic diagram indicating where this chapter fits within the overall project.	79
Figure 5-2 Example stress vs. strain plot demonstrating the use of a linear trend line used to obtain Young's modulus.	81
Figure 5-3 Stress vs. strain plots showing example curve fitting to obtain material model coefficients for an Ogden model and a Mooney-Rivlin model.	83
Figure 5-4 The process of converting a 0.5 J impact to a stress vs. strain curve.	84
Figure 5-5 Screen-shots of shear modulus vs. time plots showing example curve fitting results from ANSYS® Mechanical APDL when obtaining material model coefficients for the Prony series.	87
Figure 5-6 Example of the 'factor-of-ten' rule applied to the short protector supporting foam.	88

Figure 5-7 Example of how the plates and samples were meshed in ANSYS® Mechanical v18.2.	90
Figure 5-8 Example of how maximum compression was measured.	91
Figure 5-9 Sensitivity analysis showing the effect of changing Poisson's ratio on peak force and maximum compressive strain.	93
Figure 5-10 Example temporal force traces for the short protector pad under impact, showing the effect of using the variable stress vs. strain response (softest and stiffest) (Chapter 3, Figure 3-10) to replicate the impact behaviour within an FE model.	94
Figure 5-11 Temporal force traces comparing median FE model and experimental sample impacts.	94
Figure 5-12 Temporal force traces comparing median FE model and experimental sample impacts for the combined palmar component impacts.	95
Figure 6-1 Schematic diagram indicating where this chapter fits within the overall project.	101
Figure 6-2 Schematic of the impact rig developed by Adams (2018) and its associated mass distribution.	103
Figure 6-3 Temporal force trace showing the effect of changing the number of polychloroprene blocks when impacting the short protector at 20 J.	104
Figure 6-4 Mass vs. inbound velocity chart highlighting cadaver studies, biomechanical studies and studies using surrogates. A rigid and dynamic model of a human fall for a range of ages are also shown. The available range of velocities with the current test set up (Adams, 2018) and the achievable range of velocities for the modified setup with a reduced effective mass is also shown.	105
Figure 6-5 Schematic highlighting dimensions of the pendulum impact rig, release height and angle.	107
Figure 6-6 Schematic of the impact set up showing the position of the high-speed cameras and lights.	109
Figure 6-7 Steps followed to identify the key points from the test data (Adams, 2018).	110
Figure 6-8 Example impact trace and high-speed video images highlighting the data captured by the load cell and potentiometers for a bare hand impact and a short protector impact.	111
Figure 6-9 Peak force for 100 consecutive impacts on a stack of two polychloroprene blocks.	113

Figure 6-10 Short protector impact highlighting a sequence of high-speed photographs which showcase key points of the temporal force and temporal wrist angle traces.	115
Figure 6-11 Long protector impact highlighting a sequence of high-speed photographs which showcase key points of the temporal force and temporal wrist angle trace.	116
Figure 6-12 Example lateral wrist surrogate movement for the short protector...	117
Figure 6-13 Example temporal force traces for bare hand and untested protector impacts at each energy.	118
Figure 6-14 Force vs. wrist angle plots for (a) an untested short and long protector and (b) a consecutively tested short and long protector.	120
Figure 6-15 Temporal force, temporal wrist angle and force vs. wrist angle traces for an untested and a consecutively tested short and long protector.	121
Figure 6-16 Bar charts showing the effect of five repeated impacts on both an untested and consecutively tested protector in terms of peak force, maximum wrist angle and energy absorption.	122
Figure 7-1 Schematic diagram indicating where this chapter fits within the overall project.	126
Figure 7-2 Schematic of impact rig.	129
Figure 7-3 Mean stress vs. strain traces for (a) five samples of polychloroprene at 0.02 s^{-1} (b) one sample at 0.02 s^{-1} and 0.2 s^{-1} , highlighting the first unique curve and (c) shear modulus vs. time trace for all five samples.	130
Figure 7-4 Mean temporal force traces for 5 J impacts on five samples of polychloroprene.	131
Figure 7-5 Material model curve fits for (a) hyperelastic Ogden first order model and (b) three term Prony series curve fit to stress relaxation data at 20% strain.	132
Figure 7-6 Temporal force trace for a 5 J impact on a cylindrical sample of polychloroprene within an experiment and FE model.	133
Figure 7-7 Example comparison between an experimental polychloroprene sample (a) prior to impact and (b) at maximum compression and the FE model.	134
Figure 7-8 Cross section view of (a) short protector and (b) long protector highlighting the varied thickness of the palmar pad and the shared topology.	137
Figure 7-9 Stress vs. strain plots for the short protector supporting foam showing the highest quasi-static trace, the impact data trace and the artificially stiffened trace.	139

Figure 7-10 Coordinate system used to replicate the pendulum motion of the impactor within the FE models and the boundary conditions set.	140
Figure 7-11 Example section view of how a 3-node angle measurement was taken to obtain maximum wrist angle.....	144
Figure 7-12 Example temporal force and temporal wrist angle trace highlighting the difference between using a 4 cm and 1 cm polychloroprene block within the FE models.	145
Figure 7-13 Effect of changing the coefficient of friction between the supporting foam and wrist surrogate on peak force and maximum wrist angle.	146
Figure 7-14 Effect of changing the coefficient of friction between the supporting foam and wrist surrogate on temporal force and temporal wrist angle traces.	146
Figure 7-15 Effect of changing strapping pressure on peak force and maximum wrist angle.	147
Figure 7-16 Effect of changing strapping pressure between 1 kPa and 15 kPa on temporal force and temporal wrist angle traces.	147
Figure 7-17 Temporal force traces for a mean experimental bare hand impact and FE model.	148
Figure 7-18 Comparison of peak forces and impact duration for both the experiment and bare hand FE model.	148
Figure 7-19 Impact of the short protector at 40 J experimentally and in the FE model.	150
Figure 7-20 Impact of the long protector at 40 J experimentally and in the FE model.	151
Figure 7-21 Comparison between experimental data and FE model for the short protector at 10 to 50 J in terms of temporal force and temporal wrist angle traces.	153
Figure 7-22 Comparison between experimental data and FE model for the long protector at 10 to 50 J in terms of temporal force and temporal wrist angle traces.	155
Figure 7-23 Comparison between experimental data and FE model for the short protector at 10 to 50 J in terms of a force vs. wrist angle trace.	156
Figure 7-24 Comparison between experimental data and FE model for the long protector at 10 to 50 J in terms of a force vs. wrist angle trace.	157
Figure 7-25 Comparison of peak forces and maximum wrist angles for both the experiment and FE model.	158

Figure 7-26 Temporal force traces of the full protectors impacted at 40 J, demonstrating the effect of using the stiffest material models from Chapter 5....	159
Figure 8-1 Schematic diagram indicating where this chapter fits within the overall project.	163
Figure 8-2 Different design iterations of the short protector model.	165
Figure 8-3 Different design iterations of the long protector model.	166
Figure 8-4 The effect of design changes regarding splint length on temporal force, temporal wrist angle and force vs. wrist angle traces for the short protector.	168
Figure 8-5 The effect of design changes regarding splint length on temporal force, temporal wrist angle and force vs. wrist angle traces for the long protector.....	169
Figure 8-6 Force vs. wrist angle trace for the short protector model with 224 mm dorsal splints at 40 J. Highlighting the reason for the difference in the shape of the trace compared to other impact traces for shorter splints.	170
Figure 8-7 The effect of design changes regarding splint material on temporal force, temporal wrist angle and force vs. wrist angle traces for the short protector.	172
Figure 8-8 The effect of design changes regarding splint material on temporal force, temporal wrist angle and force vs. wrist angle traces for the long protector.....	173
Figure 8-9 The effect of design changes regarding dorsal splint thickness on temporal force, temporal wrist angle traces and force vs. wrist angle traces.	174
Figure 8-10 Example stress contour plots for the long protector at 40 J when changing the length of the palmar splint.	175
Figure 8-11 Effect of changing the splint (a) length, (b) material and (c) thickness for the short protector.....	177
Figure 8-12 Effect of changing the splint (a) length, (b) material and (c) thickness for the long protector.	178
Figure 9-1 Schematic diagram highlighting the content of the thesis.	182
Figure 10-1 Hand calculated effective mass vs. the measured effective mass of the impact rig with a linear regression.....	242
Figure 10-2 Calibration data for the pendulum and wrist potentiometers.....	242
Figure 10-3 Experimental set up from Schmitt et al. (2012b) with the shoulder angle highlighted and a rigid body diagram highlighting the parameters used.	244
Figure 10-4 Schematic of the two-link dynamic model used by Van den Kroonenberg et al. (1995).....	245

Figure 10-5 Temporal force plot showing the impact traces for this study, an impact using the unmodified rig in Adams (2018) and the loading curve from Greenwald et al. (1998).....	246
Figure 10-6 Mesh convergence study showing the total number of elements and the effect on peak force and maximum compression of a pad sample being impacted at 2.5 J.	252
Figure 10-7 Mesh convergence study showing the total number of elements and the effect on peak force of the bare hand set up being impacted at 40 J.	253
Figure 10-8 Mesh convergence study showing the total number of elements and the effect on peak force and maximum compressive strain of the palmar pad being impacted at 2.5 J.....	254
Figure 10-9 Mesh convergence study showing the total number of elements and the effect on the resultant force needed to displace the short protector dorsal splint by 7 mm within a three-point bend test.	254

List of Tables

Table 2-1 Summary of the natural range of motion of the wrist joint.....	8
Table 2-2 13 studies with fracture loads of adult cadaver forearms (adapted from Adams (2018)).	9
Table 2-3 A selection of wrist protectors currently on the market.....	15
Table 2-4 Experimental test setups and instrumentation used for impact testing of wrist protectors.....	20
Table 2-5 A selection of notable sports engineering FE papers modelling PPE impacts.	26
Table 2-6 A selection of notable sports engineering FE papers that include similar materials to those within a snowboard wrist protector.....	29
Table 2-7 A selection of notable sports engineering FE papers modelling sports PPE impacts, highlighting how the FE models were validated.....	35
Table 3-1 Pool of wrist protectors considered for modelling selection.	41
Table 3-2 Results of the selection criteria questions.....	44
Table 3-3 Break down of the identified materials for each part of the protectors. .	47
Table 3-4 Different material characterisation tests conducted for each part of the protectors.....	49
Table 3-5 Mean calculated elastic modulus for each splint sample.	60
Table 4-1 Mean values for peak force, maximum compression, maximum compressive strain and impact duration for 2.5 J impacts on all samples of the short protector.....	71
Table 4-2 Mean values for peak force, maximum compression, maximum compressive strain and impact duration for 0.5 J impacts on all samples of the long protector.....	73
Table 4-3 Mean values for peak force, maximum compression, maximum compressive strain and impact duration for the combined palmar component impacts.	74
Table 4-4 Mean values for peak force, maximum compression, maximum compressive strain and impact duration for all median samples at a range of energies.	76
Table 5-1 Different protector components and the associated type of material. ...	80
Table 5-2 Hyperelastic material model coefficients.....	85
Table 5-3 Prony series coefficients.....	87

Table 5-4 Density and Poisson's ratio values used in the FE model for each hyperelastic component.	91
Table 5-5 Peak force, maximum compression, maximum compressive strain and impact duration for the range of FE models using the softest and stiffest stress vs. strain response for each component of both wrist protectors at a range of energies.	96
Table 5-6 Difference between the median FE model and experimental sample for each component.	97
Table 6-1 Release height and angle of pendulum impactor for the setup of each impact energy.	108
Table 6-2 Lateral wrist surrogate movement for bare hand and short protector impacts at each energy.	117
Table 7-1 Mean values for peak force, maximum compression, maximum compressive strain and impact duration for 5 J impacts on all samples of polychloroprene.	131
Table 7-2 Steps taken to develop the geometries of the two wrist protector designs in CAD.	135
Table 7-3 Overview of the material models used for the impactor and wrist surrogate.	138
Table 7-4 Difference between the theoretical impact velocities and mean experimental values.	141
Table 7-5 Parts of the bare hand, short and long protector impact models, the type of elements that were used for meshing and the number of nodes and elements they were meshed with.	143
Table 8-1 Pearson's r matrix for all the relationships shown in Figure 8-11 and Figure 8-12.	176
Table 10-1 Monthly tracking record for the pool of wrist protector identified for modelling.	211
Table 10-2 Estimated fall velocities using the rigid body model and dynamic model for a range of anthropometric parameters.	245
Table 10-3 Parts within the FE model and the number of elements and nodes they were meshed with, following a mesh convergence study.	252

1 Introduction

This thesis documents the development of finite element (FE) models of snowboard wrist protectors for simulating hand/surface impacts. The validated models were used to assess the effect of wrist protector design changes on impact performance. This chapter outlines the motivation behind the research, and the aims and objectives.

1.1 Motivation for the Research

The forearm and wrist account for over a third of snowboarding injuries (Russell *et al.*, 2007). Snowboarding injuries are often the result of a fall, more specifically a backwards fall typically results in higher impact forces than a forward fall (DeGoede and Ashton-Miller, 2003; Greenwald *et al.*, 2011; Lehner *et al.*, 2014). As the feet are attached to the board via bindings, any loss of balance can result in inexperienced boarders instinctively attempting to break their fall by placing their hands out. Thus, upon contact with the ground, impact forces travel through the hand transmitting across the carpals to the wrist (Burkhart and Andrews, 2010; Maurel *et al.*, 2013). At the point of contact, bending is also created, which can exceed the wrists natural range of motion (hyperextension), and cause sprains or fractures (Yamauchi *et al.*, 2010). In general, fall-related injuries are predicted to cost the USA \$85.4 billion dollars by 2020 (Englander *et al.*, 1996). Finding preventative measures for fall-related injuries are important for both medical and economic reasons.

An alteration to the fall kinematics and/or using personal protective equipment (PPE) are methods suggested to reduce the risk of injuries in snowboarding (DeGoede *et al.*, 2003). Often PPE is a requirement set by the governing body and regulated by a safety standard (e.g. ISO, BSI) prescribing the performance criteria to obtain certification. Alongside helmets, goggles, back protectors and knee/elbow pads (McCann, 2013; Nate, 2019), snowsports injury experts recommend wrist protectors for snowboarders (Michel *et al.*, 2013). There is not a standard for snowboard wrist protectors, benchmarking the minimum protective thresholds, so it is unclear as to whether the recommendation to wear wrist protectors corresponds to any particular design, with many concepts on the market.

Mechanical tests for bending stiffness and impact performance facilitate testing of current wrist protectors (Adams, 2018; Schmitt *et al.*, 2012a). These experimental

1. Introduction
tests are limited when assessing and understanding the effect of protector design changes. This PhD project is, therefore, set to develop and validate FE models of snowboard wrist protectors for simulating hand/surface impacts. By using a model, the influence of design changes can be better assessed and understood. The FE models will be the first to accurately represent the geometry of a wrist protector when fitted to a wrist surrogate and encompass all protective elements under impact. The findings of this research will support work to develop an ISO standard (ISO/DIS 20320) for snowboard wrist protectors.

1.2 Aim and Objectives

The aim of this thesis is to develop an FE model for predicting the impact performance of snowboard wrist protectors.

In order to achieve this, the key objectives are:

1. To identify the main components and materials of contemporary snowboard wrist protectors
2. To characterise the material properties of the main components of snowboard wrist protectors.
3. To develop and validate FE models of snowboard wrist protectors for simulating hand/surface impacts.
4. To use the validated models to predict how design parameters influence the protection levels of wrist protectors.

1.3 Thesis Structure

This project is concerned with the development of FE models to simulate impacts of snowboard wrist protectors when fitted to a wrist surrogate. The project followed a reductionist methodology, where the wrist protectors were broken down into individual components to reduce the complexity of the interactions and understand the fundamentals of the protectors. Reductionism is based on the understanding that a complex system can be described by an account of its individual constituents and like a clockwork mechanism, can then be put back together to see the larger picture (Descartes, 1637). Within computer modelling projects, a reductionism methodology is commonly used, whereby the problem is simplified as much as possible without losing the accuracy (Shuttleworth, 2008).

Figure 1-1 outlines the process followed in the project and what will be shown in each chapter. Two protectors will be selected for modelling, their protective parts

1. Introduction and the associated materials will be identified and characterised (Chapter 3). The next step will be to develop and validate FE models of the protective components of the wrist protectors under impact (Chapter 4 and 5). These models of the components will then be combined and developed into wrist protector models fitted to a wrist surrogate, simulating a range of impact energies (Chapter 7). As FE models must be validated against experimental data (or established theory) to assess accuracy, protector impact testing will also be presented (Chapter 6). Once validated, the protectors within the models will be manipulated, so the effect of design parameters on impact performance can be assessed (Chapter 8).

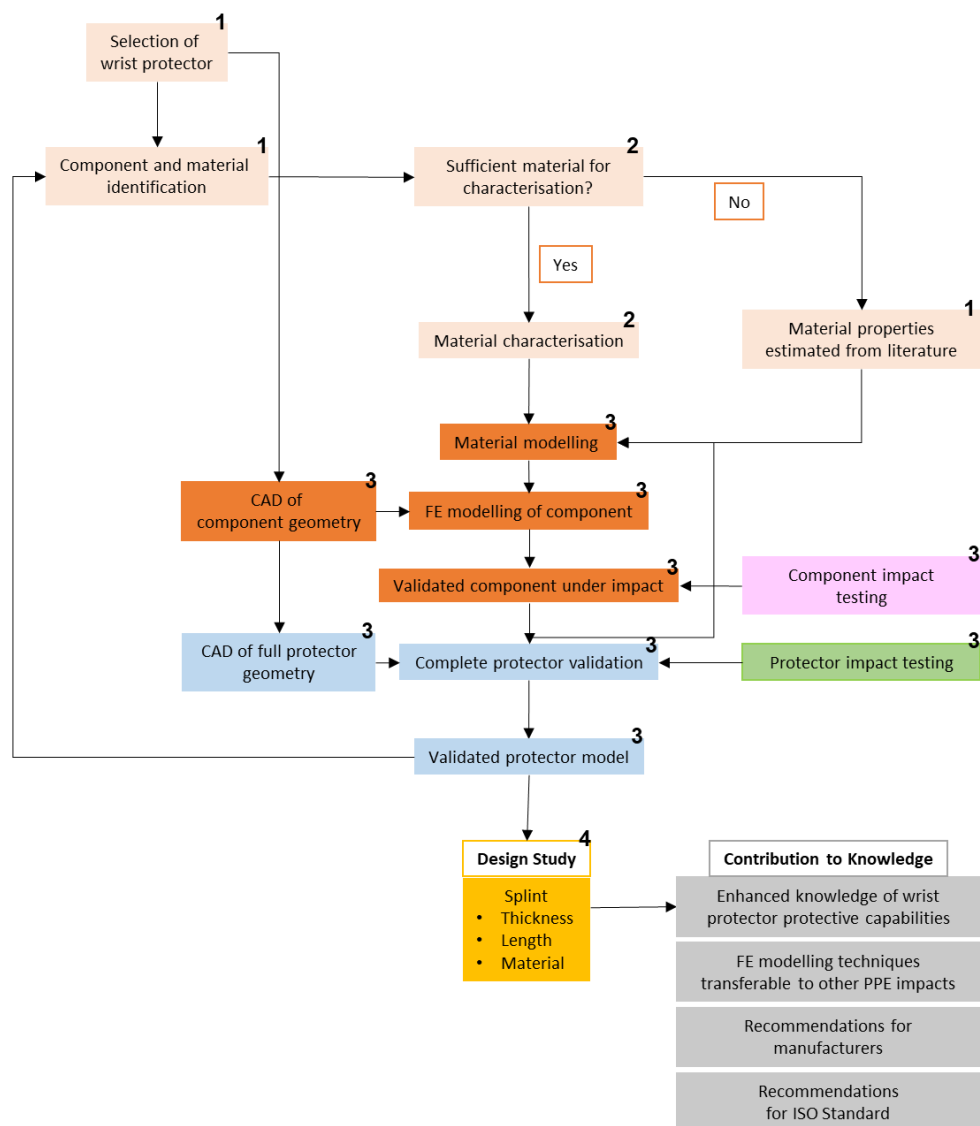


Figure 1-1 Schematic diagram indicating the content of each chapter (each colour is a separate chapter) within the overall project (numbers correlate to the objectives of the thesis).

Using the reductionist approach has limitations, as isolating one component and studying it can often change its behaviour to how it responds within the full product (Shuttleworth, 2008). For the wrist protector, the effect of characterising the

materials individually could have changed the composite effect exhibited through the multiple layers of different materials. Also, through using the reductionist approach, some of the interactions between components may not have been fully captured. A holistic approach could have therefore been utilised in this project, where all material combinations would have been characterised as one unit and modelled as one from the offset. The holistic approach, however, does not allow for incremental design changes, and after the creation of the model, it would have been challenging to identify the cause of any errors and rectify these.

2 Literature Review

2.1 Introduction

There is a large body of research concerning injury rates and severity in snowboarding injury epidemiology, the biomechanics of falls and mechanical testing (using cadavers or surrogates/anvils) identifying the protective capabilities of PPE (personal protective equipment). This literature review intends to identify, and further the understanding of, the key trends within the literature and common techniques used to assess the performance of sports PPE, with a focus on snowboard wrist protectors. The review will also highlight the gaps in knowledge. As this project is set to develop FE models of snowboard wrist protectors, the literature review is split into four sections, reflecting the sports injury prevention sequence suggested by van Mechelen *et al.* (1992) (Figure 2-1).

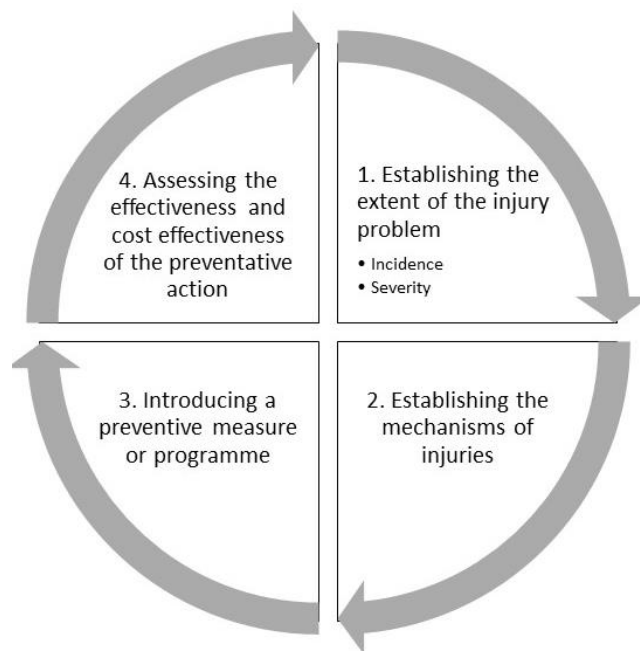


Figure 2-1 Prevention of sports injuries sequence (adapted from (van Mechelen *et al.*, 1992))

The first section (2.2) establishes the problem; examining snowboarding injury epidemiology and the mechanisms of injury. Preventative methods such as wearing PPE are assessed in section 2.3, where wrist protectors are researched in detail, highlighting the different design approaches. Section 2.4 examines techniques employed to assess the effectiveness of PPE and in particular wrist protectors using laboratory based experimental testing. Finally, FE modelling and its application within PPE design and protective performance evaluation are explored as an alternative method to experimental tests, for assessing effectiveness.

2.2 Snowboarding

Snowboarding combines elements of surfing, skateboarding and skiing (International Olympic Committee, 2018). The sport made its Olympic debut at the 1998 Nagano games, and there are an estimated 10 to 15 million snowboarders worldwide (Michel *et al.*, 2013). Compared to alpine skiing, snowboarding has a younger demographic proportion of participants (53% between 6 to 24 yrs compared to 39% for skiing (SIA research, 2014)) and a larger proportion of beginners with less than seven days' experience (snowboarders 35%, skiing 21%) (Dickson *et al.*, 2008).

2.2.1 Injury Rates

Injury rates in snowboarding are thought to be higher than alpine skiing (0.8 to 8.0 injuries per thousand snowboard days vs. 2 to 3.7 injuries per thousand skier days) (Bladin *et al.*, 1993; Hunter, 1999; Idzikowski *et al.*, 2000; Ronning *et al.*, 2001; Koehle *et al.*, 2002; Langran and Selvaraj, 2002; O'Neill, 2003; Russell *et al.*, 2007; Russell *et al.*, 2010). Novice and beginner snowboarders are at greatest risk, with this group constituting 40 to 60% of injuries (Idzikowski *et al.*, 2000; Bladin *et al.*, 2004; Hagel *et al.*, 2004; Ogawa *et al.*, 2010). Severe snowboard-associated injuries are highest amongst younger participants (Coury *et al.*, 2013; Basques *et al.*, 2018) with de Roulet *et al.* (2017) reporting almost 90% of injuries involving those under 35 years old. The majority (72%) of reported snowboarding injuries are bruises and sprains (Dickson *et al.*, 2008). The upper extremities are the most common injury site amongst snowboarders (Sutherland *et al.*, 1996; Idzikowski *et al.*, 2000; O'Neill, 2003; Matsumoto *et al.*, 2004; Hagel *et al.*, 2005; Coury *et al.*, 2013; Basques *et al.*, 2018), with the forearm and wrist accounting for approximately 35 to 45% of all injuries (Russell *et al.*, 2007).

2.2.2 Mechanisms of Wrist Injuries

Snowboarding injuries are often the result of a fall (63 to 93%) (Idzikowski *et al.*, 2000; Hagel *et al.*, 2005). Beginners may be more prone to wrist and forearm injuries as they are often less prepared for falls. A common instinctive reaction is to attempt to break a fall by placing the hands out to protect the head and trunk (Hsiao and Robinovitch, 1997). Upon contact, ground reaction forces travel through the hand transmitting across the carpals to the wrist (Burkhart and Andrews, 2010; Maurel *et al.*, 2013), which can create excessive bending, exceeding the wrists natural range of motion (hyperextension) and in turn causing sprains and/or fractures (Figure 2-2)

(Yamauchi *et al.*, 2010; Michel *et al.*, 2013). A less common mechanism of injury is rotational loading against a fixed object/surface on a hyperflexed wrist causing carpal fractures (Whiting and Zernicke, 2008; Shultz *et al.*, 2010). Studies indicate that backwards falls result in higher ground reaction impact forces than is the case with forward falls (DeGoede and Ashton-Miller, 2003; Greenwald *et al.*, 2013) (e.g. 3,500 N for a backwards fall vs. 1,950 N for a forwards fall (Lehner *et al.*, 2014)) and consequently result in twice as many fractures (Deady and Salonen, 2010). Of the more serious wrist injuries, distal radius fractures (Figure 2-2) are the most common (Basques *et al.*, 2018), accounting for approximately two-thirds of all fractures, around twice the rate for alpine skiers (Dickson *et al.*, 2008).

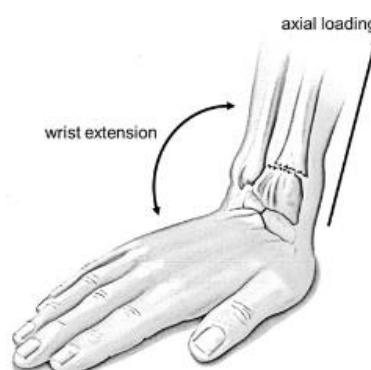


Figure 2-2 Distal forearm fracture caused by a wrist impact - causing a compressive load on a hyper-extensive wrist (Michel *et al.*, 2013)

2.2.3 Injury Criteria

To define hyperextension in terms of the wrist joint angle, the 'normal' non-injurious ranges of motion need to be quantified. The 'normal' ranges of motion of the wrist joint obtained in studies spanning healthy males and females from 17 to 54 yrs, are presented in Table 2-1, where all studies utilised active movements (Boone and Azen, 1979; Marshall *et al.*, 1999; Li *et al.*, 2005; Whiting and Zernicke, 2008; Levangie and Norkin, 2011; Shultz *et al.*, 2015). The overall mean (\pm standard deviation) across all studies for maximum extension was $73 \pm 4^\circ$, indicating that forced wrist extension exceeding $\sim 70^\circ$ may cause injury.

Table 2-1 Summary of the natural range of motion of the wrist joint found from the literature (mean \pm standard deviation) during active movement studies.

Reference	Participants		Flexion (°)	Extension (°)	Radial Deviation (°)	Ulnar Deviation (°)	Forearm Pronation (°)	Forearm Supination (°)
	No.	Age (yrs)						
(Boone and Azen, 1979)	56 ♂	>19	75 \pm 7	74 \pm 7	21 \pm 4	35 \pm 4	75 \pm 5	81 \pm 4
(Marshall <i>et al.</i> , 1999)	35 ♂	23 \pm 5	67	73	N/A	47	N/A	N/A
	19 ♀	22 \pm 5	72	79	21	46	N/A	N/A
(Levangie and Norkin, 2011)	Unknown		75 \pm 10	73 \pm 14	18 \pm 4	33 \pm 18	150	N/A
(Li <i>et al.</i> , 2005)	10 ♂	28 \pm 5	41	67	20	35	N/A	N/A
(Whiting and Zernicke, 2008)	Unknown		N/A	N/A	N/A	N/A	85 \pm 7	85 \pm 7
(Shultz <i>et al.</i> , 2010)	Unknown		90	70	20	30	83 4	90
Mean \pm SD	n = 120		70 \pm 16	73 \pm 4	20 \pm 1	38 \pm 7	98 \pm 35	85 \pm 5

There are challenges in defining the forces required to fracture the radius of a typical snowboarder, particularly ethical reasons, and the varying mechanical properties of cortical bone strength which change with age (Helelä, 1969). Studies on cadaveric wrists, in both a quasi-static and impact loading scenario, can give us an indication of the forces typically required to fracture the radius (Table 2-2– Adams (2018)). Distal radius fractures are the most prevalent wrist injuries amongst snowboarders, but many of the test scenarios for the studies in Table 2-2 were not representative of a snowboarding fall. From these studies, the mean force required to cause a fracture in the cadaveric wrist ranged from 1,104 to 3,896 N, with an overall mean (\pm standard deviation) of 2,671 \pm 787 N. The variation in fracture force between the studies could be due to many factors, such as the mix of genders, testing scenarios and the lack of knowledge relating to the cause of death.

Table 2-2 13 studies with fracture loads of adult cadaver forearms (adapted from Adams (2018)). QS = Quasi-static Compression, DC = Dynamic Compression, VI = Vertical Impact and II = Inclined Impact. (* signifies no standard deviation values available).

Reference	Samples		Experimental Setup		Mean Fracture Load \pm SD (N)
	No.	Mean Sample Age (yrs)	Velocity (ms ⁻¹)	Mass (Kg)	
(Frykman, 1967)	13 ♀	69 \pm 10	N/A	N/A	1,917 \pm 640
	9 ♂	59 \pm 17	N/A	N/A	2,769 \pm 1,266
(Horsman and Currey, 1983)	17 ♀	70 \pm 17	N/A	N/A	3,600 \pm 1,160
(Augat <i>et al.</i> , 1996)	12 ♀	85 \pm 8	N/A	N/A	2,008 \pm 913
	7 ♂	77 \pm 6	N/A	N/A	3,773 \pm 1,573
QS Mean \pm SD	n = 58	72 \pm 10	N/A	N/A	2,813 \pm 865
(Myers <i>et al.</i> , 1991)	18 ♀	76 \pm 7	0.025	N/A	3,180 \pm 1,000
	7 ♂	76 \pm 7	0.025	N/A	3,740 \pm 532
(Myers <i>et al.</i> , 1993)	11 ♀	74 \pm 9	0.025	N/A	1,580 \pm 600
	7 ♂	74 \pm 9	0.025	N/A	2,370 \pm 420
(Giacobetti <i>et al.</i> , 1997)	40	N/A	0.025	N/A	2,245*
(Augat <i>et al.</i> , 1998)	20	68 \pm 23	0.075	N/A	2,648 \pm 1,489
DC Mean \pm SD	n = 103	74 \pm 3	0.033 \pm 0.020	N/A	2,627 \pm 755
(Duma <i>et al.</i> , 2003)	17 ♀	67 \pm 13	N/A	N/A	2,820 \pm 1,205
(Lubahn <i>et al.</i> , 2005)	11 ♂	76	N/A	46	3,896 \pm 1,992
VI Mean \pm SD	n = 28	72 \pm 6	N/A	46*	3,358 \pm 761
(Frykman, 1967)	6 ♀	71 \pm 6	2.660	32	1,863*
	4 ♂	53 \pm 15	3.120	37	2,769 \pm 1,266
(Greenwald <i>et al.</i> , 1998)	12	47	2.800	23	2,821 \pm 763
(McGrady <i>et al.</i> , 2001)	10	N/A	3.900	N/A	1,104 \pm 119
(Lubahn <i>et al.</i> , 2005)	9 ♀	76	4.000	27	2,920 \pm 1,198
(Burkhart <i>et al.</i> , 2012)	8	61 \pm 10	3.400	7	2,142 \pm 1,229
(Zapata <i>et al.</i> , 2017)	15 ♀	80 \pm 16	2.000	13	2,170 \pm 811
	15 ♂	78 \pm 8	2.000	13	3,756 \pm 1,164
II Mean \pm SD	n = 79	67 \pm 13	2.985 \pm 0.769	22 \pm 11	2,443 \pm 801
Overall Mean \pm SD	n = 268	70 \pm 10	1.720 \pm 1.617	25 \pm 13	2,671 \pm 787

Cadaveric studies have also highlighted that wrist protectors can protect against wrist fractures, with an example of the experimental test setup shown in Figure 2-3a (Lewis *et al.*, 1997; Moore *et al.*, 1997; Greenwald *et al.*, 1998; Staebler *et al.*, 1999; McGrady *et al.*, 2001). Greenwald *et al.* (1998) was the only study to report forces, highlighting that a higher peak force was needed to cause fracture when a wrist protector was fitted to the cadaver, compared to no wrist protector being present ($3,808 \pm 271$ N vs. $2,281 \pm 763$ N). Other studies compared the number of drops to cause fracture (Lewis *et al.*, 1997), the strains along the cadaver arm during impact (Staebler *et al.*, 1999) and the types of fractures that occurred between cadavers impacted with and without a wrist protector (Moore *et al.*, 1997; McGrady *et al.*, 2001).

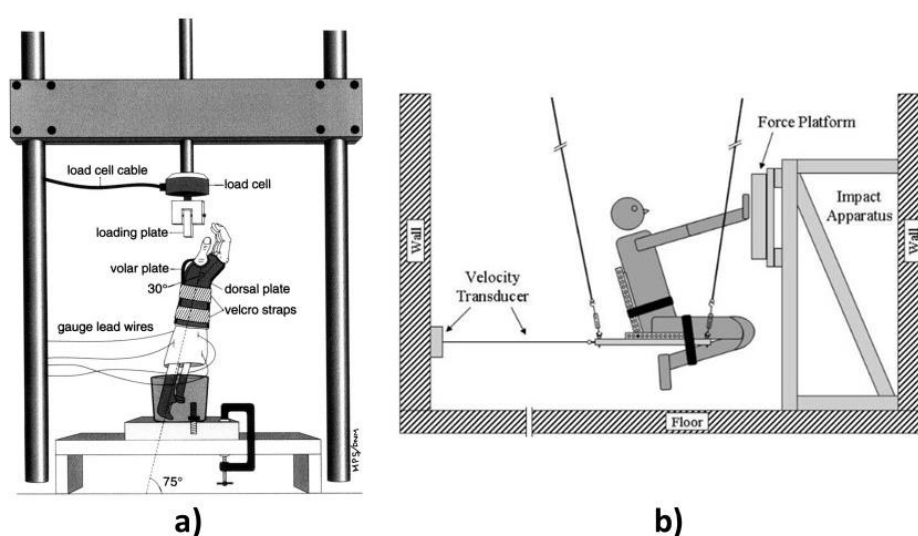


Figure 2-3 Example of experimental setups (a) impact onto a cadaveric arm (Staebler *et al.*, 1999) and (b) participant testing (Burkhart and Andrews, 2010).

A limitation of using data from these cadaveric studies is that the specimens were from an elderly population (mean \pm standard deviation = 70 ± 10 yrs old). As many snowboarders are young (SIA research, 2014), the fracture forces from these cadaveric studies may be lower than those required to fracture the wrist of a typical snowboarder. Another limitation to cadaveric studies is that the in-vitro response would be different to that of the in-vivo response. The amount of muscle tissue, tendon interaction, bone and ligament strength would all have an effect on the forces to cause a distal radius fracture (Levangie and Norkin, 2011).

An alternative to cadaveric studies is controlled non-injurious testing with participants. These types of studies typically include dropping a participant either in a linear or pendulum motion, with outstretched arms, from a low height, onto a force

platform, to obtain impact loads at the wrist region (Figure 2-3b). While these studies do not present injury thresholds, in order to protect the participants, they can provide information on non-injurious loads that could be extrapolated. Participant tests have also been able to assess wrist protectors at non-injurious loads (Hwang and Kim, 2004; Hwang *et al.*, 2006; Burkhart and Andrews, 2010).

Greenwald *et al.* (2011) obtained the wrist joint angles and hand/ground impact forces during snowboarding falls with a bespoke instrumented glove. To measure wrist joint angles, the glove had a flexible bend sensor across the knuckles, with another across the wrist. Force sensing resistors were placed on the palm and fingers to measure impact forces. The study of 20 snowboarders (11 \leq 17yrs and 9 $>$ 17 yrs, 8 beginners and 12 advanced) over 128 non-injurious falls, reported a mean peak force of 266 ± 232 N and maximum wrist extension of $80 \pm 16^\circ$. The wrist extension angles reported are higher than 73° (mean 'natural' values) as reported in Table 2-1, while peak forces were lower than the range of 1,104 to 3,896 N, reported in Table 2-2. As the falls were non-injurious with fairly high wrist extension angles, this may suggest that a distal radius fracture is caused by both a high impact force and hyperextension, and not just hyperextension. The forces reported by Greenwald *et al.* (2011) are comparable to those from the laboratory based experiments of Burkhart and Andrews (2010) (332 ± 100 N) who used a human pendulum impact device. The wrist angles reported by Greenwald *et al.* (2011) are similar to those found by Schmitt *et al.* (2012b) who documented wrist angles during controlled backwards falls of participants onto a force platform within a laboratory ($85 \pm 7^\circ$ – left hand, $82 \pm 7^\circ$ – right hand).

2.3 Protective Mechanisms

Following the van Mechelen *et al.* (1992) model, the first two stages, i) establishing the injury problem and ii) the mechanisms of the injury, have been recognised, therefore iii) a preventive measure or programme needs to be introduced. DeGoede *et al.* (2003) suggest two methods to decrease forearm and wrist injuries amongst snowboarders, i) alteration to the fall kinematics (Figure 2-4) and ii) using PPE and more specifically wrist protectors. PPE is a piece of equipment worn to reduce the risk and severity of injuries within sport (Payne *et al.*, 2015a) and is often mandatory. The International Ski Federation (FIS) require competitors to wear helmets for all events in ski jumping, ski cross and snowboarding, with goggles, back protectors and gloves recommended (International Ski Federation, 2018). PPE is also

mandatory in other sports, such as ice hockey where all participants wear helmets and under 20s wear mouthguards, neck and throat protectors (International Ice Hockey Federation, 2018). A further example is boxing where mouthguards and protective hand bandages are required for all boxers and females have to wear breast protectors (International Boxing Association, 2019).

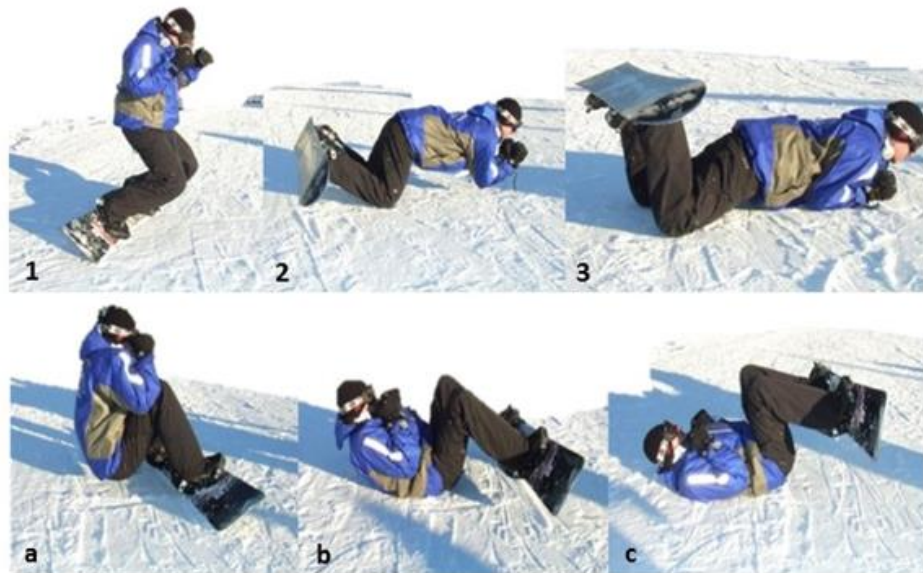


Figure 2-4 Suggested falling techniques for Snowboarding to minimise wrist injuries. 1 to 3 is the sequential steps for a forward fall and a to c for a backwards fall (modified from (Langran, 2013)).

PPE is often regulated by a standard (e.g. ISO, EN, BSI) prescribing the minimum performance criteria for its intended use. Examples of standards include (BS EN 14120:2003) - protective clothing in roller sports, (BS EN 1077:2007) – Helmets for alpine skiers and snowboarders and (BS EN 174:2001) – Personal eye-protection, Ski goggles for downhill skiing. Alongside helmets, goggles, back protectors and knee/elbow pads (McCann, 2013; Nate, 2019), wrist protectors have been recommended for snowboarders (Michel *et al.*, 2013). While there is not currently a standard for snowboard wrist protectors, a working group has been established to produce an ISO Standard for these devices (ISO/TC 94/SC 13). Details of the draft standard are in Section 2.4.3.

2.3.1 Wrist Protectors

Researchers recommend that snowboarders wear wrist protectors (Kim and Lee, 2011; Bladin *et al.*, 2004; Russell *et al.*, 2007; Michel *et al.*, 2013), as they can reduce wrist injury risk by more than half (Russell *et al.*, 2007), without increasing other injuries by translating loads, such as those to the elbow or shoulder (Chow *et al.*, 1996; Hagel *et al.*, 2005). It is unclear as to whether this reduction in injury risk

corresponds to any particular design of wrist protector, as most epidemiology studies do not mention the brand nor describe the product.

The role of a wrist protector is to reduce the risk and severity of injury by limiting hyperextension and peak forces, by spreading them over a greater amount of time to absorb impact energy (Hwang and Kim, 2004; Burkhart and Andrews, 2010; Maurel *et al.*, 2013; Michel *et al.*, 2013). When testing at non-injurious loads (250 N) with two different types of protectors fitted to a cadaveric wrist, Staebler *et al.* (1999) reported that wrist protectors transfer the applied loads away from the carpals and distal radius to the mid-forearm. The intended role of a wrist protector is clear, but there are many designs (Table 2-3), and the level of protection offered may vary between products.

2.3.2 Wrist Protector Design

Wrist protectors range in length (short/long), wearing style (integrated into a glove, splint under/over the glove) and vary in protective element constructions (splints, palmar padding etc.) (Dickson and Terwiel, 2011). Wrist protectors often consist of one or more splints and a palmar padding element, held together with fabric and foam to make a wearable device. Table 2-3 shows examples of commercial wrist protectors, demonstrating variety in protective elements, materials, and prices. The prices vary from £11 to £60, with longer protectors tending to cost more than their shorter counterparts.

The types of splints shown in Figure 2-5 are common within wrist protectors and can be situated on the palmar, dorsal or both sides (Table 2-3). Three of the protectors have just dorsal splints; three have just palmar splints and four have both. The splint absorbs energy upon impact but should be flexible enough to not limit wrist motion during normal use (Ronning *et al.*, 2001). Research involving participants suggests the anatomical position of the splint could influence protective performance (Hwang and Kim, 2004; Burkhart and Andrews, 2010; Michel *et al.*, 2013). The dorsal splint providing stabilisation and prevention of hyperextension. The palmar splint having the additional role of attenuating impact forces (Burkhart and Andrews, 2010; Michel *et al.*, 2013), reducing peak force by more than 35% when compared to a bare hand (Hwang and Kim, 2004).

Splints are often plastics fabricated by injection moulding, such as polyethylene, polypropylene or polyamide (Table 2-3). Injection moulded plastics (thermoplastics) are typically tough, rigid, and lightweight meaning they can withstand wear and

sudden impact forces without breaking, as well as being resistant to sweat and other chemicals (Higgins, 1994). Typically, thermoplastics have a Young's modulus in the range of 0.02 – 1.50 GPa and a flexural modulus in the range of 0.03 to 1.80 GPa (Matweb, 2018). One of the protectors in Table 2-3 had an aluminium palmar splint, which should exhibit a higher Young's modulus (~68 GPa (Matweb, 2019a)).

Table 2-3 A selection of wrist protectors currently on the market showing general make-up, number of splints, materials and prices (correct as of March 2019 - mean taken from 30 UK online stores over 26 months and rounded to the nearest £). Information obtained from store websites.

	Price (£)	Make-Up	Number of			Palmar Padding Element	Materials			
			Straps	Dorsal Splints	Palmar Splints		Splint	Padding	Fabric	Other
1	50	1 large splint on dorsal side	2	1	0	No	Thermoplastic - DuPont Hytrel	N/A	Neoprene / Lycra	Cotton
2	25	3 short splints on palmar side & 2 thin splints on dorsal side	2	2	3	Yes	Polyethylene	Polyurethane	Polyester Fibre Fabric	Nitrile-butadiene rubber
3	44	1 large splint with sliding mechanism for a buckle	3	1	0	No	Polypropylene	N/A	Nylon	Polyethylene, Polyurethane, Polyester
4	16	1 relatively thin palmar splint	1	0	1	No	Aluminium	N/A	Neoprene	Polyurethane, Urethane
5	60	1 large splint on each side	2	1	1	No (Skid Plate)	Thermoplastic - DuPont Hytrel	N/A	Neoprene / Lycra	Cotton, EVA, D3O®
6	17	1 relatively thin palmar splint	1	0	1	No	Aluminium	N/A	Neoprene	None
7	11	1 large splint on dorsal side	1	1	0	Yes	Polyamide	Nitrex Foam	Unknown	None
8	25	3 short splints on palmar side & 2 thin splints on dorsal	2	2	3	Yes	Information not available	Information not available	Information not available	Information not available
9	39	1 large splint on each side	2	1	1	No	Polyamide	N/A	Neoprene	Polyester

Protector



(1)



(2)



(3)



(4)



(5)



(6)



(7)



(8)



(9)



Figure 2-5 Identified protective elements of two different protectors (a) short protector and (b) long protector.

Three of the eight protectors in Table 2-3 have a palmar padding element, similar to the examples in Figure 2-5. The role of the padding element is to spread the impact force over a greater amount of time through energy absorption and dissipation (Michel *et al.*, 2013; Tyler, 2016). Not all protectors have palmar padding elements, which may be because some padding could be gained from the glove. Both Hwang and Kim (2004) and Maurel *et al.* (2013) suggest that common wrist protector designs should provide more padding on the palmar side of the protector to improve impact force attenuation. They propose achieving this through optimal material selection and biomechanical design. The padding element often consists of a foam, such as Polyurethane or Nitrex[®] foam (Table 2-3), which are typically lightweight and durable. These foams also present good energy absorption properties, as well as abrasion, and chemical resistance (Gibson and Ashby, 1999; Gama *et al.*, 2018). While a palmar padding element is not present in all protectors, many of the “other materials” that make up these products are foams, suggesting that there is padding throughout, just not necessarily concentrated at the palm.

The fabric that combines the protective elements into a protector can consist of a variety of materials (Neoprene, Nylon, Polyester fibre), all of which have good strength, durability, and abrasion resistant properties, well suited for snowboarding PPE applications (Mascia, 1982). Neoprene is commonly used for the outer fabric (Table 2-3), which could be because it is a soft rubber that can provide comfort as well as insulation and padding. Neoprene also has a low oxidation rate making it suitable for long-term outdoor use (Celina *et al.*, 2000; Thomas Publishing Company, 2018).

2.3.3 Usage Rates of Snowboard Wrist Protectors

Less than 10% of snowboarders are thought to wear wrist protectors (Idzikowski *et al.*, 2000; Langran, 2004; Hagel *et al.*, 2005; Ogawa *et al.*, 2010), and studies have investigated this lack of uptake using surveys (Langran, 2004; Kroncke *et al.*, 2007; Dickson, 2008; Dickson and Terwiel, 2011; Chaudhry *et al.*, 2012). These studies reported the main reasons for low usage were a lack of perceived need (33 to 56%) and discomfort (24 to 55%). Other reasons included a lack of trust, high cost, and a lack of knowledge of the product. Chaudhry *et al.* (2012) state that over 75% of snowboarders claimed they would wear wrist protectors if provided with strong evidence of a reduced risk of injury. This study was limited to 200 participants at one resort, giving a location bias, however this large percentage provides further justification for continued work into the performance testing of wrist protectors. Moreover, Ogawa *et al.* (2010) found from their survey of over 19,000 injured snowboarders that PPE use increased with skill level, which may partially explain why beginners have more injuries.

2.4 Experimental Testing

Van Mechelen *et al.* (1992) suggest that the fourth stage in the prevention of sports injuries sequence (Figure 2-1) is to assess the effectiveness of the preventative action. An established method for assessing the protective performance of sports products is laboratory based testing.

2.4.1 Testing of PPE

Testing of PPE should assess the roles intended for their use. Standards typically include an impact test, where the minimum acceptable levels of protection are outlined. The PPE is placed on a rigid anvil (based on a basic human surrogate) and subject to an impact from a drop mass/hammer at a prescribed energy (Figure 2-6). Load cells under the anvil, or an accelerometer in the drop mass, report

force/acceleration that usually has to fall below a specified value to pass the test (Payne, 2015).

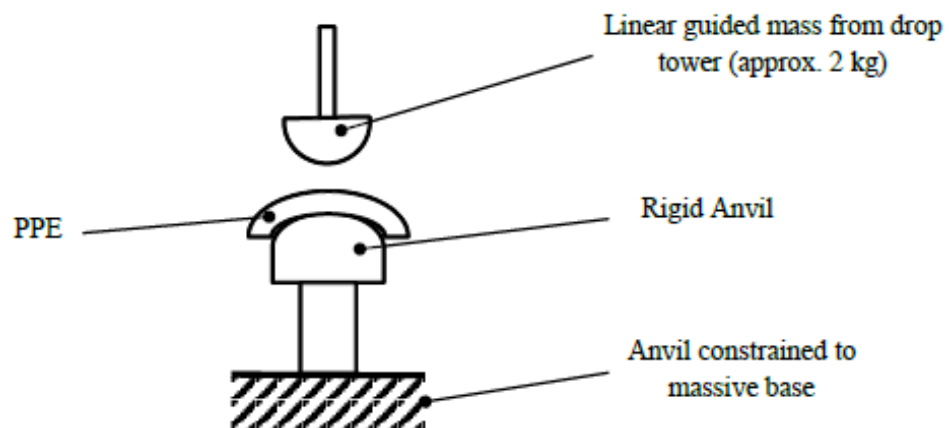


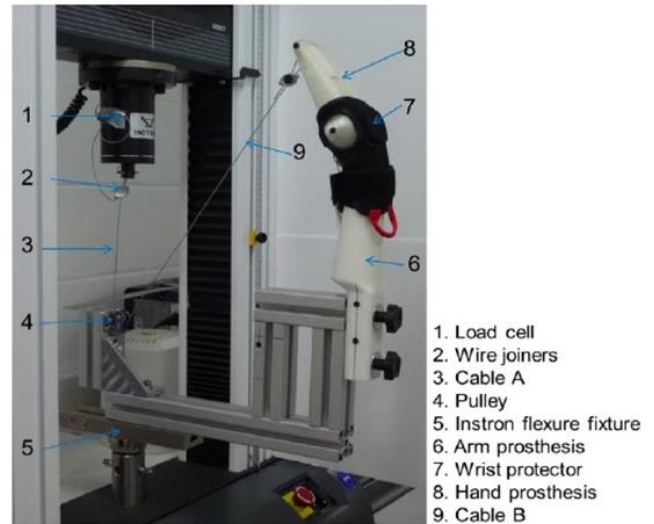
Figure 2-6 Schematic showing a typical impact test set up for a sports PPE safety standard (Payne, 2015)

Test setups within standards have been criticised for their poor representation of infield sporting scenarios. Ankrah and Mills (2003) argue that the impact energies within standards are reduced to protect the test equipment, rather than replicate the impact within the sporting scenario. Subsequently, it has been highlighted that there are discrepancies between the impact energies used in safety standards, and the reported mechanics from sports impacts (Payne *et al.*, 2013).

There is currently no standard for snowboard wrist protectors, however the roller sports standard for wrist protectors (BS EN 14120:2003) could serve as a starting point, as suggested by the white paper, arguing for a snowboard wrist protector standard (Michel *et al.*, 2013). There are two tests in EN 14120 i) an impact test to analyse the protectors ability to limit force under impact to the palm region (Figure 2-7a), and ii) a 'limitation of wrist extension' test (referred to as the bend test), to assess the ability of the protector to prevent hyperextension (Figure 2-7b) (British Standards Institution, 2003). In the impact test, the protector is mounted on a rigid hemispherical anvil (200 mm diameter), connected to a force sensor, and impacted by a 2.5 kg mass. The impact energy is 3, 4 or 5 J depending on the category of protector being tested, and the peak force should not exceed 3 kN for a pass. For the bend test, a protector is mounted on to a wrist surrogate (Figure 2-7b), a moment of 3 Nm is applied to the hand and its angle (relative to the long axis of the surrogate forearm) must be between 35° and 55° to pass.



a)



b)

Figure 2-7 Example setup of the two tests in EN 14120 (a) impact test (Schmitt et al., 2012a) and (b) limitation of wrist extension test (Adams et al., 2016).

2.4.2 Testing of Snowboard Wrist Protectors

As there is no standard for snowboard wrist protectors, alternative test methods have been explored. The two main approaches for impact testing protectors include, dropping a mass onto a static surrogate/protector or moving the surrogate onto a rigid surface, either in a linear (drop tower) or angular (pendulum) motion (Table 2-4). Using a load cell/force platform to obtain the transmitted force is common, as is using a potentiometer to measure wrist angle. To date, testing has included cadaveric studies, biomechanical studies with the use of participants and tests using surrogate arms, covering a range of impact loads from non-injurious to injurious scenarios.

Table 2-4 Experimental test setups and instrumentation used for impact testing of wrist protectors

Reference	Surrogate	Test Setup	Instrumentation
(Kim <i>et al.</i> , 2006)	Instrumented dummy arm (5 th percentile)	Free-falling surrogate on a vertical slider onto an aluminium block	Load cell and rotary potentiometer
(Schmitt <i>et al.</i> , 2011)	Rigid domed anvil (radius: 100 mm)	Protector held in place on top of anvil, free falling drop mass on vertical slider	Force sensor
(Greenwald <i>et al.</i> , 2013)	80-ShoreA cast polyurethane wrist based on a human arm.	Free-falling surrogate on a vertical slider onto a load cell covered in a laminate of latex and neoprene sponge	Force plate, wrist angle sensors, 2-D video recording and flexible bend sensors
(Maurel <i>et al.</i> , 2013)	Cast body filler hand	Free-falling weighted hand on a vertical slider onto a load cell covered in a 3mm rubber layer	Load cell and accelerometer
(Thoraval <i>et al.</i> , 2013)	Axson PX212 resin wrist and forearm based on several scans of wrists	A guided mass onto a fixed surrogate	Force plate, laser displacement sensor and accelerometer
(Adams, 2018)	CNC aluminium hand and Nylon SLS forearm	Impact pendulum onto a fixed surrogate	Load cell, potentiometer and high-speed photogrammetry

Few studies have compared commercial snowboard wrist protectors. Schmitt *et al.* (2012a) assessed the suitability of adapting the bend and impact test outlined in EN 14120 for snowboard wrist protectors, highlighting some limitations. Limitations to the bend test were due to the specified surrogate i) not allowing for testing of gloves as there are no fingers, and ii) being an overly simplified representation of the wrist, so protectors may not fit well. These concerns were addressed by Adams *et al.* (2018), who developed the EN 14120 bend test surrogate by adding fingers for gloves, while also investigating two additional surrogates. Adams *et al.* (2018) demonstrated that surrogate design influenced the stiffness of wrist protection performance. When compared to a scanned arm and the EN 14120 surrogate, the geometrically shaped surrogate gave the most repeatable results (Figure 2-8).

Adams *et al.* (2016) also found that protector strapping tightness influenced the results of the bend test.

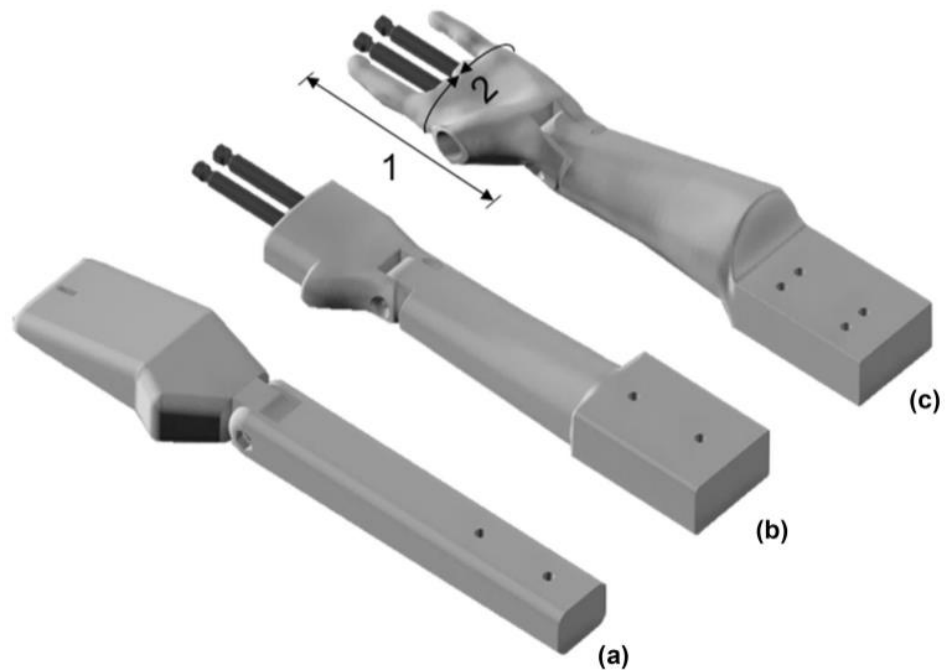


Figure 2-8 Surrogate designs that were compared by Adams *et al.* (2018) (a) EN 14120, (b) geometric (used in ISO/DIS 20320) and (c) scanned arm. Image taken from Adams *et al.* (2018). An engineering drawing of the geometric surrogate can be found in Appendix 10.A.

For the impact test, Schmitt *et al.* (2012a) highlighted limitations; i) the impact energy being low compared to backwards snowboarding falls (Schmitt *et al.*, 2009) and ii) the rigid anvil set up may be overly stiff compared to snow/ice. A further limitation of the impact test is that it only assesses the palm region, whereas a combination of force attenuation and prevention of wrist hyperextension are requirements of a wrist protector. Adams (2018) looked to overcome issues of the impact test in EN 14120, by using a more realistic impact energy, a more compliant striker and a wrist surrogate suitable for testing all roles of the protector. The rig developed by Adams (2018) had a pendulum arm, which can be released from a pre-set height to impact a wrist surrogate (Figure 2-9a). The surrogate was based on a laser scan of a human hand and forearm and consisted of an aluminium CNC machined hand (Protolabs, UK) and a steel core surrounded by a 3D-printed polyamide casing (Materialise, UK) to provide the arm profile (Figure 2-9b).

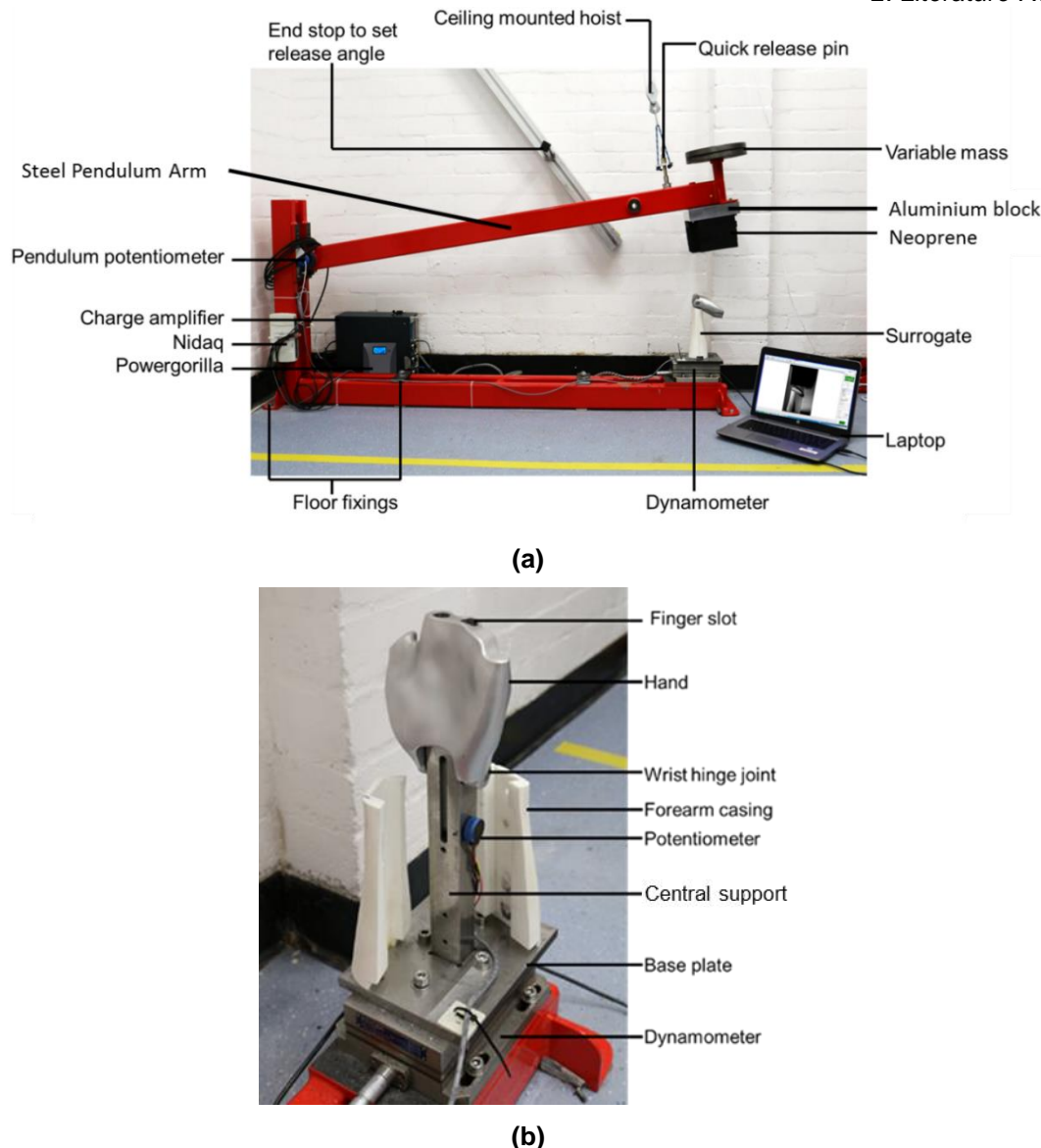


Figure 2-9 Impact rig developed by Adams (2018) (a) full impact rig set up, (b) detailed view of the wrist surrogate. Images modified from Adams (2018).

Adams (2018) developed the rig to replicate the loading case of Greenwald *et al.* (1998), who used a drop tower rig to impact test cadaveric arms. Additional mass (total of 23 kg) was attached to the cadaveric arms which were dropped from 0.4 m (impact velocity 2.8 ms^{-1} with 90 J impact energy) to generate radius fractures. Initially, Adams (2018) set the mass and release height of the pendulum arm to match those of the drop tower used in the Greenwald *et al.* (1998) study (23 kg and 0.4 m), but the gradient of the loading region of the force vs. time curve was considerably steeper than that of Greenwald *et al.* (1998). As a result, Adams reduced the mass of the pendulum arm to 15.3 kg (effective mass of 10.7 kg), and then tuned the stiffness of the rig to match the loading case of Greenwald *et al.* (1998) by attaching a stack of five polychloroprene blocks (50 ShoreA neoprene) (Boreflex Ltd., Rotherham, UK) (10 cm, 2.6 kg) to the end of the pendulum arm via

an aluminium plate (4 cm, 2.2 kg) (for more details on this process see Adams (2018)). The number of polychloroprene blocks was selected based on an iterative process until a desirable match was achieved between the loading curves. Polychloroprene within a pendulum impact test was used in a similar manner by Schmitt *et al.* (2018), whilst developing impact test methods for ice hockey boards, adding compliance to the setup whilst demonstrating repeatability.

Both Schmitt *et al.* (2012a) and Adams (2016; 2018) found differing performances between the designs of commercial wrist protectors and the range of protection offered. However, all data shows that the addition of a protector, of any design, reduced impact peak forces. Depending on the impact energy and the protector being tested, the reduction in peak forces were not always below the force required to cause a distal radius fracture (1,104 to 3,896 N - Table 2-2), indicating a wrist fracture may still be likely (Giacobetti *et al.*, 1997; Greenwald *et al.*, 1998; McGrady *et al.*, 2001).

2.4.3 Draft Standard for Snowboard Wrist Protectors (ISO/DIS 20320)

The draft standard includes two tests adapted from EN 14120; a mechanical bend test and an impact test. The bend test was based on the method proposed by Adams *et al.* (2016) and uses a more geometrically shaped surrogate, based on anthropometrics (Figure 2-8b). The impact test is adapted from EN 14120 as described by Schmitt *et al.* (2012a), despite the limitations highlighted previously. An impact test that is more applicable to snowboarding is desirable. This will ideally be a simple method that can test both roles of the wrist protector simultaneously, providing a more representative assessment of how it is required to perform. The implementation of an ISO standard for snowboard wrist protectors will help govern these devices and give users confidence that they can trust the product and increase the awareness of need, in turn increasing usage rates.

2.5 FE Modelling

Traditional experiments enable comparative testing of products and physical prototypes, but they are not always suitable for design optimisation and are limited when it comes to predicting the influence of design changes (Valentini *et al.*, 2015). FE modelling is an alternative method to assess the effectiveness of stage four of the prevention of sports injuries sequence (Figure 2-1) (van Mechelen *et al.*, 1992). An FE model can allow engineers to determine and understand the role of key aspects of a design, gaining information beyond that usually established in an

experimental environment. Gaining additional knowledge is especially true for impact scenarios where the mechanism and dynamic behaviour can be understood in detail, obtaining more information such as temporal deformation and force at specific locations, which otherwise would not be easily determined. FE analysis can be used to analyse PPE, such as wrist protectors under varying impact energies computationally, allowing analysis and simulation of the unknown prior to the need for prototypes (Mills and Gilchrist, 2008; Burkhart, 2012; Gialain *et al.*, 2016). This allows FE models to be used for improving performance, injury reduction or cost reduction through being able to vary influential parameters such as material selection or design.

2.5.1 FE Process

Fundamentally, FE modelling consists of dividing a geometry into multiple shapes (mesh), in order to compute different selected parameters (e.g. stress or strain), at locations throughout a part. There are two types of FE solvers; implicit (time-independent) and explicit (time-dependent). Implicit analysis is used for static structural problems whereas explicit is used for dynamic impact problems. The process of implicit modelling does not involve time and damping, therefore is achieved through solving the equilibrium Equation 2-1 (Lee, 2015; Balakrishnan *et al.*, 2017). Where $\{F\}$ the force vector calculated according to the loading conditions, $[k]$ is the stiffness matrix constructed according to the geometries and material properties and $\{x\}$ is the displacement vector which is the unknown parameter, but it's outputs are based on the support conditions.

$$\{F\} = [k]\{x\} \quad \text{Equation (2-1)}$$

For explicit solvers, FE modelling is accomplished through expressing the conservation of mass, momentum and energy through a series of equations known as Lagrange formulations. For each time step, Lagrange formulations are solved for each element within the model based on information provided by the previous time step. Explicit FE modelling can be expressed by Equation 2-2, which is the equation of motion for the whole domain being analysed (Lee and Liu, 2012). Where $[m]$ is the global mass matrix, $[c]$ is the global damping matrix, $[k]$ is the global stiffness matrix, $\{x\}$ is the global nodal degrees of freedom and $\{F\}$ is the load vector.

$$\{F\} = [m]\{\ddot{x}\} + [c]\{\dot{x}\} + [k]\{x\} \quad \text{Equation (2-2)}$$

Analysing wrist protectors under a dynamic impact scenario will require an explicit FE solver. There are many explicit FE codes available, such as ANSYS®/LS-DYNA®, ABAQUS, Pam-Crash® and SIMPACK. For explicit impact modelling, it appears that ANSYS®/LS-DYNA® is well used in the research sector (industrial sector unknown) (Table 2-5 and Table 2-6). ANSYS®/LS-DYNA® can solve large strain dynamic simulations making it a suitable tool for assessing the effects of impact loading. The software capabilities have been demonstrated by previous PPE impact models (Coto *et al.*, 2012; Tinard *et al.*, 2012; Mao *et al.*, 2014; Brodin and Wass, 2016; Darling *et al.*, 2016), as well as by Burkhart (2012) when simulating fall kinematics onto an outstretched hand.

The FE modelling process is cyclic but is broken down into key steps (Figure 2-10). A breakdown of these steps as interpreted from a selection of notable sports engineering FE papers, modelling PPE are shown in Table 2-5 and studies that use similar materials to those seen in snowboard wrist protectors are shown in Table 2-6.

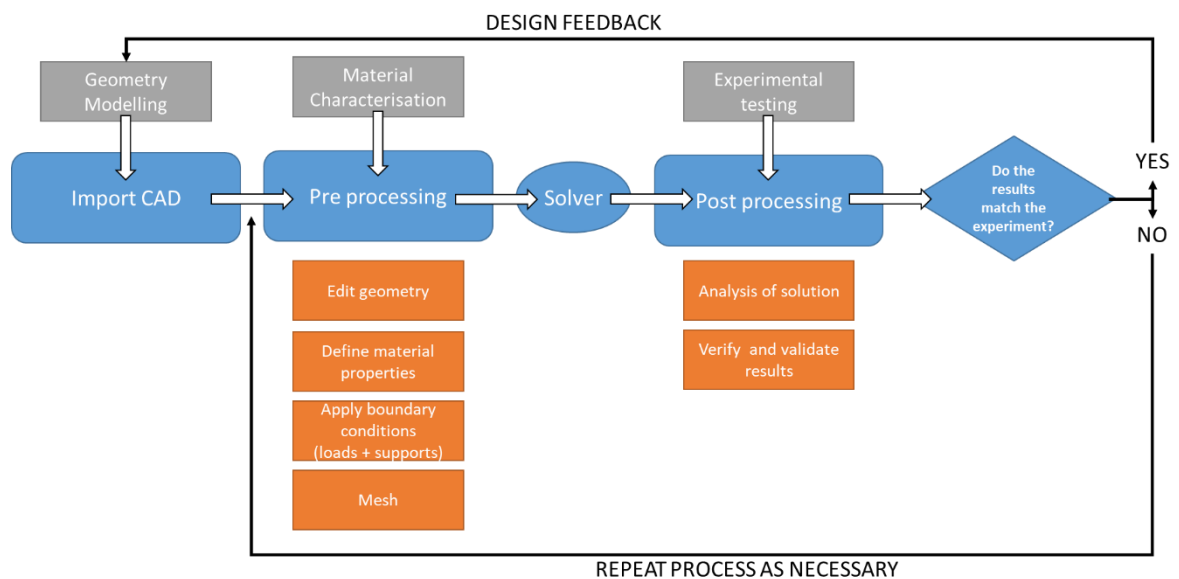


Figure 2-10 Flowchart of the FE modelling process

Table 2-5 A selection of notable sports engineering FE papers modelling PPE impacts highlighting the software used, how the geometries were created, details of supports and boundaries and the material models.

Reference	Application	Geometry Creation	Supports	Boundary Conditions	Material Models	FE Solver
(Ankrah and Mills, 2003)	Football shin guards	Tibia modelled as a hollow cross-section tube – generated in CAD	Tibia simply supported at both ends	Not stated	Zotefoams EV30 (EVA) Foam, Leg muscle/soft tissue – Hyperelastic Ogden , Tibia and shin guard shells – Linear Elastic	ABAQUS
(Ankrah and Mills, 2004)	Football ankle protection (shin guards)	Fibula modelled as a cylinder with an 8mm hemispherical end and an axis of rotational symmetry – generated in CAD	Tibia simply supported at both ends	Fibula = fixed, stud position was ramped downwards by 10mm	EVA Foam, Leg muscle/soft tissue – Hyperelastic Ogden , Tibia and shin guard shells – Linear Elastic	ABAQUS
(Schmitt <i>et al.</i> , 2004)	Hip protector impacts	Geometry created in CAD	Not stated	Not stated	Femur, Pelvis, Support, Joint surfaces - Linear Elastic	ABAQUS
(Mills and Gilchrist, 2008)	Bicycle helmet impact – comparison of helmet features	Scanned bicycle helmet & head form	Helmet shell inner surface tied to the liner outer surface.	Penalty friction formulation and tangential frictional parameters used to reproduce experimental data.	Extruded polystyrene foam – Crushable Foam	ABAQUS
(Coto <i>et al.</i> , 2012)	Nose protector impact with solid ball	CT scan of anatomical structures	Not stated	Not stated	Bone – Linear Elastic , Soft tissue – Hyperelastic Ogden , EVA flexible – Hyperelastic Ogden , EVA rigid – Von Mises bilinear elastoplastic	LS-DYNA®

Reference	Application	Geometry Creation	Supports	Boundary Conditions	Material Models	FE Solver
(Tinard <i>et al.</i> , 2012)	Impact protection of motorcycle neck braces	Geometry of the helmet was provided by the manufacturer in as a CAD file	Foam and outer shell were tied	Frictional contact between impactor + outer shell and Headform + Foam	Neck brace – Rigid , Helmet composite outer shell – *MAT_ENHANCED_COMPOSITE_DAMAGE , Helmet foam - *MAT_CRUSHABLE_FOAM	LS-DYNA®
(Luo and Liang, 2013)	Sports helmet design and virtual impact testing	CT and MRI of the subjects head, geometric shapes for the helmet	Not stated	No sliding between foam liner and composite shell. Interaction between head and foam liner described by contact elements.	Helmet (composite made of carbon fibres and polyester) – Linear orthotropic material	Not Stated
(Thoraval <i>et al.</i> , 2013)	Wrist protector effectiveness for snowboarders	Several scans of wrists and a European anthropomorphic database, wrist protector was digitised using a 3D scanner	Not stated	Pre fitting of the foam by webbing straps was realised by spring elements.	Anthropomorphic model, falling mass, wrist protector shell – Elastic Plastic , Foam – General nonlinear strain rate foam	Pam-Crash®

Reference	Application	Geometry Creation	Supports	Boundary Conditions	Material Models	FE Solver
(Mao <i>et al.</i> , 2014)	10-year-old forearm injury + wrist protector	Scaled from an adult radiologic image	The proximal end of the radius was allowed to move in a vertical direction but fixed in the other 2 degrees of freedom	Contacts between the plate & full hand defined with frictionless penalty-based surface-to-surface contacts.	Bone – Isotropic elastic plastic , cartilage – Linear Elastic	LS-DYNA®
(Lehner <i>et al.</i> , 2014)	Backwards fall in snowboarding	CT data 3D surface of the upper extremity exact bone geometries used	Not stated	Not stated	Not Stated	SIMPACK
(Brolin and Wass, 2016)	Equestrians simulation using virtual human body model	Geometries created in CAD, simplified safety-vest, horse body generated outer shape as seen from the side with splines & sweeping oval sections	Not stated	Contact defined between the ground and THUMS back. Gravity applied.	Nylon fabric (safety-vest) – Linear Elastic , foam core (safety-vest) – Low-density foam , Horse – Viscoelastic	LS-DYNA®
(Darling <i>et al.</i> , 2016)	American football helmet impacts	Geometry of the helmet created in CAD (Solidworks®, paired with a Global Human Body Model Consortium (GHBMC)	All parts of the helmet were tied	Not stated	Outer shell, headform and impactor – Linear Elastic , Energy and comfort foam - *MAT_LOW_DENSITY_FOAM	LS-DYNA®

(Signetti <i>et al.</i> , 2018)	Impact protection of back protectors for winter sports	Cylindrical impactor and a cylindrical plate to represent the protector – generated in CAD	Protector is a fixed support	2 way penalty based contact between the impactor and target	Constitutive law specifically developed for low density, closed cell foams	ABAQUS
---------------------------------	--	--	------------------------------	---	--	--------

Table 2-6 A selection of notable sports engineering FE papers that include similar materials to those within a snowboard wrist protector, highlighting the software used, how the geometries were created, details of supports and boundaries and the material models.

Reference	Application	Geometry Creation	Supports	Boundary Conditions	Material Models	FE Solver
(Tanaka <i>et al.</i> , 2006)	Golf ball impacts	Geometry created in CAD	Not stated	Frictional coefficient between the ball and target	Golf ball outer cover (ionomer resin) – Hyperelastic , Golf ball mid/core (polybutadiene rubber) – Hyperelastic Mooney-Rivlin + Viscoelastic Prony series	ABAQUS
(Price <i>et al.</i> , 2008)	Football material and model testing	Not Stated	Not stated	Not stated	Woven Fabric, EPDM Foam, PU Foam – Viscoelastic Prony Series	ABAQUS
(Ranga and Strangwood, 2010)	Quasi-static and dynamic behaviour of solid sports balls	Geometry created in CAD	Not stated	Not stated	Hockey Ball material – Viscoelastic Prony Series	ABAQUS
(Lin <i>et al.</i> , 2011)	Male leg & sportswear contact pressure and clothing deformation	Reconstruction of geometrical shapes of the commercial 3D anatomic male skin & skeleton model	Not stated	Not stated	Sports Tights – Hyperelastic Ogden	Not Stated

Reference	Application	Geometry Creation	Supports	Boundary Conditions	Material Models	FE Solver
(Nagaoka <i>et al.</i> , 2012)	Material modelling for swimwear	Not Stated	Not stated	Not stated	Swimwear – Anisotropic Hyperelastic Mooney-Rivlin	Not Stated
(Tanabe <i>et al.</i> , 2012)	Numerical analysis of competitive swimwear	Not Stated	The top & bottom surface & both side ends were constrained. For the pressure simulation, the inner surface was constrained.	Not stated	Swimwear – Anisotropic Hyperelastic Mooney-Rivlin	Not Stated
(Nevins and Smith, 2013)	Softball properties in ball-to-head impacts	2 softball models created in CAD, 50 th percentile adult male TUMS for head and neck	Neck muscles were not active in the model	Not stated	Softball (polyurethane) – Low-density foam	LS-DYNA®
(Shimana <i>et al.</i> , 2013)	Designing compressive sportswear	3D-CG-Human_Model used	Not stated	Not stated	Swimwear – Anisotropic Hyperelastic	Not Stated
(Smith and Burbank, 2013)	Foam material model in softball impact	Geometry created in CAD	Not stated	Not stated	PU foam – experimentally derived material loading response and phenomenologically developed unloading response using – Low-density foam	LS-DYNA®

Reference	Application	Geometry Creation	Supports	Boundary Conditions	Material Models	FE Solver
(Smith <i>et al.</i> , 2016)	Softball impact (ball on bat)	3D shape reconstruction from camera	Surface to surface contact defined between objects	Not stated	High-density polyurethane ball – Linear Viscoelastic, Low-density foam, Medium-density foam where the hysteretic unloading is a function of rate sensitivity, Hyperelastic	LS-DYNA®

2.5.2 Geometric Model

Techniques for creating geometries have been highlighted in Table 2-5 and Table 2-6. Arguably, the most common geometry creation method is the use of a computer aided design (CAD) package, where outer shapes have been created using images as templates (Brolin and Wass, 2016; Darling *et al.*, 2016) or adapting scans of human structures (Coto *et al.*, 2012; Luo and Liang, 2013; Thoraval *et al.*, 2013; Mao *et al.*, 2014; Lehner *et al.*, 2014). An alternative method has been to use a commercially available virtual human body model which is an advanced version of the crash test dummy with the addition of musculoskeletal components (bones, muscles, ligaments, tendons and organs) (Maeno and Hasegawa, 2001; LSTC, 2011) (Figure 2-11). While the use of a “full” virtual human model provides additional information within the FE model, the musculoskeletal components are challenging to validate experimentally, specifically when trying to replicate these in the laboratory environment. These types of models are typically used for assessing fatality and serious injury risk in high-energy automotive crash scenarios, and the accuracy of the wrist for simulating snowboarding relevant impacts is unknown.

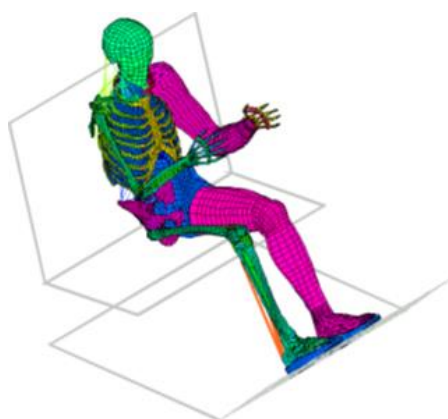


Figure 2-11 THUMS model of a male 50th percentile developed by Toyota. Half of the model is without muscles and skin to show details (Maeno and Hasegawa, 2001).

2.5.3 Material Characterisation and Modelling

It is vital to have dependable and accurate material models to achieve accurate FE simulations (Pugh *et al.*, 2010), although replicating material behaviour under different strains and strain rates is challenging (Ranga and Strangwood, 2010). Material characterisation most commonly includes uniaxial tensile, uniaxial compressive, shear and volumetric tests, if the material is compressible, providing the required strain rates and magnitudes for the material model (Lee, 2015). Other material characterisation techniques used to obtain material data at high strain rates include dynamic mechanical analysis (DMA) (Menard and Menard, 2006; Price *et*

et al., 2008), a split-Hopkinson pressure bar (Marais *et al.*, 2004) and time-temperature superposition (Schwarzl and Staverman, 1952). Alternatively, samples could be impact tested, with stress vs. strain data at high strain rates derived from temporal force (force vs. time) obtained from a load cell/accelerometer (Ankrah and Mills, 2003; Burbank and Smith, 2012; Signetti *et al.*, 2018). Characterising materials at both high strain and strain rates remains a challenge. Stress relaxation testing is also sometimes performed to obtain a materials viscoelastic response; this consists of compressing a sample at a high rate to a given strain and then holding for a period of time while measuring the force (Pugh *et al.*, 2010; Ranga and Strangwood, 2010).

In explicit simulations, a simple linear elastic material can be defined through three material constants, Young's modulus, Poisson's ratio, and density. When the material's stress vs. strain response becomes nonlinear then information beyond that defined in a linear elastic model is required to capture this behaviour. One way to describe non-linear behaviour is to use a hyperelastic material model, which can be obtained by curve fitting material test data (Ankrah and Mills, 2003; Ankrah and Mills, 2004; Mills and Gilchrist, 2008; Ranga and Strangwood, 2010; Lin *et al.*, 2011; Tanabe *et al.*, 2012; Tinarid *et al.*, 2012; Signetti *et al.*, 2018). Alternatively, a material model can be obtained through a data optimisation technique, otherwise known as "tuning", which essentially means adjusting a material's input data or adjusting the material model coefficients to match the simulations output to that of the experiment (Tanaka *et al.*, 2006; Tanaka *et al.*, 2012; Smith *et al.*, 2016; Darling *et al.*, 2016). To capture a materials viscoelastic properties within an FE model, there are two common methods; using a linear viscoelastic model (Brolin and Wass, 2016; Smith *et al.*, 2016) or through the addition of a relaxation function to a hyperelastic model in the form of a Prony series (Tanaka *et al.*, 2006; Price *et al.*, 2008; Ranga and Strangwood, 2010; Tanaka *et al.*, 2012).

Throughout the literature (Table 2-5) materials have been identified which are common to those found in wrist protectors (Table 2-3). The splint is commonly made of an injection moulded plastic, which has been incorporated into an FE model in other components of PPE as a linear elastic model (Ankrah and Mills, 2003; 2004; Thoraval *et al.*, 2013). The padding element has most often been identified as a foam, particularly polyurethane. Foam within PPE has been modelled using a low-density foam model (Brolin and Wass, 2016; Darling *et al.*, 2016) or a crushable foam model (*MAT_CRUSHABLE_FOAM) (Mills and Gilchrist, 2008; Tinarid *et al.*,

2012). Swimwear has been described as an anisotropic hyperelastic material using the Mooney-Rivlin model (Nagaoka *et al.*, 2012; Tanabe *et al.*, 2012; Shimana *et al.*, 2013), which can be related to Neoprene, a common outer fabric in wrist protectors. Another material found within wrist protectors is nylon fabric which has been modelled as a linear elastic model (Brolin and Wass, 2016) but also a viscoelastic Prony series (Price *et al.*, 2008).

2.5.4 Validation

An FE model's accuracy should be identified through validation, to enable it to become an effective tool for benchmarking and designing products. To ensure a robust validation, models should ideally be validated against an appropriate experimental test, using a variety of measurement devices (e.g. load cells, accelerometers, pressure sensors etc.) across a range of impact energies (Zaouk *et al.*, 1996). Table 2-7 shows how other researchers have validated their FE models of PPE. The use of an impact test, instrumented with either load cells placed under the sample or an accelerometer within the drop mass, is a common technique. Many researchers also include a high-speed camera/s to film the impact and track deformation of the object in the video footage.

Table 2-7 A selection of notable sports engineering FE papers modelling sports PPE impacts, highlighting how the FE models were validated. Studies involving snowboard wrist protector are highlighted in bold.

Reference	Application	Validation Technique
(Ankrah and Mills, 2003)	Impact testing of football shin guards	Impact test – accelerometer in the striker, high-speed camera. Tekscan flexiforce sensors
(Ankrah and Mills, 2004)	Impact testing of football ankle protection (shin guards)	Impact test – accelerometer in the striker, high-speed camera. Tekscan flexiforce single point button sensors.
(Schmitt <i>et al.</i> , 2004)	Impact testing of hip protectors	Impact test – accelerometer in the drop mass, load cell under sample, high-speed camera
(Tinard <i>et al.</i> , 2012)	Motorcycle helmet impact testing	Impact test based on ECE 22.05 standard - Accelerometer
(Luo and Liang, 2013)	Sports helmet design	Experimental data from the previous literature
(Thoraval <i>et al.</i>, 2013)	Wrist protector effectiveness for snowboarders	Impact test – force plate with 3 uniaxial piezoelectric load cells, laser displacement sensor, accelerometer mounted in mass
(Lehner <i>et al.</i>, 2014)	Backwards fall in snowboarding	Experimental studies described in literature-backwards fall onto a mat
(Darling <i>et al.</i> , 2016)	Impact testing of an American football helmet	Impact test – accelerometer on drop mass
(Signetti <i>et al.</i> , 2018)	Impact testing of back protectors	Impact test

2.5.5 FE Studies in Snowboarding

Previous FE studies modelling snowboard wrist protectors have not accurately recreated the geometry and materials of wrist protectors, considered all components nor recreated a representative way of attaching the wrist protector to the surrogate. Mao *et al.* (2014) accurately captured a child's forearm by scaling an adult FE model, based on radiological images (Godderidge, 1995) however, a conceptual L-shaped wrist protector was then bound directly to the arm via tied contacts (Figure 2-12a). Thoraval *et al.*'s (2013) model was based on a scan of a protector fitted to a basic wrist surrogate to produce the geometry required, however, only the palmar components were simulated (Figure 2-12b). Both studies showed that peak force was decreased when the wrist protector was applied however, Mao *et al.*'s (2014) study was not validated due to the lack of child forearm cadavers and Thoraval *et al.*'s (2013) study was only validated in terms of force.

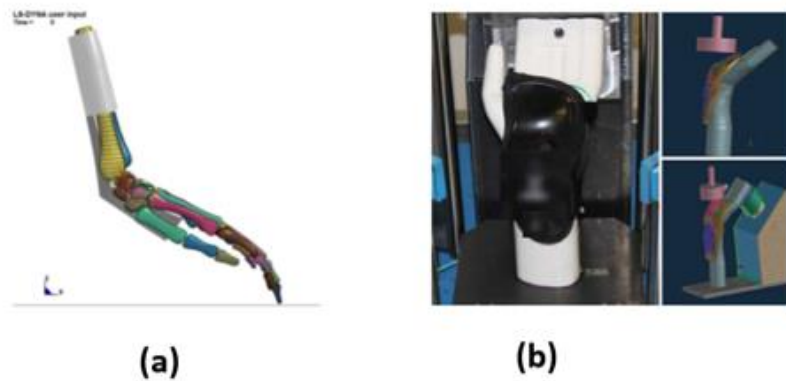


Figure 2-12 Example of previous FE studies of snowboard wrist protectors (a) conceptual L-shape wrist protector (Mao *et al.*, 2014) and (b) palmar impact replicating an experiment (Thoraval *et al.*, 2013).

Lehner *et al.* (2014) and Senner *et al.* (2019) used FE modelling in a different approach. Firstly, Lehner *et al.* (2014) used a multibody system to simulate snowboarding falls (Figure 2-13a), through detailing the exact bone geometries, based on CT data. The study concluded that the backwards snowboarding fall is the worst-case scenario, in agreement with others (DeGoede and Ashton-Miller, 2003; Schmitt *et al.*, 2012a). Senner *et al.* (2019) developed the work of Lehner *et al.* (2014) by adding a variety of wrist protector concepts to the multibody model (Figure 2-13b) and obtaining the resultant force at the forearm bone. The resultant forces predicted by the multibody model during a backwards fall, whilst wearing each concept was applied to an FE model of a radius, to determine whether they would cause fracture (Figure 2-13c). As the models were not validated against experimental data, the effect of design changes was expressed as a percentage reduction in force compared to an unprotected scenario rather than a specific peak force.

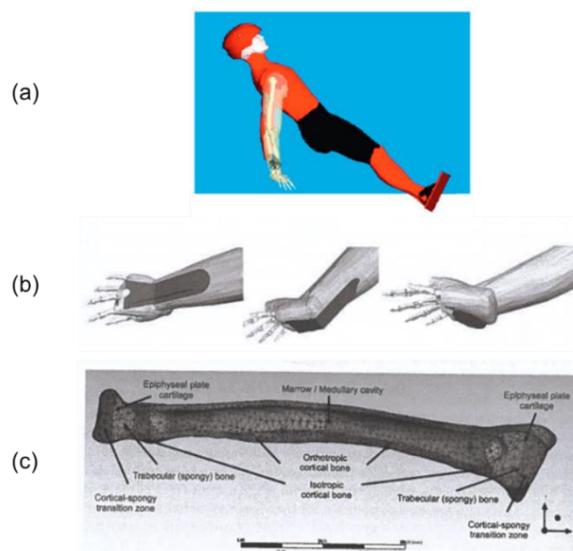


Figure 2-13 Senner *et al.* (2019) modelling process (a) multibody system model (Lehner *et al.*, 2014), (b) wrist protector concepts applied to the multibody model and (c) the FE model of a radius to determine whether the wrist protectors would prevent a fracture.

All three studies found that the high-stress area in the distal radius region decreased when a wrist protector was applied. However, Mao *et al.* (2014) found the stress was observed higher up the radius shaft when a protector was present. The authors argue that this shift in load is better as this type of break is easier to treat than a distal radius fracture, therefore proposing a load ‘shunting’ or a better energy-absorbing protector to be designed. When looking at the differences in protector designs more specifically, Senner *et al.* (2019) showed that the level of protection offered by the splint increased with its length, highlighting that a long dorsal splint or a protector with both a long palmar and dorsal splint provided the most protection. Another finding was that palmar padding added additional protection, but no advantage was gained by increasing its thickness from 5 to 10 mm.

2.6 Summary

The sports injury prevention sequence suggested by van Mechelen *et al.* (1992) (Figure 2-1) has been followed and the literature reviewed. The need to establish which wrist protectors provide the best protection for snowboarders is required. The process for achieving this will be a combination of geometrically accurate FE modelling of wrist protectors, with representative material properties, and experimental testing for validation.

Snowboarding sees injury rates that are higher than alpine skiers, with beginners being a vulnerable group who are most at risk. The wrist and forearm account for the highest injury rate, where the most common mechanism for injury is a fall and the worst case scenario is a backwards fall. Wrist injuries are most commonly

obtained through a compressive load applied to a hyperextended wrist resulting in distal radius fractures. Studies recommend that snowboarders wear wrist protectors, but there is no standardisation and it is unclear whether this injury reduction corresponds to any particular design for these products.

The role of a wrist protector is to reduce the risk and severity of injury by limiting hyperextension and peak forces, by spreading them over a greater amount of time to absorb impact energy. Wrist protectors should aim to limit loads transmitted to the wrist below a mean of ~2,670 N (range of 1,100 to 3,900 N) while preventing wrist extension from exceeding ~70°. While many wrist protector designs are available, three elements are common, a splint, a palmar padding element and a fabric/foam that combines the protective elements into a wearable device.

The protective performance of wrist protectors can be gauged through experimental testing in a laboratory. Previous experimental testing of wrist protectors has found that they decrease peak impact force, however not necessarily below a fracture threshold. There are also differences in wrist protector performance, due to design variation. In order to govern snowboard wrist protectors, an ISO standard is being developed that is based on the roller sports standard (EN 14120, 2003). Studies have highlighted some limitations with applying EN 14120 to snowboarding wrist protectors, therefore adaptations are being made accordingly. The current draft implements a bend test based on the work of Adams *et al.* (2016; 2018) and an adapted version of the impact test from EN 14120 (2003).

FE modelling can be used to analyse wrist protector designs under varying impact energies computationally, allowing analysis and simulation of the unknown prior to the need for prototypes, providing additional knowledge outside of what could be obtained experimentally. For a FE model to give the most realistic results, however, the geometry and materials of commercial wrist protectors needs to be accurately captured. Previous FE studies have not accurately recreated the geometry and materials of wrist protectors, considered all components nor recreated a representative way of attaching the wrist protector to the surrogate. There is, therefore, a gap in the literature for an FE model of a full wrist protector - surrogate impact that assesses all protective elements, which could provide more information as to which designs provide the most protection. In order to determine the models level of accuracy experimental testing should take place to validate the model across a range of variables (e.g. temporal force, deformation) and impact energies.

3 Wrist Protector Selection & Material Characterisation

3.1 Introduction

As highlighted in the published literature there is a need to establish which wrist protector designs provide the best protection. FE modelling has been identified as a technique capable of providing additional information to experimental testing alone. In addition, allowing for easier design interchangeability thus reducing the need for multiple prototypes. To build an FE model as a design tool, it is beneficial to create models of commercial protectors first, so preliminary experimental testing of these products can take place to validate these models (Figure 3-1). This chapter examined two wrist protectors for modelling based on a range of criteria. The constituent materials of these protectors were identified, allowing their properties to be estimated from the literature and/or characterised. This chapter provides an understanding of the material's behaviour which formed the basis of the material models used in the FE models in Chapter 5. This chapter addresses objectives one and two of the thesis; to identify the main components and materials of contemporary snowboard wrist protectors and to characterise the material properties of the main components.

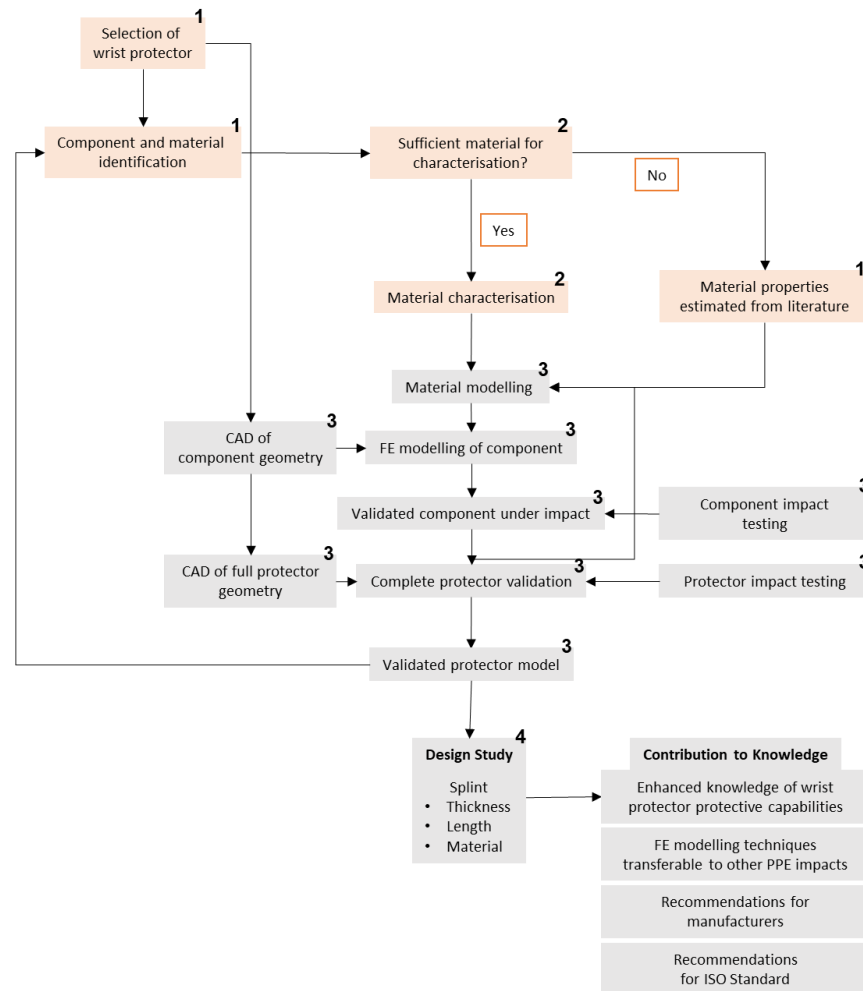


Figure 3-1 Schematic diagram indicating where this chapter (highlighted in orange) fits within the overall project (numbers correlate to the thesis objectives).

3.2 Protector Selection

There are a variety of wrist protector concepts on the market (Chapter 2, Table 2-3), with stores in the UK typically stocking two designs at a time (mean of 30 stores). The pool of protectors considered for modelling were representative of those found on the UK market, plus further designs selected in conjunction with the ISO standard working group (ISO/TC 94/SC 13) (Table 3-1). The label assigned to each protector shall be used to reference the individual protectors throughout this chapter. While not all protectors stocked in the UK were in the pool, they were represented in the sample via design similarities (e.g. one metal palmar splint).

3. Wrist Protector Selection and Material Characterisation

Table 3-1 Pool of wrist protectors considered for modelling selection, including details of the protector makeup, prices and mean number of UK stockists (data taken monthly from Nov 2016 to March 2019). Number of stockists is defined by whether the company has a website and a physical store in the UK (1 per company). Monthly data tracking can be seen in Appendix 10.B.

		A	B	C	D	E	F	G	H
Protector									
No. of stores		1 ± 0	7 ± 2	2 ± 1	15 ± 2	2 ± 1	0	1 ± 0	0
Price (£)		41	25	44	16	60	N/A	11	N/A
Overall Length (mm)		235	145	190	170	210	190	175	200
No. of straps		2	2	3	1	2	2	1	2
Dorsal Splint	No.	1	2	1	0	1	1	1	1
	Length (mm)	222	145	176	N/A	210	155	163	120
	Width (mm)	50 to 79	10 to 19	33 to 78	N/A	47 to 73	42 to 56	39 to 65	40 to 54
	Thickness (mm)	3	4	4	N/A	2	4	8 (centre), 2 (edges)	2
Palmar Splint	No.	1	3	0	1	1	1	0	
	Length (mm)	235	70	N/A	135	205	155	N/A	60
	Width (mm)	50 to 70	9	N/A	31	46 to 70	37	N/A	15
	Thickness (mm)	4	4	N/A	4	3	4	N/A	2
Padding Element		No	Yes	No	No	No (Skid Plate)	Yes	Yes	Yes

3.2.1 Selection Criteria

Using inclusion criteria as a guide (Figure 3-2), two protectors were selected from the pool of protectors (Table 3-1) for modelling. For each question, the answer “yes” was the desired outcome and the two protectors with the most “yes” responses, were chosen for modelling.

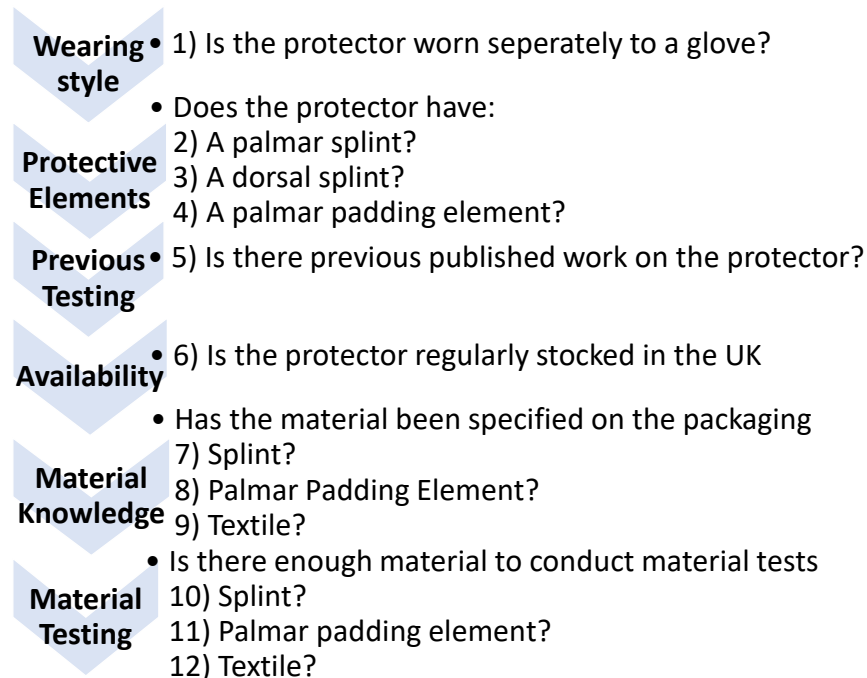


Figure 3-2 Flowchart of the inclusion criteria used to select the wrist protectors to model.

Reasoning for the criteria chosen:

1: A protector worn separately to a glove can be seen as a “worst case” scenario for injuries, due to there being less “padded material” that the glove would add. The worn separate design is also the simplest scenario to model, with a glove adding complexity.

2 to 4: Modelling a protector with all three elements of protection (palmar, dorsal splint and palmar padding element) allows future adaptations to assess individual contributions to protection levels.

5: A protector that has been used in previous experimental studies can provide additional data for validation (Adams *et al.*, 2016; Adams, 2018; Schmitt *et al.*, 2012a).

6: The project is more likely to influence consumer response if the protector chosen was commonly used. Dickson and Terwiel (2011) previously reported the type of wrist protectors worn when collecting data on injuries in snowboarding. Protector

stocks within the UK were also considered as an alternative indicator of popularity (Appendix 10.B).

7 to 9: Knowledge of the materials allows for published data to be used for initial model development, without prior need for material characterisation.

10 to 12: Having sufficient material, for the main components, to conduct material characterisation, would allow material models that are more robust to be developed compared to estimating properties from the literature.

3.2.2 Selected Protectors

Table 3-2 shows that protector B and E gave the most “yes” responses against the selection criteria questions (Figure 3-2). Both protectors have a palmar and dorsal splint and protector B has a palmar padding element. Dickson and Terwiel (2011) reported that the most popular wrist protector designs worn by snowboarders was a protector with “*a short, dorsal only or palmar and dorsal splint with some flexibility, worn separate from the glove*”, which matches the description of protector B. Out of the pool of protectors, B is the second most popular design to be stocked in the UK at a mean price of £27 RRP (March 2019). Protector E is the third most popular to be stocked at a mean price of £60 RRP (March 2019). Both protectors chosen have also been tested within the literature (Adams *et al.*, 2016; Adams, 2018; Schmitt *et al.*, 2012a). From now on protector B will be referred to as a short protector and E as a long protector (signified by the size of the splint elements Table 3-1). Modelling and validating two protectors with splint lengths at opposite extremes of those on the market will build confidence in the outputs from the model when manipulating the design to understand effects on protection.

Table 3-2 Results of the selection criteria questions (Figure 3-2) for the pool of wrist protectors (Table 3-1).

Protector	1	2	3	4	5	6	7	8	9	10	11	12	Total	✓
A	✓	✓	✓	✗	✗	✗	✓	✗	✓	✓	✗	✓	7	
B	✓	✓	✓	✓	✓	✓	✓	✓	✓	✓	✓	✓	12	
C	✓	✗	✓	✗	✓	✗	✓	✗	✓	✗	✗	✓	6	
D	✓	✓	✗	✗	✓	✓	✓	✗	✓	✓	✗	✓	8	
E	✓	✓	✓	✗	✓	✓	✓	✓	✓	✓	✗	✓	10	
F	✓	✓	✓	✓	✗	✗	✗	✗	✗	✓	✓	✓	7	
G	✓	✗	✓	✓	✗	✗	✓	✓	✗	✗	✓	✓	7	
H	✓	✓	✓	✓	✗	✗	✗	✗	✓	✓	✓	✓	8	

3.3 Material Identification

Following protector selection, the two protectors were deconstructed and the individual components were identified so their construction could be understood (Figure 3-3 and Figure 3-4 - images obtained using a flatbed scanner (Samsung MultiXpress X4300LX copier, Gyeonggi-do, Korea)).

3. Wrist Protector Selection and Material Characterisation

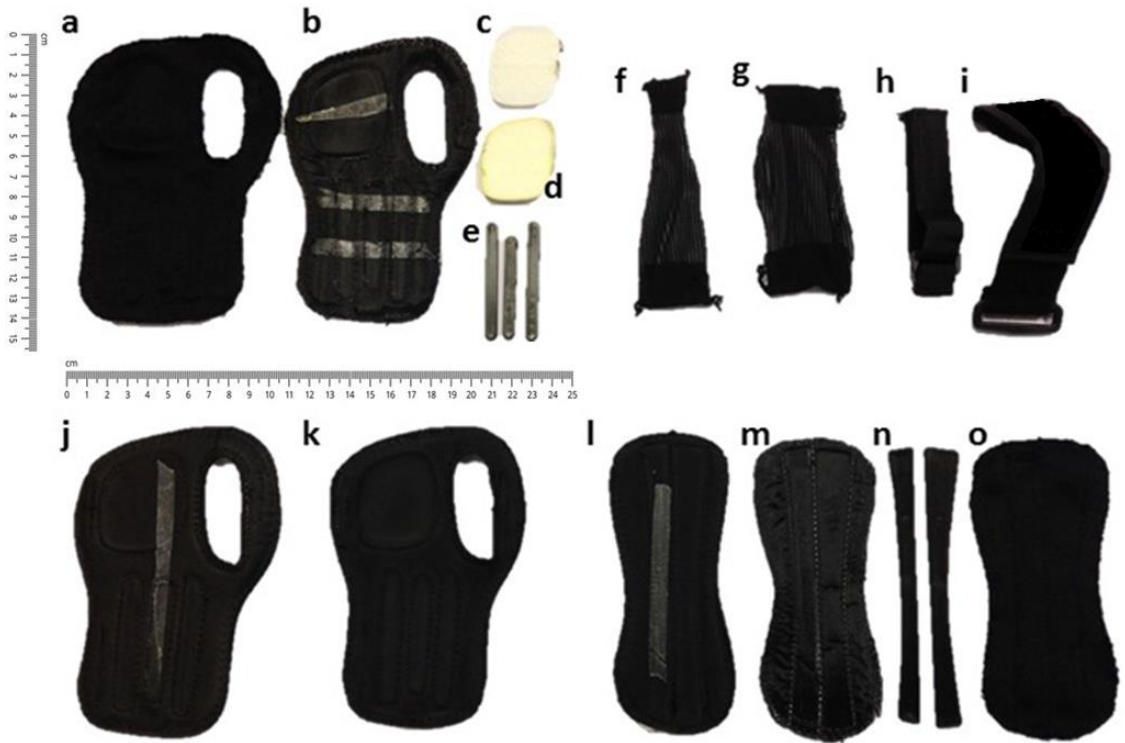


Figure 3-3 Components of the short protector chosen for modelling. a) Palmar textile front, b) palmar fabric insert, c) palmar padding element shell, d) palmar padding foam, e) palmar splints, f) side mesh, g) side mesh, h) top strap, i) bottom strap, j) palmar supporting foam, k) palmar supporting foam, l) dorsal supporting foam, m) dorsal fabric insert, n) dorsal splints and o) dorsal textile front



Figure 3-4 Components of the long protector chosen for modelling. a) palmar textile front, b) palmar supporting foam, c) side meshes, d) palmar splint, e) dorsal splint, f) dorsal supporting foam, g) skid plate, h) soft gel, i) D3O® 1, j) top strap, k) bottom strap, l) and m) foam.

3.3.1 Fourier Transform Infrared Spectroscopy (FT-IR)

Material identification was conducted using infrared spectroscopy (Spectrum Two™, Diamond ATR L1600235, PerkinElmer®). Through identifying the materials used during manufacture, an estimate of material properties could be gathered from the literature and employed into the FE model. FT-IR is the analysis of molecular vibrations within infrared light (Larkin, 2011). The absorption of the infrared radiation is measured and represented graphically in the form of wavelength vs. percentage absorption. Absorption rates at different wavelengths respond to particular chemical bonds, with stronger bonds vibrating at higher wavelengths (Kuptsov and Zhizhin, 1998). The FT-IR trace produced (Figure 3-5) is unique to each material, and comparison against those in the software library allows material identification. The match is given as a percentage where high is ranked at $\geq 90\%$, good is 80 to 89% and fair is 70% to 79%. Any material below 70% was reanalysed.

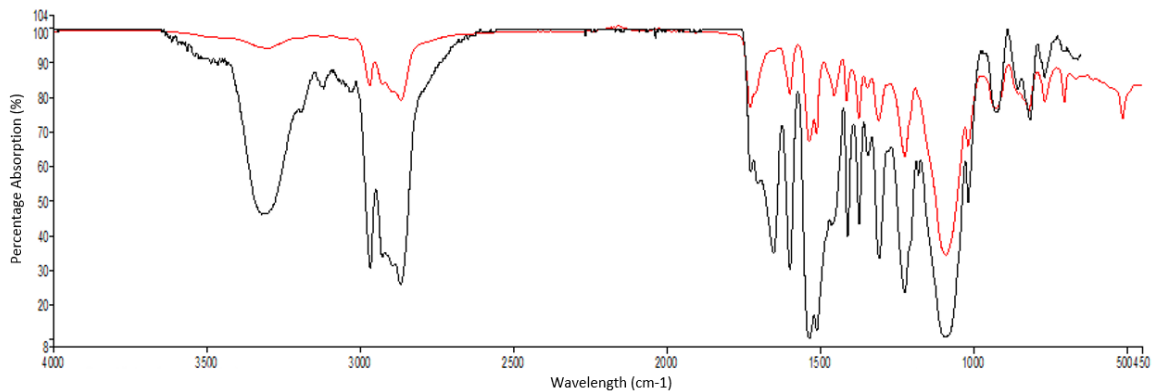


Figure 3-5 Example FT-IR trace for protector B, part d. The red line showing the analysed material and the black line showing the similar trace for a polyurethane foam (88% match).

Table 3-3 shows the identified materials and the confidence of match for each part, as well as typical mechanical properties identified from the literature (FT-IR traces in Appendix 10.C). The FT-IR trace is the result of eight scans at a resolution of 4 cm^{-1} . FT-IR has previously been used for identifying similar materials (ethylene vinyl acetate, nitrile butadiene rubber and polyurethane blend containing polydimethylsiloxane) used in winter sport back protectors (Nicoitra *et al.*, 2014).

Table 3-3 Break down of the identified materials for each part of the protectors in Figure 3-3 and Figure 3-4 and typical mechanical properties obtained from the literature.

	Part (Figure 3-3 and Figure 3-4)	Description	Identified Material	Infrared Spectroscopy Match	Mechanical Properties ¹			
					Density (g.cc ⁻¹)	Modulus of Elasticity (GPa)	Flexural Modulus (GPa)	Poisson's Ratio
Short Protector	A and O	Outer fabric	Polyester	High	1.38	2.500	5.500	0.33
	B and M	Fabric Insert	Polyester based blend	Good	1.38	2.500	5.500	0.33
	C	Palmar padding element shell	High Density Polyethylene (HDPE)	Good	0.92 to 2.55	0.031 to 1.500	0.280 to 1.810	0.40
	D	Palmar padding foam	Polyurethane foam (PU)	Good	0.01 to 1.39	0.0001 to 3.450	0.006 to 1.930	0.30 to 0.50
	E and N	Splints	High Density Polyethylene (HDPE)	Good	0.92 to 2.55	0.031 to 1.500	0.280 to 1.810	0.40
	F and G	Side mesh	80% Nylon, 20% Spandex	High	1.36	2.000 to 2.500	Unknown	0.32
	J, K and L	Supporting foam	Acrylonitrile Butadiene Rubber (NBR) ²	FT-IR inconclusive	1.00	0.007 to 0.024	Unknown	0.40 to 0.49
Long Protector	A	Outer fabric	Polyester	High	1.38	2.500	5.500	0.33
	B and F	Supporting foam	Polybutylene Terephthalate (PBT)	High	1.3 to 1.38	0.505 to 2.460	0.500 to 2.460	0.39 to 0.40
	C	Side mesh	80% Nylon, 20% Spandex	High	1.36	2.000 to 2.500	Unknown	0.32
	D and E	Splint	High impact Polypropylene (PP)	High	1.07 to 1.28	0.023 to 1.200	0.027 to 1.150	0.44 to 0.50
	G	Skid plate	High impact Polypropylene (PP)	High	1.07 to 1.28	0.023 to 1.200	0.027 to 1.150	0.44 to 0.50
	H	Soft gel	Unknown	FT-IR inconclusive	N/A	N/A	N/A	N/A
	I	Foam 1	D3O ^{®2}	FT-IR inconclusive	0.1 to 0.22	Unknown	Unknown	Unknown
	L and M	Foam 2	Poly ethylene Vinyl Acetate (EVA)	High	0.92 to 1.21	0.011 to 0.480	0.002 to 0.345	0.48

¹ Material properties obtained from a textbook (Higgins, 1994), online sources (MatWeb, 2019b; Michigan Tech, 2019) and literature in Table 2-5 (Ankrah and Mills, 2003; Ankrah and Mills, 2004; Coto *et al.*, 2012; Thoraval *et al.*, 2013)

² Material identified on product packaging

3.4 Material Characterisation

Material properties from the literature often consists of density and quasi-static material properties, such as Young's modulus and Poisson's ratio, which can serve as a starting point when building an FE model. However, this information may not be based on an identical material and published literature suggests that not all of a material's mechanical behaviour can be accurately modelled using solely these properties (Tanaka *et al.*, 2006; Pugh *et al.*, 2010). Materials from Table 3-3, such as polyurethane foam and polybutylene terephthalate rubber, have been shown to exhibit hyperelastic and viscoelastic behaviour (Cecere *et al.*, 1990; Lu, 2014; Mane *et al.*, 2017). To capture and quantify these behaviours, a range of tests were conducted, including tensile, compression and three point bend quasi-static tests, and stress relaxation tests. The methodologies used were developed based on previous literature (Pugh *et al.*, 2010; Ranga and Strangwood, 2010), the machine capabilities and pilot studies.

3.4.1 Methodology

Five size Medium pairs of each protector were purchased from the same stores at the same time (07/06/2018) (Mainpeak, AU and Demon, USA). The right hand of each pair was deconstructed for material characterisation and the left hand was reserved for impact testing (see Chapter 6). Table 3-4 shows an overview of the material characterisation tests conducted on each part of the protectors. Not all materials identified were characterised, due to material availability, or the component had limited thickness so was assumed to not add to the overall impact performance of the wrist protector, and was therefore not included in the model. The thickness of samples was measured using Vernier callipers (Composite Digital Vernier Caliper, Silverline[®]) to within ± 0.2 mm. The parts not included in the present model included the outer fabric (~0.7 mm), fabric insert (~0.1 mm), side mesh (~0.6 mm) and soft gel (~2.0 mm). For the other parts not characterised, their material properties were estimated using data from the literature (Table 3-3), due to the following reasons:

- Shell (short protector)/ Skid Plate (long protector) – This part was too small (~45 by ~38 mm) to obtain a tensile sample and too thin (~3 mm) to perform a compression test.
- EVA Foam (long protector) – This part was too thin (~3 mm) to obtain samples for testing.

Table 3-4 Different material characterisation tests conducted for each part of the protectors

		Strain Rates (s ⁻¹)						Percentage Strain (%)				
Part	Component Thickness (mm)	Compression Testing			Tensile Testing			Stress Relaxation			Three point bend test	
		0.02	0.2	2	0.02	0.2	2	50	20	10		
Short Protector	Pad	5.6 to 6.2	✓	✓	✓	x	x	x	✓	✓	✓	x
	Supporting Foam	7.2 to 7.4	✓	✓	✓	x	x	x	✓	✓	✓	x
	Splint	3.0	x	x	x	x	x	x	x	x	x	✓
	Strap	2.0	x	x	x	x	✓	x	x	x	x	x
Long Protector	D30 [®]	4.5	✓	✓	✓	x	x	x	✓	✓	✓	x
	Supporting Foam	4.5	✓	✓	✓	x	✓	x	✓	✓	✓	x
	Splint	1.9 to 4.5	x	x	x	x	x	x	x	x	x	✓
	Strap	3.0	x	x	x	x	✓	x	x	x	x	x

Uniform 38 mm diameter compression and dog bone tensile samples (BS 903-A2, 1995, type 4 with a gauge length of 35 mm) were extracted from the different parts of the protectors (Table 3-4). All samples were punched out of the parts using a die cutter and press (Figure 3-6).

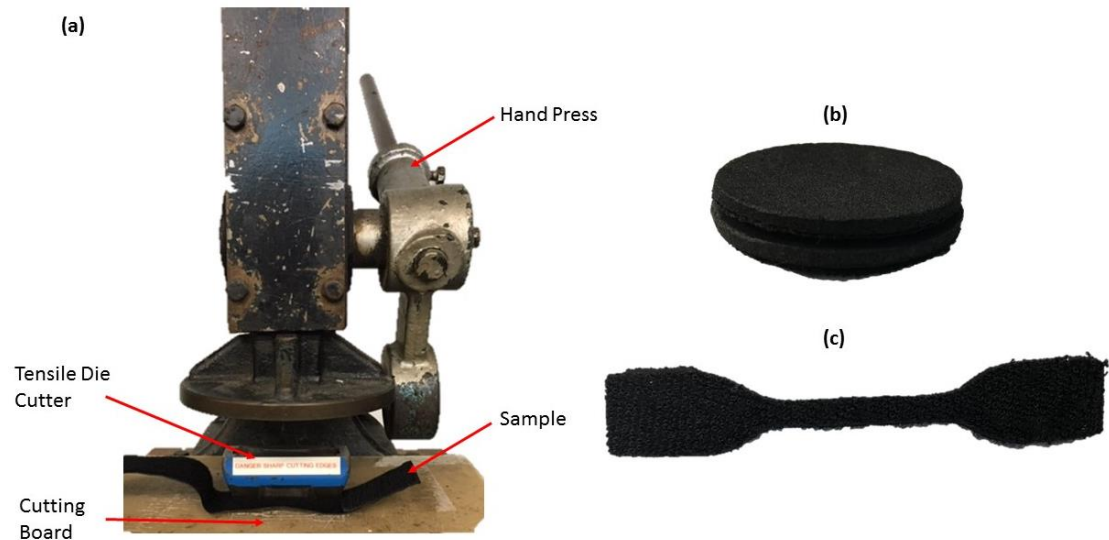


Figure 3-6 Example (a) set up for obtaining samples for material characterisation and a (b) compression and (c) tensile sample.

Compression tests were performed on a Hounsfield HK10S and Instron® Universal testing machine, to 50% strain to obtain stress vs. strain relationships, with the plates lightly greased. Pilot testing showed that compressing samples to more than 50% strain damaged samples. Each sample was compressed five times to check for stress softening e.g. Mullin's effect (Mullins, 1969; Diani *et al.*, 2009) and sample repeatability, with a 2-minute rest between loading cycles where the plates were wiped free from any debris and re-greased. For tensile testing, the sample was placed in pneumatic grips (HT400, Tinius Olsen Ltd) with a clamping pressure of 0.4 MPa and stretched until fracture. An approach speed of 1 mm.min⁻¹ was applied until a preload of 1 N for all testing. This was to remove "slack" in the system and to ensure the compression plate was fully engaged with the sample before testing. Tests were performed at room temperature (~22°), over four consecutive days, however, humidity was not measured or controlled, providing a limitation to this study.

Three strain rates were chosen, along a logarithmic scale of base 10, for quasi-static testing, which was in line with previous research (Pugh *et al.*, 2010; Ranga and Strangwood, 2010). Ideally, samples would be compressed at the strain and strain rates experienced during snowboarding falls, but there is limited knowledge in this

field of research. Staebler et al. (1999) measured bone strain when impacting a cadaver forearm with and without a wrist protector (Figure 2-3). The study found higher strains without a protector ($757 \pm 156 \text{ s}^{-1}$) compared to when a wrist protector was present (range of 267 to 768 s^{-1}), providing an indication as to the magnitude of strains, materials should be characterised at. However, for the range of material sample thicknesses (1.9 to 7.4 mm) and the machine capabilities, 2 s^{-1} was the highest rate achievable for compression testing, therefore, the three strains chosen were 0.02, 0.2 and 2 s^{-1} .

While the Hounsfield HK10S material testing machine is capable of displacement rates up to $500 \text{ mm}\cdot\text{min}^{-1}$, it cannot accelerate quickly enough up to these velocities at such small displacements; $300 \text{ mm}\cdot\text{min}^{-1}$ was the maximum displacement rate considered achievable. Therefore, low strain rates (0.02 to 0.2 s^{-1}) were performed on a Hounsfield HK10S material testing machine with a 100 N (Support Foam – Long protector) or 1 kN load cell (all other samples) and for high strain rates (2 s^{-1}) an Instron® Universal testing machine with a 5 kN load cell was used. Due to the Instron® having only a large load cell, it was not appropriate for testing at the lower strain rates (Davis, 2004). Instron® (2019) report that their load cells have an accuracy within $1/1,000^{\text{th}}$ of the load cells capacity. For a 5 kN cell this would be an accuracy of $\pm 5 \text{ N}$. Pilot testing indicated that this tolerance would result in errors of ~ 4 to 6% if tested on the Instron® with a 5 kN load cell, compared to $<1\%$ when using a 100 N or 1 kN load cell on the Hounsfield HK10S.

For each test, force vs. displacement data was obtained at 30 Hz, which was output as a Microsoft Excel 2013 sheet (.xlsx). The force was divided by the cross-sectional area of the samples ($1,134 \text{ mm}^2$ for compression samples and 8 mm^2 (short protector strap), 16 mm^2 (long protector fabric) and 12 mm^2 (long protector strap) for tensile samples) to obtain stress and the displacement was divided by the original thickness/length (Table 3-4) to calculate strain. Mean and standard deviation stress vs. strain curves were calculated for each sample at each strain rate to observe repeatability and rate dependency.

Compression testing samples were also subjected to stress relaxation testing to assess for viscoelastic response. Each sample was compressed to 50%, 20% and 10% strain at the highest displacement rate the Instron® Universal testing machine could achieve ($1,000 \text{ mm}\cdot\text{min}^{-1}$, equating to a mean ramp time of $0.18 \pm 0.03 \text{ s}$ for 50%, $0.08 \pm 0.01 \text{ s}$ for 20% and $0.05 \pm 0.01 \text{ s}$ for 10%) and held for 300 seconds,

3. Wrist Protector Selection and Material Characterisation

while force was recorded at a rate of 1 kHz (Instron® WaveMatrix™, v1.8). Samples were then rested for at least 30 minutes between compressions to allow for viscoelastic recovery (Pugh *et al.*, 2010). The force vs. time data was converted to shear response using Equation 3-1, ready to be fitted to a material model in ANSYS®/LS-DYNA®. The Poisson's ratio values used for each part were the median values taken from the literature (Table 3-3) (pad – 0.31, supporting foam – 0.48, D3O® – 0.48). Shear modulus was calculated; however, shear testing was not considered. The reason for not conducting shear testing was due to machine capabilities and the lack of material available to conduct these tests.

$$G = \frac{E}{2(1 + \nu)} \quad (\text{Equation 3-1})$$

Where G is shear modulus, E is Young's modulus and ν is Poisson's ratio

Issues arose whilst obtaining tensile and/or compression samples for the plastic splints from both protectors. The small splints from the short protector were trialled within a tensile test using two clamping methods including, i) clamping the ends of the splints directly and ii) setting the ends of the splints into acrylic (Figure 3-7) (cold cured Methyl Methacrylate, Mr Dental Supplies Ltd, UK) and then clamping the acrylic. All trials resulted in the samples failing at the grips, Davis (2004) states, “*any fracture outside of the gauge section may be sufficient to determine that the test is invalid*”, therefore these results could not be used and the samples were discarded. Five dorsal splints for each protector were therefore 3-point bend tested according to the ASTM D790 standard.



Figure 3-7 Example modifications to splints that were trialled to create a tensile sample

ASTM D790 standard states that the tests should be performed on “*uniform beams*” (ASTM, 2016). Pilot testing trialled making the splints from the protectors into a uniform cross sectional area through grinding the excess material away. This technique, however, resulted in imperfections and weak points along the splint length. It was, therefore, decided the splints should be tested using their original form and when calculating Young's modulus it was assumed they were uniform and a mean cross section of the splints (measurements taken every 20 mm) was used (short protector 10.4 x 3.0 mm, long protector 59.5 x 3.0 mm). The splints were

3. Wrist Protector Selection and Material Characterisation

therefore taken directly from the protectors and placed on a flexural fixture in the Hounsfield HK10S material testing machine, with the crosshead at the centre of the sample (Figure 3-8). For the short protector splint, the machine was equipped with a 100 N load cell, while pilot testing indicated that the long protector splint was stiffer and required a 1 kN load cell.

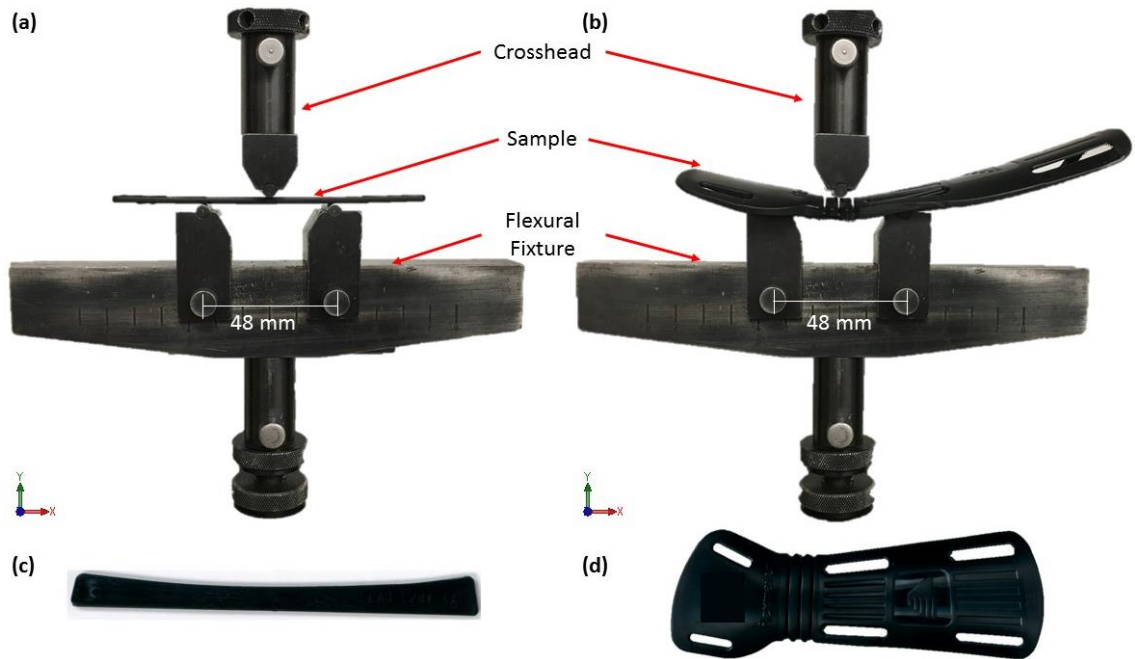


Figure 3-8 Three point bend test setup of the two protector splints: (a) short protector, (b) long protector. Top view of the splint geometry (c) short protector and (d) long protector.

ASTM D790 states that “a support span of 16:1 times the depth of the specimen is used” (ASTM, 2016) therefore, as both protector splints were 3 mm in depth, the flexural fixture was set to a span of 48 mm. The rate of the crosshead motion (R) of the testing machine was set to $13 \text{ mm}\cdot\text{min}^{-1}$ as calculated by Equation 3-2. A pre-load of 1 N was applied to ensure the crosshead was engaged with the specimen prior to the start of the test. ASTM D790 specifies that samples should be “deflected until rupture occurs or until a maximum strain of 5% is reached” therefore, the test was terminated at a displacement of 6.4 mm (Equation 3-3). Samples were tested five times, producing force vs. deflection data, with two minutes between repeats. A mean and standard deviation force vs. deflection curve was calculated for each splint.

3. Wrist Protector Selection and Material Characterisation

$$R = \frac{ZL^2}{6d} \quad \text{Equation 3-2}$$

$$D = \frac{rL^2}{6d} \quad \text{Equation 3-3}$$

$$\sigma_f = \frac{3PL}{2bd^2} \quad \text{Equation 3-4}$$

$$\varepsilon_f = \frac{6Dd}{L^2} \quad \text{Equation 3-5}$$

$$E_B = \frac{L^3m}{4bd^3} \quad \text{Equation 3-6}$$

Where: b is the width of the beam, D is maximum deflection, d is the depth of the beam, ε_f is the strain in the outer surface, E_B is the modulus of elasticity in bending, L is the support span, m is the slope of the tangent to the initial straight-line portion of the load vs. deflection curve, P is the load at a given point on the load vs. deflection curve, r is strain (0.05), R is the rate of the crosshead motion, Z is the rate of straining of the outer fibre (0.01), σ_f is the flexural stress

Using the output data, flexural stress (σ_f), flexural strain (ε_f) and modulus of elasticity (E_B) were calculated (Equation 3-4 to 3-6). The mean value for each sample was calculated and compared to those in the literature. For the short protector, made of HDPE, flexural modulus is reported to be in the range of 280 to 1810 MPa (Matweb, 2018). The long protector is made of DuPont Hytrel (specific grade unknown), who report the flexural modulus of this material to be in the range of 27 to 1,150 MPa (DuPont, 2017).

For uniform beams Equation 3-7 and Equation 3-8 can predict the force needed to achieve 5% strain within a three point bend test. As the samples were not uniform beams, a comparison was made to determine the effect of the additional sample design features and non-uniformity. The mean cross section of the splints (as previously described) was used to calculate the area moment of inertia about the horizontal axis (Equation 3-8).

$$P = \frac{D(48EI)}{L^3} \quad \text{Equation 3-7}$$

$$I = \frac{bd^3}{12} \quad \text{Equation 3-8}$$

Where: b is the width of the beam, D is the maximum deflection, d is the depth of the beam, E is the modulus of elasticity, I is the moment of inertia, L is the support span, P is the load at a given point on the load vs. deflection curve

Statistical analysis was conducted using Minitab® (v18 Statistical software, USA) to determine whether the samples were repeatable and similar to each other using a

3. *Wrist Protector Selection and Material Characterisation*
one-way analysis of variance (ANOVA). The stress for each sample at 50% strain for compression testing and 40% strain for tensile testing, as well as the force required to displace the splints of both protectors to 6.4 mm were compared. A coefficient of variance, expressed as a percentage, was also calculated to understand inter and intra sample repeatability (Equation 3-9) (Kennedy and Neville, 1986).

$$V = \frac{\sigma}{\mu} \times 100 \quad \text{Equation 3-9}$$

Where: V is the coefficient of variance, σ is standard deviation and μ is the mean.

3.4.2 Results

The results of the compression test at three strain rates for the supporting foams, pad and D3O® are presented in Figure 3-9. All components demonstrated a hyperelastic behaviour and can be seen to be rate dependent across all three strain rates tested because higher strain rates resulted in higher stress for a given strain. The palmar pad (Figure 3-9b) and D3O® (Figure 3-9d) demonstrated a typical foam curve, a high stiffness quasi-linear phase at low strain (~0.08 for 2s⁻¹ data), followed by a plateau region (between a strain of ~0.08 and 0.2) and finally densification at high strain (Gibson and Ashby, 1999). The plateau region occurs due to the cell walls collapsing, following which densification leads to an increase in stress as the cell walls come together making a solid base (Mane *et al.*, 2017). The two supporting foams presented an upturned S-shaped hyperelastic curve (Figure 3-9a and c), where force increased at a faster rate, the higher the strain applied.

3. Wrist Protector Selection and Material Characterisation

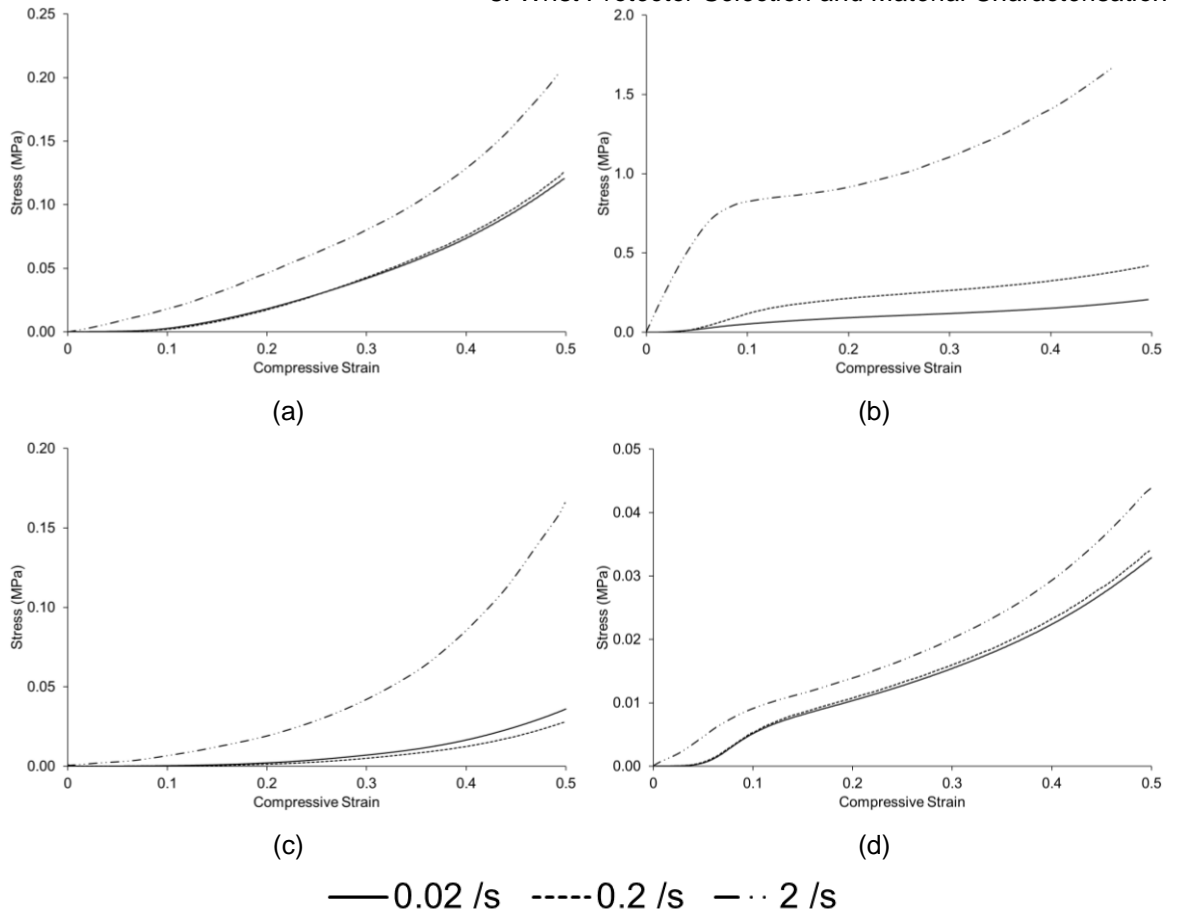


Figure 3-9 Mean stress vs. strain plot for an example compression sample, at 3 strain rates for: Short protector a) supporting foam and b) pad, Long protector c) supporting foam and d) D3O[®].

Within the 0.02 s^{-1} results, the first compression for all samples, except the short protector palmar pad, had a unique curve that was different from the subsequent repeats (Figure 3-10a). After the first compression, all samples were clearly repeatable and showed no signs of further softening or degradation after multiple compressions at the same rate. Sample consistency was low, (Figure 3-10b to e) (percentage variance at a strain of 0.5: short protector supporting foam = 7%, pad = 33%, long protector supporting foam = 20%, D3O[®] = 24%), where samples taken from the same part from five different protectors ranged in stress for the same applied strain. In compression testing, all samples were statistically different [short protector supporting foam $F(4, 20) = 74$, $p < 0.001$, pad $F(4, 20) = 273$, $p < 0.001$, long protector supporting foam $F(4, 20) = 122$, $p < 0.001$, D3O[®] $F(4, 20) = 2,779$, $p < 0.001$] (statistical analysis details in Appendix 10.D.1).

3. Wrist Protector Selection and Material Characterisation

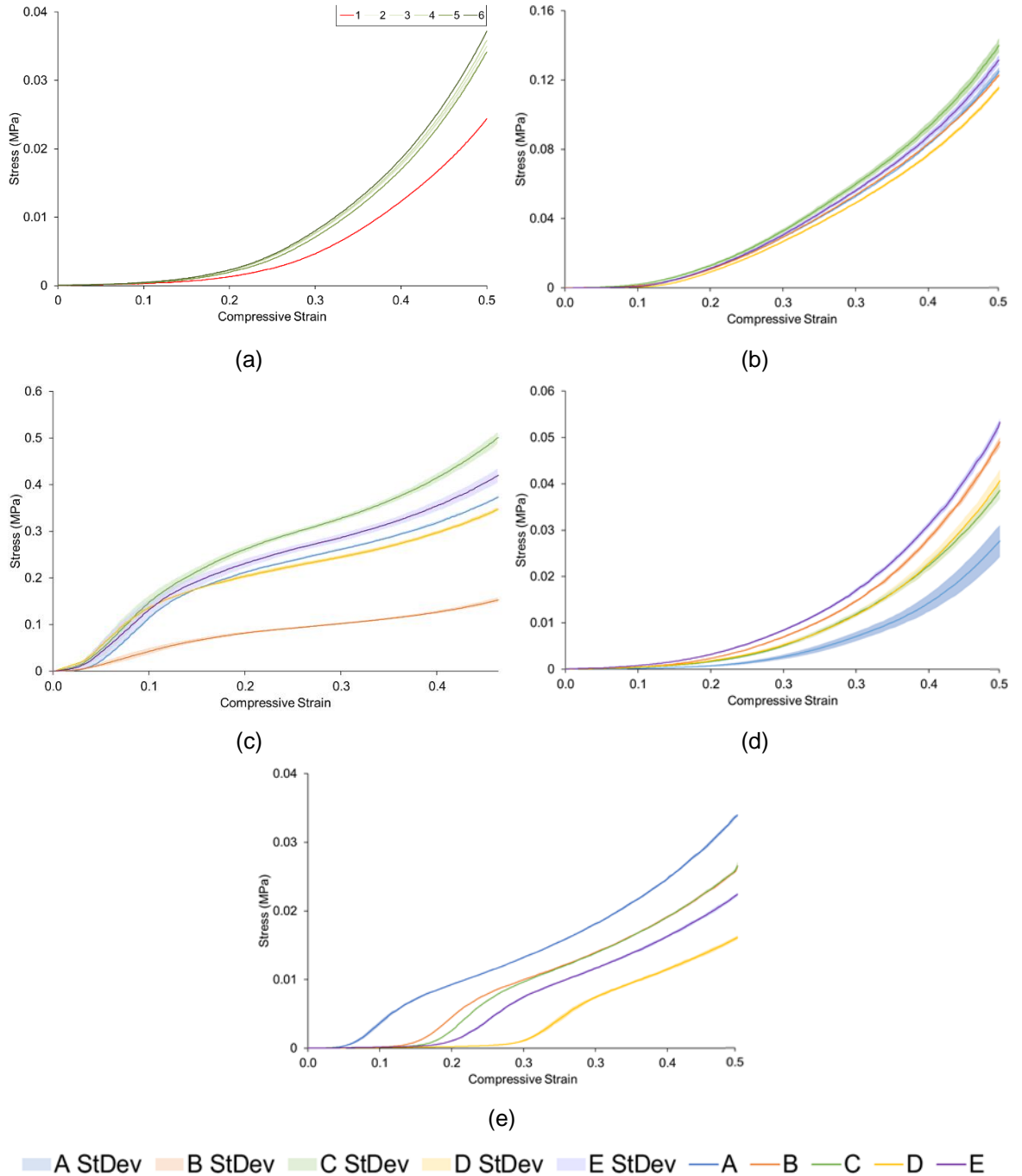


Figure 3-10 Stress vs. strain response for compression samples, showing (a) the unique first compression of the long protector supporting foam. Mean (\pm standard deviation) of five samples at 0.2 s^{-1} : short protector b) supporting foam and c) pad, long protector d) supporting foam and e) D30®.

Results of the tensile test for each part are presented in Figure 3-11. Pilot testing indicated that none of the parts were rate dependent in tension, therefore only the strain rate 0.2 s^{-1} was used for tensile testing. The long protector supporting foam exhibited a similar stress vs. strain response as that seen when under compression; a hyperelastic up-turned S-shaped curve (Figure 3-11b). The two strap samples (Figure 3-11a and c) exhibited a quasi-linear elastic response up until a strain of ~ 0.3 . After this point stress started to plateau until the samples fractured.

3. Wrist Protector Selection and Material Characterisation

Sample consistency in tension (Figure 3-11) was higher than samples in compression (percentage variance at a strain of 0.4: short protector strap = 7%, long protector supporting foam = 18% and strap = 5%). There was no significant difference between samples during tensile testing, apart from the strap of the short protector (Figure 3-11a) where one sample (d) out of five was significantly different to the others [F (4, 20) = 4, p = 0.018].

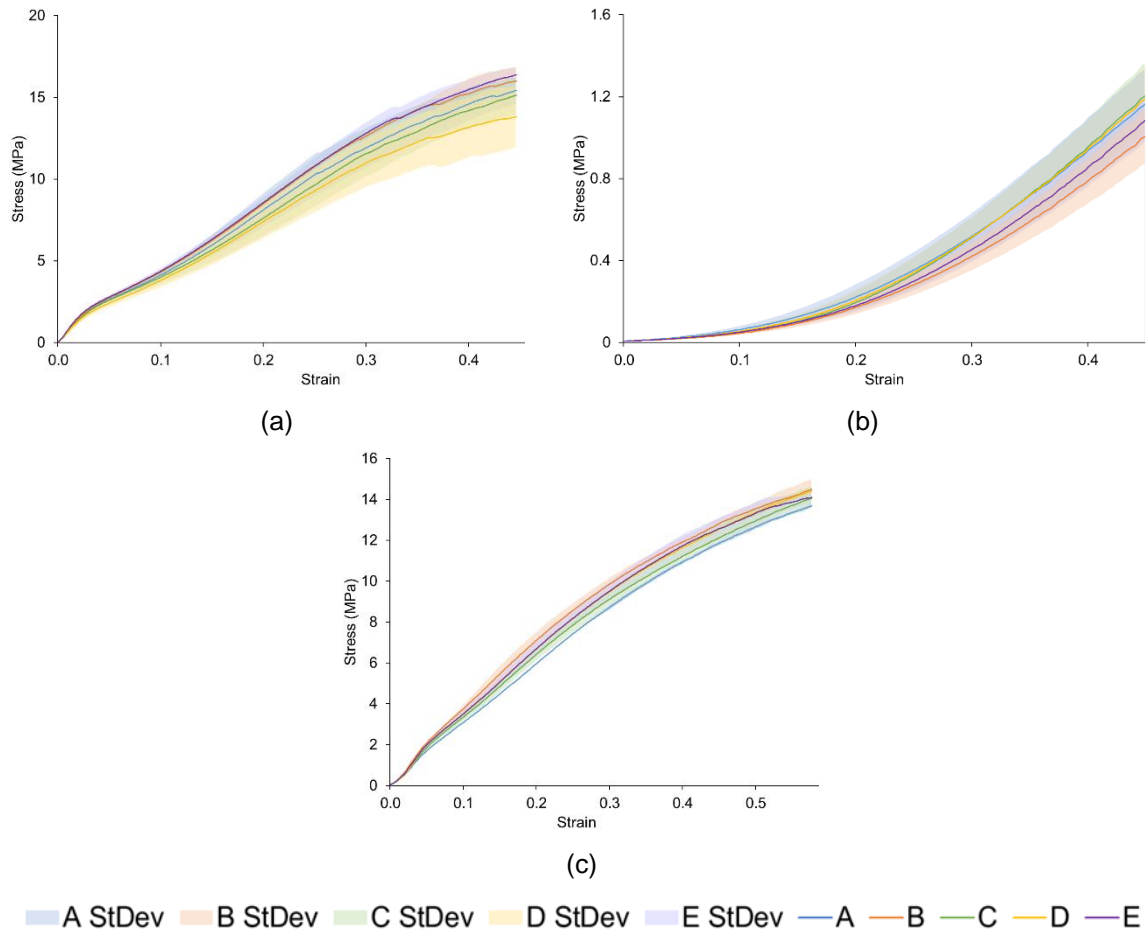


Figure 3-11 Mean (\pm standard deviation) stress vs. strain plots for five tensile samples at 0.2 s^{-1} of: short protector a) strap and long protector b) supporting foam, c) strap.

The shear modulus response over a logarithmic scale of time is shown for all compressive strains (50%, 20% and 10%) in Figure 3-12 for all parts and samples. All components demonstrated a viscoelastic response that was highlighted by a load vs. deformation relationship that was time dependent. When deformation was applied quickly, high stresses were initially produced but then the materials slowly moved molecules into a position to accommodate the force, causing a decrease in stress at a constant strain. The palmar pad can be seen to be more viscoelastic than the other three materials (Figure 3-12b) because it was able to re-distribute its molecules to lower stress areas quicker (Lakes and Lakes, 2009). The palmar pad (Figure 3-12b) did not change shear modulus with varying applied strains, meaning

it was linear viscoelastic (Lakes and Lakes, 2009; Pugh *et al.*, 2010). The supporting foams (Figure 3-12a and c) however, produced increasingly higher shear modulus, the higher the applied strain, demonstrating they exhibited non-linear viscoelastic behaviour. D3O[®] also produced different shear modulus at different applied strains, however, 20% strain produced higher shear moduli than 10% strains (Figure 3-12d). Tang *et al.* (2017) also found a cross over in moduli at intermediate strain rates for D3O[®] when looking at the mechanical properties. It is suggested by Tang *et al.* (2017) that the material initially has an elastic state at low strain rates, transitioning into a viscoelastic state at higher strain rates, and then further transitioning back to an elastic state at even higher strain rates.

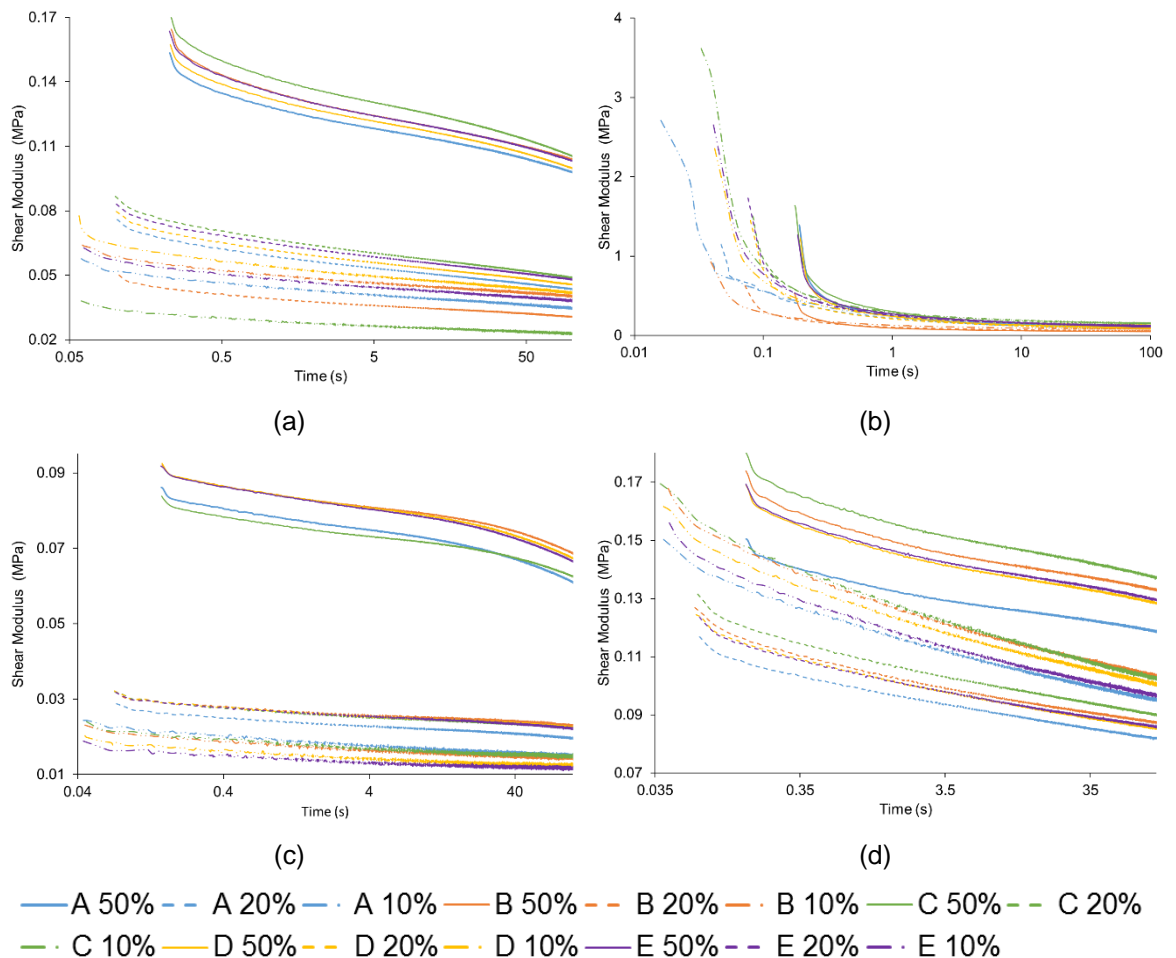


Figure 3-12 Shear modulus vs. time plots obtained from stress relaxation testing up to 50% , 20% and 10%, for five samples of: short protector a) supporting foam and b) pad, long protector c) supporting foam and d) D3O[®].

Figure 3-13 shows the results of the three-point bend test conducted on the non-uniform splints for both protectors according to ASTM D790. Both splints exhibited different shaped force vs. deflection plots where the short protector plateaued in force as it reached ~5.5 mm deflection, while the long protector tended to stiffen above ~5 mm. When each sample was subject to five repeats, no degradation was observed. However, as can be seen in Figure 3-13a all samples for the short

3. Wrist Protector Selection and Material Characterisation

protector were significantly different [F (4, 20) = 1,060, p < 0.001] from each other, apart from D and E, in terms of force for a given deflection (6.4 mm). For the long protector (Figure 3-13b), there was no significant difference between samples, apart from sample B which was significantly different to the others [F (4, 20) = 50, p < 0.001] (statistical analysis details in Appendix 10.D.1).

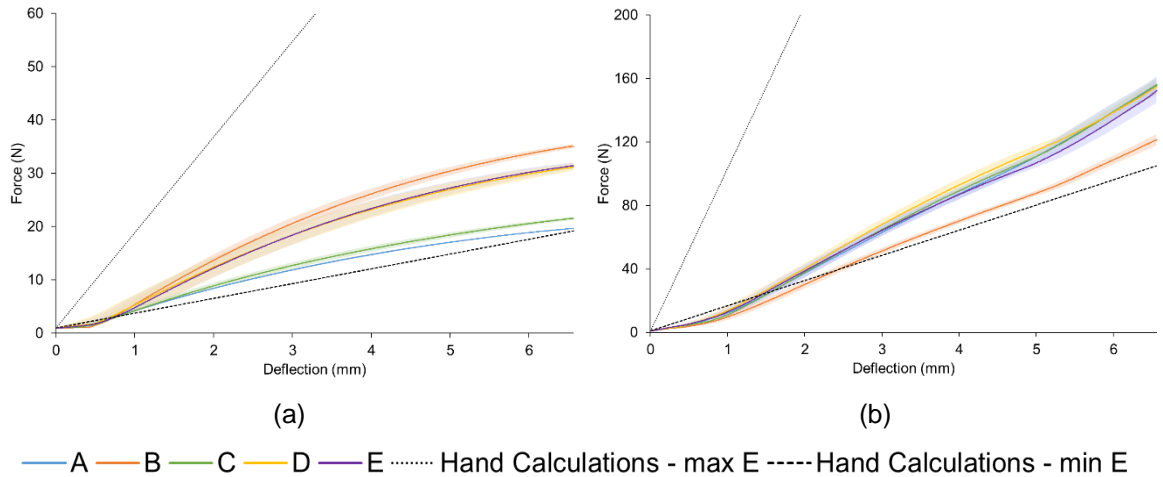


Figure 3-13 Mean (\pm standard deviation) force vs. deflection plots for three point bend testing of splint samples for (a) short protector and (b) long protector. Also shown by the black dashed lines are the hand calculation boundary limits using the maximum and minimum values of elastic modulus from the literature and the mean cross sectional areas of the samples.

By using the obtained force vs. deflection data found in Figure 3-13, the corresponding elastic modulus (MPa) for each sample was calculated and compared to values from the literature for the same materials (Matweb, 2018; DuPont, 2017) as shown in Table 3-5. Using the upper and lower limit for elastic modulus for each material from the literature, and the mean cross sectional areas of the samples, the force to achieve 5% strain was calculated for a uniform beam (black lines – Figure 3-13) and compared to the experimental three point bend test results.

Table 3-5 Mean (\pm standard deviation) calculated elastic modulus (MPa) for each splint sample for both protectors using the mean cross sectional area and the obtained force vs. deflection plots (Figure 3-13). Corresponding ranges of elastic modulus from the literature are shown for comparison.

	Elastic Modulus \pm St dev (MPa)					Literature Range		
	A	B	C	D	E	Mean	Min	Max
Short Protector	327 \pm 3	603 \pm 7	360 \pm 7	531 \pm 10	540 \pm 12	472 \pm 121	280	1,810
Long Protector	358 \pm 20	286 \pm 14	359 \pm 10	377 \pm 20	357 \pm 23	347 \pm 35	27	1,150

3.4.3 Discussion

All compression samples demonstrated hyperplastic behaviour, with the supporting foams demonstrating upturned S-shaped curves and the pad and D3O® demonstrating more typical foam curves. The hyperelastic and rate dependent characteristics exhibited by the short protector polyurethane pad, NBR supporting foam and long protector PBT supporting foam, reflect the findings from previous research (Cecere *et al.*, 1990; Neilsen *et al.*, 1995; Degrange *et al.*, 2005; Lu, 2014; Mane *et al.*, 2017). D3O® is reported to use “a combination of patented, patent-pending and proprietary technologies to make rate-sensitive, soft, flexible material with high shock absorbing properties” (D3O, 2019). The rate dependency described by D3O® is reflected in the findings from the material characterisation in this study. The two stress-strain curve shapes reflect the characteristics of two hyperelastic material models, the Ogden and Mooney-Rivlin model respectively, which will be explored further in Chapter 5.

During three point bend testing, the splints from both protectors were seen to have high intra-sample repeatability but inter-sample repeatability was low (percentage variance for the short and long protector: intra-sample mean = 1 and 3%, inter-sample = 22 and 10%), with samples being significantly different from each other for the short protector. When compared to hand calculations for uniform beams, experimental results fell within the wide range of elastic modulus values found in the literature. The splints from the short and the long protectors exhibited different shaped force vs. deflection plots within the three-point bend test. The difference in response could be due to geometric differences in splints. The long splint has three horizontal grooves (Figure 3-8), facilitating flexing at lower angles while providing increased stiffness at higher angles, as the gaps between the grooves close. Adams *et al.* (2018) found a similar trait when testing a long protector (of the same type) in their bend test, where the force to achieve a set torque increased rapidly between 55° and 80°, compared to a short and a roller-skating protector. Due to the addition of these grooves and the overall geometric profile of the long splint, assuming the splint to have a uniform cross sectional area when calculating elastic modulus introduced errors. Therefore, the material properties obtained in the three-point bend test for this splint (long protector) were not used for modelling. A median value from the literature provided by the manufacturer was deemed more accurate (range of 27 to 1150 MPa – median value of 550 MPa used for modelling).

Ideally, material characterisation tests should be conducted at typical strains and strain rates seen within the protectors during snowboarding falls. However, these rates are currently not known and hard to identify, especially at injurious conditions, due to ethical reasons. It was presumed, as it is an impact scenario, that the strains and strain rates would be high, therefore, obtaining this information using the Hounsfield HK10S or Instron® would be challenging (Ranga and Strangwood, 2010). Other material characterisation techniques could be used to obtain material data at high strain rates as detailed in the literature review (Section 2.5.3). However, characterising materials at both high strain and strain rates remains a challenge.

3.5 Chapter Summary

Two wrist protectors have been selected for modelling, both with palmar and dorsal splints and padding in the palmar region. The protectors have been deconstructed to identify their parts and the associated materials have been identified, addressing objective one of the thesis. Where sufficient material was available, each component's material was characterised through uniaxial compression, tension, 3 point bend or stress relaxation testing, addressing objective two of the thesis. While materials had high intra-sample repeatability, inter-sample repeatability was low. The materials found within the wrist protectors demonstrated linear elastic, hyperelastic and both linear and non-linear viscoelastic properties. The data obtained in this chapter will form the basis of material model algorithms to describe the different behaviours of the materials within an FE model within Chapter 5. The following chapter will examine the performance of the compression samples under impact, both in isolation and when components are combined.

4 Experimental Impact Testing of Wrist Protector Components

4.1 Introduction

From Chapter 3 two wrist protectors were selected for modelling, their parts and associated materials were identified and characterised. This chapter assesses the performance of the same compression samples (from Chapter 3) under impact loading, both in isolation and when combined with the other components which form the palmar padding region of the protector (Figure 4-1). Impact testing provided experimental data for comparison against FE models developed in Chapter 5. It also helped to determine whether there was still variability between samples from the same size/brand protectors as evidenced in Chapter 3. This chapter began to address objective three of the thesis; to develop and validate FE models of snowboard wrist protectors for simulating hand/surface impacts.

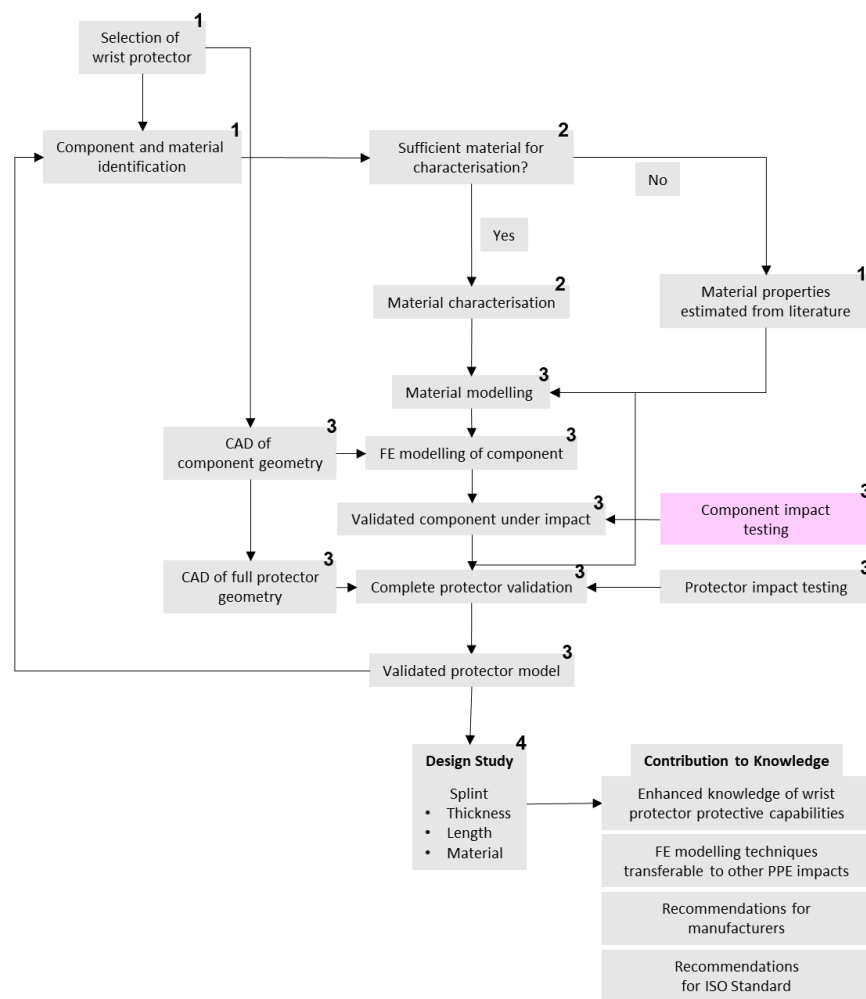


Figure 4-1 Schematic diagram indicating where this chapter (highlighted in purple) fits within the overall project (numbers correlate to the objectives of the thesis).

4.2 Methodology

A common approach to assess an FE model's level of accuracy (when modelling sports PPE) is through comparison against an experimental impact test (Chapter 2.5.4, Table 2-7). The experimental setup typically consists of an instrumented drop tower rig, with an accelerometer attached to the drop mass and/or load cells located under the anvil that the sample rests on, combined with high-speed camera/s for data analysis (Ankrah and Mills, 2003; Ankrah and Mills, 2004; Schmitt *et al.*, 2004). The samples used for material characterisation in Chapter 3, were subject to a series of impact tests.

Tests were performed on a bespoke drop tower impact rig (Figure 4-2) which consisted of a 1.608 kg mass (Figure 4-2, part b) on a linear guide carriage (488-5136, RS Components Ltd., Corby, UK) mounted on a linear guide rail (WS-10-40-1000 488-5243, RS Components Ltd., Corby, UK). The samples rested on a steel plate (base plate/anvil) (0.75 x 0.45 x 0.4 m). A manually operated magnet coupling device (Figure 4-2, part a) (F4M905 70kg Pull, First4Magnets[®], Tuxford, UK) ensured a consistent drop height when releasing the mass. A single axis accelerometer (352B01 PCB[®], ± 0.02 g equating to ± 0.3 N) was placed close to the centre of the flat faced drop mass, and connected to a digital oscilloscope (PicoScope[®] 4424) via an ICP[®] sensor signal conditioner (480B21, PCB[®]), sampling at 100 kHz. A high-speed camera (Figure 4-2, part c) (Phantom[®] Miro R110, Vision Research UK Ltd., Bedford, UK) was used to film the impact from the side of the drop rig and an LED light (Figure 4-2, part d) (GS Vitec, GS01127) was used to provide lighting. The high-speed camera was set to a resolution of 512 x 320 with a capture rate of 10 kHz. The camera and accelerometer were synchronised using the digital oscilloscope and triggered with a falling edge of 1 V, generated by a manual trigger.

4. Experimental Impact Testing of Wrist Protector Components

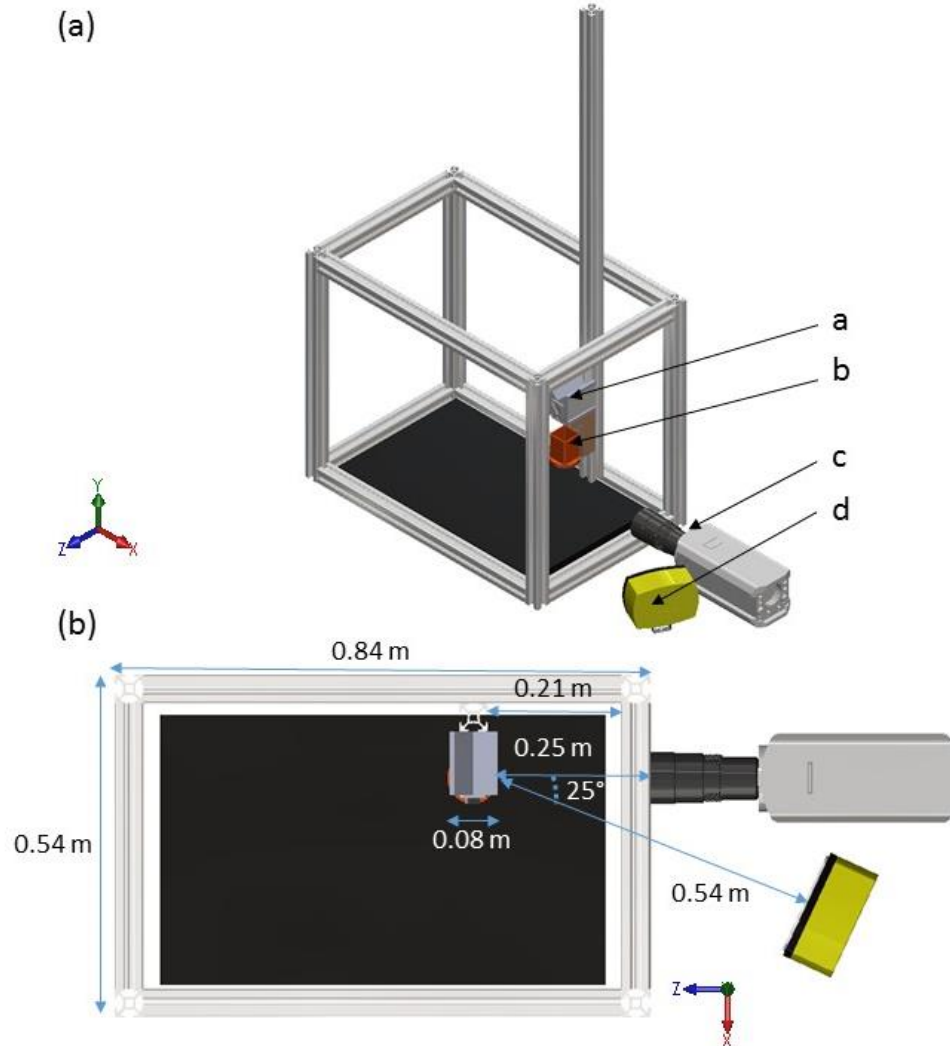


Figure 4-2 (a) Isometric and (b) top view of the bespoke drop tower rig used for impact testing of individual components. Letters in the figure correspond to: a) magnet coupling (F4M905), b) 1.608 kg drop mass with accelerometer placed in the centre, c) high-speed camera (Miro R111) and d) LED light (GS01127).

Individual components of the palmar region, from all five samples of each protector, were subject to five impacts at one energy per component (short protector components: 2.5 J, long protector components: 0.5 J), with two minutes between impacts. Pilot testing indicated that after the first impact, subsequent impact traces followed a similar trend (example shown in Figure 4-6d) for all materials except the palmar pad of the short protector where all impacts were similar. A two minute recovery period between subsequent impacts (determined through pilot testing) was sufficient to prevent any further stress softening of the samples from affecting the results, which would be evidenced as clear changes in temporal acceleration or maximum deformation. Testing was performed over two days at room temperature (~22 °C). The pad and supporting foam from the short protector were impacted at 2.5 J (0.16 m, 1.6 kg) (Figure 4-3a and c), corresponding to half the energy specified in EN 14120 for an impact on the palm of a roller sports protector (Level 1, range C

4. *Experimental Impact Testing of Wrist Protector Components* protector). Half the energy was used as the components were impacted in isolation, to limit degradation and/or to avoid “bottoming out” (> 80% compression). Within the short protector there is a 3 mm shell constructed of HDPE (High density Polyethylene), which is fastened to the outer surface of the pad with double sided tape (Figure 3-3, part c, Chapter 3.3). Therefore, the pad was also impacted with the shell on top at 2.5 J (Figure 4-3b). The supporting foam and D3O[®] from the long protector were impacted at 0.5 J (0.03 m, 1.6 kg) (Figure 4-3e and f). A lower energy was used for these parts, as pilot testing indicated that higher energies caused some of the samples to bottom out.

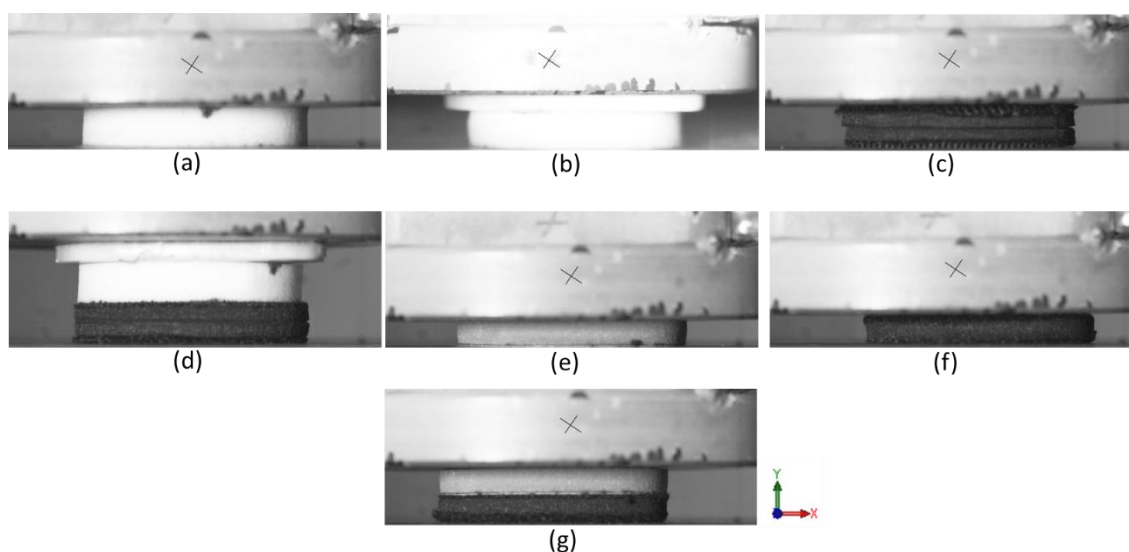


Figure 4-3 Example of components being impacted: short protector (a) pad, (b) pad + shell, (c) supporting foam, (d) combined components and long protector (e) D3O[®], (f) supporting foam and (g) combined components.

The components were also impacted as a combined unit, which included the HDPE shell, pad and supporting foam for the short protector and the D3O[®] and supporting foam for the long protector (Figure 4-3d and g). The combined components were impacted five times at 5.0 J for the short protector and 2.5 J for the long protector, following the same procedure used for the individual component impacts. As all the components of the palmar region were being impacted together, 5.0 J was chosen, corresponding to the impact energy specified in EN 14120 (Level 1, range C protector). As with the individual impacts, the long protector components were impacted at a lower energy (2.5 J), as pilot testing indicated that higher energies caused the samples to “bottom out”.

A median sample, based on visual inspection of the temporal force traces, was selected for comparison against FE models. To ensure a robust validation, testing across a range of impact energies is important (Zaouk *et al.*, 1996), therefore the

median sample was subject to additional impacts at a range of energies to cover an array of strains and strain rates that may be present during a full wrist protector impact, prior to “bottoming out”. Pilot testing indicated that adding the HDPE shell on top of the pad made no difference in terms of peak force, so only the pad was subject to further testing. The energies chosen for the short protector were; 5.0 J for the pad (EN 14120 impact test energy), 0.5 J for the supporting foam (possibility to be converted into stress vs. strain data for use with a material model in FE, Chapter 5) and 2.5 and 6.0 J for the combined components (half the EN 14120 impact test energy and the largest energy prior to “bottoming out”). For the long protector the energies chosen were; 1.0 J for the D3O[®] and the supporting foam (highest energy prior to “bottoming out” for the median sample) and 0.5 and 1.0 J for the combined components (provided a range of strains and strain rates for comparison).

Impact force was obtained as the product of the output voltage from the accelerometer, a calibration factor (0.953 mV.g^{-1} , as per the accelerometer calibration certificate) and dropper mass (1.608 kg). A gain factor of x10 (via the signal conditioner) was used to amplify the signal on the oscilloscope, allowing visual confirmation that the impact peak signal generated by the accelerometer had been captured and synchronisation of the accelerometer data and high-speed camera was successful (Figure 4-4). The force data was low-pass filtered (4-pole phaseless Butterworth digital filter) at Channel Frequency Class (CFC) 1,000 (1,650 Hz), as specified by SAE J211/1 (2007), in MATLAB[®] (vR2017a, MathWorks[®], USA), using a modified script (Meade Spratley, 2013). A low-pass filter is commonly used in both experimental and modelling impact scenarios, in order to reduce high-frequency noise (Fasanella and Jackson, 2002; Derler *et al.*, 2005; Petrone *et al.*, 2010; Hansen *et al.*, 2013). The CFC was chosen based on recommendations in line with sample rate (CFC 1,000 to be used for a sampling frequency of $\geq 10 \text{ kHz}$) (Weisang, 2018). Following filtering, the start of impact was identified as shown in Figure 4-4. Data prior to this point was discarded and the impact trace was moved to time = 0 s. Mean and standard deviation plots were calculated for each sample from the four impacts following the first trace and all five impacts for the pad and pad + shell scenarios.

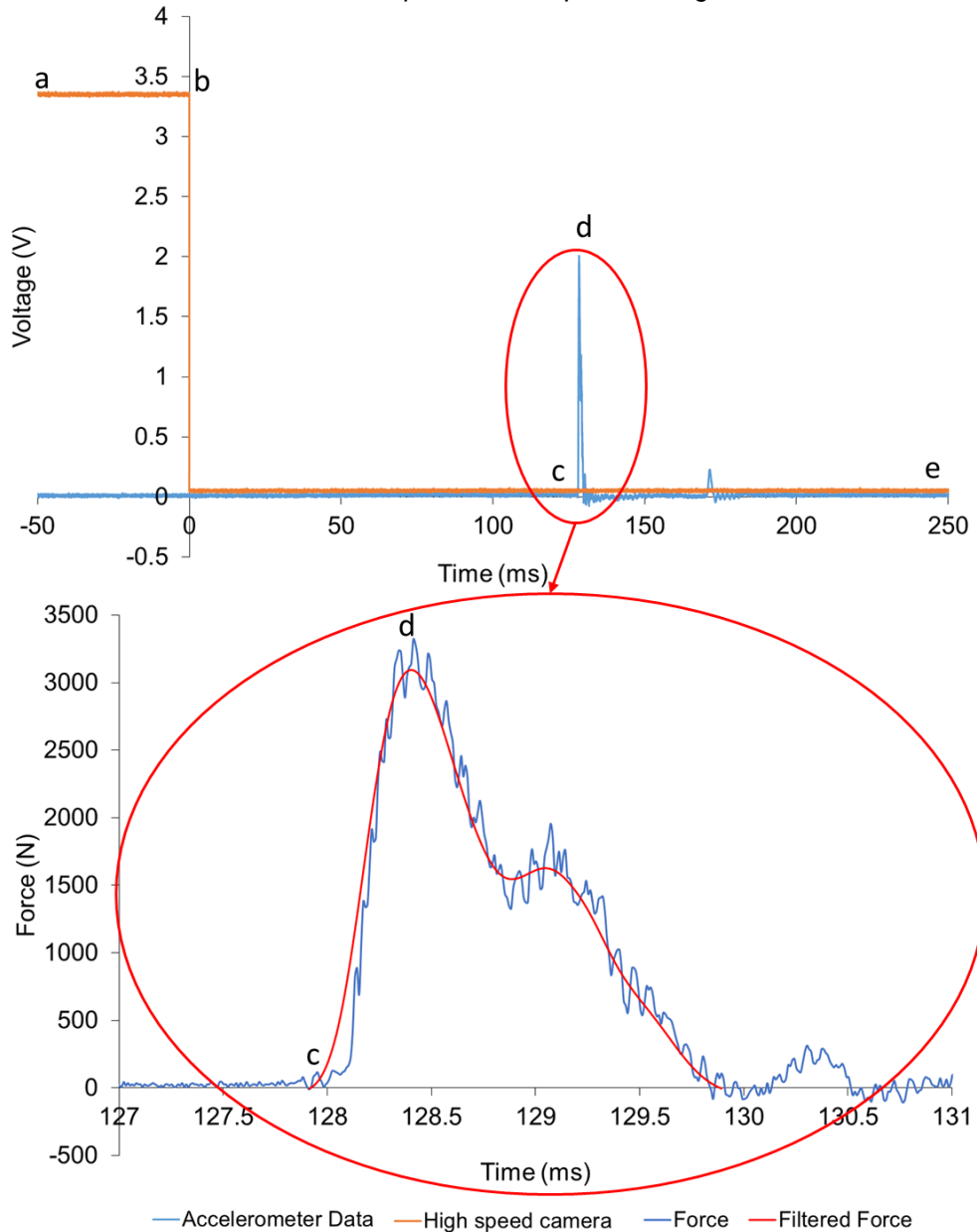


Figure 4-4 Example data obtained from the oscilloscope (a) start of oscilloscope capture window (pre-trigger), (b) trigger of camera causing voltage drop, signalling frame 0, (c) initiation of contact on sample, (d) peak force and (e) end of capture window. The call out shows the converted accelerometer to force data showing the start of impact, and the subsequent trimmed filtered data that was used for comparison.

High-speed videos (.cine) were imported into Phantom[®] CineViewer (CV 3.0) for post processing and analysis. The camera was calibrated using images of a ruler, placed where the components were impacted (Figure 4-5a). The calibration factor was calculated as $0.121 \text{ mm}\cdot\text{pixel}^{-1}$, allowing sample deformation to be measured from the video footage by manually tracking a mark on the impactor ($\pm 1 \text{ mm}$) (Figure 4-5b and c).

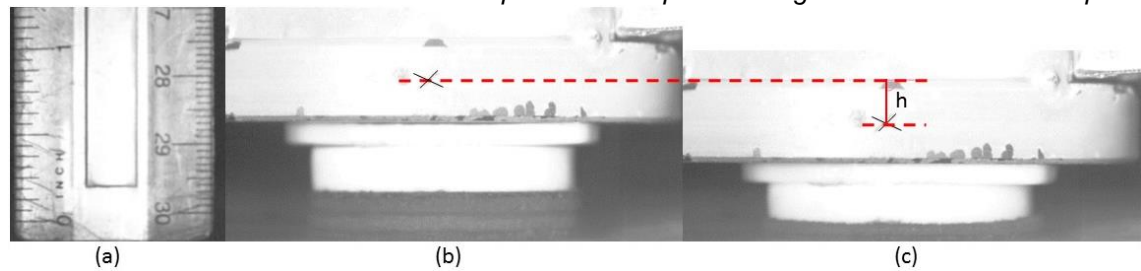


Figure 4-5 Example of how maximum deformation was measured in Phantom® CineViewer (a) image of ruler taken for calibration (b) combined short protector sample at start of impact and (c) at maximum compression (2.5 J). The black x on the impactor is tracked and the distance between the two images is measured (h).

Statistical analysis was conducted in Minitab® (v18 Statistical software, USA) using a coefficient of variance, expressed as a percentage and a one-way ANOVA test to determine whether samples were repeatable (intra-sample) and all five samples of the same component were similar to each other (inter-sample).

4.3 Results

4.3.1 Individual Component Impacts

Figure 4-6 shows the mean \pm standard deviation filtered temporal force traces for all 2.5 J individual impacts of the short protector components (pad, pad + shell and supporting foam). Peak force and impact duration varied between samples, where lower peak forces resulted in longer impact durations. The impact trace for the pad (a) included a rapid increase in force following initial contact until peak force and maximum compression were reached. In addition, there was a reduction in force as the sample then started to de-compress. When a HDPE shell was added on top of the palmar pad the impact response followed a similar pattern (b), with no observed differences in terms of peak force. However, impact duration was longer with the additional shell. Pad and pad + shell impacts were repeatable (shaded region on traces), however inter-sample repeatability was low, where peak force, impact duration and maximum compression ranged for the same impact energy (percentage variance between samples ranged from 16 to 21%) (Table 4-1).

4. Experimental Impact Testing of Wrist Protector Components

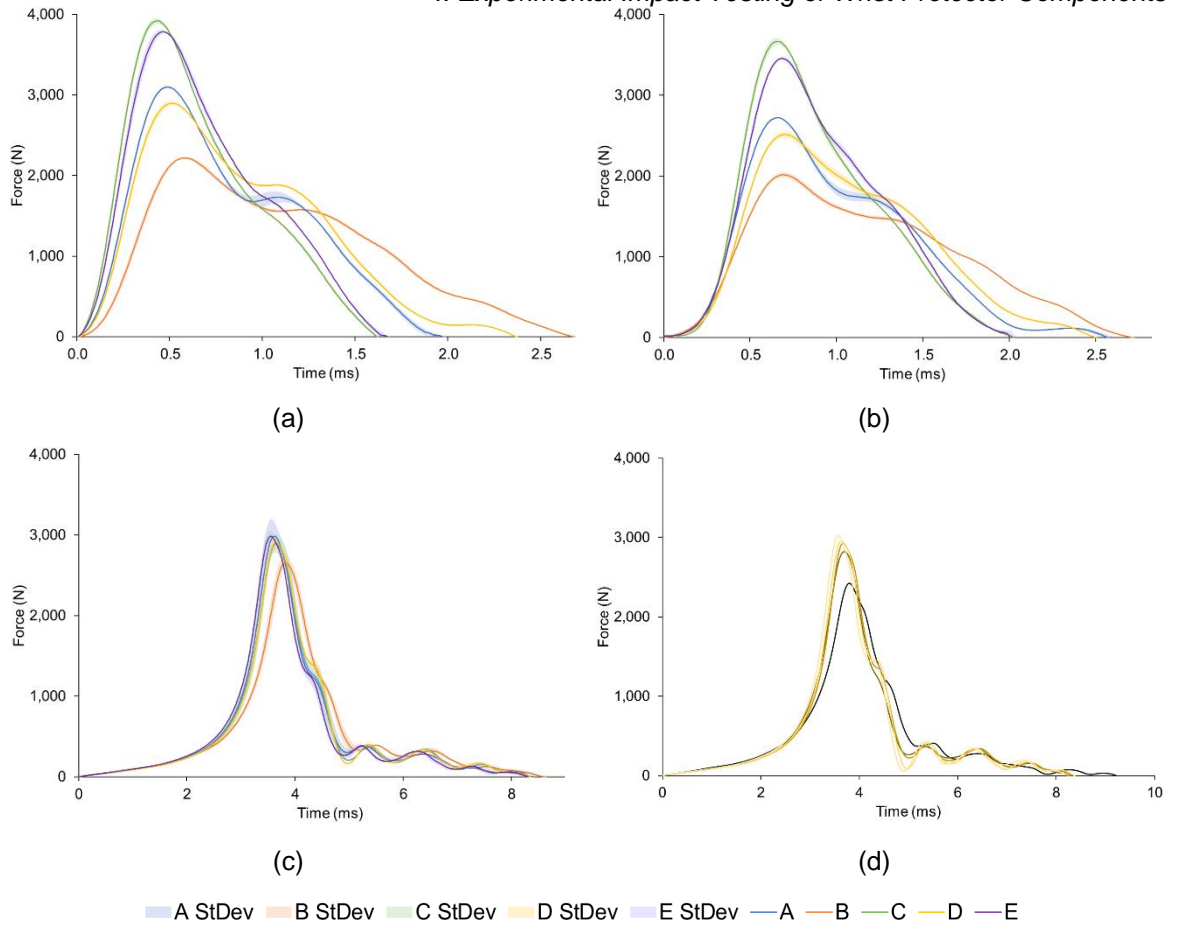


Figure 4-6 Mean (\pm standard deviation) temporal force traces for 2.5 J impacts on five samples of the short protector (a) pad, (b) pad + shell and (c) supporting foam. (d) Shows an example of the unique first impact (black line) compared to the subsequent four impacts for one supporting foam sample (D).

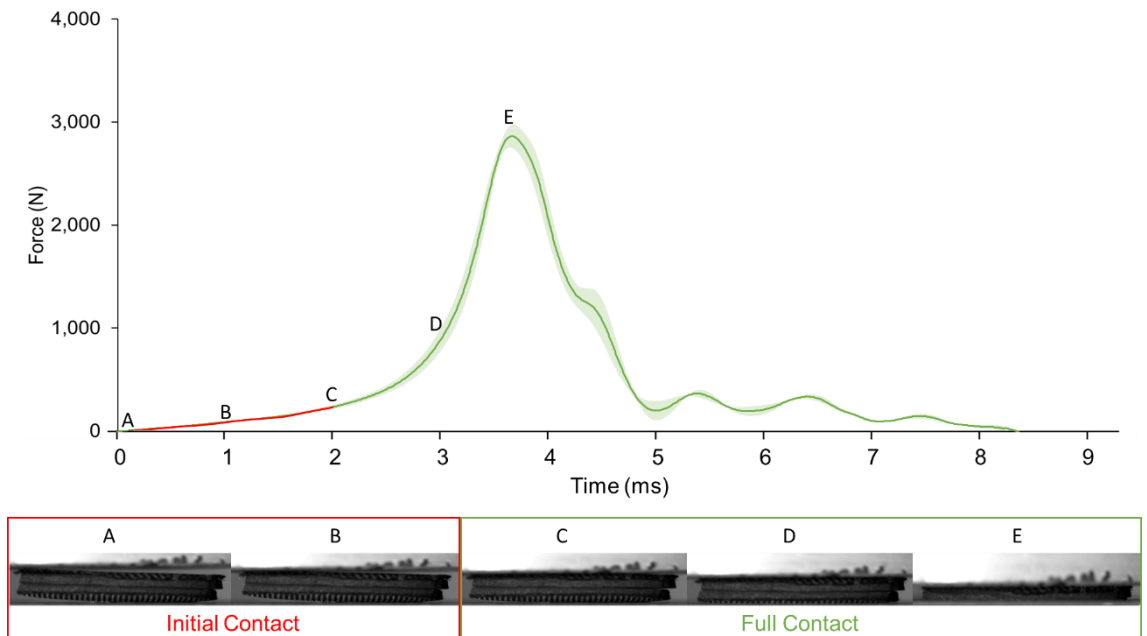


Figure 4-7 An example (sample C) mean (\pm standard deviation) temporal force trace for the short protector supporting foam impact at 2.5 J and corresponding high-speed camera images at 1 ms intervals (A to D) and at maximum compression (E), highlighting that the sample does not become fully engaged until \sim 2 ms.

The supporting foam impact (c) had a period of low force following initial contact of the impactor before there was a rapid increase up to peak force and maximum

4. *Experimental Impact Testing of Wrist Protector Components*
 compression (Figure 4-6c and Figure 4-7). The reason for this period of low force may be due to the supporting foams not sitting completely parallel to the dropper face when placed on the base plate in the experimental setup. Thus, the samples were not fully engaged until ~2 ms. After reaching peak force and maximum compression, non-uniform decompression occurred (due to the non-uniformity of the samples), causing fluctuations in the temporal force data. Following the initial impact (Figure 4-6d), subsequent impacts were comparative with a mean percentage variance of 4% for peak force, 3% for impact duration and 7% for maximum compression (shaded region on traces). The supporting foam samples had less variance between samples compared to the pad impacts (percentage variance between samples ranged from 2 to 8%) (Table 4-1 - statistical analysis details in Appendix 10.D.2).

Table 4-1 Mean (\pm standard deviation) values for peak force, maximum compression, maximum compressive strain and impact duration for 2.5 J impacts on all samples of the short protector pad, pad + shell and supporting foam (Figure 4-6).

Component	Sample	Peak Force \pm St Dev (N)	Maximum compression \pm St Dev (mm)	Maximum compressive Strain \pm St Dev (%)	Impact Duration \pm St Dev (ms)
Pad (Figure 4-6a)	A	3,099 \pm 13 ^{bcde}	0.60 \pm 0.05 ^b	10 \pm 1 ^b	1.94 \pm 0.04 ^{bcde}
	B	2,204 \pm 37 ^{acde}	0.91 \pm 0.08 ^{acde}	15 \pm 1 ^{acde}	2.71 \pm 0.09 ^{acde}
	C	3,922 \pm 35 ^{abde}	0.60 \pm 0.05 ^b	10 \pm 1 ^b	1.62 \pm 0.01 ^{abd}
	D	2,897 \pm 29 ^{abce}	0.65 \pm 0.07 ^b	10 \pm 1 ^b	2.37 \pm 0.01 ^{abce}
	E	3,791 \pm 16 ^{abcd}	0.65 \pm 0.05 ^b	10 \pm 1 ^b	1.66 \pm 0.03 ^{abd}
	Mean	3,183 \pm 640	0.68 \pm 0.13	11 \pm 2	2.06 \pm 0.43
Pad + Shell (Figure 4-6b)	A	2,830 \pm 10 ^{bcde}	0.65 \pm 0.06 ^{bde}	7 \pm 1 ^{bde}	2.80 \pm 0.04 ^{bcde}
	B	2,073 \pm 57 ^{acde}	0.94 \pm 0.08 ^{ac}	10 \pm 1 ^{ac}	2.86 \pm 0.02 ^{acde}
	C	3,669 \pm 41 ^{abde}	0.63 \pm 0.07 ^{bde}	7 \pm 1 ^{bde}	2.00 \pm 0.02 ^{abd}
	D	2,614 \pm 40 ^{abce}	0.81 \pm 0.10 ^{ac}	9 \pm 1 ^{ac}	2.64 \pm 0.02 ^{abce}
	E	3,496 \pm 20 ^{abcd}	0.84 \pm 0.05 ^{ac}	9 \pm 1 ^{ac}	2.00 \pm 0.02 ^{abd}
	Mean	2,936 \pm 598	0.77 \pm 0.14	8 \pm 1	2.46 \pm 0.39
Supporting Foam (Figure 4-6c)	A	3,043 \pm 125 ^b	5.03 \pm 0.18 ^{bcde}	72 \pm 3 ^{bcde}	8.39 \pm 0.14
	B	2,644 \pm 80 ^{acde}	6.17 \pm 0.15 ^{ac}	86 \pm 2 ^{ac}	8.70 \pm 0.27 ^{cde}
	C	2,902 \pm 102 ^b	5.67 \pm 0.10 ^{ab}	79 \pm 1 ^{ab}	8.33 \pm 0.07 ^b
	D	2,932 \pm 85 ^b	6.00 \pm 0.18 ^a	83 \pm 3 ^a	8.33 \pm 0.06 ^b
	E	2,986 \pm 68 ^b	5.99 \pm 0.18 ^a	83 \pm 3 ^a	8.29 \pm 0.05 ^b
	Mean	2,901 \pm 164	5.77 \pm 0.44	80 \pm 6	8.41 \pm 0.20

Subscript text highlights the letter of the samples that are significantly different at $p < 0.05$.

4. Experimental Impact Testing of Wrist Protector Components

Mean \pm standard deviation filtered temporal force traces for all 0.5 J individual impacts of the long protector components (D3O[®] and supporting foam) are shown in Figure 4-8. The D3O[®] (a) impact exhibits characteristics of a typical foam compression curve, an initial quasi-linear phase, followed by a plateau in force followed by densification up to peak force. Following peak force, the sample decompresses in a similar manner. The supporting foam (b) impact had very similar characteristics as the short protector supporting foam, where there was a period of low force following initial contact of the impactor, due to samples not sitting parallel to the dropper on the base plate. This was followed by a rapid increase to peak force and maximum compression (Figure 4-8b). Samples for the long protector were more consistent than those of the short protector during impact testing (percentage variance ranged from 2 to 6%) (Table 4-2).

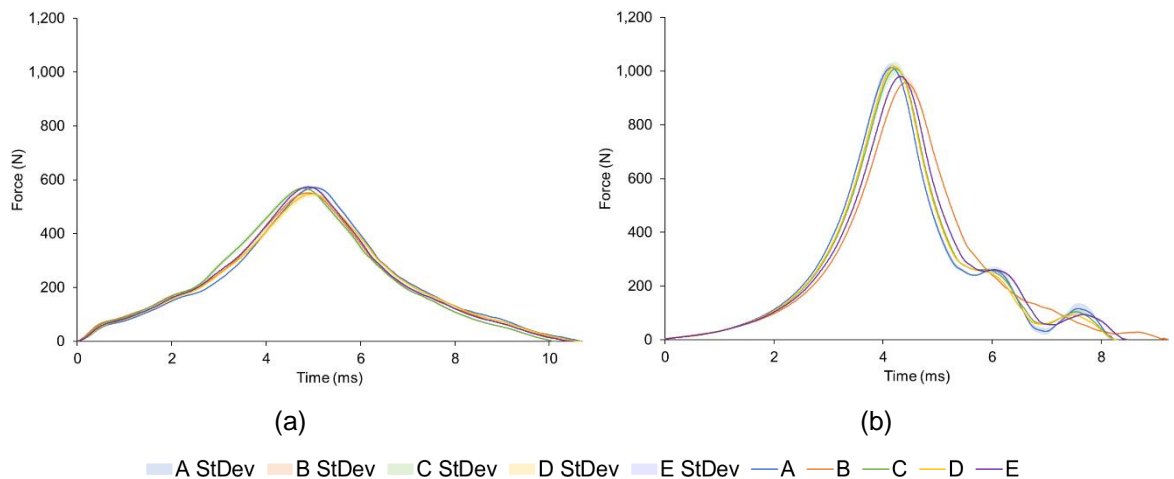


Figure 4-8 Mean (\pm standard deviation) temporal force traces for a 0.5 J impact on five samples of the long protector (a) D3O[®] and (b) supporting foam.

4. Experimental Impact Testing of Wrist Protector Components

Table 4-2 Mean (\pm standard deviation) values for peak force, maximum compression, maximum compressive strain and impact duration for 0.5 J impacts on all samples of the long protector D3O[®] and supporting foam (Figure 4-8).

Component	Sample	Peak Force \pm St Dev (N)	Maximum compression \pm St Dev (mm)	Maximum compressive Strain \pm St Dev (%)	Impact Duration \pm St Dev (ms)
D3O [®] (Figure 4-8a)	A	571 \pm 5 ^{bd}	2.99 \pm 0.07	66 \pm 2	10.66 \pm 0.02 ^{bce}
	B	551 \pm 3 ^{ace}	2.93 \pm 0.17	65 \pm 4	10.41 \pm 0.08 ^{acd}
	C	569 \pm 2 ^{bd}	2.87 \pm 0.07 ^d	64 \pm 2 ^d	10.09 \pm 0.07 ^{abde}
	D	547 \pm 10 ^{ace}	3.14 \pm 0.12 ^{ce}	70 \pm 3 ^{ce}	10.56 \pm 0.10 ^{bc}
	E	573 \pm 7 ^{bd}	2.83 \pm 0.06 ^d	63 \pm 1 ^d	10.43 \pm 0.03 ^{acd}
	Mean	562 \pm 12	2.95 \pm 0.15	66 \pm 3	10.43 \pm 0.21
Supporting Foam (Figure 4-8b)	A	1,019 \pm 14 ^{be}	3.48 \pm 0.21	77 \pm 5	8.18 \pm 0.06 ^b
	B	966 \pm 16 ^{acd}	3.75 \pm 0.12 ^c	83 \pm 3 ^c	9.12 \pm 0.02 ^{acd}
	C	1,016 \pm 23 ^{be}	3.32 \pm 0.21 ^b	74 \pm 5 ^b	8.22 \pm 0.02 ^b
	D	1,017 \pm 3 ^{be}	3.51 \pm 0.12	78 \pm 3	8.25 \pm 0.04 ^b
	E	980 \pm 10 ^{acd}	3.47 \pm 0.12	77 \pm 3	8.67 \pm 0.51
	Mean	1,000 \pm 26	3.51 \pm 0.20	78 \pm 4	8.49 \pm 0.42

Subscript text highlights the letter of the samples that are significantly different at $p < 0.05$.

4.3.2 Full Palmar Impacts

Mean \pm standard deviation filtered temporal force traces for all combined sample impacts at 5.0 J for the short protector and 2.5 J for the long protector are shown in Figure 4-9. When combining the supporting foam with the pad/D3O[®], peak force and maximum compressive strain decreased, while impact duration increased, suggesting that in combination the components act more effectively, providing more cushioning than when individually impacted. This was also reflected in the shape of the trace, where the effect of the supporting foam can be seen via the longer period of low force before a rapid increase to peak force and maximum compression. The results also indicate that the short protector is likely to pass the EN 14120 impact test, as the 5.0 J impact on the combined components of the palmar region resulted in a peak force below the threshold of 3,000 N, whereas the long protector would not.

When combining the components of the palmar region for the short protector at 5.0 J, intra-sample repeatability remained high, while, inter-sample repeatability remained low (percentage variance ranged from 9 to 19%) (Table 4-3). In comparison to the short protector, when components were combined for the long

4. Experimental Impact Testing of Wrist Protector Components

protector impact, both inter and intra-sample repeatability was high (percentage variance ranged from 1 to 3%) (Table 4-3).

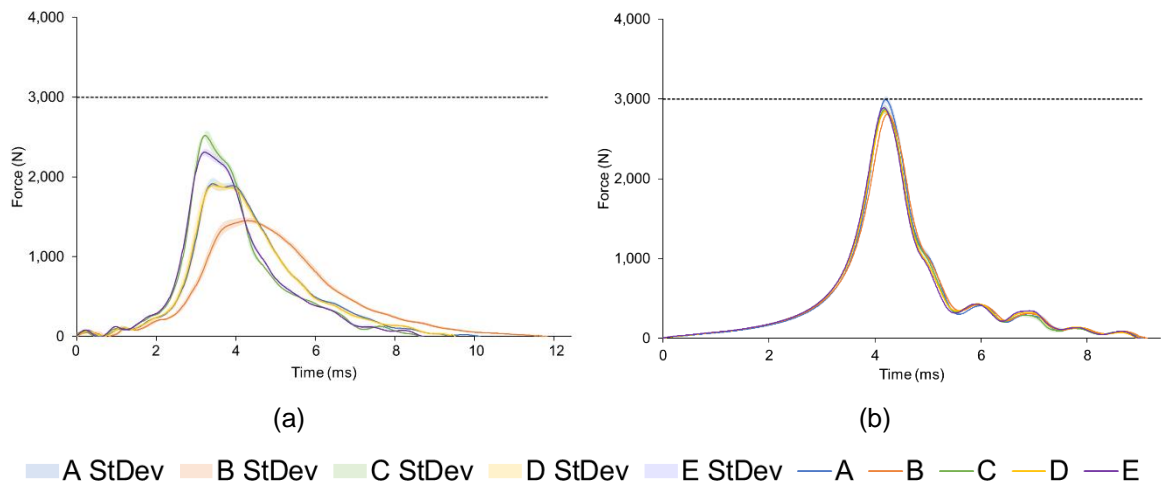


Figure 4-9 Mean (\pm standard deviation) temporal force traces for all five samples of combined palmar components (a) short protector at 5.0 J and (b) long protector at 2.5 J. The black dashed line shows the EN 14120 pass threshold (3,000 N).

Table 4-3 Mean (\pm standard deviation) values for peak force, maximum compression, maximum compressive strain and impact duration for the combined palmar component impacts at 5.0 J for the short protector and 2.5 J for the long protector (Figure 4-9).

Component	Sample	Peak Force \pm St Dev (N)	Maximum	Maximum	Impact Duration \pm St Dev (ms)
			compression \pm St Dev (mm)	compressive Strain \pm St Dev (%)	
Combined components – Short Protector (Figure 4-9a)	A	1,915 \pm 71 ^{bce}	7.49 \pm 0.28 ^{ce}	46 \pm 2 ^{ce}	10.63 \pm 0.44 ^{bcde}
	B	1,454 \pm 34 ^{acde}	8.00 \pm 0.46 ^{ce}	49 \pm 3 ^{ce}	11.67 \pm 0.14 ^{acde}
	C	2,534 \pm 52 ^{abde}	6.43 \pm 0.18 ^{abd}	39 \pm 1 ^{abd}	8.62 \pm 0.05 ^{abd}
	D	1,906 \pm 48 ^{bce}	7.47 \pm 0.16 ^{ce}	46 \pm 1 ^{ce}	9.43 \pm 0.06 ^{abce}
	E	2,311 \pm 45 ^{abcd}	6.75 \pm 0.18 ^{abd}	41 \pm 1 ^{abd}	8.69 \pm 0.08 ^{abd}
	Mean	2,024 \pm 385	7.23 \pm 0.63	44 \pm 4	9.81 \pm 1.23
Combined components – Long Protector (Figure 4-9b)	A	2,992 \pm 41 ^{bcd}	7.22 \pm 0.34	80 \pm 4	9.01 \pm 0.03
	B	2,810 \pm 54 ^a	7.06 \pm 0.13	78 \pm 1	9.05 \pm 0.06 ^{de}
	C	2,868 \pm 57 ^a	6.90 \pm 0.10	77 \pm 1	8.99 \pm 0.03
	D	2,847 \pm 39 ^a	7.16 \pm 0.10	80 \pm 1	8.94 \pm 0.04 ^b
	E	2,890 \pm 55	7.06 \pm 0.10	80 \pm 1	8.96 \pm 0.02 ^b
	Mean	2,882 \pm 77	7.08 \pm 0.20	79 \pm 2	8.99 \pm 0.05

Subscript text highlights the letter of the samples that are significantly different at $p < 0.05$.

4.3.3 Median Component Impacts at a Range of Energies

Mean \pm standard deviation filtered temporal force traces for the median component (D for the short protector and C for the long protector) impacts at a range of energies are shown in Figure 4-10. Peak force and maximum deformation increased with impact energy, while time to peak decreased for all components and samples, with the exception of the pad of the short protector between 1.0 and 2.5 J where time to peak increased. The data values from Table 4-4 were used for FE model comparison in Chapter 5.

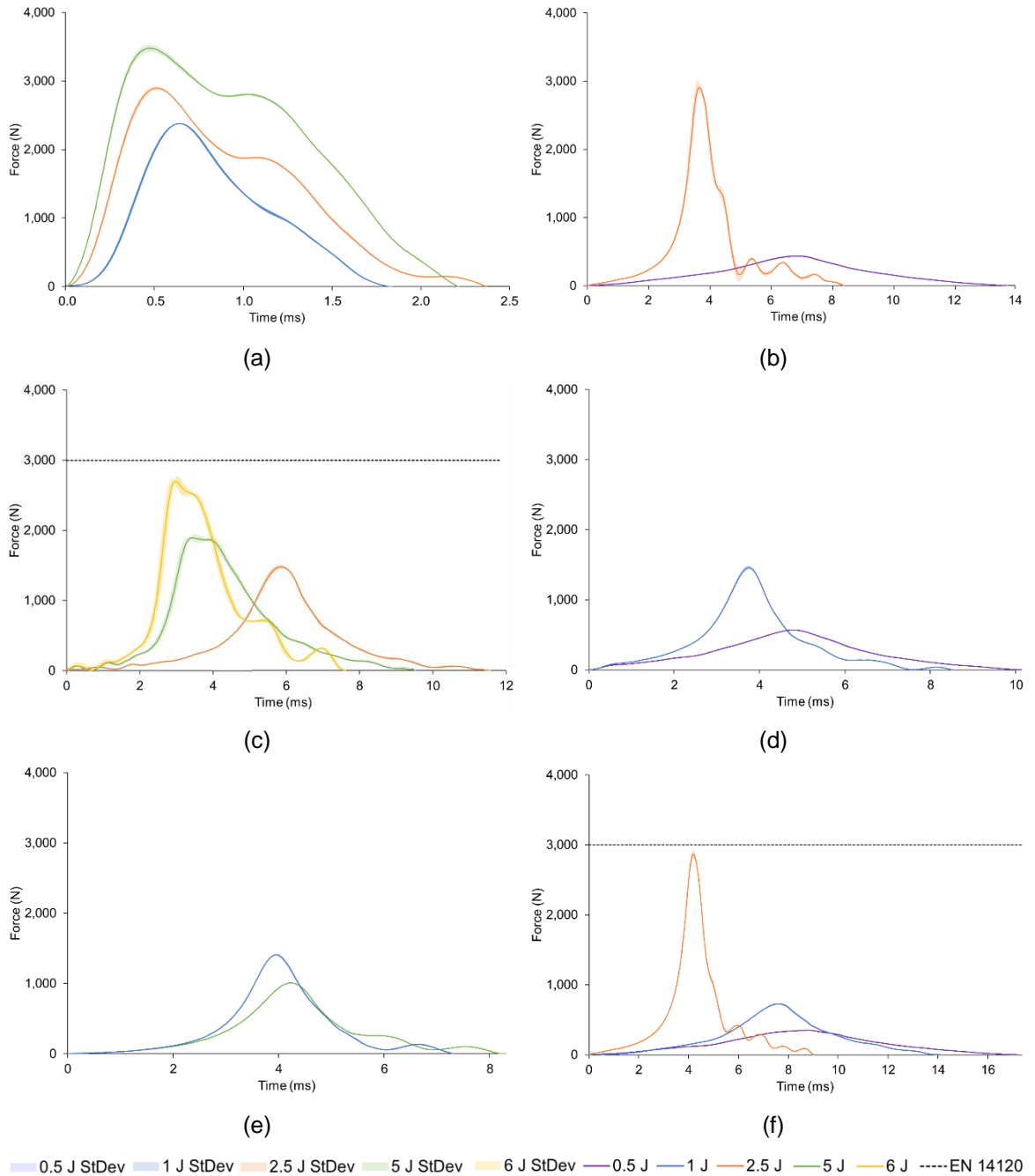


Figure 4-10 Mean (\pm standard deviation) temporal force traces for the short protector (a) pad at 1.0, 2.5 and 5.0 J, (b) supporting foam at 0.5 and 2.5 J, (c) combined parts at 2.5, 5.0 and 6.0 J and the long protector (d) D30® at 0.5 and 1.0 J, (e) supporting foam at 0.5 and 1.0 J and (f) combined parts at 0.5, 1.0 and 2.5 J. The black dashed line shows the EN 14120 pass threshold (3,000 N).

4. Experimental Impact Testing of Wrist Protector Components

Table 4-4 Mean (\pm standard deviation) values for peak force, maximum compression, maximum compressive strain and impact duration for all median samples at a range of energies (Figure 4-10).

	Component	Energy (J)	Peak Force \pm St Dev (N)	Maximum compression \pm St Dev (mm)	Maximum compressive Strain \pm St Dev (%)	Impact Duration \pm St Dev (ms)
Short	Pad (Figure 4-10a)	1.0	2,381 \pm 5	0.39 \pm 0.06	6 \pm 1	1.82 \pm 0.01
		2.5	2,897 \pm 29	0.65 \pm 0.07	10 \pm 1	2.37 \pm 0.01
		5.0	3,479 \pm 54	1.57 \pm 0.06	25 \pm 1	2.21 \pm 0.01
	Supporting Foam (Figure 4-10b)	0.5	436 \pm 19	4.05 \pm 0.05	56 \pm 1	13.74 \pm 0.16
		2.5	2,932 \pm 85	5.99 \pm 0.18	83 \pm 3	8.33 \pm 0.06
		5.0	1,479 \pm 23	5.86 \pm 0.14	36 \pm 1	11.87 \pm 0.77
	Combined components (Figure 4-10c)	5.0	1,906 \pm 48	7.47 \pm 0.16	46 \pm 1	9.43 \pm 0.06
		6.0	2,732 \pm 59	7.44 \pm 0.08	45 \pm 0	7.55 \pm 0.06
		0.5	569 \pm 2	2.87 \pm 0.07	64 \pm 2	10.09 \pm 0.07
Long	D3O [®] (Figure 4-10d)	1.0	1,459 \pm 31	3.27 \pm 0.10	73 \pm 2	8.04 \pm 0.55
		0.5	1,016 \pm 23	3.32 \pm 0.21	74 \pm 5	8.22 \pm 0.02
	Supporting Foam (Figure 4-10e)	1.0	1,410 \pm 13	3.97 \pm 0.18	88 \pm 4	8.24 \pm 0.67
		0.5	349 \pm 4	5.95 \pm 0.23	66 \pm 3	17.12 \pm 0.19
	Combined components (Figure 4-10f)	1.0	727 \pm 11	6.41 \pm 0.25	71 \pm 3	14.01 \pm 0.42
		2.5	2,868 \pm 57	6.90 \pm 0.10	77 \pm 1	8.99 \pm 0.03

4.4 Discussion

When impacted, individual components showed high intra-sample repeatability across all samples (mean \pm standard deviation percentage variance 3 \pm 3%), however inter-sample repeatability was low (mean \pm standard deviation percentage variance 10 \pm 7%). The short protector components had a higher percentage variation compared to the long protector components (percentage variance for short protector vs long protector: peak force = 15% vs 3%, impact duration = 14% vs 4% and maximum compression = 15% vs 6%), however, the long protector parts were subjected to lower impact energies due to “bottoming out”. When components were impacted as a combined unit there was less variation for both protectors in terms of impact duration and maximum compression (percentage variation of peak force individually vs. combined for short and long protector: impact duration = 14% vs. 13% and 4% vs. 1%, maximum compression = 15% vs. 8% and 6% and 3%). However, variation in peak force increased for the short protector (percentage

variation of peak force individually vs. combined: 15% vs. 19%) and remained the same for the long protector (percentage variation of peak force individually vs combined: 3% vs. 3%).

Adding the HDPE shell on top of the pad of the short protector did not significantly change the peak force under impact, but the impact duration and maximum compression both significantly increased (2.06 ± 0.47 ms vs. 2.46 ± 0.43 ms and 0.68 ± 0.13 mm to 0.77 ± 0.13 mm). Incorporating a shell on top of a foam is a common concept often used in PPE, with examples including snowsport back protectors and football/hockey shin guards. With these products the foam layer is the energy absorber (Ankrah and Mills, 2003), and the shell is intended to prevent abrasion and penetration from objects such as rocks and studs (Signetti *et al.*, 2018). The findings from this study also suggest that because peak force remained constant between the pad and pad + shell scenarios, that the plastic is placed on top of the pad for the same reason. However, further studies looking at impacting with a concentrated load rather than a flat faced impactor would need to be conducted to back up this suggestion.

The supporting foams were quantified to be softer than the pad/D3O[®] during quasi-static compression testing (short protector: 0.33 vs. 3.85 MPa and long protector: 0.08 vs. 0.24 MPa) (Chapter 3), which was also evident in the impact test, where at 0.5 J, maximum compressive strain for the D3O[®] was ~65% compared to ~75% for the supporting foam. Due to such high compression, displacement measurements became harder, which may explain why some samples, such as the 2.5 J impact on the short protector supporting foam, are seen to be significantly different to each other in terms of maximum compression but not peak force.

The results indicate that the short protector is likely to pass the EN 14120 impact test, as the 5.0 J impact on the combined components of the palmar region resulted in a peak force below the threshold of 3,000 N. The short protector is certified to EN 14120, therefore these results are as expected. The long protector, however, is unlikely to pass because at 2.5 J, peak force was within ~120 N (4%) of the 3 kN threshold, suggesting that if tested at 5.0 J the threshold would be exceeded. These predictions would need to be confirmed through testing of the protectors against EN 14120, which falls outside the scope of this work, which is focusing on developing a FE model of a protector fitted to a wrist surrogate.

When the palmar components were impacted as a combined unit for the short protector at 2.5 and 5.0 J, the resultant peak forces were similar ($1,479 \pm 23$ N vs. $1,906 \pm 48$ N), while the impact time decreased for the higher energy (11.87 ± 0.77 vs. 9.43 ± 0.06 ms). When impacting at 6.0 J compared to 5.0 J there was a large difference between peak forces ($1,906 \pm 48$ N vs. $2,732 \pm 59$ N), but minimal difference in maximum compression values (45 to 46%). High-speed video footage confirmed that the large increase in peak force was because at 6.0 J the supporting foam was bottoming out. A large difference was also seen between a 1.0 J and 2.5 J impact (727 ± 11 vs. $2,868 \pm 57$ N) for the combined parts of the long protector, and maximum compression increased from 71 to 77%, again suggesting one or both elements were “bottoming out” during impact. High-speed footage confirmed that both the supporting foam and D3O[®] were bottoming out at 2.5 J.

At 1.0 J for D3O[®] and 2.5 J for the supporting foam of the short protector and the combined components of the long protector, there was evidence of degradation, with peak force increasing with each impact for all samples. The increase was quantified as a mean of 5% of the peak force (range of 3 to 10%), which in this case was not deemed significant. However, this was something that was noted and examined when testing full wrist protectors in Chapter 6 as Adams (2018) found that for 72% of the protectors tested, peak force was the lowest for the first impact.

4.5 Chapter Summary

Compression samples obtained from two styles of wrist protectors were impact tested both in isolation and as a combined unit across a range of energies from 0.5 to 6.0 J. Peak force and maximum deformation increased with impact energy, while time to peak decreased, for all components and samples, apart from the pad of the short protector between 1.0 and 2.5 J where time to peak increased. Impact testing of individual components of the protectors highlighted variability between samples from the same size/brand protector, supporting the quasi-static compression testing results of Chapter 3. When components were impacted as a combined unit there was a small decrease in percentage variation in terms of impact duration and maximum compression compared to when components were individually tested, while variability in peak force was unchanged. FE models replicating the impact scenario in this chapter will be created in Chapter 5 and compared to the experimental data for accuracy.

5 FE Modelling of Wrist Protector Components Under Impact

5.1 Introduction

Chapter 4 reviewed the results from impact testing of compression samples both in isolation and as a combined palmar unit across a range of energies from 0.5 to 6.0 J. This chapter uses the material data from Chapter 3, and where necessary the 0.5 J data from Chapter 4, to select material model algorithms which replicate the different behaviours of the materials within an FE model. Models replicating the impact scenario in Chapter 4 are created and compared to the median samples experimental data for each component (Figure 5-1). This chapter contributed to objective three of the thesis; to develop and validate FE models of snowboard wrist protectors for simulating hand/surface impacts.

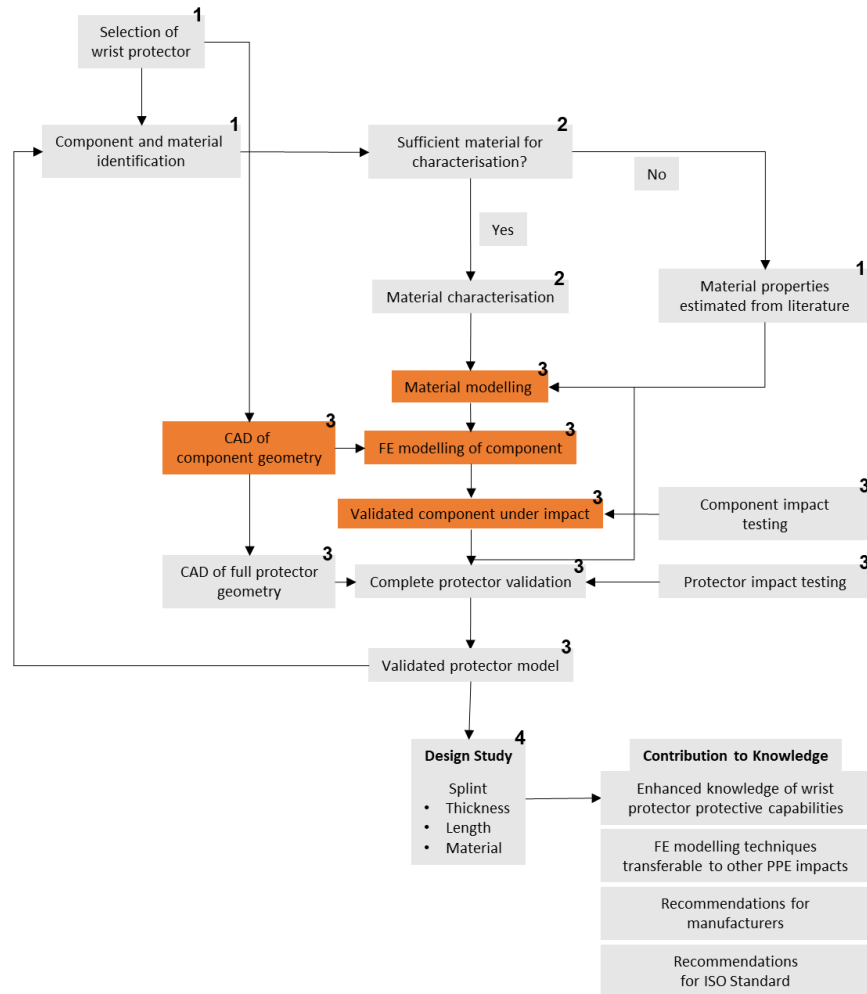


Figure 5-1 Schematic diagram indicating where this chapter (highlighted in orange) fits within the overall project (numbers correlate to the objectives of the thesis).

5.2 Material Models

According to the material characterisation (compression, tensile and stress relaxation) results in Chapter 3, there are four key types of materials within a wrist protector: linear elastic, hyperelastic, linear viscoelastic and non-linear viscoelastic (Table 5-1). This material behaviour should be reflected within an FE model through using an appropriate material model. Within ANSYS®/LS-DYNA® there is a vast array of material models able to define material behaviour; essentially they are mathematical models used to describe a material's stress vs. strain relationship. There are three main categories: linear elastic, hyperelastic and viscoelastic.

Table 5-1 Different protector components and the associated type of material.

Protector	Component	Type of material
Short	Pad	Hyperelastic, Linear Viscoelastic
	Supporting Foam	Hyperelastic, Non-linear Viscoelastic
	Splint	Linear Elastic
	Strap	Linear Elastic
Long	D3O®	Hyperelastic, Non-linear Viscoelastic
	Supporting Foam	Hyperelastic, Non-linear Viscoelastic
	Splint	Linear Elastic
	Strap	Linear Elastic

5.2.1 Linear Elastic Models

The simplest of all the isotropic material models, the linear elastic model, requires the user to define density (ρ), Young's modulus (E) and Poisson's ratio (ν). This model is used to describe a material demonstrating a linear stress vs. strain response obeying Hooke's law (Hooke, 1678). For the wrist protector an isotropic linear elastic material model was used for the straps, splints and short protector HDPE shell. Ankrah and Mills (2004) and Thoraval *et al.* (2013) also used a linear elastic model to describe the splints and shell components of PPE in their studies on football shin guards and wrist protectors respectively. The Young's modulus is obtained either from an estimate based on the literature or through fitting a linear trend line through the uniaxial stress vs. strain test data (Figure 5-2). Literature data was used for the long protector splint ($\rho = 1,150 \text{ kg.m}^{-3}$, $E = 0.55 \text{ GPa}$, $\nu = 0.4$) (DuPont, 2017) and the HDPE shell ($\rho = 970 \text{ kg.m}^{-3}$, $E = 0.3 \text{ GPa}$, $\nu = 0.4$) (Ankrah and Mills, 2004), whereas stress vs. strain data obtained in Chapter 3 was used for

the straps (short - $\rho = 1,384 \text{ kg.m}^{-3}$, $E = 0.04 \text{ GPa}$, $\nu = 0.48$, long - $\rho = 888 \text{ kg.m}^{-3}$, $E = 0.03 \text{ GPa}$, $\nu = 0.48$) and short protector splints ($\rho = 970 \text{ kg.m}^{-3}$, $E = 0.47 \text{ GPa}$, $\nu = 0.4$).

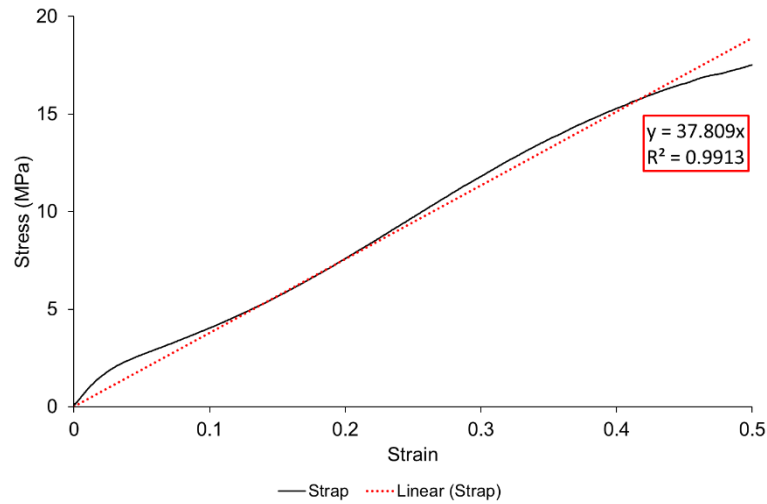


Figure 5-2 Example stress vs. strain plot demonstrating the use of a linear trend line used to obtain Young's modulus for the short protector strap ($E = 37.8 \text{ MPa}$).

5.2.2 Hyperelastic Models

When the material's stress vs. strain response becomes nonlinear then more information beyond that defined in a linear elastic model is required to capture this behaviour within an FE model. One way to describe this behaviour is through the use of a hyperelastic material model. There are different material models that can describe hyperelastic behaviour, each being variants of a polynomial form made up of parameters input as material constants (Ansys, 2015). The two hyperelastic models most frequently used for materials identified in a wrist protector include the Mooney-Rivlin model and the Ogden model (Chapter 2.5, Table 2-5 and Table 2-6). The Mooney-Rivlin model (Equation 5-1) (Mooney, 1940; Rivlin, 1948) is known to work well for moderately large strains (200%) (Kim *et al.*, 2012). However, the material model cannot accurately capture an upturn S curvature shaped stress vs. strain relationship (Figure 5-3b and d).

$$W = \sum_{i,j=0}^N C_{ij}(\bar{I}_1 - 3)^i(\bar{I}_2 - 3)^j + \sum_{m=1}^M D_m(J - 1)^{2m} \quad \text{Equation 5-1}$$

Where: W is strain energy, $c_{i,j}$ are coefficients related to the distortional response, \bar{I}_i are the invariants of the strain energy density functions, D_m is the volumetric response (assumed to be 1 for a compressible material, (Bower, 2009)) and J is the determinant of the deformation gradient.

The Ogden Model (Equation 5-2) (Ogden, 1972) is able to capture an upturn S shaped stress vs. strain curve and can model rubbers accurately when large strains (700%) (Figure 5-3a and c) and large ranges of deformation are applied (Shahzad *et al.*, 2015).

$$W = \sum_{i=1}^N \frac{2\mu_i}{\alpha_i^2} (\lambda_1^{\alpha_i} + \lambda_2^{\alpha_i} + \lambda_1^{-\alpha_i} \lambda_2^{-\alpha_i} - 3) \quad \text{Equation 5-2}$$

Where: W is strain energy, λ_i are the principal extension ratios, μ_i are shear moduli and α_i are material constants (curve fitting coefficients).

The material models do not give any special insight into material behaviour they are simply curve fits to material test data. The number of terms used within the model capture different points within a stress vs. strain curve, with a general rule being $N = 1$ is a linear relationship, $N = 2$ having one point of inflexion and $N = 3$ having two points of inflexion (Ansys, 2015). The number of terms can be as large as nine; however, the more terms the more computationally expensive the model is. Uniaxial test data obtained in Chapter 3.4.2 was imported into ANSYS® Workbench v18.2 via the engineering data tab, a material model was then selected and the curve fitting option was used. The match between the material model algorithm and the stress vs. strain response was presented (examples in Figure 5-3) and it was decided whether that model fitted well or a different material model needed to be trialled. An iterative approach was employed by using the rules presented earlier; an informed estimate was used as a starting point.

5. FE Modelling of Wrist Protector Components Under Impact

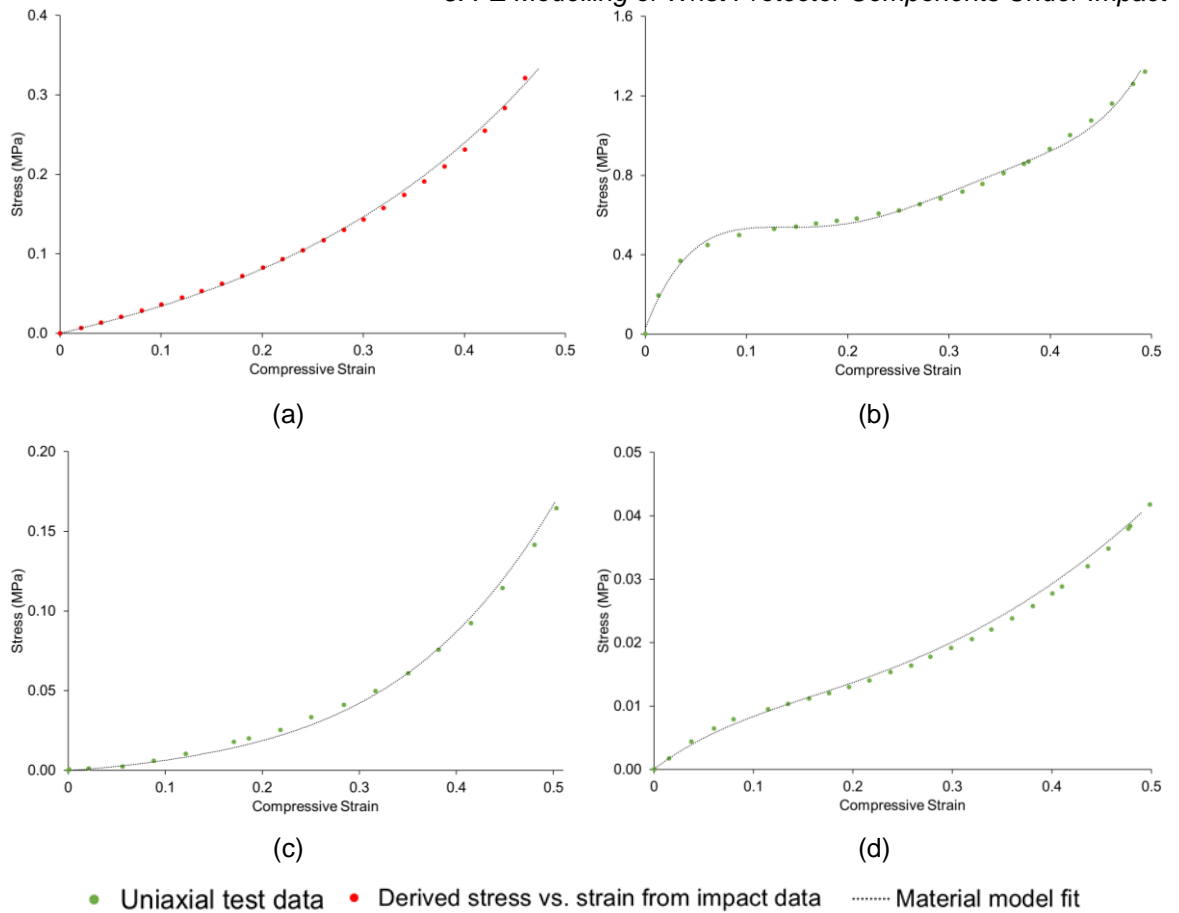


Figure 5-3 Stress vs. strain plots showing example curve fitting to obtain material model coefficients for an Ogden model (a) short protector supporting foam and (c) long protector supporting foam and a Mooney-Rivlin model (b) short protector pad and (d) long protector D30®.

An alternative to using the uniaxial stress vs. strain test data obtained in Chapter 3.4.2 was to use the 0.5 J impact data from Chapter 4.3.1, with stress vs. strain data at high strain rates derived using linear equations of motion (Ankrah and Mills, 2003; Burbank and Smith, 2012; Signetti *et al.*, 2018). The filtered temporal force data presented in Chapter 4 (Figure 4-10) was fitted with a second order polynomial trend line up to maximum compression (Figure 5-4b). Acceleration vs. time data was generated from the polynomial trend line equation and the trapezium method was applied in order to obtain a strain vs. time trace (Figure 5-4c). Calculated strain was validated against the strain obtained in the high-speed videos. A linear trend line placed on the strain vs. time trace was used to estimate the strain rate during loading, as fundamentally, the drop mass is decelerating upon impact. The acceleration data generated from the polynomial trend line was converted to force using Newton's second law ($F = ma$) and plotted against strain to obtain a stress vs. strain relationship (Figure 5-4d). The process of curve fitting explained above could then be applied to the higher strain rate data in the same way to obtain material model coefficients (Figure 5-3a). Pilot data identified that the supporting foam of the

short protector required this method as the 2 s^{-1} stress vs. strain data was too soft, therefore causing errors in simulations due to negative volume elements.

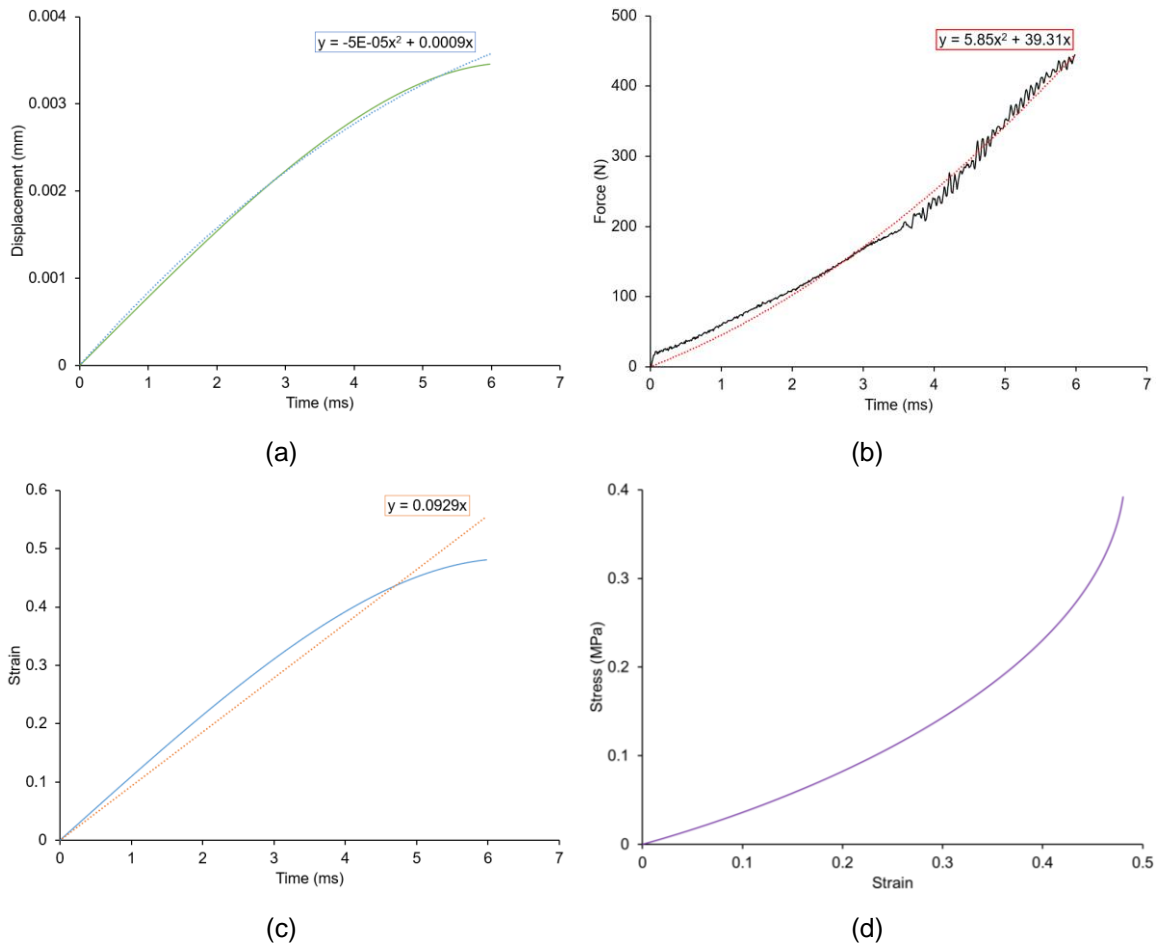


Figure 5-4 The process of converting a 0.5 J impact on the short protector foam to a stress vs. strain curve, (a) displacement vs. time plot, (b) force vs. time plot with a second order polynomial trend line, (c) strain vs. time plot calculated from the polynomial trend line with a linear trend line used to estimate strain rate, (d) stress vs. strain plot.

A further method to using higher strain rate data would have been to artificially stiffen the quasi-static test data and tune the material models in the simulation until the results were similar to the experimental data. Smith and Duris (2009) used a similar technique, tuning the parameters of the linear viscoelastic model for a sports ball, as did Andena *et al.* (2018) who extrapolated low strain rate data when modelling sports surfaces. Using raw data rather than stiffened or tuned data is preferable as it means the modelling technique can be used for other applications and is not specific to one particular scenario. Therefore, also providing the opportunity to use the FE model as a design tool.

Hyperelastic material models were used in the wrist protector for the supporting foams of both protectors, pad of the short protector and D3O[®] of the long protector. The pad and D3O[®] demonstrated stress vs. strain behaviour best represented by a Mooney-Rivlin model. The supporting foams, which are more rubber like and

presented up-turned S-shaped curves, were represented with an Ogden model. **Error! Reference source not found.** shows each component, and the corresponding material model coefficients obtained from curve fitting the 2 s^{-1} stress vs. strain data for the median samples from Chapter 3 and the impact data at 0.5 J for the supporting foam of the short protector. Generally, hyperelastic materials are deemed incompressible, therefore $D1$ is equal to zero throughout (Ansys, 2015). Poisson’s ratio was not measured due to material availability. If a tensile sample could be obtained, the sample area where digital image correlation could be used to calculate Poisson’s ratio was small (12 mm by 2 mm - BS 903-A2, 1995, type 4), meaning accurate measurements could not be achieved. Therefore, Poisson’s ratio was estimated from the literature (Chapter 3.3, Table 3-3) and a sensitivity study of the effect of changing the Poisson’s ratio in the material models was assessed.

Table 5-2 Hyperelastic material model coefficients replicating the behaviour of the median sample of each component.

Component	Material Model	Mooney-Rivlin Coefficients (MPa)					Ogden Coefficients		
		C10	C01	C11	C20	C02	MU1 (MPa)	A1	
Short	Pad	Mooney-Rivlin	-	31.697	-	58.126	139.220		
	Supporting Foam	Ogden						0.030	7.244
Long	D30®	Mooney-Rivlin	-0.072	0.097	0.036				
	Supporting Foam	Ogden						0.003	11.028

5.2.3 Viscoelastic Models

Four of the materials within the two wrist protectors (supporting foams, pad and D30®) had rate dependent and viscoelastic properties. Previously, two methods within the sports engineering sector have been used to replicate viscoelastic behaviour (Chapter 2, Table 2-5 and Table 2-6). A linear viscoelastic model (Equation 5-3) has been used to describe the flesh of a horse (Brolin and Wass, 2016) and the addition of a relaxation function, in the form of a Prony series (Equation 5-4) (LSTC, 2017a) has been commonly used to describe the rate dependency of sports balls (Tanaka *et al.*, 2006; Price *et al.*, 2008; Ranga and Strangwood, 2010). Within this study, the addition of a Prony series, in the form of

a second card added to the hyperelastic material model, within the input k file was used (k file inputs for all material models shown in Appendix 10.F).

$$g(t) = G_{\infty} + (G_0 - G_{\infty})e^{-\beta t} \quad \text{Equation 5-3}$$

$$g(t) = \sum_{i=1}^n \alpha_i e^{-\beta_i t} \quad \text{Equation 5-4}$$

Where: $g(t)$ is shear relaxation moduli, G_{∞} is long-term shear modulus, G_0 is short-term shear modulus, i is the number of Prony series terms, α_i are the shear moduli, β_i are the decay constants and t is time.

As with the hyperelastic material models, a Prony series can have multiple terms, providing a more detailed fit to the test data. To obtain the Prony series material coefficients, a curve fitting technique was used within ANSYS® Mechanical APDL v18.2. The first 30 s of the 50% compression stress relaxation data (obtained in Chapter 3) after full compression, was imported and a Prony series curve fitting option was then selected. The first 30 s of data was used because when the full 300 s was trialled in pilot testing, although the coefficients were different, the impact model results were the same. ANSYS® Mechanical APDL runs through 1,000 iterations of combinations of constants and presents the best fit within a residual tolerance level of 1% and the match is presented as shown in Figure 5-5. Table 5-3 shows each component and the Prony series coefficients chosen to replicate the median sample stress relaxation data from Chapter 3. The calculated residual between the raw material data and the material model curve fit is also presented for the plots shown in Figure 5-5.

5. FE Modelling of Wrist Protector Components Under Impact

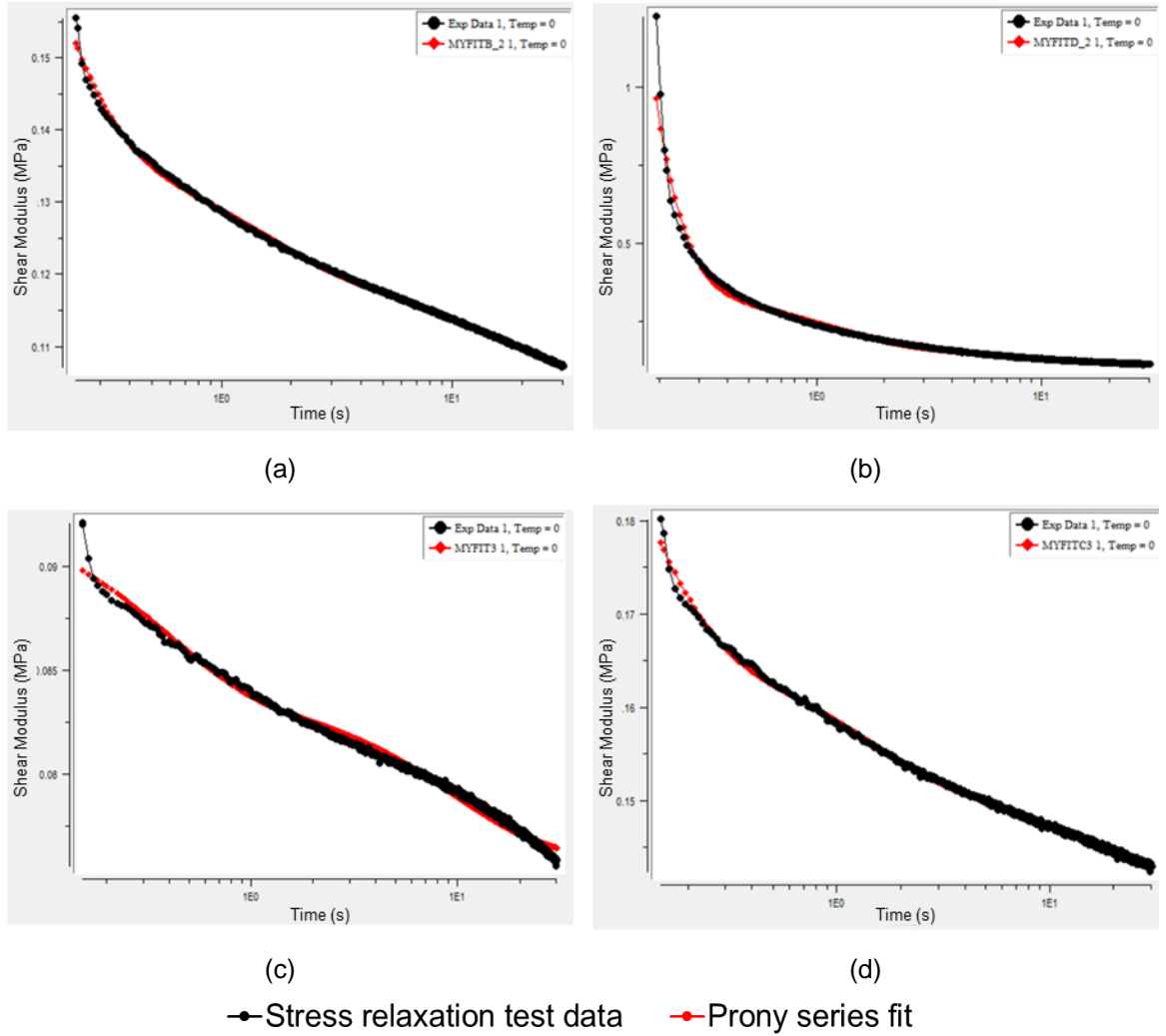


Figure 5-5 Screen-shots of shear modulus vs. time plots showing example curve fitting results from ANSYS® Mechanical APDL when obtaining material model coefficients for the Prony series (Table 5-3). Short protector (a) supporting foam and (b) pad and long protector (c) supporting foam and (d) D30®.

Table 5-3 Prony series coefficients required to reproduce the viscoelastic behaviour of the median sample components of the wrist protectors. The calculated residual between the curve fit and the raw material data is also shown for the plots in Figure 5-5.

Protector	Component	Prony Series Coefficients (α_i units are MPa)						Calculated Residual
		α_1	β_1	α_2	β_2	α_3	β_3	
Short	Pad	0.004	7.064	0.976	0.058	0.013	0.833	0.323
	Supporting Foam	0.471	0.110	0.071	1.188	0.063	15.817	0.005
Long	D30®	0.049	14.602	0.273	0.088	0.064	1.153	0.004
	Supporting Foam	0.084	9.782	0.097	0.374	4.75e-05	1.759	0.038

Ranga and Strangwood (2010) highlighted that when using stress relaxation data the ‘factor-of-ten’ rule (Sorvari and Malinen, 2006) should be used. Due to machines not being infinitely quick to compress the sample, there is a proportion of

5. FE Modelling of Wrist Protector Components Under Impact acceleration and therefore pure relaxation data is not obtained. When this rule was applied to the stress relaxation data obtained for the materials of the wrist protector however, the important relaxation phase is lost (example for the short protector supporting foam Figure 5-6a – red shaded area). By losing this portion of data, the rate dependency effect is minimised therefore, the material behaviour is not accurately captured and the response is too soft when tested across multiple energies (Figure 5-6b). The ‘factor-of-ten’ rule was therefore not used throughout this modelling process.

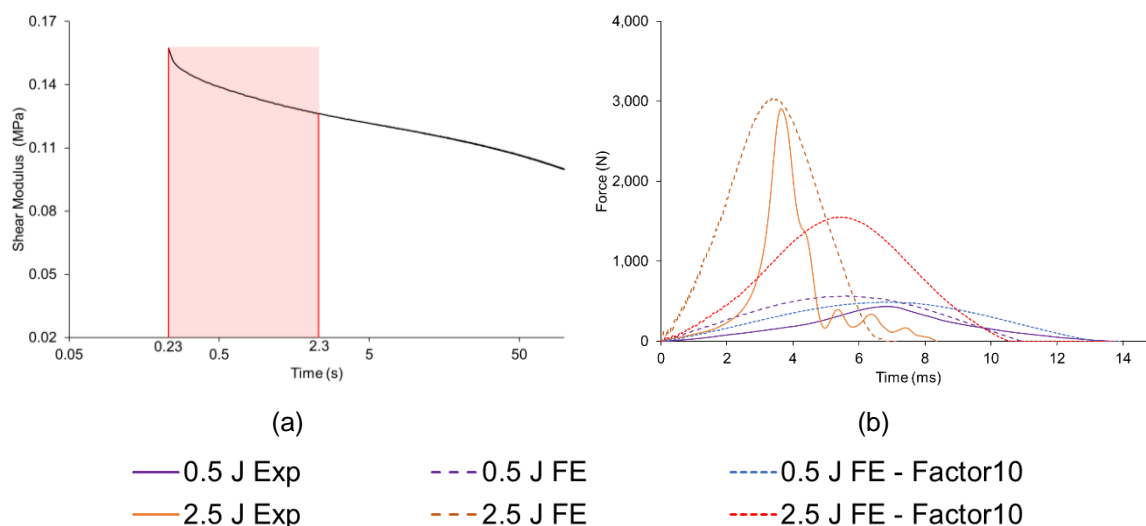


Figure 5-6 Example of the ‘factor-of-ten’ rule applied to the short protector supporting foam. (a) Loss of relaxation data if the rule was applied to the shear modulus vs. time response. (b) Temporal force data when using the full shear modulus response vs. the ‘factor-of-ten’ rule in a 0.5 and 2.5 J modelled impact compared to the experimental data in Chapter 4.

5.3 FE Model Methodology

FE models replicating the setup of the experimental impact in Chapter 4.2 were created in ANSYS® Workbench v18.2 and solved using the explicit dynamics code LS-DYNA® vR8.1.0 (Livermore Software Technology Corporation, Livermore, CA, USA). The results of the experimental impact test were used for comparison to validate the models. Models were validated visually in terms of the full impact trace, as well as numerically in terms of peak force, impact duration and maximum compression. Through validating individual parts under impact, each material model could be assessed for accuracy prior to combining them all in a full wrist protector impact, minimising the number of uncertainties. Models of the impact test were conducted over multiple energies to check the behaviour of parts within the model were still accurately captured, as multiple components were identified as being rate dependent in Chapter 3 (pad, D3O® and supporting foams).

The models consisted of a rigid plate (drop mass, \varnothing 80 mm) of thickness 2 mm and density $1.6E+05 \text{ kg.m}^{-3}$ (1.6 kg), constrained in the y-axis, striking the palmar components of both the short and long protector placed on a rigid base plate (80 x 80 x 2 mm). Thickness of the drop mass was modified from the actual thickness in the experiment (20 mm) as pilot testing indicated that changing the density had minimal effect on the impact response but reduced simulation run time. The dimensions of the palmar components were a replication of the median sample for each component showcased in Chapter 3.4 (Table 3-4) (Thicknesses - short protector - pad 6.2 mm, shell 3 mm, supporting foam 7.4 mm, long protector – D3O[®] and supporting foam 4.5 mm). Components were modelled at impact energies replicating the experimental set up in Chapter 4.2 both as individual components and as a combined palmar unit. The higher impact energies of 6.0 J (short protector) and 2.5 J (long protector) within the experiment caused one or multiple components to bottom out, therefore these energies were not modelled.

Geometries of the individual components were created in Solidworks[®] 2017 (Dassault Systems[®]). All samples, apart from the short protector shell, were uniform cylinders, meaning a 38 mm diameter circle could be drawn and extruded to the desired thickness for each part. For the shell of the short protector, the CAD technique 'sketch to image' was used, where a scanned 2D image (Samsung MultiXpress X4300LX copier, Gyeonggi-do, Korea) (Chapter 3, Figure 3-3) was used to obtain the correct outer profile of the object and extruded to the required thickness. For the combined impacts, the geometries of the individual components were created into an assembly in ANSYS[®] SpaceClaim, where parts were connected via shared topology. The technique of shared topology is used where bodies touch, meaning that the parts act as one unit rather than separate bodies and a continuous mesh can be applied (SpaceClaim, 2014). When parts were deconstructed from the wrist protectors (Chapter 3, Figure 3-3 and Figure 3-4), they were all held together by double-sided tape, therefore, sharing topology reflected the experimental setup.

Each part of the protector and the two plates were meshed with solid brick elements (ELFORM 1) apart from the shell of the short protector, which was meshed with solid tetrahedral elements (ELFORM 10) (Figure 5-7). The element ELFORM 1 is a constant stress solid hexahedra element (default element type in LS-DYNA[®]), which is quoted as being "*efficient and accurate and even works for severe deformations*"

5. *FE Modelling of Wrist Protector Components Under Impact* (LS-DYNA, 2011). ELFORM 10 is a one point constant stress solid tetrahedron element, which is often used when modelling foams (LS-DYNA, 2011). The number of elements for each part was chosen based on a mesh convergence study (Table 10-3, Appendix 10.G.1). The total number of elements for the combined impact of the short protector was 92,031 and for the long protector was 56,782.

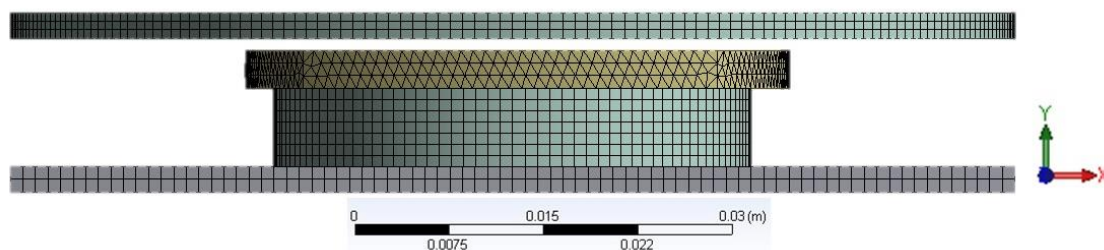


Figure 5-7 Example of how the plates and samples were meshed in ANSYS® Mechanical v18.2.

The base plate was fully constrained and the drop mass was assigned an initial velocity corresponding to the energies being tested ($0.5 \text{ J} = 0.79 \text{ ms}^{-1}$, $1.0 \text{ J} = 1.12 \text{ ms}^{-1}$, $2.5 \text{ J} = 1.76 \text{ ms}^{-1}$ and $5.0 \text{ J} = 2.49 \text{ ms}^{-1}$). A static and dynamic coefficient of friction of 0.5 (*Contact_Automatic_Surface_to_Surface) was applied between the individual parts, the base plate and the drop mass. The effect of varying the friction coefficient on the impact response was studied due to the lack of literature determining the frictional response between the aluminium drop mass and individual parts (polyurethane, HDPE, NBR rubber or PBT). As the impacting plate was $\sim 2\text{E}+6$ times stiffer than the supporting foams, $\sim 5\text{E}+4$ times stiffer than the pad, ~ 700 times stiffer than the HDPE shell and $\sim 8\text{E}+5$ times stiffer than D3O®, the contact setting SOFT = 1 was used (LSTC, 2017b). The default time step scale factor of 0.9 was also changed to 0.5. These contact settings were changed to prevent elements becoming distorted, resulting in negative volume errors, causing errors in termination of the simulations (LS-DYNA Support, 2019).

Pilot testing investigated the use of different material models to represent the behaviour of the wrist protector materials, based on previous research (Chapter 2, Table 2-5 and Table 2-6). Material models included a linear elastic model, linear viscoelastic model, hyperelastic model and an LS-DYNA® specific material model for foam (*Mat_Low_Density_Foam). After investigation, it was found that a hyperelastic model + Prony series represented the material's response under impact the best and did not require artificial stiffening, unlike other models. The median samples material models for the pad, D3O® and supporting foams consisted

5. FE Modelling of Wrist Protector Components Under Impact of the hyperelastic material model coefficients in **Error! Reference source not found.**, the Prony series coefficients in Table 5-3 and density and Poisson's ratio in Table 5-4. Density was calculated by weighing the compression samples from Chapter 3 (KERN ABS Analytical Balance 220-4N, Germany, 0.1 mg resolution) and dividing by the volume. Poisson's ratio was tuned to match the experimental impact data, in order to prevent the need for artificial stiffening of the compression data, using the sensitivity analysis as a guide (Figure 5-9). The Poisson's ratio's chosen within the models after 'tuning' were still realistic as they fell within the ranges found within the literature in Table 3-3. Chapter 3 showed variance between the five samples for each materials stress vs. strain response (Chapter 3, Figure 3-10). The effect of this variability on the material models and in turn the FE model response was explored.

Table 5-4 Density and Poisson's ratio values used in the FE model for each hyperelastic component.

	Component	Density (kg.m ⁻³)	Poisson's ratio
Short	Pad	312	0.310
	Supporting Foam	184	0.495
Long	D3O [®]	154	0.497
	Supporting Foam	294	0.499

Each simulation was post-processed in LS-PrePost v4.3 where the temporal reaction force (rforc) between the impactor and the top of the sample was obtained, mimicking the accelerometer in the experiment. A section view, cutting the sample in half along the y-axis was performed where a node to node measurement between the two plates was taken to determine the deformation of the sample (Figure 5-8).



Figure 5-8 Example of how maximum compression was measured ($h2 - h1$). Image shows the FE model of the short protector pad + shell impact at 2.5 J (a) prior to impact and (b) at maximum compression. The drop mass is blue, shell is green, pad is yellow and the base plate is red.

The temporal force trace at each energy, for each component, was compared to the median samples obtained in Chapter 4.3. The range (softest and stiffest stress vs. strain response) produced by the different material models for each material was compared to the experimental mean impact data in terms of peak force, impact duration and maximum compression. The difference between the median FE model

5. FE Modelling of Wrist Protector Components Under Impact and median experimental data was directly compared to assess accuracy. A root mean squared error (RMSE) was calculated for each parameter of the FE model using Equation 5-5.

$$RMSE = \sqrt{\frac{\sum_{i=1}^n (P_i - O_i)^2}{n}} \quad \text{Equation 5-5}$$

Where: P_i is the predicted value from the model, O_i is the observed value from the experiment and n is the number of observations

5.4 Results

A sensitivity study was conducted to understand the effect of changing Poisson's ratio and the coefficient of friction between the drop mass/base plate and the material samples as these values were not measured or obtained from the literature. Increasing the coefficient of friction from 0.1 to 0.9 was found to decrease peak force by 1.3% and decrease maximum compression by 0.3%, therefore a value of 0.5 was used throughout. Poisson's ratio, when increased from 0.1 to 0.499 caused a stiffening effect (Figure 5-9). The stiffening effect can be linked to Equation 5-6. As you increase Poisson's ratio from 0.1 to 0.5, bulk modulus will increase, with 0.5 giving an infinite result (as you cannot divide by 0). As bulk modulus increases, the materials resistance to volumetric change increases, hence maximum compression decreases and peak force increases.

$$K = \frac{E}{3(1 - 2\nu)} \quad \text{Equation 5-6}$$

Where: K is bulk modulus (volumetric), E is Young's modulus and ν is Poisson's ratio.

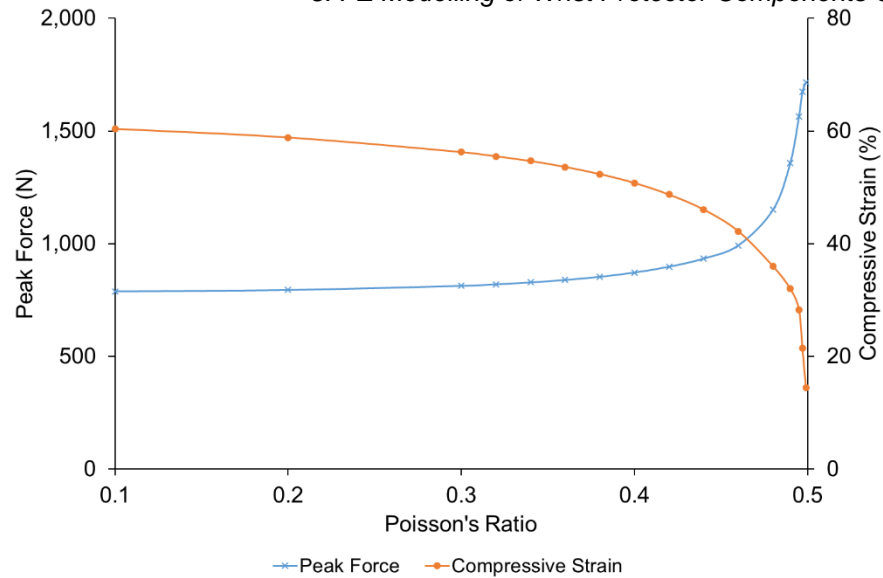


Figure 5-9 Sensitivity analysis showing the effect of changing Poisson's ratio for a 2.5 J impact on the short protector palmar pad on peak force and maximum compressive strain.

5.4.1 FE of Individual Components

Using the softest and stiffest stress vs. strain response from the five samples of the pad had a large effect on the temporal force trace produced by the FE model, with a similar trend seen for the other materials too (Figure 5-10). Therefore, only the median sample temporal force trace for each impact scenario is shown as a comparison against the experimental impact data. Figure 5-11 shows both the short and long protector individual component impact temporal force traces at a range of energies (0.5 to 5.0 J). The full range of FE data from using the different material responses is shown in Table 5-5 with a direct comparison of the median FE model and experiment highlighted in Table 5-6.

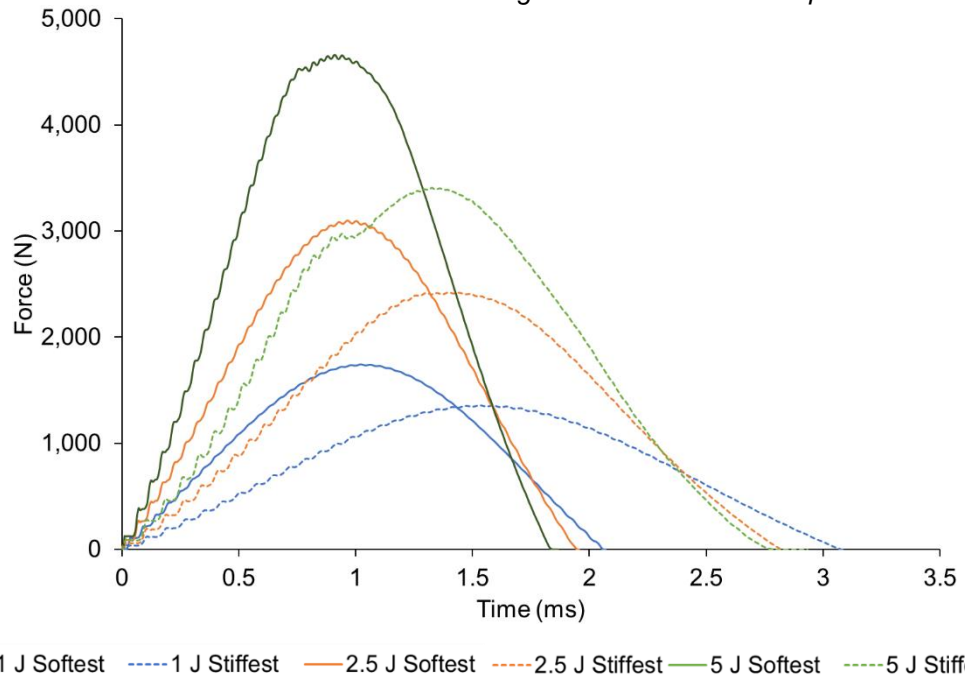


Figure 5-10 Example temporal force traces for the short protector pad under impact at 1.0 to 5.0 J, showing the effect of using the variable stress vs. strain response (softest and stiffest) (Chapter 3, Figure 3-10) to replicate the impact behaviour within an FE model.

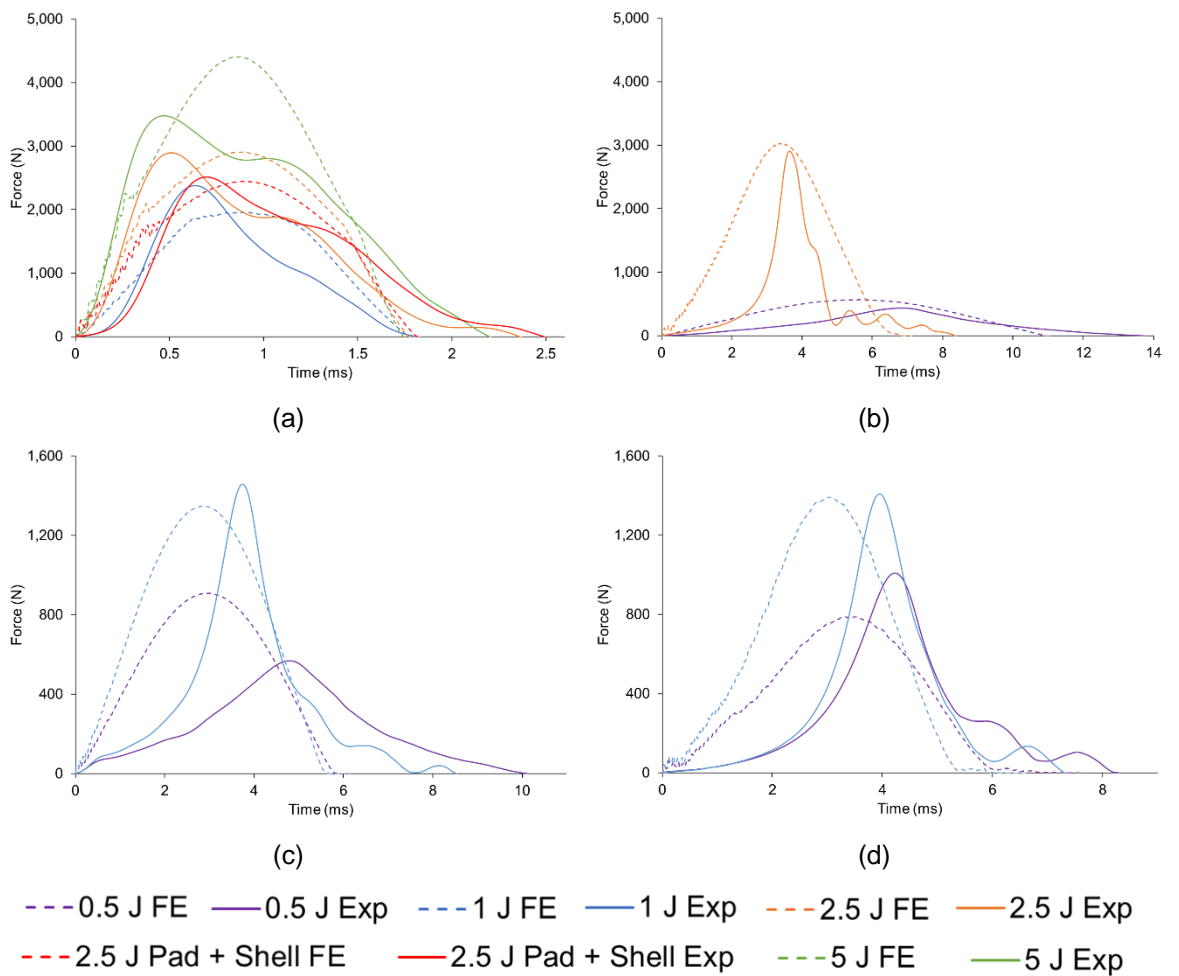


Figure 5-11 Temporal force traces comparing median FE model and experimental sample impacts. Short protector components (a) pad at 1.0, 2.5 and 5.0 J and pad + shell at 2.5 J and (b) supporting foam at 0.5 and 2.5 J. Long protector components (c) D30® at 0.5 and 1.0 J and (d) supporting foam at 0.5 and 1.0 J.

5.4.2 FE of Full Palmar Impact

Temporal force traces for the combined palmar component impacts for the short protector at 2.5 and 5.0 J and the long protector at 0.5 and 1.0 J for the median FE model and experiment are shown in Figure 5-12. The full range of FE data derived from the different material responses (softest and stiffest), is also shown for the combined palmar component impacts in Table 5-5.

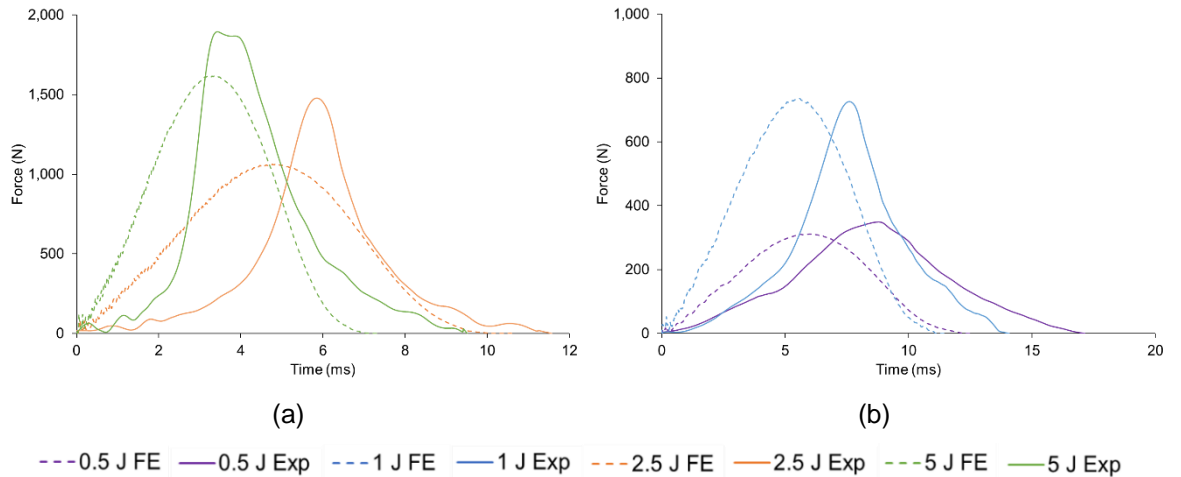


Figure 5-12 Temporal force traces comparing median FE model and experimental sample impacts for the combined palmar component impacts (a) short protector at 2.5 and 5.0 J and (b) long protector at 0.5 and 1.0 J.

Table 5-5 Peak force, maximum compression, maximum compressive strain and impact duration for the range of FE models using the softest and stiffest stress vs. strain response for each component of both wrist protectors at a range of energies. The median experimental impact data (mean ± standard deviation) is shown for comparison.

Component		FE					Experiment			
		Energy (J)	Peak Force (N)	Maximum compression (mm)	Maximum compressive Strain (%)	Impact Duration (ms)	Peak Force ± St Dev (N)	Maximum compression ± St Dev (mm)	Maximum compressive Strain ± St Dev (%)	Impact Duration ± St Dev (ms)
Short	Pad (Figure 5-11a)	1.0	1,360 to 1,965	0.63 to 1.13	10 to 18	1.79 to 3.10	2,381 ± 5	0.39 ± 0.06	6 ± 1	1.82 ± 0.01
		2.5	2,421 to 3,100	1.12 to 2.16	18 to 35	1.81 to 2.84	2,897 ± 29	0.65 ± 0.07	10 ± 1	2.37 ± 0.01
		5.0	3,410 to 4,661	1.51 to 2.75	24 to 44	1.77 to 2.93	3,479 ± 54	1.57 ± 0.06	25 ± 1	2.21 ± 0.01
	Pad + Shell (Figure 5-11a)	2.5	1,829 to 2,560	1.13 to 2.15	12 to 23	1.84 to 2.82	2,614 ± 40	0.81 ± 0.10	13 ± 2	2.64 ± 0.02
	Supporting Foam (Figure 5-11b)	0.5	569	2.40	33	11.05	436 ± 19	4.05 ± 0.05	56 ± 1	13.74 ± 0.16
		2.5	3,034	3.92	54	7.12	2,932 ± 85	5.99 ± 0.18	83 ± 3	8.33 ± 0.06
	Combined components (Figure 5-12a)	2.5	911 to 1,063	3.82 to 4.19	23 to 25	10.68 to 11.78	1,479 ± 23	5.86 ± 0.14	36 ± 1	11.87 ± 0.77
5.0		1,683*	4.85*	29*	7.32*	1,906 ± 48	7.47 ± 0.16	46 ± 1	9.43 ± 0.06	
Long	D3O® (Figure 5-11c)	0.5	888 to 934	1.42 to 1.90	32 to 42	5.79 to 6.16	569 ± 2	2.87 ± 0.07	64 ± 2	10.09 ± 0.07
		1.0	1,320 to 1,430	1.76 to 2.26	39 to 50	5.58 to 5.98	1,459 ± 31	3.27 ± 0.10	73 ± 2	8.04 ± 0.55
	Supporting Foam (Figure 5-11d)	0.5	767 to 791	2.09 to 2.13	46 to 47	7.54 to 7.75	1,016 ± 23	3.32 ± 0.21	74 ± 5	8.22 ± 0.02
		1.0	1,323 to 1,402	2.42 to 2.46	54 to 55	6.61 to 6.66	1,410 ± 13	3.97 ± 0.18	88 ± 4	8.24 ± 0.67
	Combined components (Figure 5-12b)	0.5	309 to 316	2.86 to 2.90	32	12.45 to 12.71	349 ± 4	5.95 ± 0.23	66 ± 3	17.12 ± 0.19
		1.0	732 to 747	3.48 to 3.54	39	11.35 to 11.56	727 ± 11	6.41 ± 0.25	71 ± 3	14.01 ± 0.42

*Denotes that the FE model failed due to negative volume errors. **Bold text** indicates the FE range falls within the experimental standard deviation for the median component.

Table 5-6 Difference between the median FE model and experimental sample for each component, highlighting the overall RMSE for peak force, maximum compression and impact duration for each protector.

Component		Energy (J)	Peak Force (N)	Maximum Compression (mm)	Impact Duration (ms)
Short	Pad (Figure 5-11a)	1.0	-638	0.36	0.25
		2.5	9	0.85	-0.41
		5.0	928	0.33	-0.34
	Pad + Shell (Figure 5-11a)	2.5	-165	0.71	-0.68
	Supporting Foam (Figure 5-11b)	0.5	133	-1.65	-2.69
		2.5	102	-2.14	-1.21
	Combined components (Figure 5-12a)	2.5	-443	-1.95	-1.19
		5.0	-287	-2.65	-2.06
RMSE		448	1.56	1.38	
Long	D3O® (Figure 5-11c)	0.5	339	-1.01	-4.28
		1.0	-111	-1.08	-2.25
	Supporting Foam (Figure 5-11d)	0.5	-228	-1.21	-0.65
		1.0	-17	-1.55	-1.59
	Combined components (Figure 5-12b)	0.5	-37	-3.06	-4.54
		1.0	9	-2.90	-2.51
RMSE		174	2.00	3.00	

5.5 Discussion

The impact behaviour of the palmar components of two styles of wrist protector have been replicated within FE models via appropriate material model algorithms using the material characterisation data from Chapter 3. A hyperelastic model, such as an Ogden or Mooney-Rivlin, paired with a Prony series, was the most common material model selected. Hyperelastic models paired with a Prony series have been previously used to describe the behaviour of foams and woven fabrics, similar to the materials found within wrist protectors (Price *et al.*, 2008), as well as rate dependent sports balls (Tanaka *et al.*, 2006; Ranga and Strangwood, 2010).

The highest quasi-static strain rate of 2 s^{-1} was required for the hyperelastic material models to replicate the behaviour of the samples under impact. The supporting foam of the short protector, however, required stiffer data due to the model failing due to negative volume errors when quasi-static data was used. Artificial stiffening of the

data could have been used until there was agreement between the simulation and experimental results, however this was not preferable. Using impact data at 0.5 J (average strain rate of $\sim 93 \text{ s}^{-1}$), a similar technique to that used by Burbank and Smith (2012) and Ankrah and Mills (2003), was utilised to obtain coefficients for the Ogden model for this material. By fitting material models to material characterisation data, it provides scope for the FE models created to be used as a design tool in the future. However, there are associated limitations with this method, such as the accuracy of data provided by the material testing machines as they were operating close to maximum capacity. When using impact data there are also limitations as the resultant stress vs. strain response is dependent on both assumptions made and a large amount of post-processing of the impact data (Brizard *et al.*, 2017). Future work should explore other techniques to characterise the materials at high strain rates, as discussed in Chapter 4. Ideally, the strains and strain rates experienced within a wrist protector during a fall would be understood so materials could be characterised at these rates for use within the FE models, a similar strategy to that used by Lane *et al.* (2018) when modelling tennis balls.

The FE models of individual and combined palmar component impacts for both protectors showed the same trends as the experimental testing seen in Chapter 4. As energy increased, peak force and maximum compression increased, while impact duration decreased. The variance between samples from the same size and brand protector seen within compression testing (short protector supporting foam = 7%, pad = 33%, long protector supporting foam = 20%, D3O[®] = 24%) had a large effect on the FE model output of an impact (Figure 5-10). The difference between using the softest and stiffest compressive response within a material model increased peak force by a mean of 33 and 4%, decreased maximum compression by 39 and 9%, and decreased impact duration by 32 and 3% (short and long protector). Therefore, when comparing simulations to experimental data, broad agreements in data trends and close approximations were used rather than precise numerical matches.

Peak force had a RMSE of 448 N for the short protector, which falls within the variance seen within the experimental impact. The long protector had a RMSE of 162 N for the long protector, which falls outside the variance of the experiment for this protector. However, if the outlier of the D3O[®] being impacted at 0.5 J is not included, peak force is predicted within 6% of the experiment. Discrepancies in peak

force could be because uniaxial compression testing was conducted to 50% strain; however, the supporting foams within the experimental impact were reaching 80 to 90% strain. As these materials are hyperelastic, this could mean that the stiffer portion of the stress vs. strain curve was being missed. In order to obtain repeatable measurements within quasi-static compression testing, however, 50% strain was the largest strain achievable prior to sample damage and consequently samples stiffening upon every compression.

Impact duration was under predicted by ~2 ms across all models. Two milliseconds corresponds to the same time frame seen in the experiment before the samples become fully engaged (Chapter 4, Figure 4-7). Therefore, the model can be said to give a good prediction of this parameter. Within the FE models, samples were presumed to have uniform thickness, however, in reality, this was not the case, with some short protector pad samples varying in thickness by ~0.5 mm (Chapter 3, Table 3-4). The non-uniformity of samples could affect both impact duration as well as maximum compression.

Maximum compression was within a RMSE of ~1.60 to ~2.00 mm across both protectors. With an experimental measuring error for displacement being ~1 mm the difference between the model and experiment could be because of this reason. Alternatively, discrepancies between the models and experiment could be due to high values of Poisson's ratio being used. A sensitivity study showed Poisson's ratio to have a stiffening effect when increased from 0.1 to 0.499. To avoid tuning or artificial stiffening of data, Poisson's ratio was increased to 0.497 for D3O® and 0.499 for the long protector supporting foam. Experimental impact data, as used for the supporting foam of the short protector could have been used, however, this caused the impact response of the model to become too stiff both in terms of peak force and maximum compression, therefore it was not used.

The FE model for all components of the wrist protectors both under and over predicts peak force, maximum compression and impact duration, suggesting that the material models are neither too stiff or too soft and differences between the data could be due to other factors. These factors include materials not being completely isotropic and homogeneous as presumed in the material models. Friction being present between the drop mass and linear guide rail meaning inbound velocity and therefore impact energy differs slightly to the theoretical value being used within the model.

5.6 Chapter Summary

The material data from Chapter 3 and the 0.5 J data from Chapter 4 were used to select material model algorithms to replicate the different behaviours of the materials from two wrist protectors within an FE model. A linear elastic or a hyperelastic (Mooney-Rivlin and Ogden) model paired with a Prony series were the two material models chosen. Models replicating the impact scenario in Chapter 4 were created and compared to the experimental data for each component and material across a range of energies. FE models showed the same trends where, as energy increased, peak force and maximum compression increased, while impact duration decreased. As both the models and experimental data are approximations of the reality (Senner *et al.*, 2019), the validated material models selected were deemed sufficient to predict the behaviour of the materials under impact. Therefore, the material models selected will be applied to FE models of snowboard wrist protectors for simulating hand/surface impacts (Chapter 7) and compared to experimental data for validation. Chapter 6 will collect the experimental data for comparison, across a range of impact energies.

6 Impact Testing of Wrist Protectors

6.1 Introduction

Chapter 5 developed FE models to simulate impact on the palmar components of two wrist protectors. In this present chapter, the impact rig developed by Adams (2018) (Chapter 2.4.2, Figure 2-9) was modified, so impact data of full wrist protectors fitted to a surrogate could be collected over a range of energies. This data will be used for validation of the full wrist protector models that will be developed in Chapter 7 (Figure 6-1). This chapter will also contribute towards objective three of the thesis; to develop and validate FE models of snowboard wrist protectors for simulating hand/surface impacts.

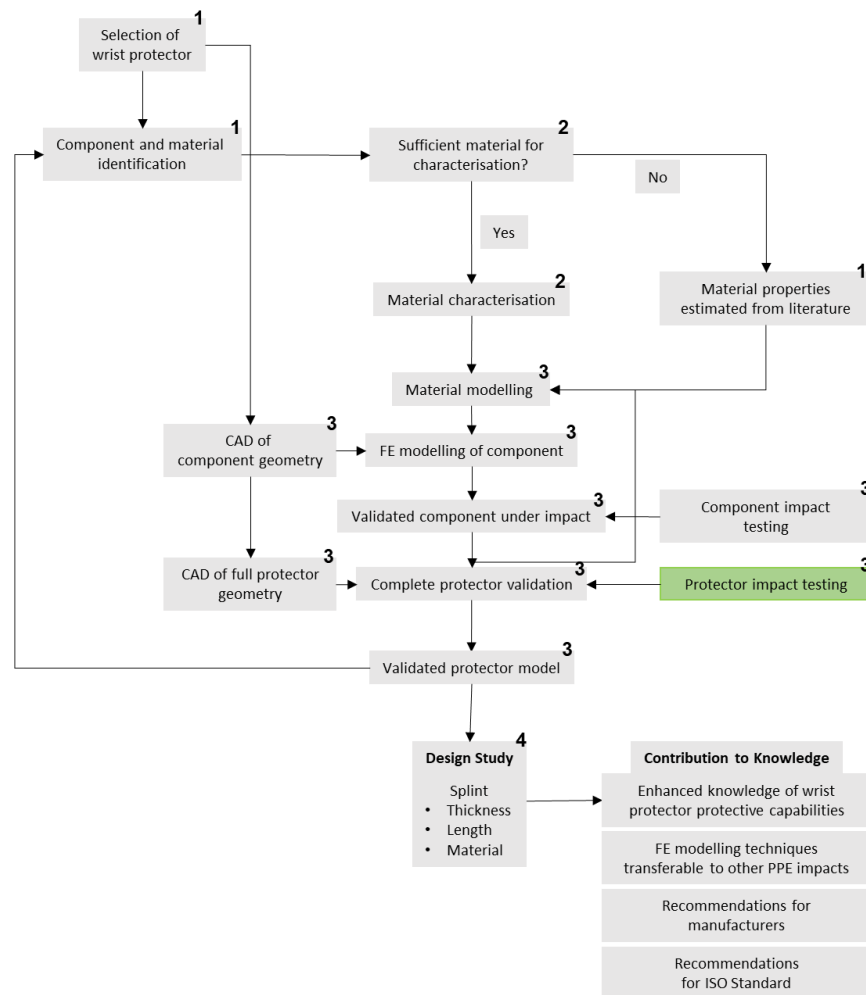


Figure 6-1 Schematic diagram indicating where this chapter (highlighted in green) fits within the overall project (numbers correlate to the objectives of the thesis).

6.2 Impact Rig Development

The rig developed by Adams (2018) had a pendulum striking arm, which can be released from a pre-set height to impact a wrist surrogate (Chapter 2.4.2, Figure

2-9). The surrogate was based on a laser scan of a human hand and forearm and consisted of an aluminium CNC machined hand (Protolabs®, UK) and a steel central support surrounded by a 3D-printed polyamide casing (Materialise, UK). The base of the surrogate was attached to a tri-axial dynamometer (referred to as a load cell) (Kistler 9257A, Switzerland) for measuring impact loads. The rig was also fitted with two potentiometers; one to obtain the angle of the surrogate wrist (Metalux POL 200, USA) and the other the pendulum arm (Bourns® 6657, USA).

The entire mass of the pendulum arm does not contribute to the impact, so the effective striking mass should be calculated (van Huffelen *et al.*, 2004). The effective mass is the concentrated mass of the striking object, which comes to a stop during the period of peak impact force (Addison and Lieberman, 2015). The effective mass of the pendulum striking arm of Adams (2018) was calculated as 10.7 kg using Equation 6-1 (Cross, 2014), allowing impact energies to be obtained for given release heights. Siegkas *et al.* (2019) used a version of this equation to calculate effective mass of a pendulum when impact testing motorcycle helmets.

$$\frac{1}{M_e} = \frac{1}{M} + \frac{b^2}{I_{cm}} \quad \text{Equation 6-1}$$

Where: M_e is effective mass, M is total mass, b is the distance from the pivot to impact point and I_{cm} is the moment of inertia about an axis through the centre of mass.

When attempting to simulate a person falling on an outstretched arm in an impact test there are many parameters to consider, such as the mass of the body acting on the wrist, the fall height and corresponding impact velocity. Adams (2018) developed the rig to replicate the loading scenario of Greenwald *et al.* (1998), who used a linear drop tower rig to impact test cadaveric arms (23 kg, 0.4 m, 2.8 ms⁻¹, 90 J). In the present study, 10 to 50 J (in 10 J increments) was seen as a suitable range of impact energies for FE model validation. While the rig setup was well suited for the work of Adams', it was not versatile enough to allow for impacts at the lower energies required in this project, without limiting inbound velocities to unfeasibly low values (did not generate force readings). Therefore, the effective mass of the pendulum arm was reduced, enabling testing at higher impact velocities, which were more representative of falls for the selected range of impact energies.

Incorporating Equation 6-1 the contribution of effective mass from the parts of the pendulum striking arm (Adams, 2018) were quantified (Figure 6-2). The steel bar

6. *Experimental Impact Testing of Wrist Protectors* (Hillsborough Steelstock Ltd, UK) contributed 5.6 kg to the effective mass of the pendulum striking arm (10.7 kg), while the other 5.1 kg was from the aluminium plate (2.1 kg) and polychloroprene blocks (3.0 kg). To check the calculations for effective mass, scales (Mettler Toledo PM16, UK) were placed under the impacting face for different configurations of the pendulum arm (bar in isolation, bar fitted with aluminium plate and bar fitted with aluminium block and polychloroprene blocks).

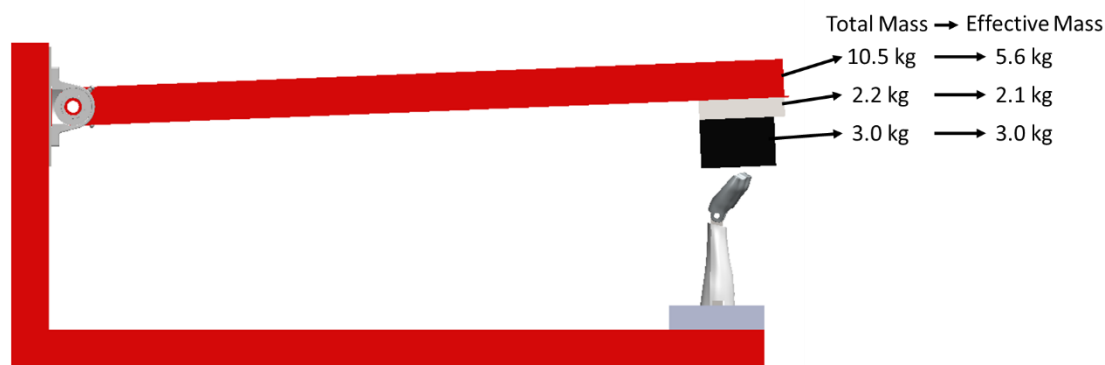


Figure 6-2 Schematic of the impact rig developed by Adams (2018) and its associated mass distribution.

To reduce the effective mass of the pendulum striking arm and in turn facilitate testing at a range of impact energies, two steps were taken. Step one reduced the thickness of the aluminium plate from 4 to 1 cm, lowering its contribution to the effective mass to 0.5 kg. Step two reduced the amount of polychloroprene, as each block contributed 0.6 kg to the effective mass of the pendulum arm. To select an appropriate number of blocks, a pilot test was undertaken impacting a short protector at an energy of 20 J, with the release height increased to compensate for the reduction in mass when a polychloroprene block was removed. Temporal force traces did not change noticeably when the number of polychloroprene blocks was reduced from five to two, however, with two blocks, the impact force associated with initial contact started to increase (Figure 6-3). To avoid damage to instrumentation, the surrogate and the impact rig, two polychloroprene blocks and a 1 cm thick aluminium plate were used for data collection, in turn reducing the effective striking mass of the pendulum arm to 7.2 kg.

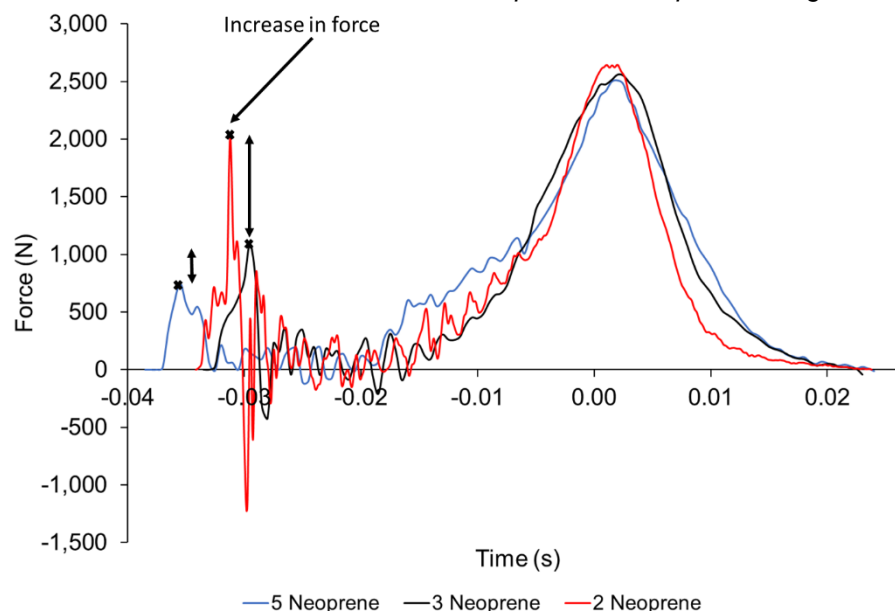


Figure 6-3 Temporal force trace showing the effect of changing the number of polychloroprene blocks when impacting the short protector at 20 J.

6.2.1 Impact Velocities from the Literature

Justifications for velocities as well as the effective mass and corresponding impact energy are not always provided by other researchers investigating falls and wrist injuries, however, they can provide a guide. Previous studies impact tested wrist surrogates (Maurel *et al.*, 2013; Schmitt *et al.*, 2009; Schmitt *et al.*, 2011; Hwang *et al.*, 2006) or cadaveric wrists (Greenwald *et al.*, 1998; Frykman, 1967; Moore *et al.*, 1997; Lewis *et al.*, 1997; Lubahn *et al.*, 2005; Burkhart, 2012; Zapata *et al.*, 2017; Giacobetti *et al.*, 1997b), along with controlled biomechanical studies (DeGoede and Ashton-Miller, 2002; DeGoede *et al.*, 2003; Schmitt *et al.*, 2012) were plotted for comparison alongside the velocities corresponding to the target energies of 10 to 50 J, for the unmodified and modified rig (Figure 6-4). Models utilising anthropometric data, for a range of ages, were also used to estimate fall velocities of the hand/surface impact from standing and compared in Figure 6-4, including; a rigid body model (Adams, 2018) and a more complex dynamic model (Van den Kroonenberg *et al.*, 1995) (details in Appendix 10.E.4).

The rigid body model predicted impact velocities that were higher than most of those reported in the literature (apart from Lewis *et al.* (1997) and Lubahn *et al.* (2005)). The dynamic model predicted lower velocities than the rigid body model, but higher than many of the other impact studies (apart from Lewis *et al.* (1997), DeGoede and Ashton-Miller (2002) and Lubahn *et al.* (2005)). The impact velocities corresponding to the target energies for the modified rig (red line) fall closer to those from the

literature and models than those for the unmodified rig used by Adams (2018) (blue line). Impact velocities for specific target energies for the modified rig corresponded closely to estimated fall velocities from standing when using the dynamic model of Van den Kroonenberg *et al.* (1995); 40 J corresponding to a 12 year old ($\sim 3.32 \text{ ms}^{-1}$ vs. $\sim 3.31 \text{ ms}^{-1}$) and 50 J corresponding to a 50th percentile male ($\sim 3.69 \text{ ms}^{-1}$ vs. $\sim 3.71 \text{ ms}^{-1}$).

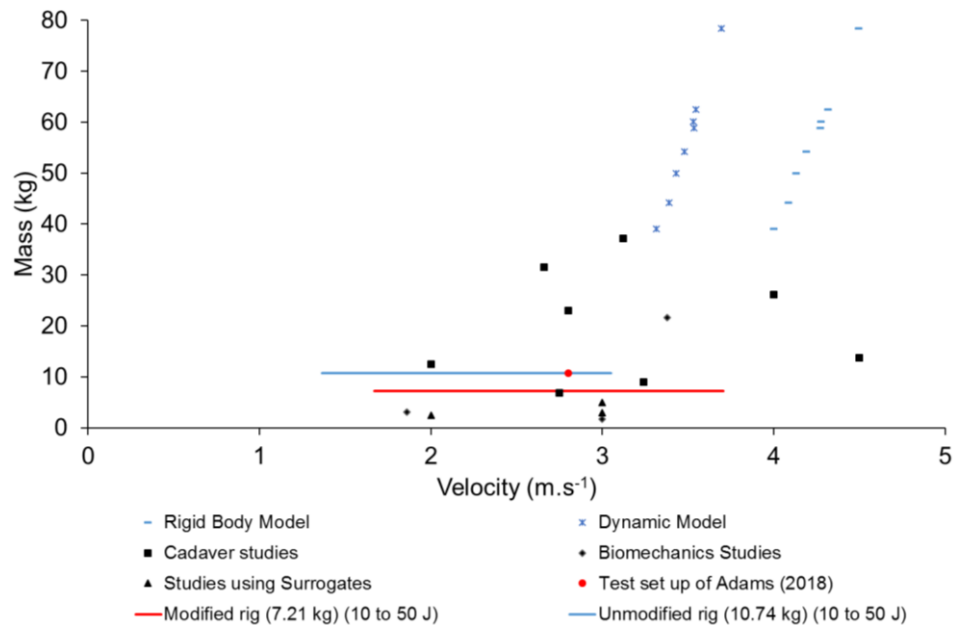


Figure 6-4 Mass vs. inbound velocity chart highlighting cadaver studies (Greenwald *et al.*, 1998; Frykman, 1967; Moore *et al.*, 1997; Lewis *et al.*, 1997; Lubahn *et al.*, 2005; Burkhart, 2012; Zapata *et al.*, 2017; Giacobetti *et al.*, 1997b), biomechanical studies (DeGoede and Ashton-Miller, 2002; DeGoede *et al.*, 2003; Schmitt *et al.*, 2012) and studies using surrogates (Maurel *et al.*, 2013; Schmitt *et al.*, 2009; Schmitt *et al.*, 2011; Hwang *et al.*, 2006) (black symbols). A rigid (Adams, 2018) and dynamic (Van den Kroonenberg *et al.*, 1995) model of a human fall for a range of ages (blue symbols) are also shown. The available range of velocities with the current test set up (Adams, 2018) (blue line with a red dot showing current set up) and the achievable range of velocities for 10 to 50 J for the modified setup with a reduced effective mass is also shown (red line).

During pilot testing at 10 J (using the modified rig) when the surrogate was impacted without a protector (bare hand), a peak force of $3,100 \pm 200 \text{ N}$ was produced, which falls within the range of published literature for distal radius fractures (1,104 to 3,896 N) (Chapter 2.2.3, Table 2-2). The peak force was also close to the draft ISO standard (ISO/DIS 20320) impact test pass threshold of 3,000 N. For 10 J impacts without a protector, the modified pendulum arm produced a loading curve with a similar slope to those of Greenwald *et al.* (1998) for cadaveric impacts, and the work of Adams (2018) (Appendix 10.E.5).

6.3 Impact Testing of Two Wrist Protector Designs - Methods

6.3.1 Pre Testing

A sheet (1.00 x 0.94 x 0.02 m) of polychloroprene (50 ShoreA hardness neoprene) was sourced from Boreflex Ltd., Rotherham, UK and the blocks required for testing were cut (OMAX[®] water jet 2626) (0.13 x 0.16 m) across its length and glued together (Alpha Thixofix[®], RS Components). The polychloroprene had a density of 1,450 kg.m⁻³ and a tensile strength of 40 kg.cm⁻² (data sheet in Appendix 10.E.3, (Boreflex Ltd, no date)).

Adams (2018) reported a 3.4% decrease in peak force over 50 consecutive impacts for a stack of five polychloroprene blocks impacting the surrogate without a protector. As the number of polychloroprene blocks was reduced from five to two in this current study, it was deemed necessary to check the repeatability of the polychloroprene response under impact to determine if there was any degradation. One hundred impacts were conducted at 10 J on a stack of two polychloroprene blocks using a bespoke drop tower rig (5 kg flat faced drop mass – 130 mm Ø, 15 mm thick, 0.2 m) (details of the rig are in Chapter 7.2.2) with two minutes between repeats. Data was filtered using a low-pass filter at 1 kHz and the peak force checked for evidence of degradation.

During preparation for impact testing, all protectors were placed onto the wrist surrogate when it was detached from the load cell. To ensure consistent strap tightness and to reduce variability, a 2 kg mass was attached to the end of each strap when the surrogate was held horizontal and slowly rotated about its longitudinal axis until they were fastened, a technique described by Adams *et al.* (2016). Markings were made on the protectors so the straps could be consistently fastened to the surrogate for testing.

6.3.2 Impact Testing

Impact testing was conducted on the left hand of the five size medium pairs of each protector (short and long – Chapter 3.2.2) across five energies (10 to 50 J). Numerous factors were explored during impact testing, through examining plots such as force vs. time and force vs. wrist angle, as well as key outputs such as peak force, maximum wrist angle and energy absorption. Testing took place over three consecutive days at room temperature (~21 °C).

One protector of each style was consecutively tested five times at all impact energies, starting with the lowest (denoted by A in the results section). Untested protectors were also impacted five times at either 20, 30, 40 and 50 J (denoted as B, C, D and E, respectively). To ensure consistency, testing of both protectors was performed at a given energy before the pendulum release height was increased. The order of protector testing was randomised for each impact energy. To compare a protected scenario against an unprotected one (referred to as a bare hand impact); three bare hand impacts were conducted pre and post protector testing at each energy. At 10, 30 and 50 J polychloroprene blocks were changed to limit the effect of any degradation affecting the results. At these three energies there was an extra bare hand impact, conducted before protector testing to condition the polychloroprene blocks, although this was not included within the data analysis.

Each protector was placed on the surrogate, strapped as marked and the hand angle manually set to $\sim 30^\circ$ (Figure 6-5). Each protector was impacted five times with three minutes between repeats, during which the protector was removed and then refitted to the surrogate, and the hand angle reset to $\sim 30^\circ$. The pendulum arm was raised to the required release height (Table 6-1) using a pulley. The release height was measured using a tape measure (± 0.5 mm), from the top of the hand (for a protector impact) or the top of the surrogate core (for a bare hand impact) to the base of the polychloroprene on the pendulum.

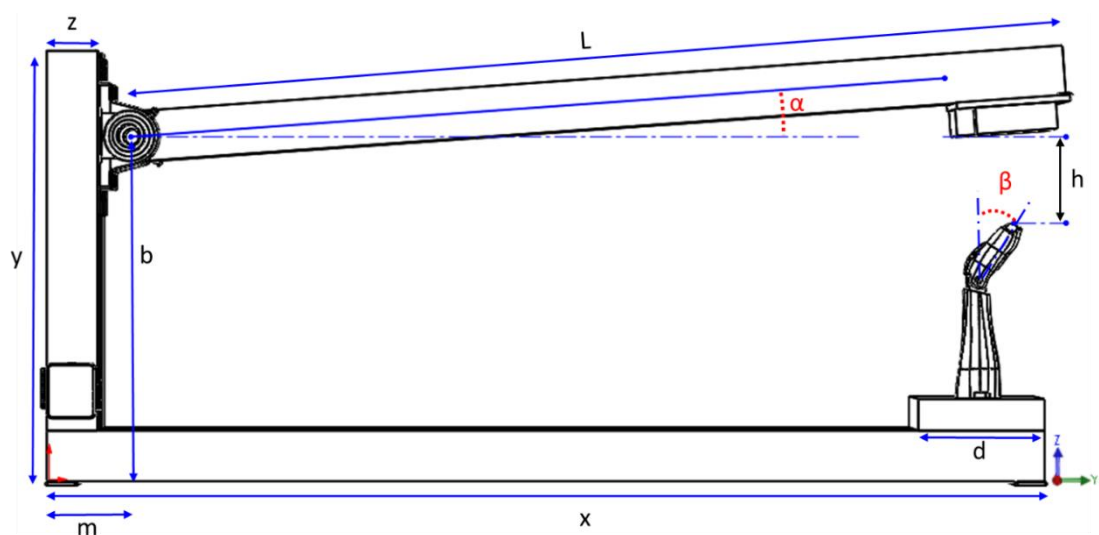


Figure 6-5 Schematic highlighting dimensions of the pendulum impact rig, release height and angle. Dimensions include: $L = 1.49$ m, $b = 0.55$ m, $m = 0.13$ m, $d = 0.20$ m, $x = 1.58$ m, $y = 0.68$ m, $z = 0.08$ m and $\beta = \sim 30^\circ$ (for more dimensions see Adams (2018)).

Table 6-1 Release height and angle of pendulum impactor for the setup of each impact energy (Figure 6-5).

Impact Energy (J)	Release height, h (m)	Angle, α (°)
10	0.14	4.1
20	0.28	10.2
30	0.42	16.4
40	0.56	22.7
50	0.70	29.3

Three high-speed cameras (2 x Phantom[®] Miro M110 and 1 x Phantom[®] Miro R111, Vision Research UK Ltd., Bedford, UK) were placed as shown in Figure 6-6 to film; a) the surrogate and protector from the side (replicating Adams (2018)), b) the palmar region of the protector from the side and c) any movement of protector splints from behind. Two LED lights provided lighting for the cameras (Figure 6-6). Two cameras (A and C) were set to a resolution of 320 x 480, and the third (b) was set to 512 x 320. The cameras filmed at 10 kHz and were synchronised with the load cell and potentiometers. Both potentiometers were connected to a power source (Powertraveller, powergorilla 24000MAH, UK) and the dynamometer was connected to a charge amplifier (Fylde, FE-128-CA, UK). All instrumentation were connected via the devices detailed above via a data acquisition device (DAQ) (National Instruments[™], USB-6211, USA), which recorded at 10 kHz and was triggered with a falling edge of 1 V, generated by a manual trigger as the pendulum was released. A sample rate of 10 kHz provided sufficient data points to capture the impact response and aligned with previous impact testing of wrist protectors (Kim *et al.*, 2006; Greenwald *et al.*, 2013; Thoraval *et al.*, 2013).

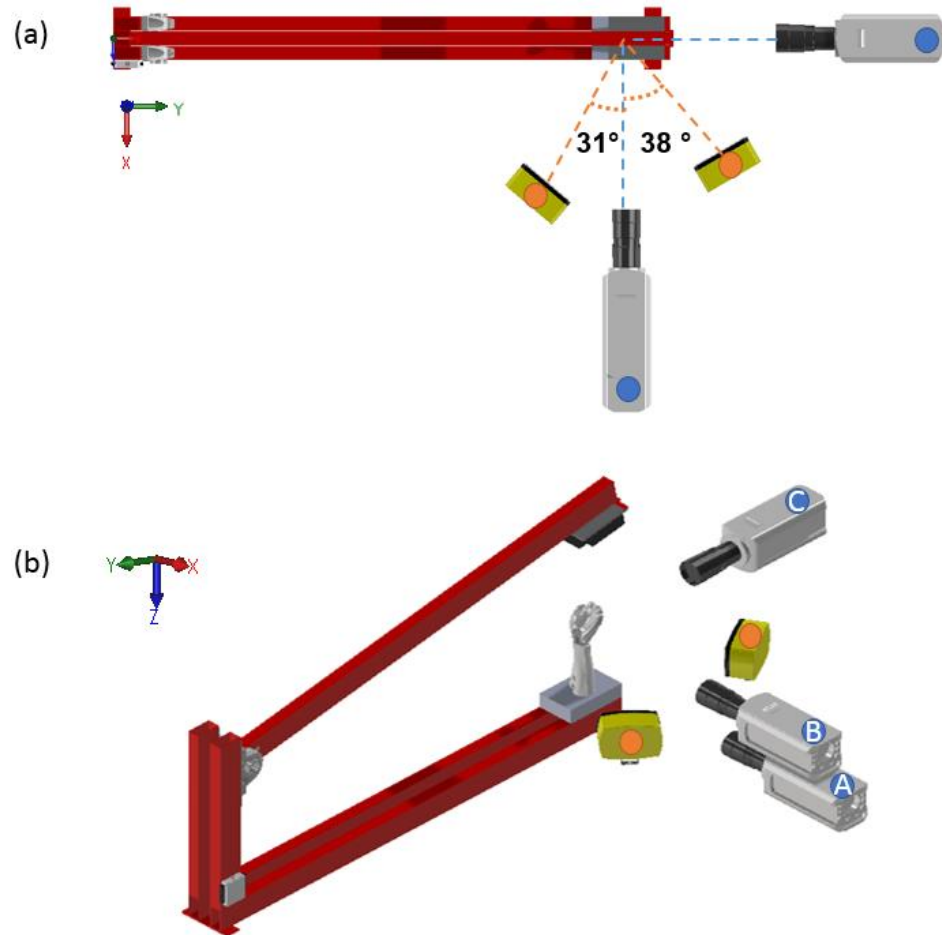


Figure 6-6 Schematic (a) aerial view and (b) isometric view of the impact set up showing the position of the high-speed cameras (blue circles) and lights (orange circle).

6.3.3 Post-Processing

For post-processing and analysis, all data from the DAQ (load cell and potentiometers) was imported into Microsoft Excel 2013, as a .txt file. Temporal forces and angles were calculated as the product of the output voltage and corresponding calibration factor from Adams (2018) (force ± 0.01 N, angles $\pm 0.01^\circ$). Prior to testing, the calibration factors reported by Adams (2018) for the potentiometers were checked by placing the pendulum arm and surrogate hand at set angles and reviewing the associated voltages (Appendix 10.E.2). Once converted, any non-zero force readings prior to impact were removed and neutralised (to 0 N) by determining the mean (and standard deviation) of the first 0.05 s of data prior to impact and subtracting this from all data (Figure 6-8). Force data was then filtered as described in Chapter 4.2. A cut-off frequency of 1 kHz (CFC 600) was used within the low-pass filter (4-pole phaseless Butterworth digital filter), as recommended when the sampling frequency is ≥ 6 kHz (Weisang, 2018).

After the data was filtered, the start of impact was identified following the steps outlined by Adams (2018) (Figure 6-7). For a test involving a protector, the start of impact was identified when the wrist angle first exceeded its mean starting angle after the pendulum was released (Figure 6-8a), plus two standard deviations of the offset data (Figure 6-8c). The start of an impact for a bare hand was identified when the peak force (z-axis) first exceeded the mean peak force prior to impact plus two standard deviations (Figure 6-8d). Peak force was used for the bare hand condition as the wrist angle was already at maximum extension prior to impact (Figure 6-8 – dotted orange line). The end of the impact for both scenarios was defined when force (z-axis) first fell below 0 N (Figure 6-8f) following the peak force reading (Figure 6-8e). The start and end times for the impacts identified from the load cells and potentiometers were crosschecked by visual inspection of the high-speed video footage (to within ± 6 frames equating to ± 0.6 ms) using Phantom[®] CineViewer (CV 3.0).

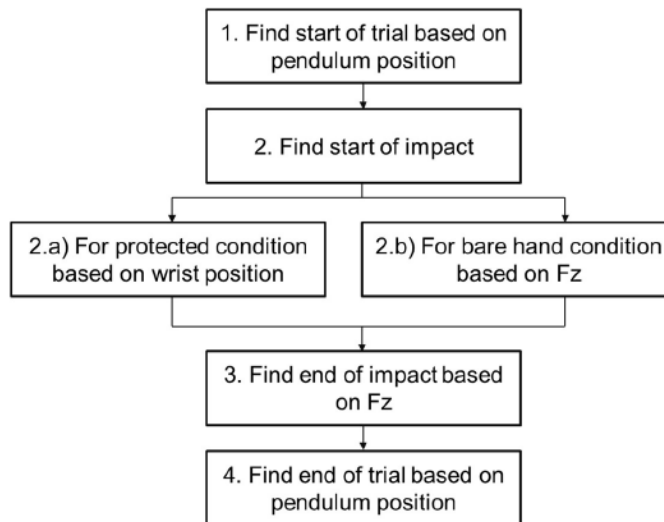


Figure 6-7 Steps followed to identify the key points from the test data (Adams, 2018).

6. Experimental Impact Testing of Wrist Protectors

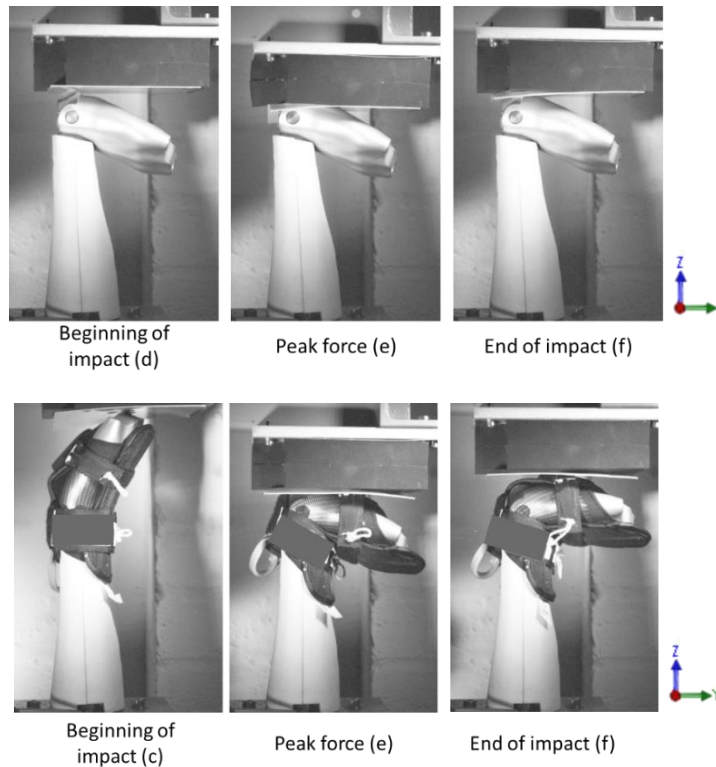
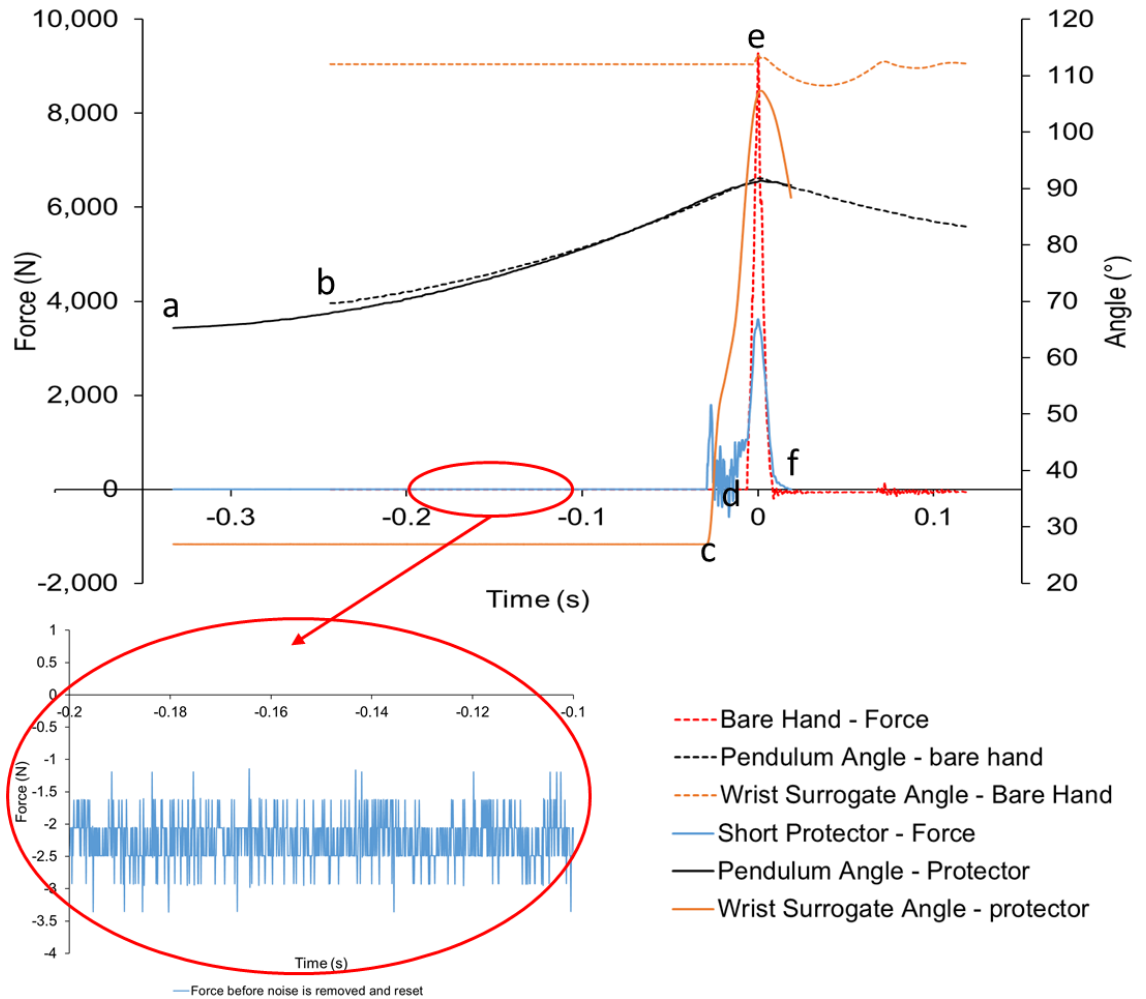


Figure 6-8 Example impact trace and high-speed video images (camera A) highlighting the data captured by the load cell and potentiometers for a bare hand impact and a short protector impact at 40 J. The following key points of the impact are highlighted: a) pendulum release (protector impact), b) pendulum release (bare hand impact), c) start of protector impact, d) start of bare hand impact, e) peak force, f) end of impact.

The energy absorbed by the wrist protectors was calculated through quantifying the area under the force vs. wrist angle plots. To do this, wrist angle had to be converted into radians and the perpendicular distance travelled by the hand was calculated using trigonometry. The MATLAB® function “trapz(x,y)” was then used, which utilises the trapezium function by integrating y with respect to the specified x values.

Statistical analysis was conducted using a two sample t-test in Minitab® (v18 Statistical software, USA) to determine the following questions when comparing peak force and maximum wrist angle across all energies:

1. Is there a difference between a bare hand and protected impact scenario?
2. Is there a difference between an untested protector and one that has already been subjected to impact?
3. Is there a difference between the two styles of protector?

6.4 Impact Testing of Two Wrist Protector Designs - Results

6.4.1 Polychloroprene Degradation

Peak force for one hundred consecutive impacts on two polychloroprene blocks are shown in Figure 6-9. The first impact was unique (yellow dot in), supporting previous findings of Adams (2018) who suggested conditioning the polychloroprene with one impact prior to testing. After the first impact, peak force was repeatable up to ~62 impacts, following which spread in the data increased (coefficient of variation for impacts 2 to 62 = 1.39, SD = 40.7 N and 2 to 72 = 1.64, SD = 47.9 N), suggesting the polychloroprene degraded. As this testing was performed using a different rig and at the lower end of the energy range at 10 J, degradation of the polychloroprene block may have occurred faster in the pendulum scenario and at higher energies. Therefore, polychloroprene degradation was checked by comparing the peak force of three bare hand impacts at the beginning and end of testing at each impact energy. Sets of polychloroprene blocks were changed after testing at two impact energies (e.g. at the start of 30 and 50 J) and each set of blocks were pre-conditioned by a single bare hand impact.

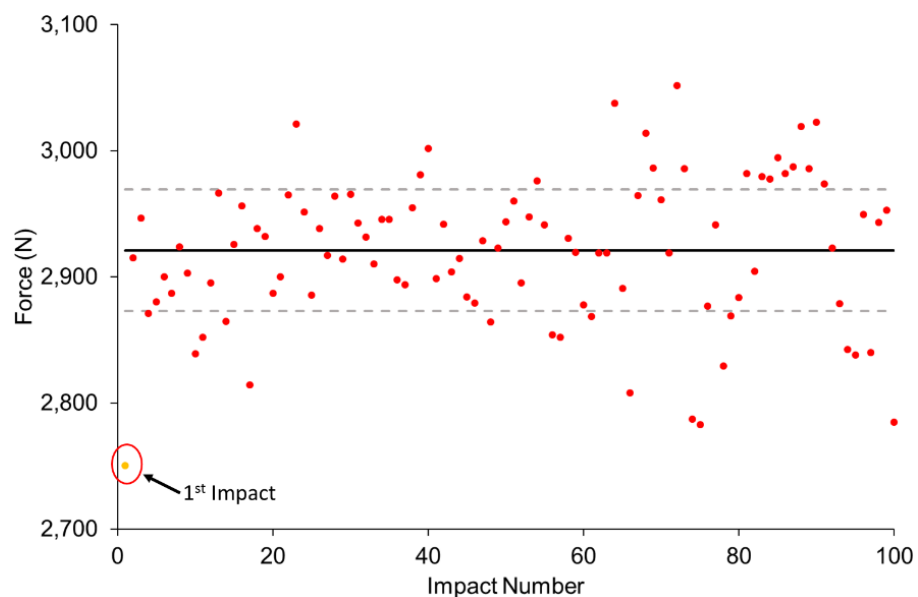


Figure 6-9 Peak force for 100 consecutive 10 J impacts on a stack of two polychloroprene blocks. The black and grey dotted lines represent the mean \pm standard deviation, with the first unique impact highlighted in yellow.

6.4.2 Example Impact Traces

Impact data were plotted as temporal force, temporal wrist angle and force vs. wrist angle traces. Temporal force and temporal wrist angle traces were plotted with peak force aligned at $t = 0$ s, to aid comparison between tests. Example traces (40 J), and images from cameras A and C (referred to as HSC) are shown in Figure 6-10 for the short protector and Figure 6-11 for the long protector. The traces highlight key

wrist positions, corresponding to the start of impact, maximum wrist angle and peak force. The range for a cadaveric fracture (1,104 to 3,896 N) (Chapter 2.2.3, Table 2-2) is highlighted in Figure 6-10 and Figure 6-11 as a shaded region and will be included in force plots throughout this chapter.

The pendulum first struck the wrist surrogate hand (HSC 1) generating an initial spike in force (HSC 2), following which there was a period of low force between ~200 and 1,000 N (HSC 3) due to the wrist extending and the pendulum breaking contact with the protector. At 93° (t = -0.0059, HSC 5, short protector) and 73° (t = -0.0082 s, HSC 4, long protector), the splints engaged resulting in a rapid increase in the force required to extend the wrist past these angles. Force continued to increase until peak (HSC 6), for the short protector maximum wrist angle (107°) coincided with peak force (t = 0 s); while, for the long protector the wrist continued to extend following peak force until its maximum angle was reached (102°, t = 0.0034 s, HSC 7). After peak force, the impactor rebounded off the protector and following maximum wrist angle the hand returned towards its initial position (HSC 8).

For the long protector, the force vs. wrist angle trace was more square in shape (three-part curve) compared to that of the short protector that had a two-part curve between the initial peak (HSC 3) and peak force (HSC 6). For the short protector (Figure 6-10), a relatively low force (~1,000 N) was required to displace the wrist up to ~93° (t = -0.006 s), following which a rapid increase in peak force was required to reach the maximum angle of 107°. In contrast, for the long protector (Figure 6-11), a rapid increase in force was required to extend the wrist between ~73 and 80° (t = -0.0078 to -0.005 s), following which the force increased in a quasi-linear fashion, at a lower gradient from 80 to ~100°, where peak force was reached.

6. Experimental Impact Testing of Wrist Protectors

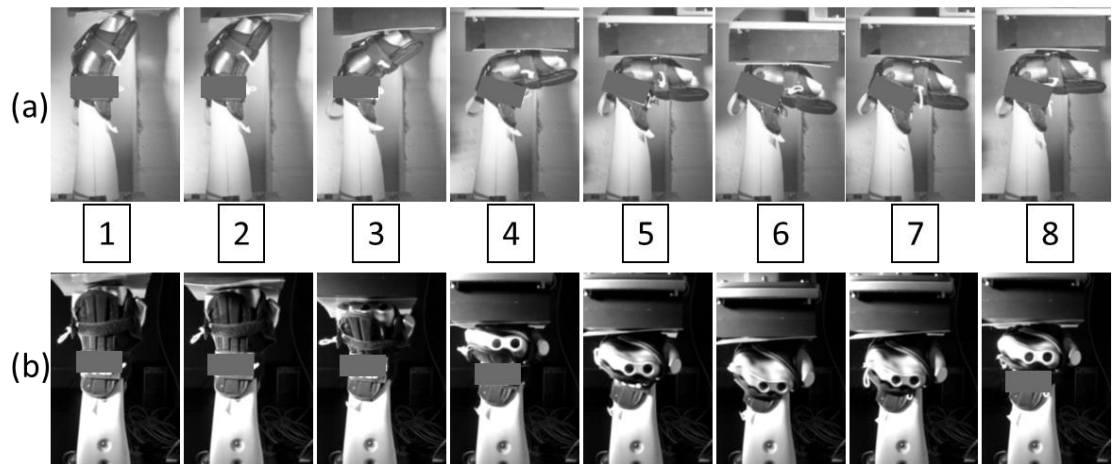
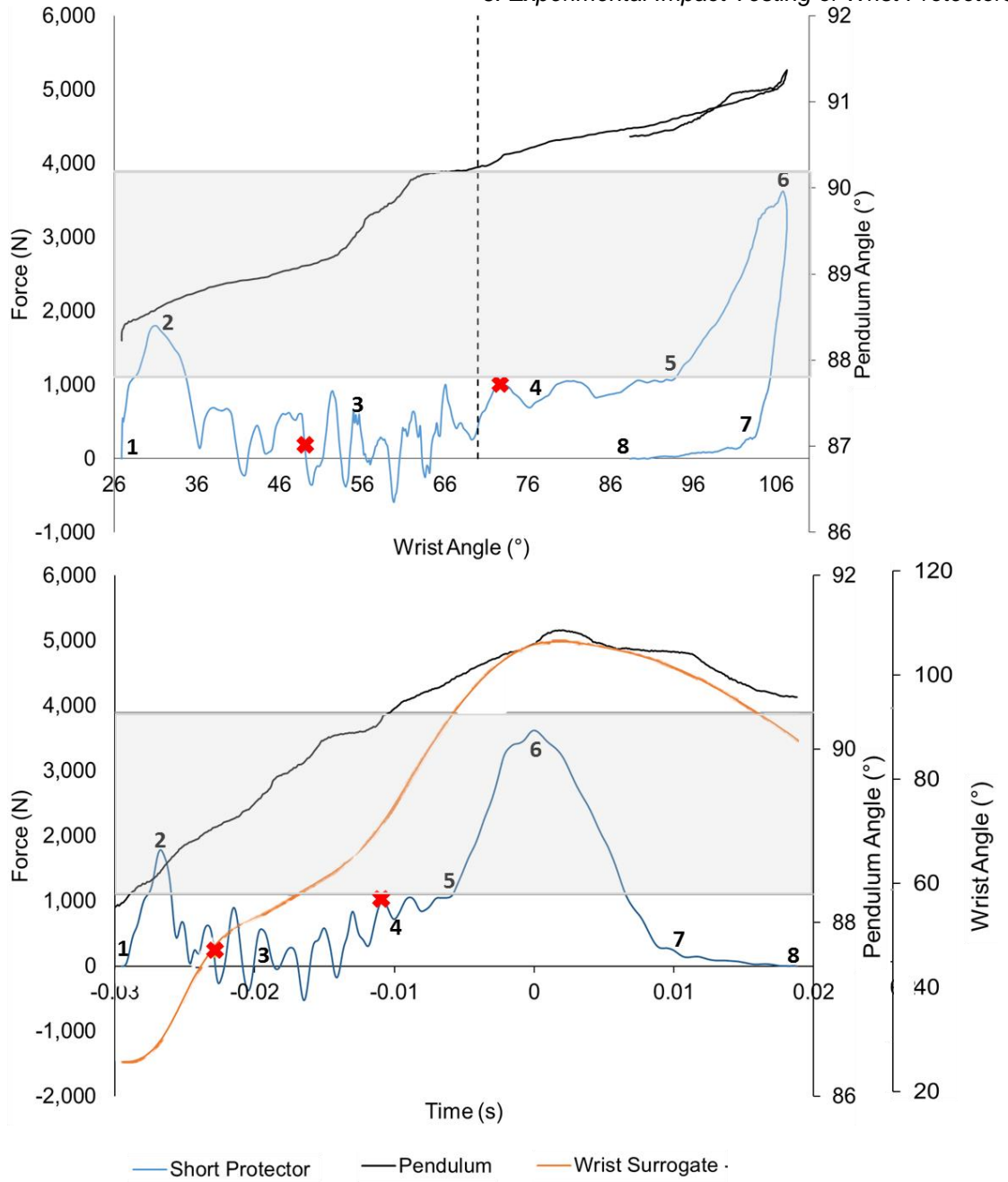


Figure 6-10 Short protector impact at 40 J highlighting a sequence of high-speed photographs (camera A and C) which showcase key points of the temporal force and temporal wrist angle traces.

6. Experimental Impact Testing of Wrist Protectors

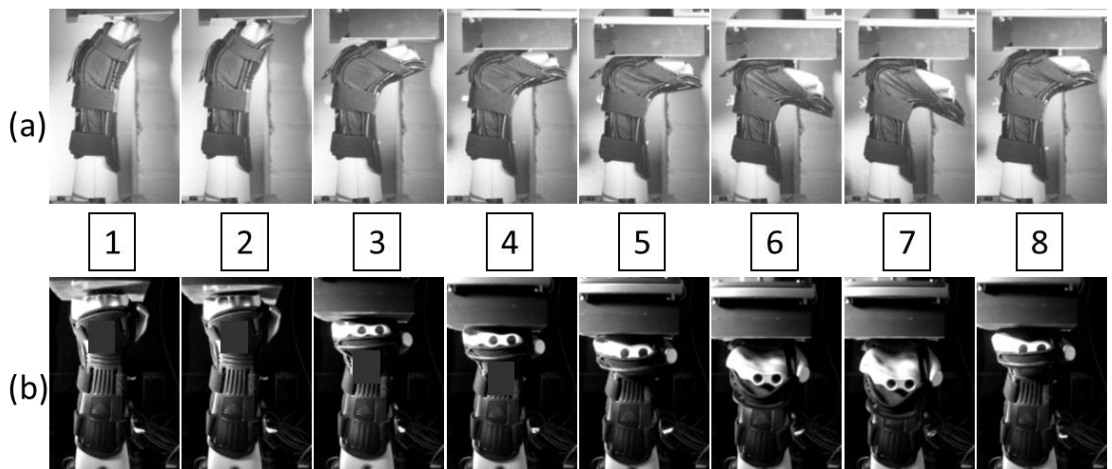
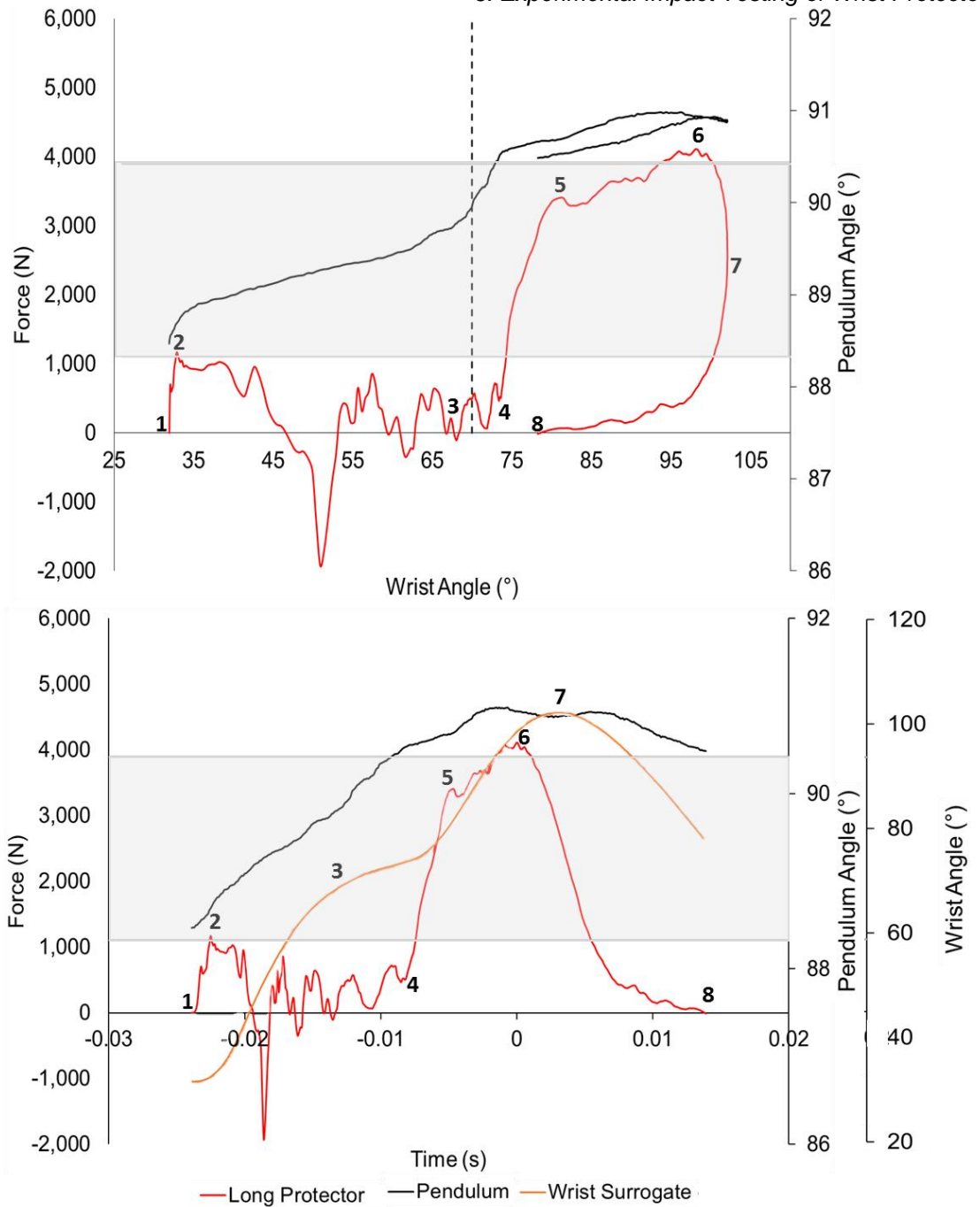


Figure 6-11 Long protector impact at 40 J highlighting a sequence of high-speed photographs (camera A and C) which showcase key points of the temporal force and temporal wrist angle trace.

High-speed photogrammetry showed that the surrogate forearm deflected laterally (y-axis) under impact (Figure 6-12). The location of the axis of rotation of the surrogate wrist joint (Figure 6-12a) was tracked in the video footage to obtain the maximum lateral displacement using Phantom® CineViewer. Motion in the negative y-direction (towards the pendulum arm axis of rotation) occurred after initial contact of the pendulum arm with the top of the hand (first red x in Figure 6-10, $t = -0.023$ s, Figure 6-12c). The forearm then propelled forward in the positive y-direction as it extended to the point of maximum deflection (second red x in Figure 6-10, $t = -0.011$ s, Figure 6-12d). The mean deflection for the short protector and a bare hand impact are presented in Table 6-2. A measurement could not be taken for the long protector because it obscured the joint.

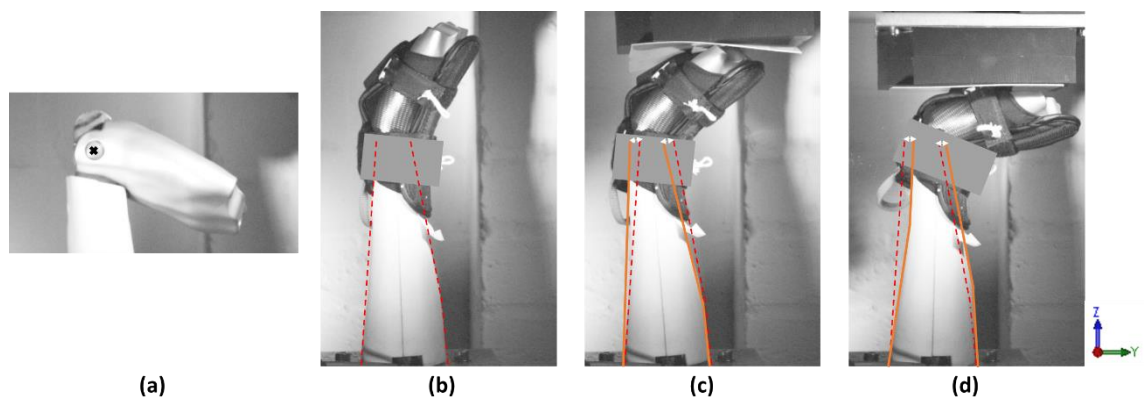


Figure 6-12 (a) bare hand with x marked for movement measurements. Example lateral wrist surrogate movement for the short protector at 40 J (b) prior to impact, (c) maximum -y motion and (d) maximum +y motion. The red dotted line shows the initial position of the surrogate in all instances for comparison.

Table 6-2 Mean (\pm standard deviation) lateral wrist surrogate movement (y-axis) for bare hand and short protector impacts at each energy.

	10 J		20 J		30 J		40 J		50 J	
	-Y (mm)	+Y (mm)	-Y (mm)	+Y (mm)	-Y (mm)	+Y (mm)	-Y (mm)	+Y (mm)	-Y (mm)	+Y (mm)
Bare Hand	2.2		2.8		3.1		3.1		3.1	
Short Protector	5.5 \pm	4.4 \pm	7.1 \pm	3.0 \pm	8.2 \pm	5.8 \pm	8.9 \pm	6.4 \pm	9.8 \pm	8.7 \pm
	1.8	2.4	0.9	1.5	1.3	2.7	1.2	2.4	1.6	2.7

6.4.3 Bare Hand vs. Protector

Figure 6-13 shows the first and last bare hand impact at each energy and for comparison the first impact on an untested protector for each style. Peak force increased with impact energy for both protected and bare hand impacts, whilst time to peak decreased. The addition of a wrist protector significantly decreased peak force across all energies ($t(37) = 6.18, p < 0.001$), although not always below the range reported for a cadaveric fracture (1,104 to 3,896 N) (Chapter 2.2.3, Table 2-2).

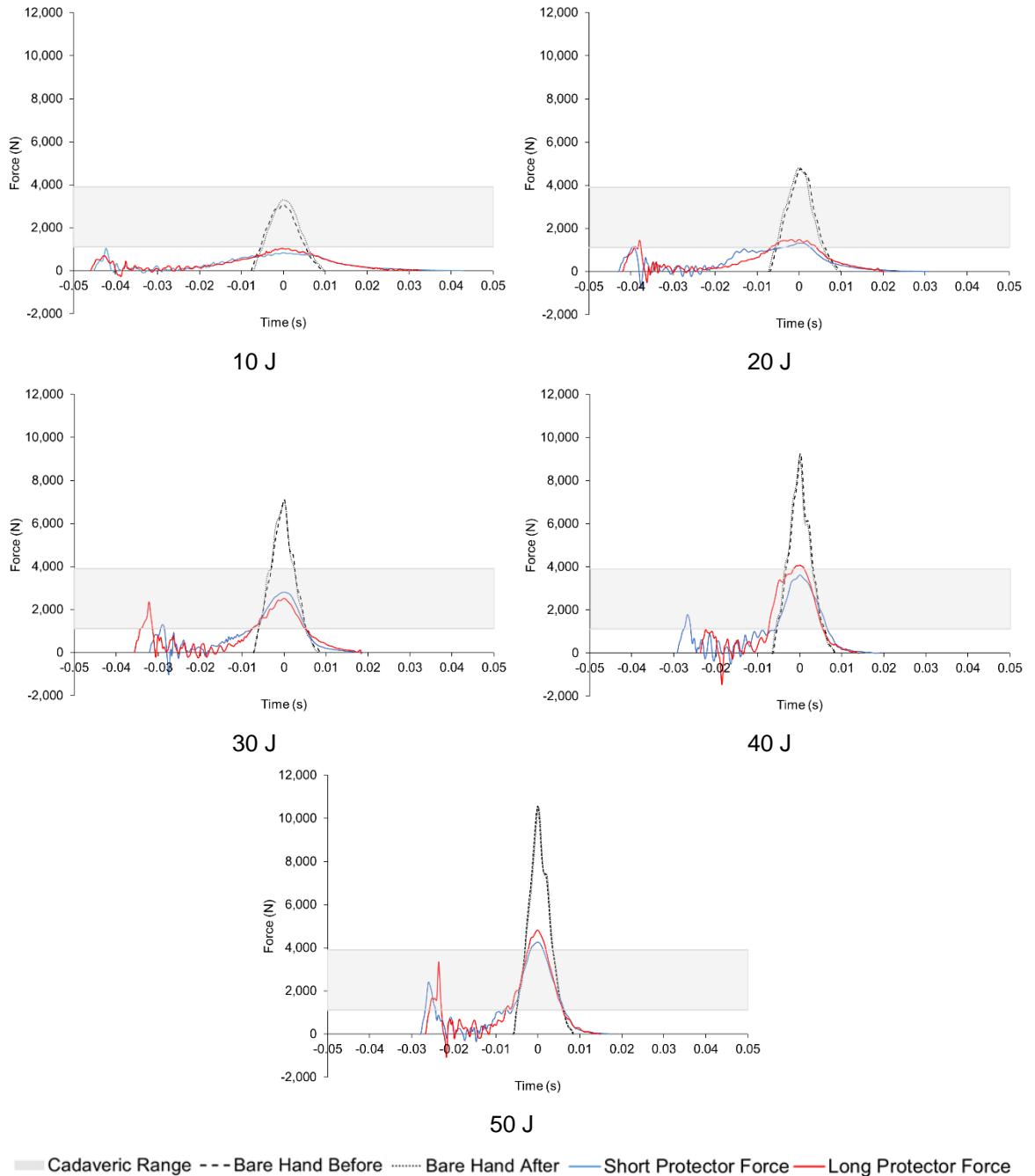


Figure 6-13 Example temporal force traces for bare hand and untested protector impacts at each energy. The grey region represents the cadaveric fracture range (Chapter 2.2.3, Table 2-2).

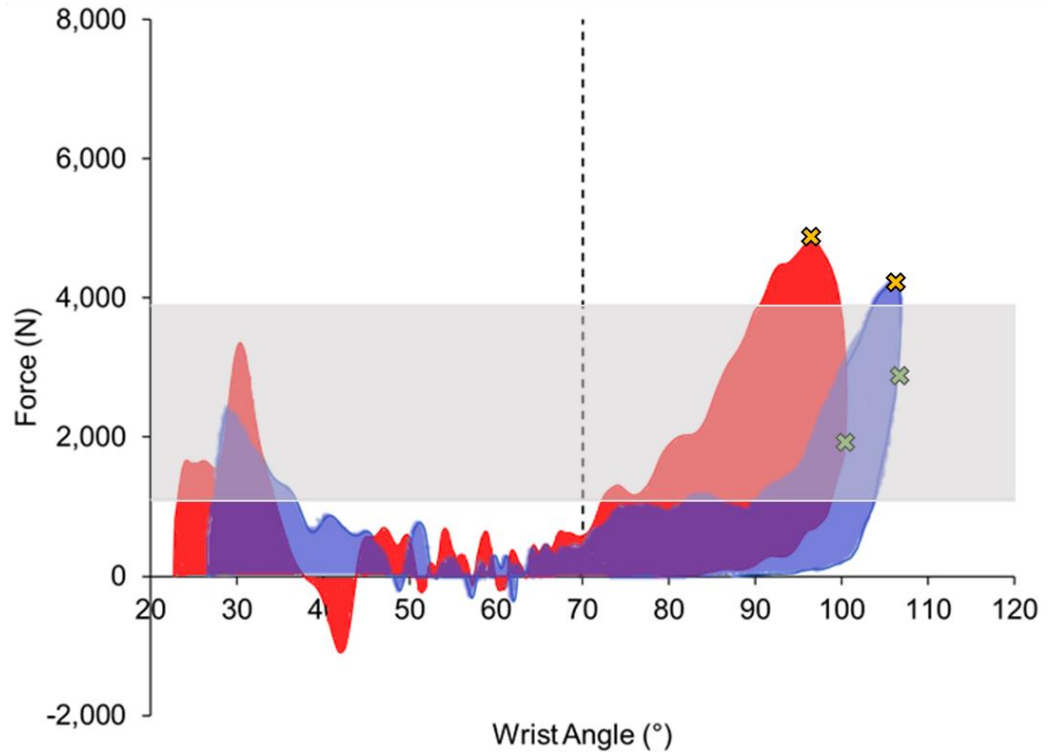
6.4.4 Untested vs. Tested Protector

The first impact of an untested and consecutively tested protector at each energy are compared in a temporal force, temporal wrist angle and force vs. wrist angle trace for both protector styles at energies between 20 and 50 J (Figure 6-15). An example force vs. wrist angle trace at 50 J comparing the short and long protector is also shown in Figure 6-14, with peak force, maximum wrist angle and the area calculated for energy absorption highlighted for an untested (Figure 6-14a) and consecutively tested protector (Figure 6-14b).

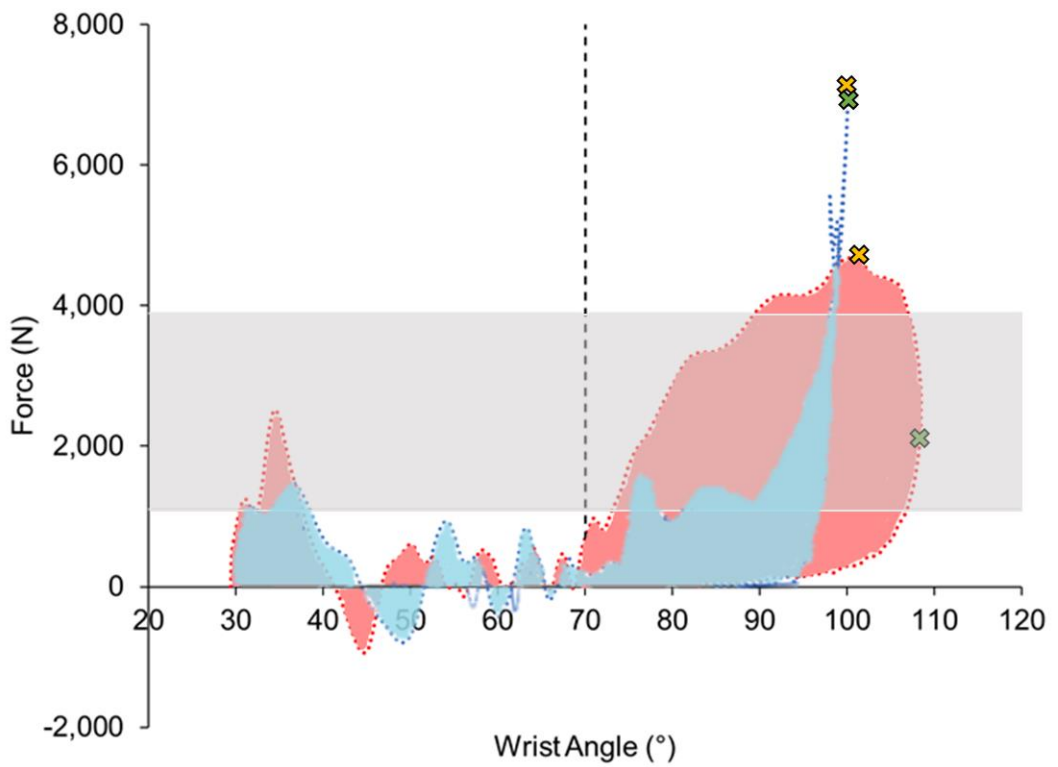
There was a significant difference between an untested and consecutively tested protector in terms of peak force for the short protector at 30 J and above (30 J $t(4) = 6.08$, $p = 0.004$, 40 J $t(6) = 3.50$, $p = 0.013$, 50 J $t(5) = 3.40$, $p = 0.019$). In contrast, there was no significant difference at any energy for the long protector when comparing an untested and a consecutively tested protector (statistical analysis details in Appendix 10.D.3). Comparing peak force between the two styles of untested protectors (short vs. long) showed a significant difference at 10 J ($t(4) = 2.92$, $p = 0.043$) and 50 J ($t(9) = 4.09$, $p = 0.003$).

For the short protector, a previously tested protector had a shorter impact duration than an untested protector. Maximum wrist angle was lower for the previously tested short protector compared to an untested one, however, the opposite effect was seen for the long protector (an untested protector had a greater wrist angle than a tested one). Comparing maximum wrist angle between the two styles of untested protectors (short vs. long) showed a significant difference at 20 J ($t(13) = 11.07$, $p < 0.001$) and 30 J ($t(17) = 5.08$, $p < 0.001$).

Like when comparing force, there was a significant difference between an untested and consecutively tested protector in terms of energy absorbed for the short protector at 30 J and above (30 J $t(4) = -4.57$, $p = 0.010$, 40 J $t(4) = -4.95$, $p = 0.008$, 50 J $t(4) = -8.27$, $p = <0.001$). However, there was no significant difference at any energy for the long protector when comparing energy absorbed between an untested and a consecutively tested protector. Comparing energy absorbed between the two styles of untested protectors (short vs. long) showed a significant difference at 30 J and above (30 J $t(17) = -5.27$, $p = <0.001$, 40 J $t(13) = -11.27$, $p = <0.001$, 50 J $t(17) = -10.84$, $p = <0.001$).



(a)



(b)

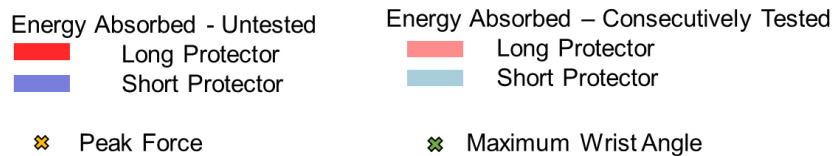


Figure 6-14 Force vs. wrist angle plots for (a) an untested short and long protector and (b) a consecutively tested short and long protector at 50 J. Peak force, maximum wrist angle and the energy absorbed are highlighted on both plots for comparison.

6. Experimental Impact Testing of Wrist Protectors

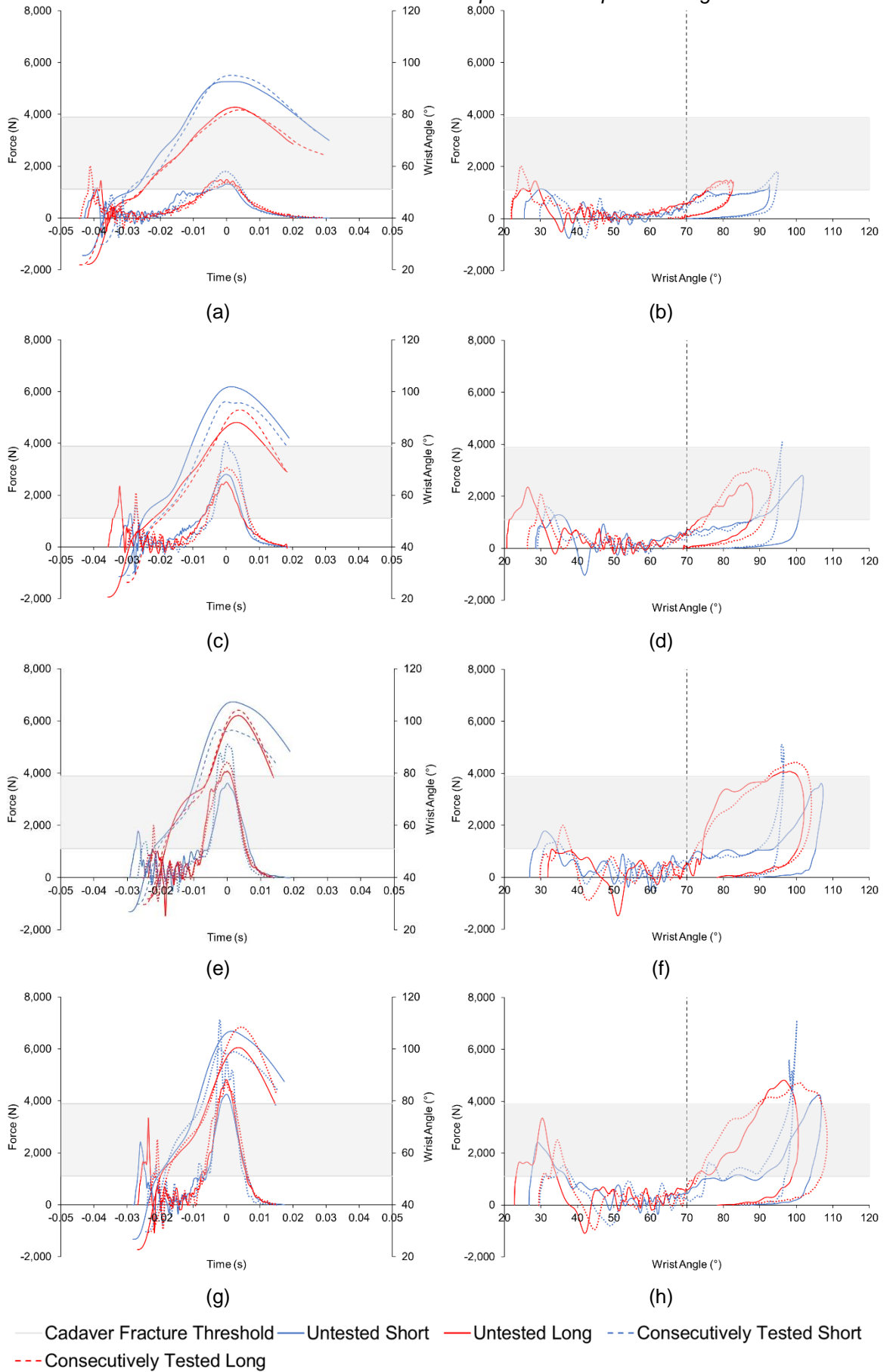


Figure 6-15 Temporal force, temporal wrist angle and force vs. wrist angle traces for an untested and a consecutively tested short and long protector at 20 (a and b), 30 (c and d), 40 (e and f) and 50 J (g and h).

6. Experimental Impact Testing of Wrist Protectors

Figure 6-16 shows the effect of repeated impacts on both protectors in terms of peak force (Figure 6-16a and b), maximum wrist angle (Figure 6-16c and d) and energy absorbed (Figure 6-16e and f). The effect of repeated impacts appears to be greater for the short protector than the long protector for peak force. Averaged across all energies, the mean difference between the first and fifth impact in terms of peak force was 42% for the short and 15% for the long protector. There was minimal difference between the first and fifth impact in terms of maximum energy wrist angle (1% short protector and 6% long protector), however for energy absorption a larger difference was seen for the long protector compared to the short (36 vs. 23%).

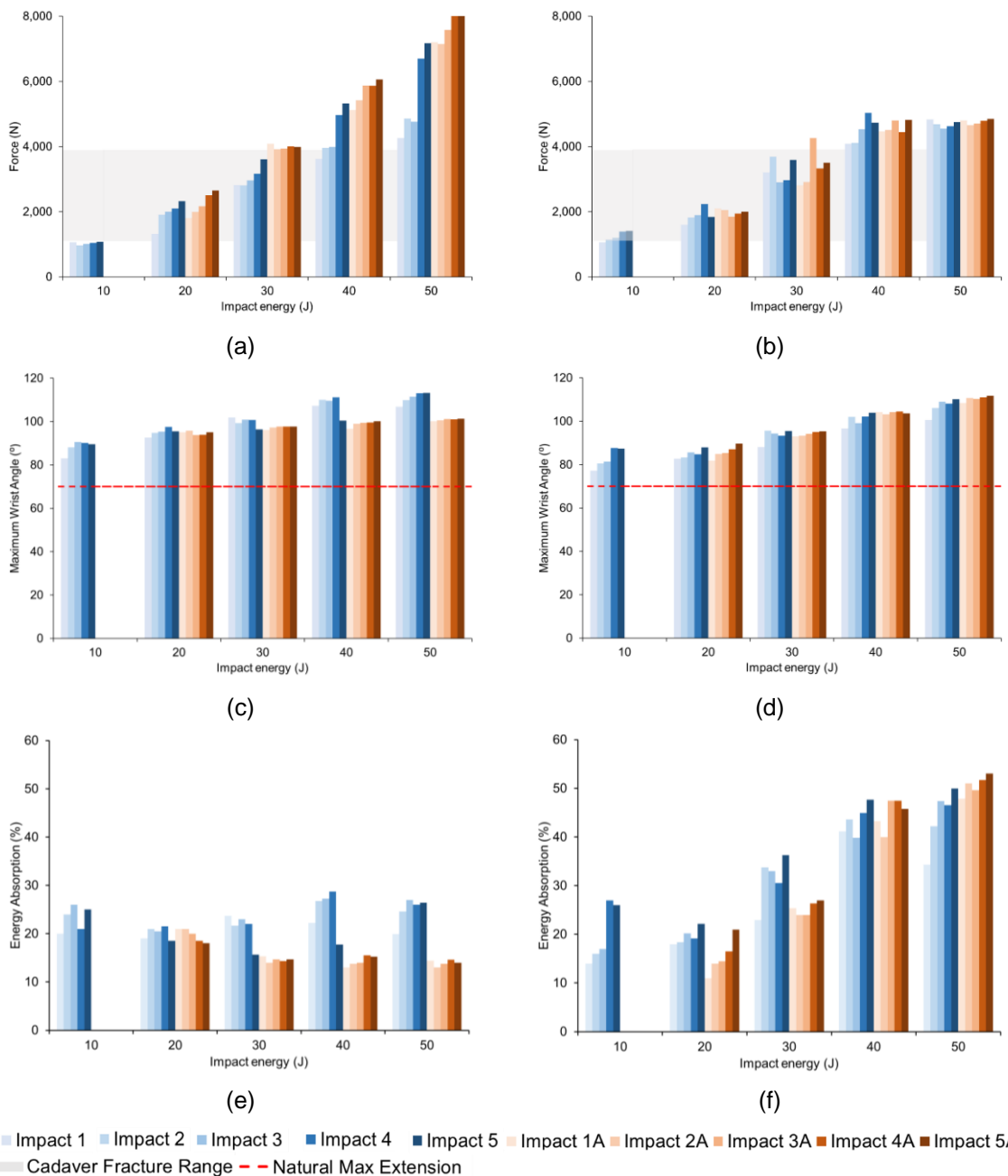


Figure 6-16 Bar charts showing the effect of five repeated impacts on both an untested (blue) and consecutively tested (orange) protector in terms of peak force (a) short and (b) long protector, maximum wrist angle (c) short and (d) long protector and energy absorption (e) short and (f) long protector. The protector marked as untested at 10 J is the same protector highlighted in orange at 20, 30, 40 and 50 J.

6.5 Discussion

By reducing the effective mass of the pendulum arm of the impact rig developed by Adams (2018), a bare hand scenario and two styles of wrist protectors have been tested across a range of energies (10 to 50 J) for FE model validation. Previous research has found that an impact involving a wrist protector significantly reduces peak force compared to an unprotected scenario (Lewis *et al.*, 1997; Kim *et al.*, 2006; Burkhart and Andrews, 2010; Adams, 2018). This current research complements these findings by showing a significant reduction in peak force across all energies for both wrist protector designs. Significant differences were also discovered between the two styles of protectors in terms of peak force at 10 and 50 J and maximum wrist angle at 20 and 30 J. Differences between the levels of protection could be due to a combination of materials and design features, which will be explored further using the validated FE models in Chapter 8. Despite protectors reducing peak force compared to a bare hand scenario, peak force was not always lowered below the cadaveric fracture threshold of 1,104 to 3,896 N (short protector – 20 J = 1,314 N, 30 J = 2,807 N, 40 J = 3,621 N, 50 J = 4,256 N, long protector – 20 J = 1,488 N, 30 J = 2,515 N, 40 J = 4,080 N, 50 J = 4,816).

Both protectors followed a similar temporal force trace, consisting of an initial peak where the impactor struck the hand, followed by a period of low force as the wrist extended. The impactor then struck the protector causing a large rapid increase in force up to peak force and maximum wrist angle. The impactor then rebounded off the protector, producing a reduction in force. Force vs. wrist angle traces showed differences between the two wrist protector designs, with the short protector exhibiting a two part loading curve and the long protector a three part loading curve. The differences in shape of the force vs. wrist angle traces also meant that the long protector absorbed a larger amount of energy compared to the short protector (mean of 32 vs. 23% across all energies). Temporal force and force vs. wrist angle traces were similar to those of Adams (2018) despite the reduction in the effective mass of the pendulum (Appendix 10.E.6). Peak forces were also comparable to those of Adams (2018) (short protector – 3,995 N vs. 3,621 N and long protector 3,972 N vs. 4,080 N), however, maximum wrist angles were higher in this study (short protector – 97° vs. 107° and long protector – 92° vs. 102°) when comparing the same styles of protectors at 40 J. These differences between the wrist angles could be because Adams (2018) bend tested the protectors according to EN 14120

prior to impact testing, which may have affected the performance of the splints under impact.

Five repeated impacts at a given energy highlighted that the protectors showed signs of degradation. This finding was re-iterated when comparing a brand new protector and one that had been consecutively tested across all energies. Between the first and fifth impact at each energy, the short protector increased in peak force by an overall mean of 42% and energy absorption decreased by 23%. In contrast, peak force for the long protector increased by 15% with a plateau in peak force occurring after the second repeat. Adams (2018) reported a similar trend when recording peak force across three impacts. Energy absorption for the long protector however, increased by an overall mean of 36% when comparing the first and fifth impact at each energy. Earlier chapters highlighted variance between protector samples under compression and individual impact testing, therefore, future work could test multiple samples of a protector at the same energy to see if variance (in terms of performance and degradation) at a full protector level is still apparent.

Analysis of high-speed videos highlighted lateral motion of the surrogate, which could result in energy loss and produce lower peak forces compared to a static wrist. The wrist joint movement observed within this testing was more prominent than reported in the setup used by Adams (2018) (bare hand 2.9 to 1.0 mm vs. 3.1 mm and short protector 1.9 to 4.8 mm vs. 8.9 to 6.4 mm). The larger surrogate motion could be due to the higher velocities used within this study (2.8 ms^{-1} vs. 3.3 ms^{-1}) or due to uncertainties within measurements. The wrist surrogate movement is a limitation to the test setup, which should, ideally, be reflected within the FE models in Chapter 7. Future work could look to improve the surrogate setup to reduce any unwanted movement currently present.

A further limitation to the current wrist surrogate is that the joint has zero resistance which is not reflective of the human wrist joint. Utilising a zero resistance joint meant that wrist angle could not be compared for a bare hand impact to an impact with a protector. The resistance experienced within the human wrist joint may also cause the protectors to perform differently under impact. Therefore, future work should look to make the wrist surrogate more bio-fidelic both in terms of materials and function.

6.6 Chapter Summary

Through adaptations to the pendulum impact rig designed by Adams (2018), two styles of wrist protectors have been impact tested at energies between 10 and 50 J. By reducing the effective mass of the pendulum arm, a wider range of impact energies at more realistic fall velocities were achieved, taking into account the large demographic of adolescents in snowboarding. Chapter 7 will create FE models replicating the impact scenario reported in this chapter, using the experimental data for comparison and validation. As the polychloroprene attached to the pendulum arm will be included in the model, material characterisation and independent validation tests for this part will be included in Chapter 7. Due to the degradation highlighted, the FE models will only be compared against the first impact for a fresh protector at each energy.

7 FE Model of Wrist Protectors Under Impact

7.1 Introduction

Chapter 6 made adaptations to the pendulum impact rig of Adams (2018) and collected data for an unprotected case and two styles of wrist protectors fitted to a wrist surrogate at energies between 10 and 50 J. This chapter discusses the FE models created, replicating the impact scenario in Chapter 6 (Figure 7-1). As degradation of protectors from repeated impacts was apparent, the FE models were compared against the first impact for an untested protector at each energy. The rig used for the experiment had polychloroprene on the striking region, so this chapter highlights the material characterisation and independent validation of this material. This is the final chapter to contribute to objective three of the thesis; to develop and validate FE models of snowboard wrist protectors for simulating hand/surface impacts.

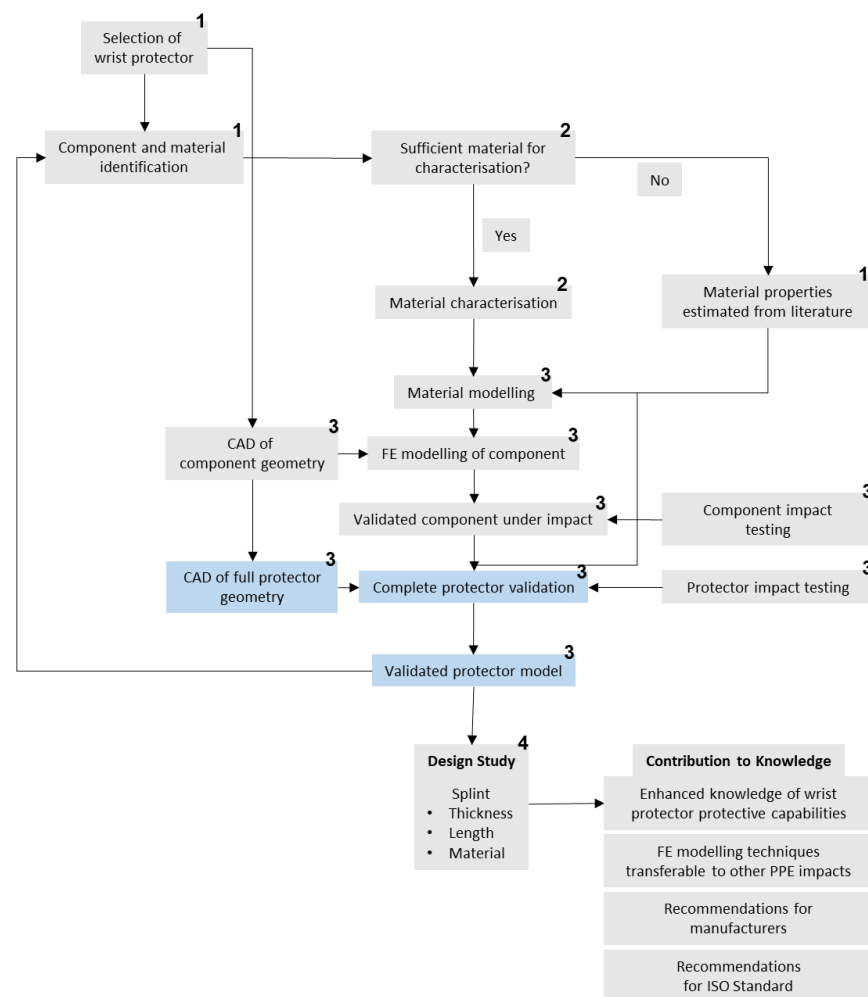


Figure 7-1 Schematic diagram indicating where this chapter (highlighted in blue) fits within the overall project (numbers correlate to the objectives of the thesis).

7.2 Polychloroprene

As seen in Chapter 6, the impactor incorporated a stack of two polychloroprene blocks, whose behaviour needed to be understood before an FE model of a full wrist protector impact could be created.

7.2.1 Material Characterisation - Methods

The methodology used in previous chapters to characterise the palmar padding of both wrist protectors was replicated to characterise the polychloroprene. Five 38 mm \varnothing cylinders were cut from the same sheet of polychloroprene as the blocks used on the pendulum arm in Chapter 6.3.1, for material characterisation. The five cylindrical samples were subject to compression testing using similar methods outlined in Chapter 3.4.1. Samples were compressed to 50% at two strain rates (0.02 s^{-1} and 0.2 s^{-1}) on a Hounsfield HK10s universal material testing machine equipped with a 10 kN load cell. Compression plates were greased to minimise friction and prevent barrelling of the sample. A 1 N pre load was applied to ensure the compression plates were engaged with the sample at the start of testing. At the first strain rate (0.02 s^{-1}), Mullin's effect was accounted for by compressing samples six times, because pilot testing highlighted that the first compression of the polychloroprene sample was unique. Testing took place in one day at room temperature ($\sim 22^\circ\text{C}$). Stress was calculated by dividing the force by the cross-sectional area ($1,134 \text{ mm}^2$) and strain was calculated as the change in height divided by the original height (20 mm).

All five samples were also subject to a stress relaxation test on an Instron[®] Universal testing machine equipped with a 5 kN load cell. Samples were compressed to both 10 and 20% strain at the highest displacement rate the machine could achieve ($1,000 \text{ mm}\cdot\text{min}^{-1}$) and held for 300 s. The high stiffness of the samples and the range of the load cell did not allow testing at higher strains. The force vs. time data was converted to shear response using (Equation 3-1, ready to be fitted to a material model in ANSYS[®]/LS-DYNA[®], where a Poisson's ratio of 0.48 was used (from Katholieke Universiteit Leuven (2011))).

Statistical analysis, as previously described (Chapter 3.4.1), was conducted using a one-way ANOVA and a coefficient of variation expressed as a percentage, using Minitab[®] (v18 Statistical software, USA). Analysis was performed to understand whether samples were repeatable and similar to each other in terms of stress at 50% compressive strain (details in Appendix 10.D.4).

7.2.2 Impact Testing – Methods

Following material characterisation, the cylindrical samples of polychloroprene were subject to five impacts at 5 J (5 kg, 0.10 m) using a bespoke drop tower impact rig (Figure 7-2). Pilot testing indicated that 2 minutes between impacts was sufficient for the samples to recover and prevent stress softening from influencing the results. Testing took place in one day at room temperature ($\sim 20^{\circ}\text{C}$). The impact rig consisted of two vertical poles with a 5 kg flat faced drop mass (striking face = 130 mm \varnothing , 15 mm thick) (Figure 7-2, part b) sliding on two linear ball bearings (67122040, Bosch Rexroth), with the sample resting on a steel plate (75 x 50 x 2.5 cm). A manually operated magnet coupling (Figure 7-2, part a) (F4M905 70kg Pull, First4Magnets[®], Tuxford, UK) ensured a consistent height when releasing the drop mass. A single axis accelerometer (352B01 PCB[®], ± 0.02 g equating to ± 0.3 N) was placed close to the centre of the flat faced drop mass, and connected to a digital oscilloscope (PicoScope[®] 4424) sampling at 10 kHz, via an ICP[®] sensor signal conditioner (480B21, PCB[®]).

The impact rig described here is larger and capable of higher impact energies than the one outlined in Chapter 4 (Chapter 4, Figure 4-2). The larger rig was used for testing the polychloroprene as the drop mass (5 kg compared to 1.6 kg) was closer to that of the pendulum used for full protector testing (7.2 kg effective mass, Chapter 6). As with previous impact testing, a high-speed camera (Figure 7-2, part c) (Phantom[®] Miro R110, Vision Research UK Ltd., Bedford, UK) was used to film the impact and an LED light (Figure 7-2, part d) (GS Vitec, GS01127) was used for lighting. The camera was set to a resolution of 512 x 320 and a capture rate of 10 kHz, to match the accelerometer, allowing synchronisation via the oscilloscope.

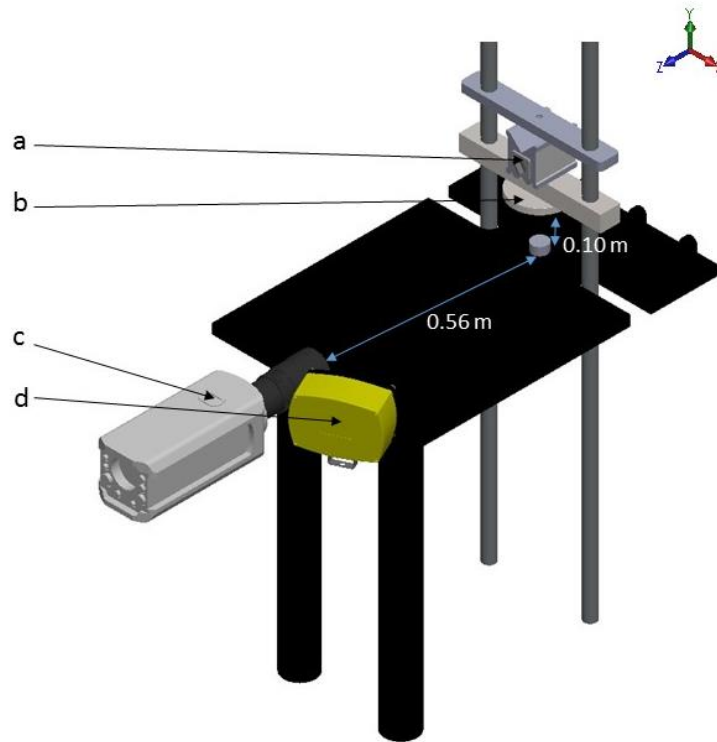


Figure 7-2 Schematic of impact rig, a) magnetic coupling, b) drop mass, c) High-speed camera and d) LED light.

Voltage from the accelerometer was converted to force, and filtered using a low-pass filter at CFC 600 (1 kHz), as previously described (Chapter 4.2). As with the impacting of the protectors' palmar components (Chapter 4, Figure 4-5), high-speed videos were analysed in Phantom® CineViewer, where sample deformation was measured (calibration of $0.232 \text{ mm}\cdot\text{pixel}^{-1}$, deformation to $\pm 1 \text{ mm}$). Statistical analysis was conducted using a one-way ANOVA and a coefficient of variance, expressed as a percentage, to determine whether the samples were repeatable and similar to each other when comparing peak force, impact time and maximum compressive strain.

7.2.3 Material Characterisation – Results and Discussion

The polychloroprene exhibited non-rate dependent, hyperelastic material characteristics under compression (Figure 7-3a). The first compression of each sample was seen to be unique when compared to subsequent compressions (Figure 7-3b), reiterating the findings from Chapter 6.4.1 (Figure 6-9) and Adams (2018). Samples showed high repeatability across the sheet of polychloroprene, with only 6% variation between samples when comparing stress at 50% strain. The stress relaxation testing showed the polychloroprene to be linear viscoelastic (Figure 7-3c); because when there was a change in strain, there was no change in shear modulus.

Hyperelastic behaviour is typical of polychloroprene and it has previously been modelled using an Ogden model (Kim *et al.*, 2012).

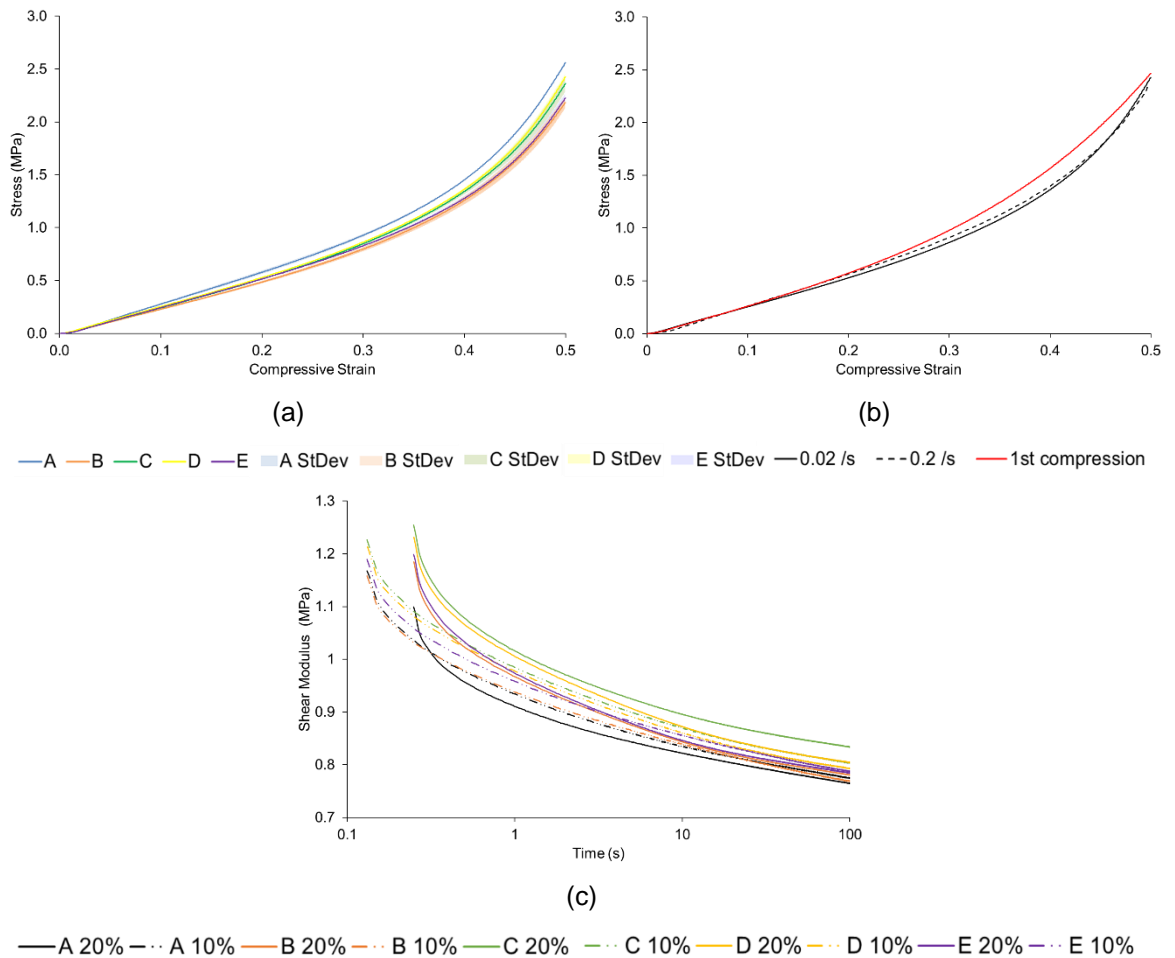


Figure 7-3 Mean (\pm standard deviation) stress vs. strain traces for (a) five samples of polychloroprene at 0.02 s^{-1} (b) one sample at 0.02 s^{-1} and 0.2 s^{-1} , highlighting the first unique curve and (c) shear modulus vs. time trace for all five samples subject to a stress relaxation test up to 10 and 20% strain (time scale is logarithmic).

7.2.4 Impact testing – Results and Discussion

Mean (\pm standard deviation) temporal force traces are shown in Figure 7-4 for 5 J impacts on five cylindrical polychloroprene samples. In terms of peak force and maximum compression, there was no significant difference between samples [F (4, 20) = 0.87, $p = 0.409$, F (4, 20) = 1.81, $p = 0.079$]. There was also no significant difference between samples in terms of impact duration, except when comparing sample b and c (Table 7-1 – statistical analysis details in Appendix 10.D.4). It can, therefore, be said that samples from different locations on the sheet of polychloroprene had consistent impact properties. The temporal force traces for the impacts on the polychloroprene were noisier than those in Chapter 4 for the palmar padding (Figure 4-6), even though they were filtered in the same way. Differences are likely to be because the polychloroprene was stiffer than the palmar padding from the protectors. As there was no difference between samples, one was chosen

(sample A, median sample for compression and impact duration) for comparison against the FE models.

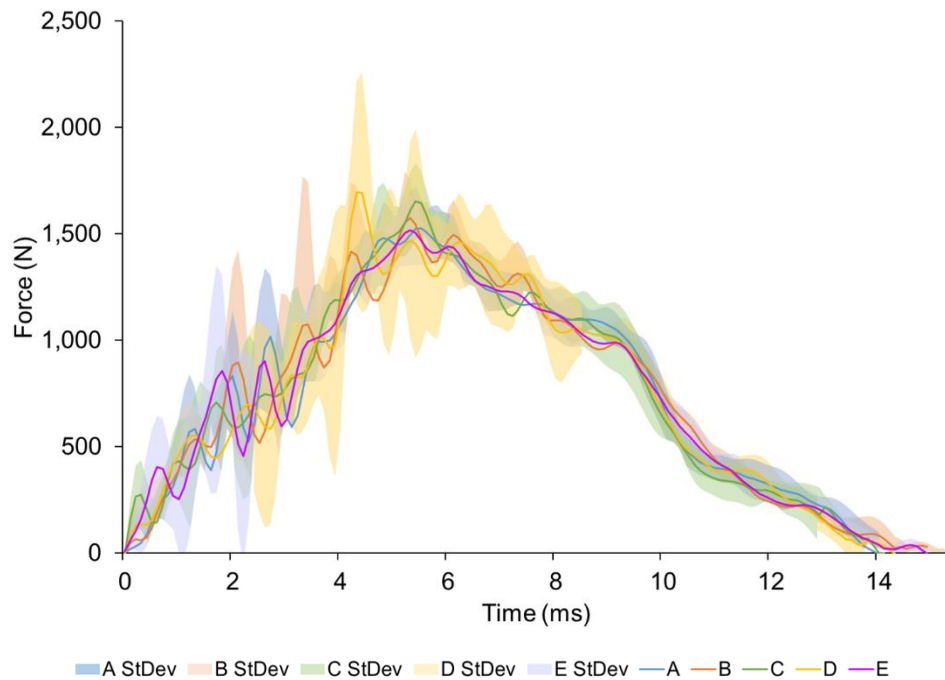


Figure 7-4 Mean temporal force traces (\pm standard deviation) for 5 J impacts on five 38 mm \varnothing cylindrical samples of polychloroprene.

Table 7-1 Mean (\pm standard deviation) values for peak force, maximum compression, maximum compressive strain and impact duration for 5 J impacts on all samples of polychloroprene (Figure 7-4).

Component	Sample	Peak Force \pm St Dev (N)	Maximum compression \pm St Dev (mm)	Maximum compressive Strain \pm St Dev (%)	Impact Duration \pm St Dev (ms)
Polychloroprene (Figure 7-4)	A	1,649 \pm 159	5.17 \pm 0.18	26 \pm 1	14.10 \pm 0.64
	B	1,779 \pm 308	5.08 \pm 0.12	25 \pm 1	14.82 \pm 0.48 ^c
	C	1,745 \pm 77	5.17 \pm 0.10	26 \pm 1	13.76 \pm 0.51 ^b
	D	1,873 \pm 456	5.25 \pm 0.10	26 \pm 1	13.88 \pm 0.44
	E	1,589 \pm 142	5.03 \pm 0.18	25 \pm 1	14.48 \pm 0.40
	Mean	1,727 \pm 263	5.14 \pm 0.15	26 \pm 1	14.21 \pm 0.61

Subscript text highlights the letter of the samples that are significantly different at $p < 0.05$.

7.2.5 FE Model of Polychloroprene Impact – Methods

An FE model replicating the setup of the experimental impact described above (Section 7.2.2) was created using the same techniques as described in Chapter 5.3 FE Model Methodology. The results of the impact test were used for comparison to assess the model’s accuracy in terms of the temporal force trace and, in particular, peak force, maximum compression and impact duration. Geometries of the

7. FE Model of Wrist Protectors Under Impact
 impactor, base plate and polychloroprene were created in Solidworks® 2017 (Dassault Systems®) and imported into ANSYS® Workbench Mechanical v18.2. The model was set up as previously described and meshed with solid brick elements (ELFORM 1, constant stress solid hexahedra). As the polychloroprene had the same cross sectional area as the cylinders modelled in Chapter 5, the same element size was used (Appendix 10.G.1, Table 10-3).

Polychloroprene demonstrated hyperelastic properties, so a hyperelastic material model was chosen to replicate its behaviour within an FE model (0.2 s^{-1} strain rate for sample A). As the stress vs. strain data obtained had an upturn S shape with no inflexions, a first order Ogden model was chosen (Figure 7-5). The corresponding coefficients of the model were, $\text{MU} = 0.139 \text{ MPa}$ and $\alpha = 8.380$, with density taken as the mean of the compression samples ($1,457 \pm 10 \text{ kg.m}^{-3}$). Stress relaxation testing highlighted that the polychloroprene exhibited linear viscoelastic behaviour, but it was not seen to be rate dependent during the compression tests at the strain rates tested. Therefore, a model of a 5 J impact on the cylindrical polychloroprene sample, both with and without a Prony series coupled with the Ogden model, were simulated. The Prony series coefficients when curve fitting the 20% strain stress relaxation data for sample A (Figure 7-5b) were 0.055, 0.535 and 0.038 MPa for α_i and 1.199, 0.110, 12.369 for β_i .

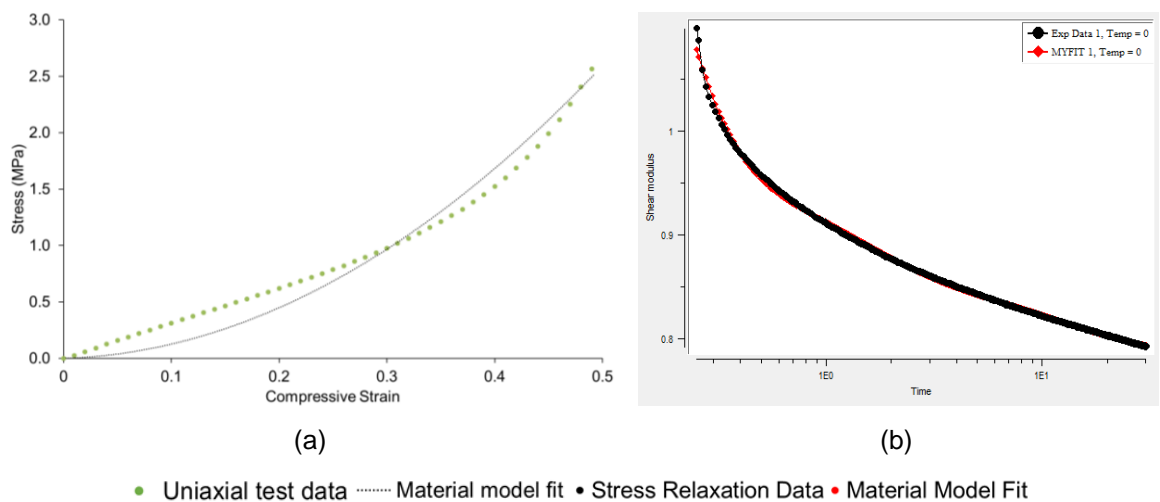


Figure 7-5 Material model curve fits for (a) hyperelastic Ogden first order model and (b) three term Prony series curve fit to stress relaxation data at 20% strain. Both curve fits are for sample A.

Each simulation was post-processed as in Chapter 5 where the temporal reaction force (rcforc) between the impactor and the top of the sample was obtained. The force data was filtered using the same low-pass filter as the experimental data (Chapter 4.2) and maximum compression was measured as previously described. A percentage difference in terms of peak force and maximum compression of the

FE model compared to the experimental data was calculated in order to assess accuracy.

7.2.6 FE model of Polychloroprene Impact – Results and Discussion

Temporal force vs. time results for the model (with and without the addition of a Prony series) and experiment are compared in Figure 7-6. The addition of a Prony series had little effect on the resultant temporal force trace (89 N in peak force = 6%, 0.06 ms in impact duration = 3%), although the signal corresponding to the model with the Prony series had fewer fluctuations. Simulation run time increased by 19% with the addition of the Prony series, and it was deemed unnecessary for the polychloroprene material model. The FE model produced a similar fluctuating trace and predicted peak force within 328 N (20%), impact duration within 0.6 ms (4%) and maximum compression within 0.6 mm (11%) (Figure 7-7) of the experiment. The setup described was different from the experimental impact test in Chapter 6 (linear drop mass vs. pendulum impact, polychloroprene stationary vs. moving, small cylindrical sample vs. large block) and only one impact energy was investigated. Therefore, the material behaviour needed to be tested within the pendulum impact rig and across a range of energies, to check the polychloroprene behaviour was still closely replicated in the model.

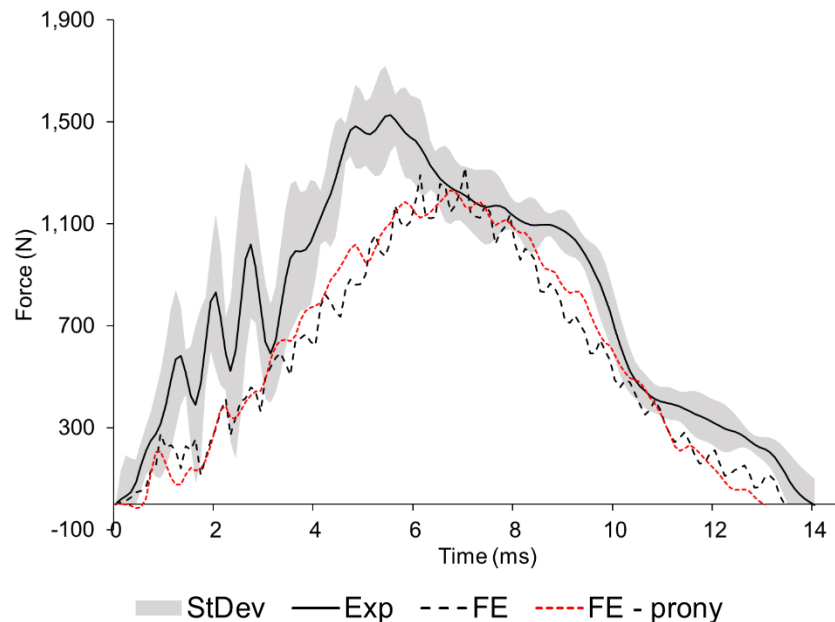


Figure 7-6 Temporal force trace for a 5 J impact on a cylindrical sample of polychloroprene within an experiment (mean \pm standard deviation) and FE model (with and without a Prony series).

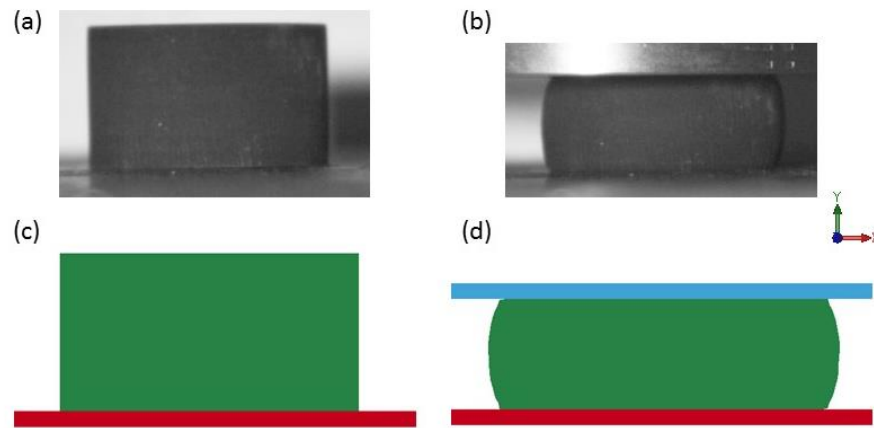


Figure 7-7 Example comparison between an experimental polychloroprene sample (a) prior to impact and (b) at maximum compression and the FE model (c) before impact and (d) at maximum compression.

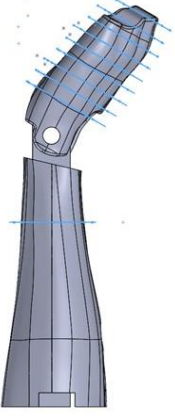
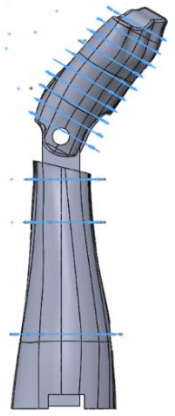
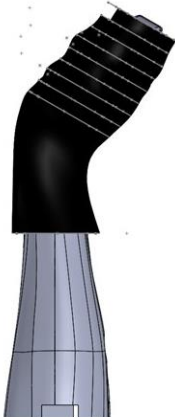
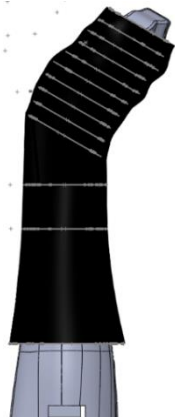
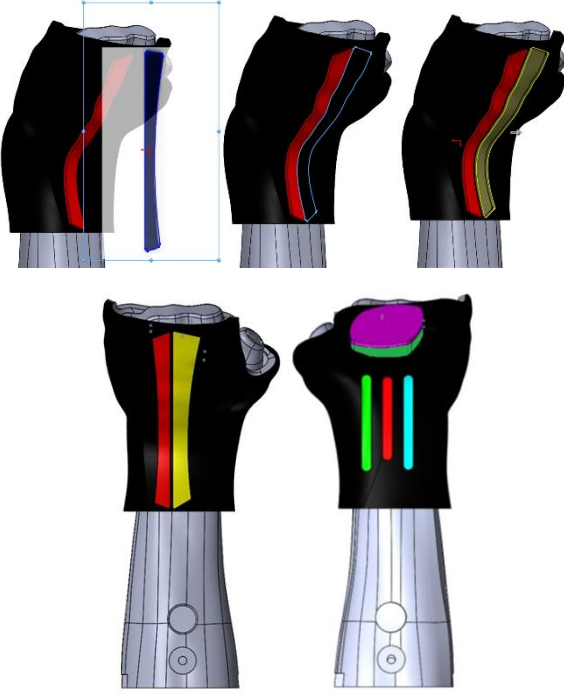
7.3 FE Modelling of Full protector – Methodology

7.3.1 Geometry Creation

The .stl files used to manufacture (CNC machine and 3-D print) the parts of the wrist surrogate (Adams, 2018) were imported into Solidworks® 2017 (Dassault Systems®) and assembled. The two 3D-printed arm profile sections were merged into one part and the bolts used to join them were not modelled. For a bare hand impact, the hand of the surrogate was set to an angle of 111° (from the vertical) and for a protected impact, the hand was set to 30° , replicating the experiment. The impactor was modelled as a $16.0 \times 12.5 \times 2.03$ cm cuboid and a $16.0 \times 12.5 \times 5.03$ cm cuboid, with 1 cm of the thickness for the aluminium plate, 1 or 4 cm for the polychloroprene and 0.03 cm for the polypropylene sheet. The effect changing the thickness of the polychloroprene from 4 to 1 cm was compared to see if the two modelling scenarios exhibited a similar impact performance, as it was believed that modelling the polychloroprene as a 1 cm block would reduce simulation time significantly.

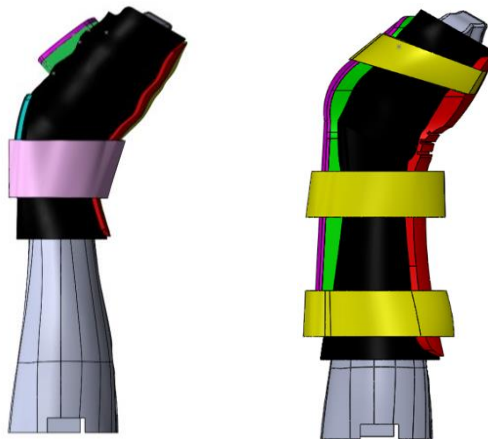
Wrist protector geometries fitted to the surrogate were modelled in Solidworks®, as detailed in Table 7-2. Developing CAD models from measurements is an established technique for modelling PPE design (Schmitt *et al.*, 2004; Tinard *et al.*, 2012; Brolin and Wass, 2016; Darling *et al.*, 2016). The main reason for developing CAD models rather than scanning the protector whilst fitted to the surrogate was so the protector could be more easily manipulated, to enable design changes to be assessed (Chapter 8).

Table 7-2 Steps taken to develop the geometries of the two wrist protector designs in CAD.

Short	Long	Description
		<p>Multiple planes at 10 mm intervals on the cross section of the hand and at various intervals on the arm were created and contours offsetting the geometry of the wrist surrogate were produced.</p>
		<p>Guide curves were drawn using a 3D sketch feature, connecting the sketches on the planes. A loft function connected all the sketches, and in turn, created the supporting foam of the protectors.</p>
		<p>The 2D scanned images of the different components of the two protectors (Chapter 3, Figure 3-3 and Figure 3-4) were used as a template while the 'sketch from image tool' was used to obtain the outer profile of the splints and pad/shell, a technique used by Brolin and Wass (2016). For the different components of the short protector, the sketches were scaled as measured, projected onto the supporting foam and extruded to the desired thickness (thicknesses obtained from Chapter 3, Table 3-4).</p>



Due to the curved nature of the long protector splints, the sketch for the dorsal splint was extruded onto the supporting foam and a sweep cut was used to recreate the profile and thickness. The palmar splint and D30[®]/EVA of the long protector were created by projecting the outer profile sketches and extruding onto the supporting foam. Two sweep cuts (7.5 and 4.5 mm from the supporting foam) were used to create the profile and thickness of the D30[®]/EVA and palmar splint.



The width of the three long protector straps and the large strap of the short protector were measured and planes were created for each distance along the profile of the protectors. Straps were modelled using the protector geometry and offsetting sketches, which were joined using the loft feature.

The surrogate and protector CAD models were imported into ANSYS[®] SpaceClaim (.STEP file) for 'cleaning'. This was to ensure there were no small or sharp edges nor interference between parts and/or the protector that may have led to small or distorted elements and a poor mesh. Within SpaceClaim, the shared topology feature was used, a technique previously described in Chapter 5.3. Shared topology was applied to parts of the impactor, mimicking the experimental setup. For the short protector, the splints and pad shared topology with the supporting foam and the shell was set to have shared topology with the pad (Figure 7-8a). For the pad and shell to share topology, the pad needed a flat upper face (where the connection was made). In turn, this meant that the pad was modelled with varying thickness, reflecting the irregularities in thickness found in Chapter 3 (Table 3-4). The long

protector also had parts sharing topology (Figure 7-8b), the dorsal splint to the supporting foam and the D3O® and EVA to the supporting foam and the palmar splint. Sharing the topology of parts within the protectors reflected the parts being sewn together as one unit within the models.

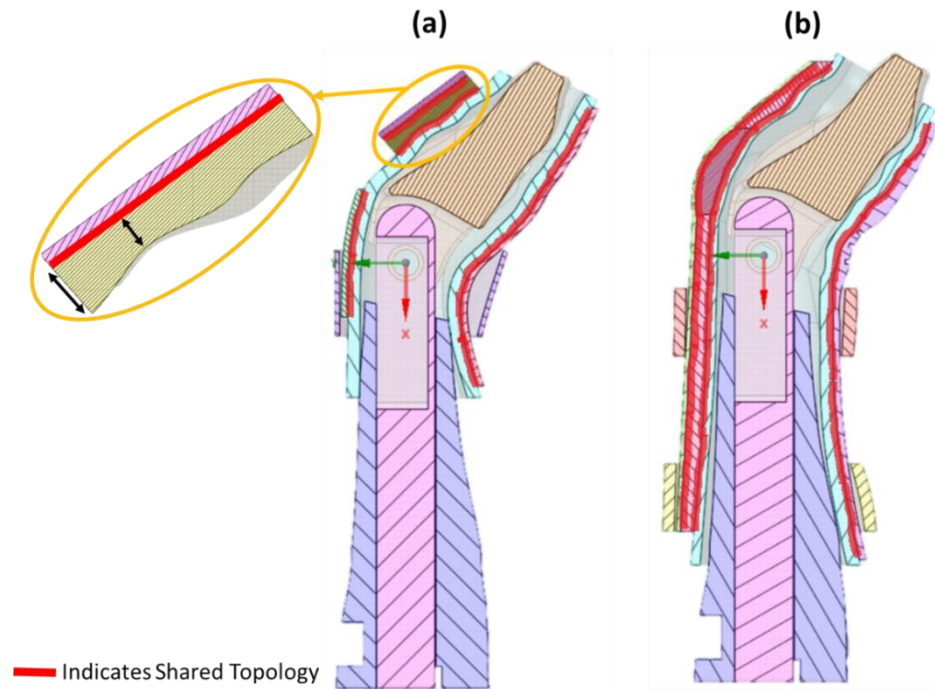


Figure 7-8 Cross section view of (a) short protector and (b) long protector highlighting the varied thickness of the palmar pad and the shared topology.

Following geometry preparation, the FE models were set up in ANSYS® Workbench where contacts, boundary conditions, materials and a mesh were applied. The model set up was developed for the short protector with the aim that all settings would then be transferable to the long protector and future protectors. Therefore, all sensitivity and mesh convergence studies were only in relation to the short protector.

7.3.2 Material Models

The polychloroprene within the impactor was assigned the material model coefficients established earlier in this chapter (Section 7.2.5). The other parts of the impactor and surrogate were assigned the material properties shown in Table 7-3 where density of the aluminium and polychloroprene was increased from 2,770 kg.m⁻³ and 1,457 kg.m⁻³ respectively, to reflect the effective mass of the pendulum arm in the experiment (7.2 kg).

Table 7-3 Overview of the material models used for the impactor and wrist surrogate, including density, Young's modulus and Poisson's ratio.

Part	Material	Material model	Density (kg.m ⁻³)	Young's modulus (GPa)	Poisson's ratio	Source
Plate	Aluminium	MAT_ELASTIC	31,500	71	0.33	(Ansys, 2018)
Plastic Sheet	Polypropylene	MAT_ELASTIC	905	1.6	0.4	(Direct Plastic Ltd, no date)
Hand	Aluminium	MAT_RIGID	2,770	71	0.33	(Ansys, 2018)
Central Support	Structural Steel	MAT_ELASTIC	7,850	200	0.3	(Ansys, 2018)
Arm	Nylon SLS	MAT_ELASTIC	950	1.65	0.33	(Materialise, 2018)

Linear elastic (*MAT_ELASTIC) models were used for the protector splints. For the short protector splint, Young's modulus was the mean from the 3-point bend test (472 MPa, Chapter 3, Table 3-5) and the Poisson's ratio of 0.4 was from Ankrah and Mills (2003). For the long protector, Young's modulus was the median value of 550 MPa from datasheets from the manufacturer (DuPont, 2017) and the Poisson's ratio of 0.4. Material models for the strap were linear elastic with Young's modulus obtained from a linear trend line fitted to the tensile data (short = 37 MPa and long = 29 MPa), as shown in Chapter 5 (Figure 5-2).

For the supporting foams, pad and D3O[®], the hyperelastic material models (Table 5-2) and the Prony series (Table 5-3) validated in Chapter 5 were used. While developing the full protector FE models it was found that the short protector supporting foam needed to be artificially stiffened, due to bottoming out at the higher energies causing negative volume errors and the model to fail when run. The impact data used for the hyperelastic model was therefore artificially stiffened by a factor of three and a new material model was selected (Figure 7-9). For the artificially stiffened curve, a Mooney-Rivlin model provided a better match and the coefficients for this model were C10 = 0.021 MPa, C01 = 0.233 MPa and C11 = 0.454 MPa. The Prony series coefficients paired with this hyperelastic model were not changed (k file inputs for all material models shown in Appendix 10.F). It was not possible to characterise the EVA foam in the long protector (Chapter 3, Figure 3-4) due to its low thickness. The material properties used by Ankrah & Mills (2004) for modelling EVA were trialled, but this resulted in negative volume errors. Footage from the high-

speed video cameras used in the experimental impact testing (Chapter 6.3.2, Figure 6-11, HSC 5 to 7) indicated impact was prominently on the D3O[®] section of the protector, therefore, all the foam sections within the long protector were assigned the D3O[®] material properties.

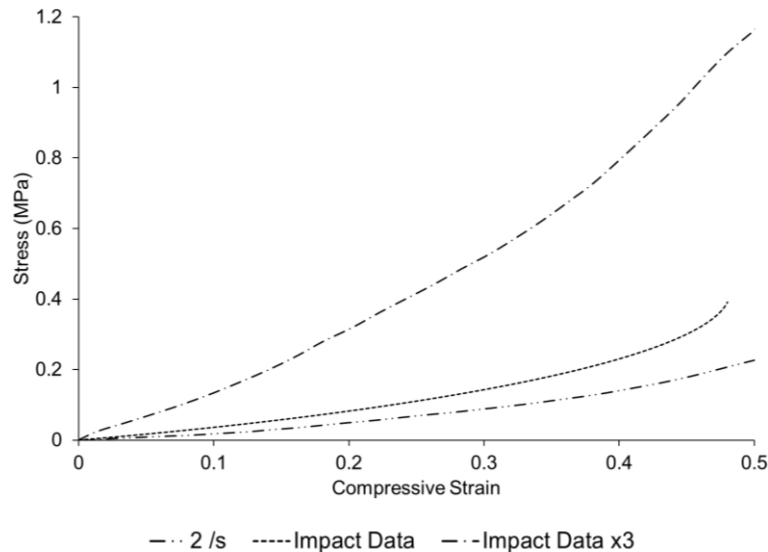


Figure 7-9 Stress vs. strain plots for the short protector supporting foam showing the highest quasi-static trace (2 s^{-1}), the impact data trace and the artificially stiffened trace used in the final model.

7.3.3 Boundary Conditions

To replicate the motion of the pendulum arm a co-ordinate system was created at its axis of rotation (Figure 7-10), and to reduce simulation time, the bar was reduced to 1 mm in length, to act as a point of rotation. The top face of the impactor was assigned a remote displacement about the pendulum arm coordinate system, meaning that it was free to rotate about the z-axis in relation to this point, but was constrained in all other orientations. Within ANSYS[®]/LS-DYNA[®] there is the ability to apply static preloads to a body through a dynamic relaxation which occurs prior to the start of the simulation ($t = 0 \text{ s}$). The preload, within the dynamic relaxation phase, is applied until a set convergence tolerance is reached (LSTC, 2017b). Allen *et al.* (2009) used dynamic relaxation when modelling tennis rackets to create the tension within the woven string bed, prior to impact from a tennis ball. Dynamic relaxation, therefore, seemed appropriate for this study, where a pressure of 10 kPa to the outer surface of all straps could be applied. However, even with a low convergence tolerance, this resulted in a long run time. Therefore, the impactor was set 5 mm from the top of the surrogate ($\sim 3^\circ$ from the horizontal), allowing sufficient time for a pressure to be applied ($t = 0.001 \text{ s}$) to the outer surface of the straps, at the start of the simulation prior to impact occurring. Following the applied pressure ($t = 0.002 \text{ s}$), a tied contact (*Contact_Tied_Surface_To_Surface) was applied

between the contacting surface of the strap, dorsal splint and supporting foam, prior to impact. As it was unclear as to the exact pressure being applied by the straps, using the strapping method of Adams *et al.* (2016) (Chapter 6.3.1), a sensitivity study was conducted between 1 and 15 kPa to understand the effect within the model.

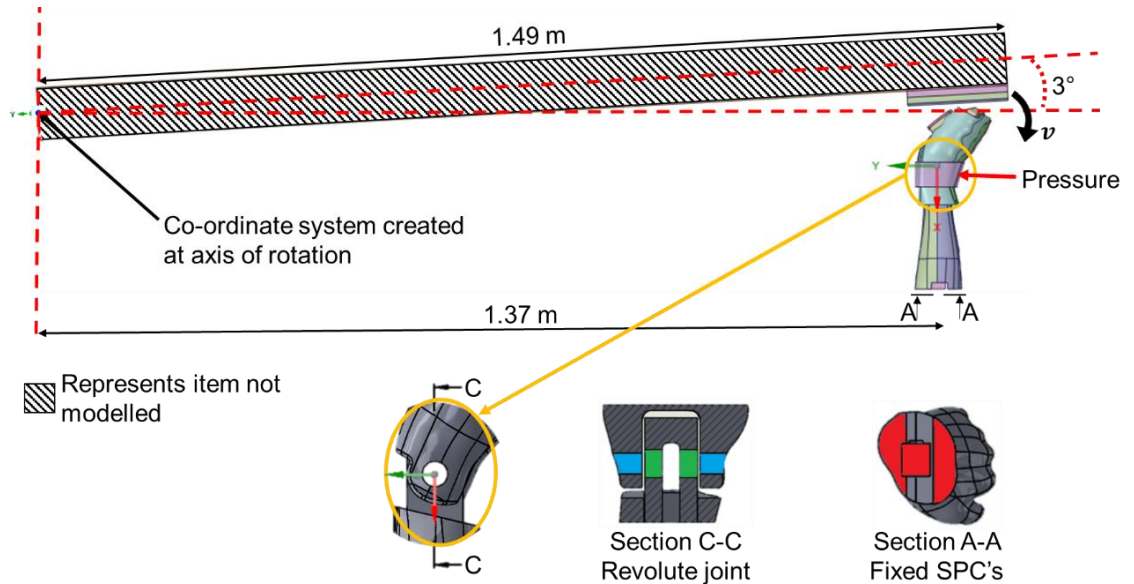


Figure 7-10 Coordinate system used to replicate the pendulum motion of the impactor within the FE models and the boundary conditions set.

The impactor (aluminium sheet, polychloroprene and polypropylene sheet) was assigned an initial angular velocity about the pendulum arm coordinate system, according to the impact energy being replicated (Figure 7-10). Theoretical angular velocity was calculated and compared to a mean of the experiment across all energies (Table 7-4). The experimental mean of the pendulum arm angular velocity was calculated as an average of the last ten data points prior to impact. A sensitivity study was undertaken to see the effect of using both the theoretical and experimental velocities within the model, with the experimental values used for validation. Using the measured velocity gave a better match to the experimental temporal force data, so the measured velocity was used (mean difference of 500 N in peak force and 2° in maximum wrist angle).

Table 7-4 Difference between the theoretical impact velocities and mean experimental values across 10 to 50 J.

Angular Velocity \pm SD (rad.s ⁻¹)	Impact Energy (J)				
	10	20	30	40	50
Theoretical	1.111	1.572	1.926	2.223	2.486
Experimental	1.216 \pm 0.089	1.611 \pm 0.016	2.069 \pm 0.005	2.491 \pm 0.008	2.758 \pm 0.006
Difference (%)	0.105 (9)	0.039 (2)	0.143 (7)	0.268 (12)	0.272 (11)

A revolute joint was applied to replicate the hinge in the wrist surrogate assembly, where the central support was the reference and the hand was mobile (Figure 7-10). As the holes for these parts were coincident, the nodes were aligned and fixed meaning a bolt was not needed in the assembly for the joint to work. Joint controls were set to explicit within 'analysis settings'. The collection of nodes on the proximal faces of the arm and central support were fixed using SPC's (single point constraint's) (Figure 7-10) to replicate the experiment.

All boundary conditions and mesh settings for models involving a wrist protector, were optimised for the short protector. The same settings were then used for the long protector and future models in Chapter 8. The reason for not conducting sensitivity studies for the long protector as well, was so the transferability of the model between different designs could be checked. If the model was still producing results reflective of the experimental set up, the model would then have the potential to be used as a design tool in the future, as opposed to having to optimise parameters for every single protector modelled, which would not be very efficient.

Frictional contacts (*Contact_Automatic_Surface_To_Surface) were applied between the inner surface of the supporting foam and the outer surface of the wrist surrogate (hand, arm and central support) as well as between the contacting surfaces of the strap and palmar splints. The coefficient of friction (both static and dynamic) was set to 0.4 between the supporting foam and surrogate and 0.7 between the strap and the supporting foam. As the coefficient of friction between the supporting foam and the surrogate was unknown, a sensitivity study using the model, changing the coefficient between zero and one, at 40 J, was run to understand its effect. An alternative to conducting a sensitivity study could have been to obtain the coefficient of friction experimentally using techniques such as those described by Blau (2008), which include the inclined plane and horizontal

tribometer methods. A coefficient of friction of 0.3 was also applied between the plastic of the impactor and the wrist surrogate (Direct Plastic Ltd, no date). Specific contact settings were used in order to prevent negative volume errors within the simulation, this including reducing the time step scale factor to 0.5 and changing the contact setting SOFT = 1, as the surrogate central support ($E = 200$ GPa) was considerably stiffer (x 125) than the polychloroprene impactor ($E = 1.6$ GPa) (LSTC, 2017b).

7.3.4 Mesh

When possible, structures should be meshed with hexahedral elements particularly in dynamic models (Burkhart *et al.*, 2013). However, due to recommendations to prevent negative volume errors (LS-DYNA Support, 2019) and studies suggesting that simulation accuracy between tetrahedral and hexahedral elements was comparable (Cifuentes and Kalbag, 1992; Ramos and Simoes, 2006), a tetrahedral mesh was selected. The mesh was generated using solid brick elements (ELFORM 1, constant stress hexahedra) and solid tetrahedral elements (ELFORM 10, constant stress solid tetrahedra) (Table 7-5). A mesh convergence study was undertaken for the bare hand set up (surrogate and impactor) and the resulting element size was used in all models. During pilot testing, mesh convergence studies were undertaken for one of the short protector dorsal splints, in a quasi-static three point bend test, and an impact of the palmar pad in isolation, which had a similar geometry to those used in the full wrist protector model. The number of nodes and elements resulting from the mesh convergence studies (Appendix 10.G) for each component are shown in Table 7-5.

Table 7-5 Parts of the bare hand, short and long protector impact models, the type of elements that were used for meshing and the number of nodes and elements they were meshed with.

Model	Component	ELFORM	Number		Through the thickness
			Elements	Nodes	Elements
Bare Hand	Aluminium plate	1	3,744	5,280	3
	Polychloroprene	1	3,744	5,280	3
	Plastic sheet	1	1,248	2,640	1
	Hand	10	36,566	7,514	-
	Central Support	10	12,068	2,926	-
	Arm	10	27,629	6,421	-
Total			84,999	30,061	
Short Protector	Supporting Foam	10	56,321	13,298	3
	Right Dorsal splint	10	6,102	1,775	3
	Left Dorsal splint	10	4,843	1,428	3
	Shell	10	7,319	1,891	2
	Pad	10	16,954	3,623	5
	Left Palmar Splint	10	1,750	537	2
	Middle Palmar Splint	10	516	1,501	2
	Right Palmar Splint	10	516	1,501	2
	Strap	10	3,002	1,138	2
Total			97,323	26,692	
Long Protector	Supporting Foam	10	29,827	8,719	3
	Palmar Splint	10	24,389	7,516	3
	Dorsal Splint	10	7,684	2,318	3
	D3O®	10	20,045	4,208	6
	EVA	10	29,201	6,779	5
	Top Strap	10	1,966	733	2
	Middle Strap	10	4,619	1,411	2
	Bottom Strap	10	4,865	1,506	2
Total			122,601	33,190	

The overall mesh quality was assessed in terms of aspect ratio, which had a mean (\pm standard deviation) of 1.94 ± 0.97 for the short protector and 1.96 ± 1.10 for the long protector, which met recommendations of Tsukeman and Plaks (1998) for aspect ratios between 1 and 4 when using a tetrahedral mesh. The mesh had a mean (\pm standard deviation) element quality of 0.81 ± 0.12 for the short protector and 0.81 ± 0.13 for the long protector, where a value of 1 is indicative of a perfect tetrahedral (Sharcnet., 2016), suggesting the meshes were acceptable.

7.3.5 Post-Processing

In post-processing, the temporal force located at the SPC nodes on the proximal face, providing the fixed support (Figure 7-10), was obtained for each simulation in the x-axis via the `spcforc` output (LSTC, 1998). The support force was used as this replicated the output from the load cells in the experiment. Temporal force data was filtered using the same method as the experimental data in MATLAB® (Chapter 4.2) and wrist angle was obtained using a 3-node angle measurement within LS-PrePost. To ensure consistency across energies, the same three nodes were used (Figure 7-11).

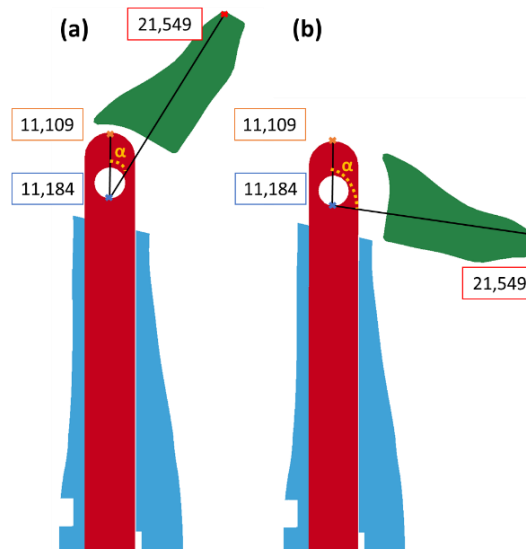


Figure 7-11 Example section view of how a 3-node angle measurement was taken to obtain maximum wrist angle (a) prior to impact - starting angle of 30° and (b) at maximum displacement (94°) for the short protector.

Temporal force traces for a bare hand impact were compared to the mean experimental impact from Chapter 6. For both wrist protectors temporal force, temporal wrist angle and force vs. wrist angle traces were compared to the first experimental impact on an untested protector from Chapter 6 across all five energies.

7.4 Results

7.4.1 Pilot Results Informing Methods

Pilot testing indicated that reducing the polychloroprene thickness in the model from 4 to 1 cm, had minimal effect on the temporal force and temporal wrist angle traces for the short protector impact at 40 J (Figure 7-12). Differences were evident in the force spike at initial impact where a 4 cm block of polychloroprene produced a lower force (1,680 vs. 805 N); however, the 1 cm block was closer to the experimental impact (1,783 N). Impact duration was 2.5 ms longer for the 4 cm impactor

compared to the 1 cm impactor (49.4 vs. 47.9 ms), with experimental data was closer to the 1 cm model (48.4 ms). Temporal wrist angle traces did not change in shape, but maximum angle was larger for the 4 cm impactor (94° vs. 99°). The effect on the impact trace was minimal and peak forces were comparable (3,885 vs. 3,538 N). However, the run time was reduced by ~7 hours (38 hours to 31 hours), which in turn meant that over 39 days could be saved for all full protector simulations (~135 simulations in total). Therefore, due to the minimal difference in temporal force and temporal wrist angle, but the large decrease in run time, a 1 cm block was chosen for modelling.

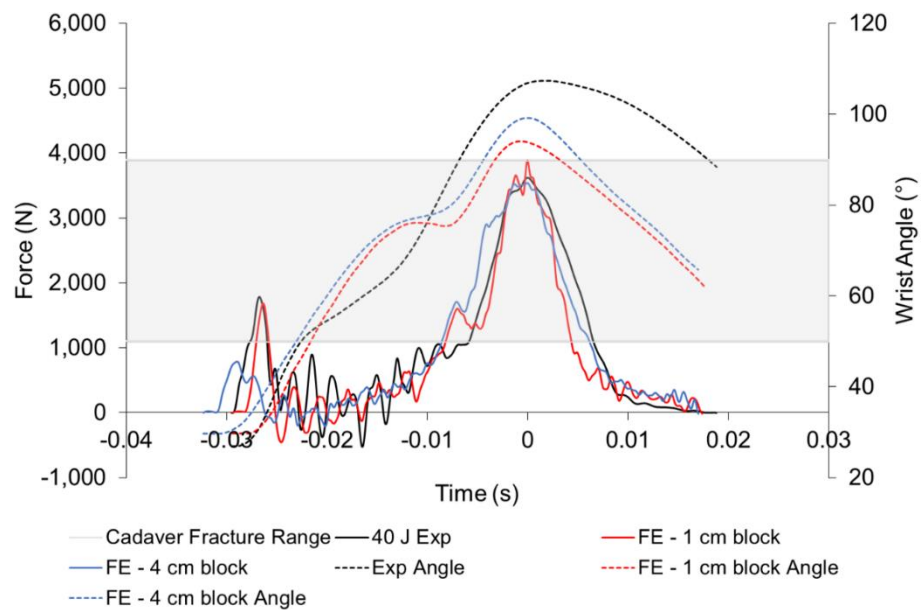


Figure 7-12 Example temporal force and temporal wrist angle trace highlighting the difference between using a 4 cm and 1 cm polychloroprene block within the FE models of a short protector impact at 40 J. The experimental data is also shown for comparison.

The coefficient of friction between the supporting foam and surrogate was changed between 0.3 and 1. Values below 0.3 resulted in negative volume errors. Figure 7-13 shows peak force and maximum wrist angle decreased as the coefficient of friction increased. Higher friction between the protector and surrogate limited the extension angle of the hand and allowed the palmar padding element to become more engaged with the impactor. At the lower coefficients, a higher peak force is seen as the pad is no longer being struck and the supporting foam is being impacted (Figure 7-14). A coefficient of 0.4 was chosen for simulations as it gave the closest match to the experimental impact in terms of peak force, maximum wrist angle and visually throughout the simulation when compared to the high-speed videos.

7. FE Model of Wrist Protectors Under Impact

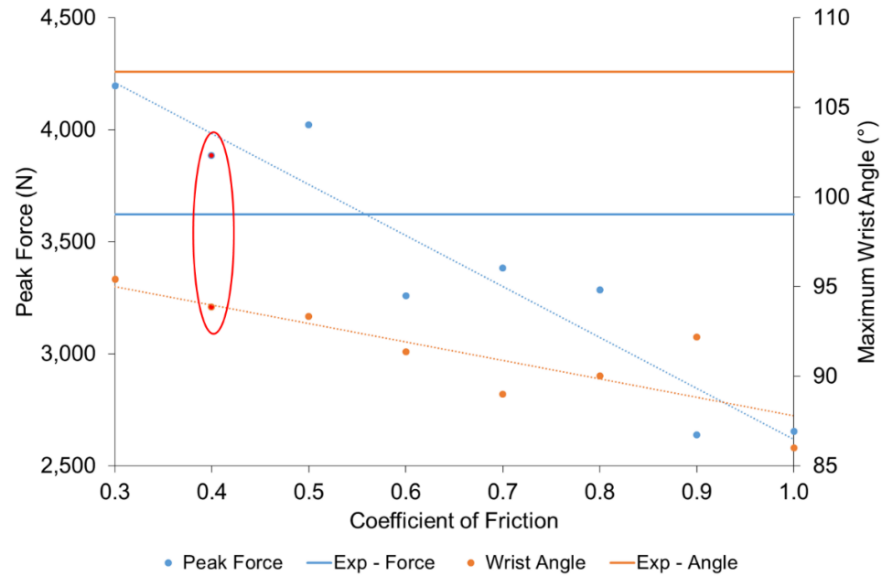


Figure 7-13 Effect of changing the coefficient of friction between the supporting foam and wrist surrogate on peak force and maximum wrist angle for a 40 J impact on the short protector. The red ring highlights the values used in the final models.

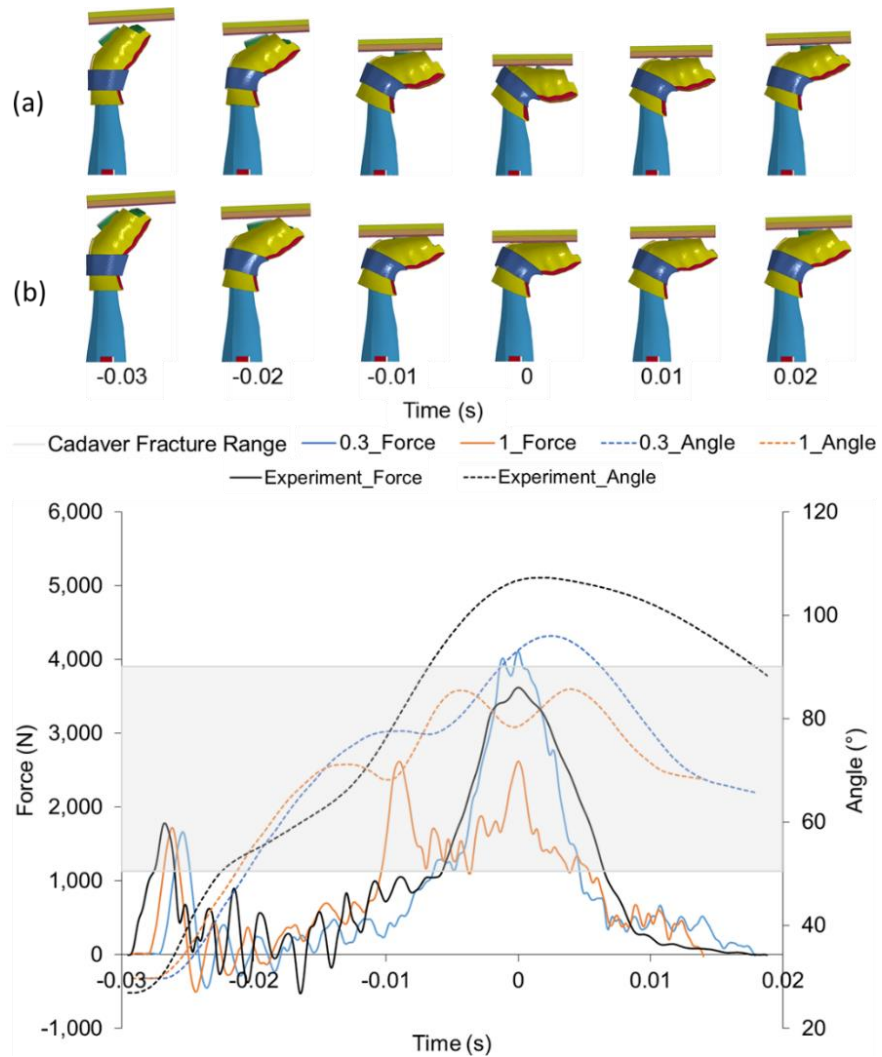


Figure 7-14 Effect of changing the coefficient of friction between the supporting foam and wrist surrogate on temporal force and temporal wrist angle traces for a 40 J impact on the short protector. Including images from the models (a) coefficient of friction of 0.3 and (b) 1.0. Experimental data is shown for comparison.

The sensitivity study on strapping pressure showed that when changed between 1 and 15 kPa, peak force increased by ~550 N (12%) and wrist angle increased by 3° (4%) (Figure 7-19). The temporal force traces did not change considerably in shape, but impact duration decreased with a higher strapping pressure (49.8 vs. 44.3 ms) and maximum wrist angle occurred later ($t = 0$ vs. 0.0028 s) (Figure 7-16). As there was not much change in strapping pressure, 10 kPa was chosen.

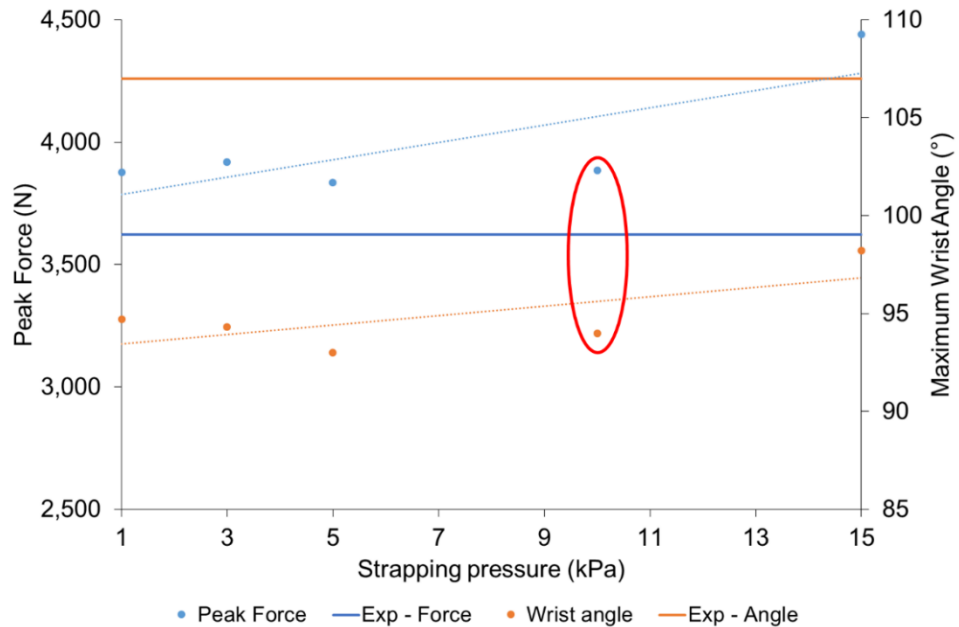


Figure 7-15 Effect of changing strapping pressure on peak force and maximum wrist angle for a 40 J impact on the short protector. The red ring highlights the values used in the final models.

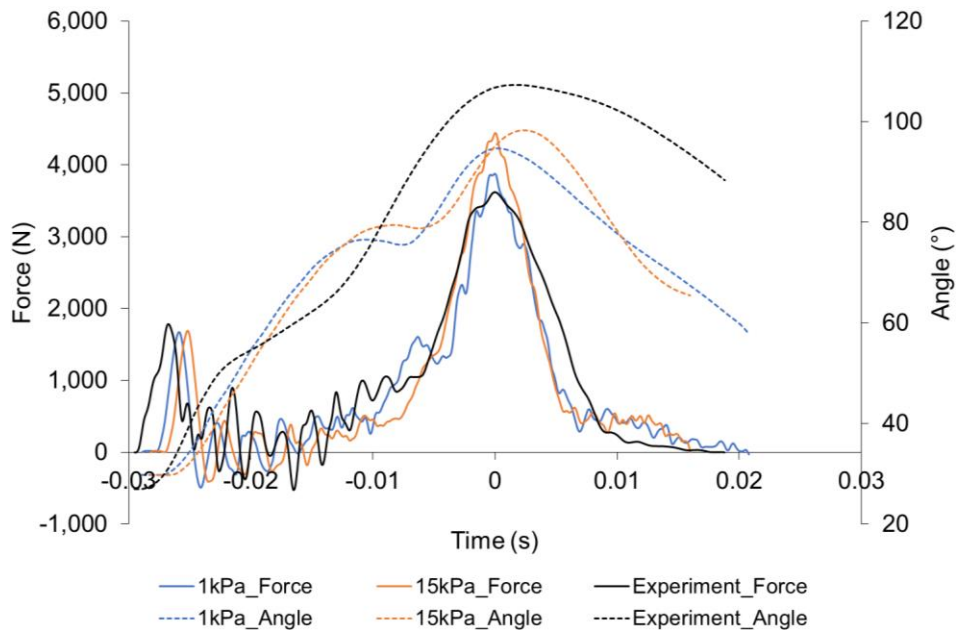


Figure 7-16 Effect of changing strapping pressure between 1 kPa and 15 kPa on temporal force and temporal wrist angle traces for a 40 J impact on the short protector. The experimental data is shown for comparison.

7.4.2 Bare Hand

Temporal force traces showing a mean experimental bare hand impact and the results of the FE model at 10 to 50 J are shown in Figure 7-17. The experiment and model showed peak force to increase with impact energy, while impact duration decreased. The mean percentage difference between the model and experiment across all energies was 11% for peak force and 14% for impact duration. A comparison across all energies is shown in Figure 7-18.

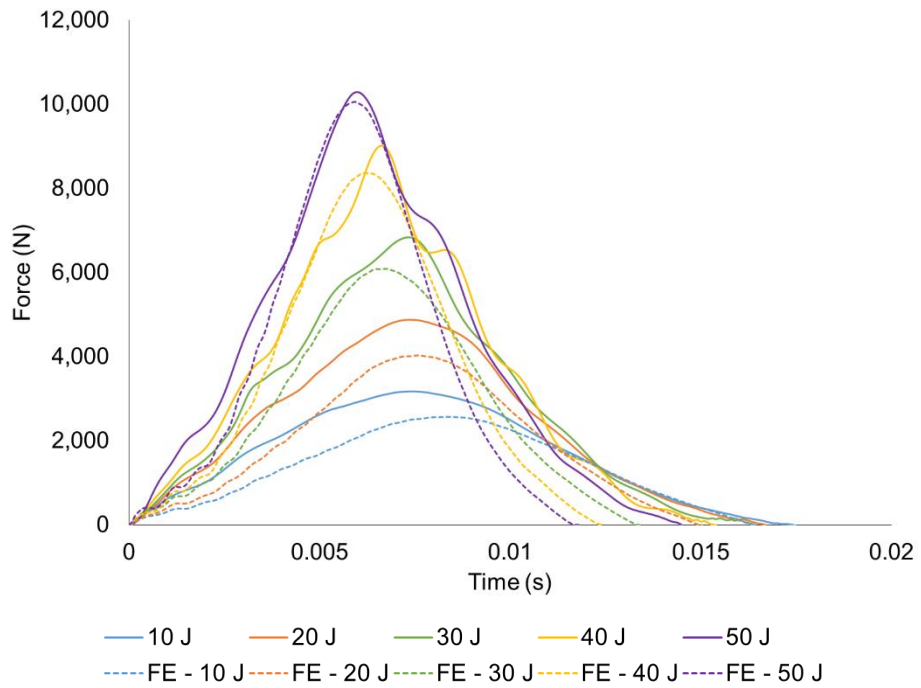


Figure 7-17 Temporal force traces for a mean experimental bare hand impact (solid line) and FE model (dashed line) across 10 to 50 J.

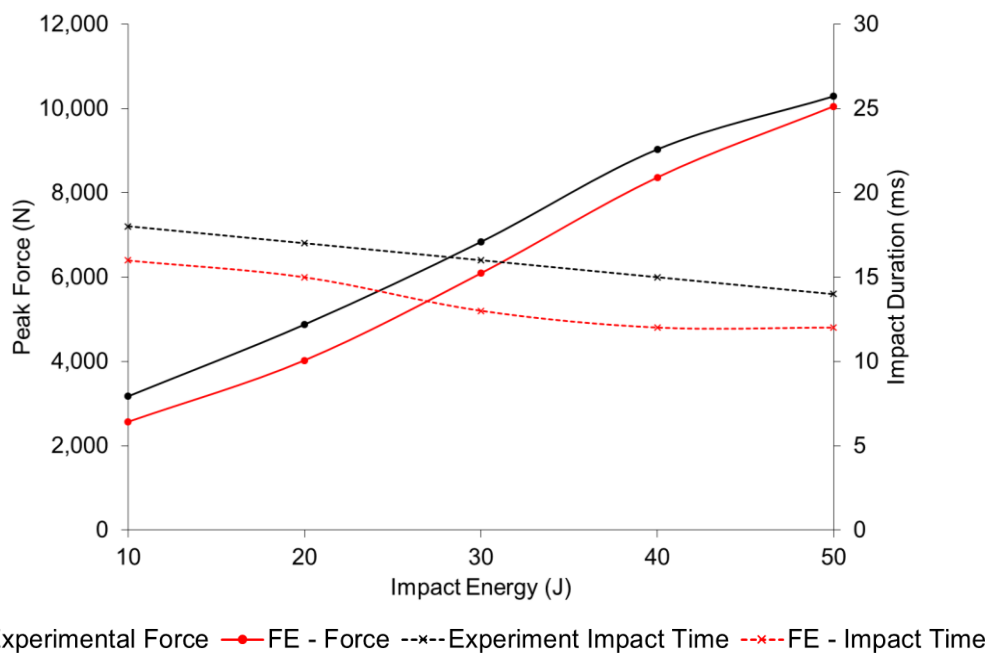


Figure 7-18 Comparison of peak forces and impact duration for both the experiment and bare hand FE model at 10 to 50 J.

7.4.3 Example Comparison of the Model and Experimental Impact

Figure 7-19 and Figure 7-20 show temporal force and temporal wrist angle traces for the experiment and model for a 40 J impact on the short and long protector respectively. Images from the high-speed cameras (A and B) and the model at 1 ms intervals are also included. Both models captured the phases (as described in Chapter 6.4.2) of the experimental impact (highlighted by the upper sequence of high-speed camera and model images). There is agreement between the model and experiment when comparing temporal force traces, but temporal wrist angle traces showed differences. The differences occurred after the initial impact, during the period of low force when the wrist extended and broke contact with the protector (lower sequences of high-speed camera and model images). In the experiment, the duration of broken contact between the impactor and surrogate/protector was shorter and less apparent than in the model (0.0047 vs. 0.0149 s for the short protector and 0.0060 vs. 0.0190 s for the long protector).

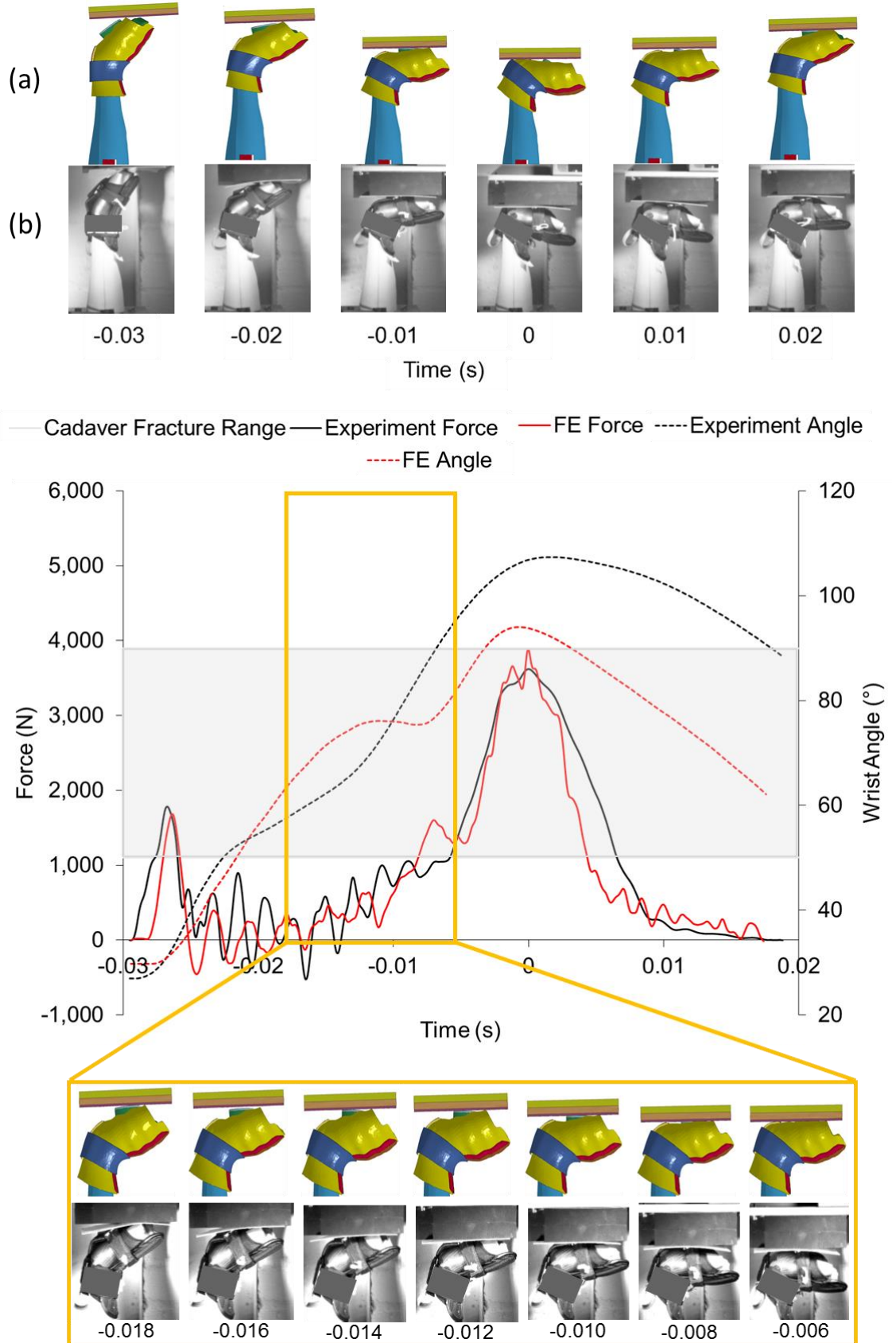


Figure 7-19 Impact of the short protector at 40 J experimentally and in the FE model. A sequence of high-speed photographs (camera A) and corresponding images from the FE model showing key points of the temporal force traces. Photos are at 1 ms intervals for (a) FE model and (b) experimental test. Temporal force and temporal wrist angle traces are also shown with a further sequence of high-speed photographs (camera B) and corresponding images from the FE model showing discrepancies between the two at 0.002 s intervals.

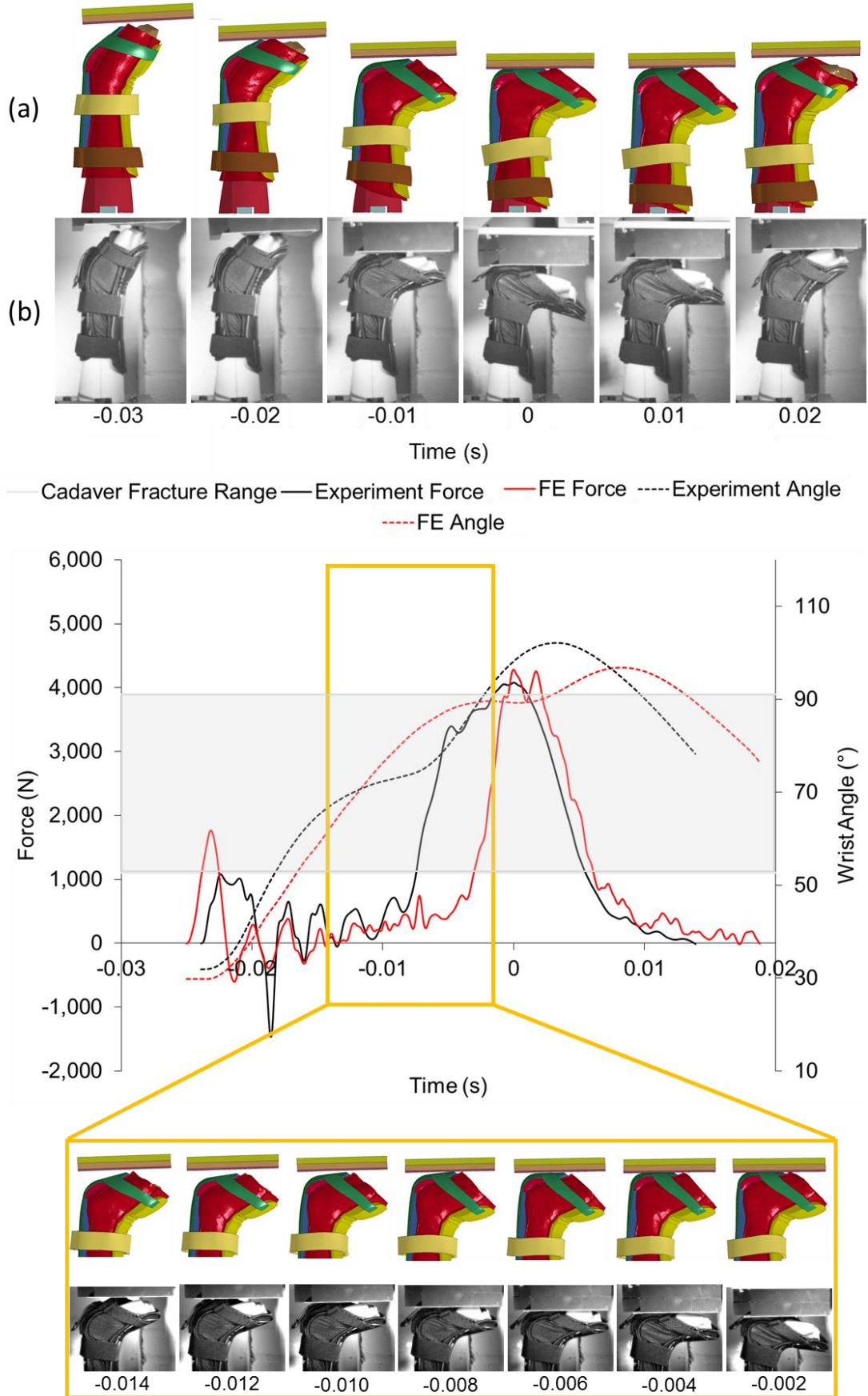
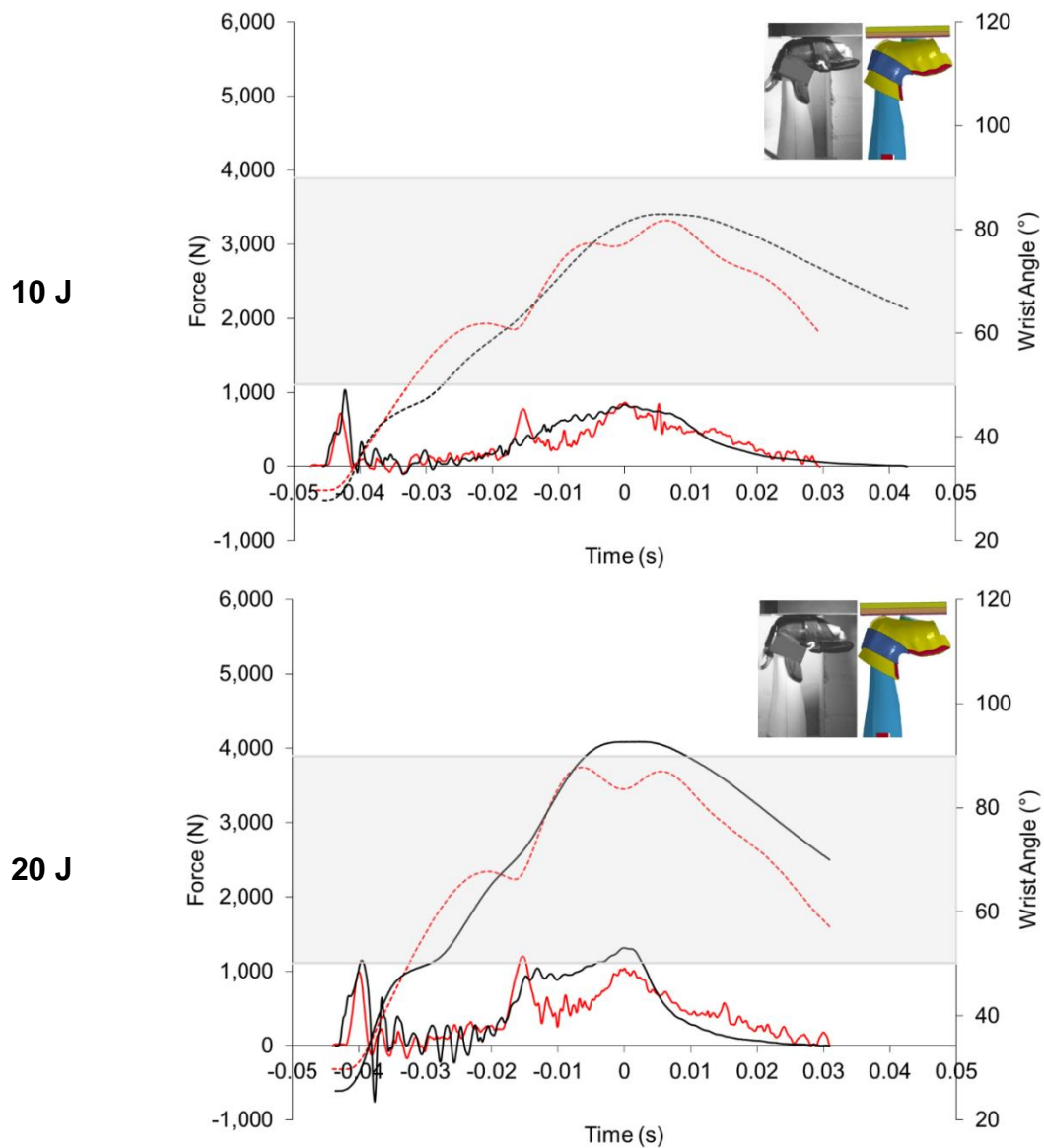


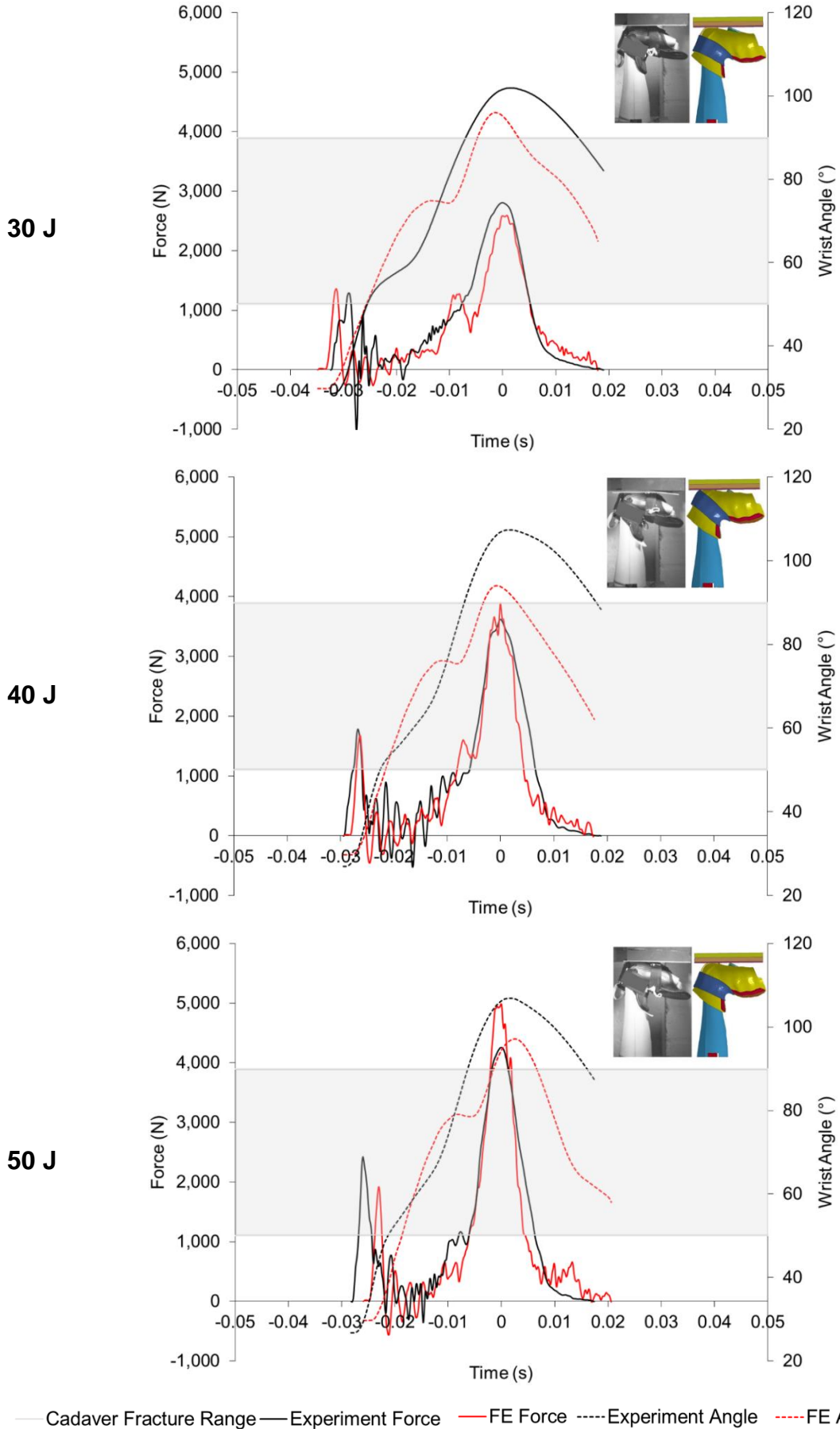
Figure 7-20 Impact of the long protector at 40 J experimentally and in the FE model. A sequence of high-speed photographs (camera A) and corresponding images from the FE model showing key points of the temporal force traces. Photos are at 1 ms intervals for (a) FE model and (b) experimental test. Temporal force and temporal wrist angle traces are also shown with a further sequence of high-speed photographs (camera B) and corresponding images from the FE model showing discrepancies between the two at 0.002 s intervals.

7.4.4 Model and Experiment Comparison – Temporal Force and Temporal Wrist Angle Traces

A comparison of the model (red line) against the experimental impact (black line) across five energies (10 to 50 J) as temporal force and temporal wrist angle traces are shown for the short (Figure 7-21) and long (Figure 7-22) protector. Images from a high-speed camera (A) and the model at maximum wrist angle are included with each plot. Temporal force showed good agreement between the experiment and model, while temporal wrist angle showed differences, as explained in Section 7.4.3. Whilst differences were evident for temporal wrist angle, at maximum wrist angle, the model and images showed agreement.



7. FE Model of Wrist Protectors Under Impact

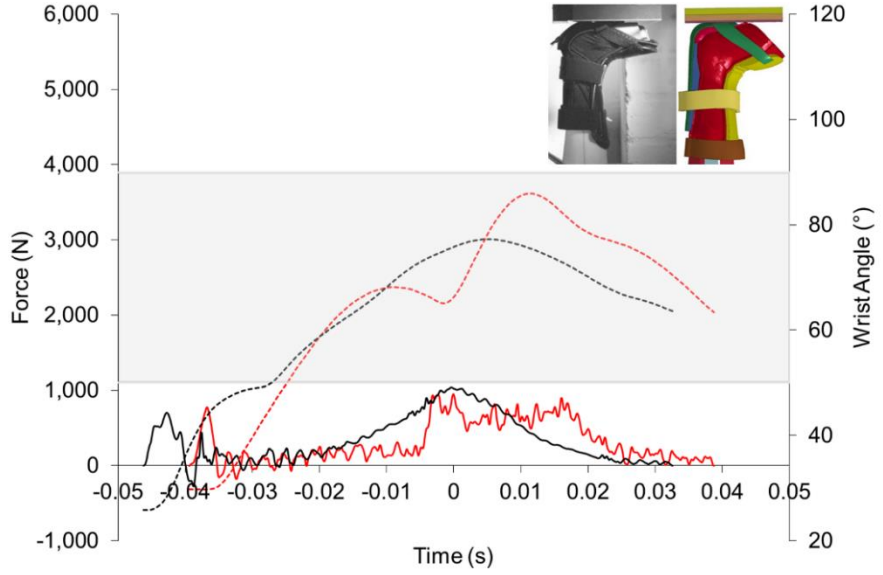


— Cadaver Fracture Range — Experiment Force — FE Force - - - Experiment Angle - - - FE Angle

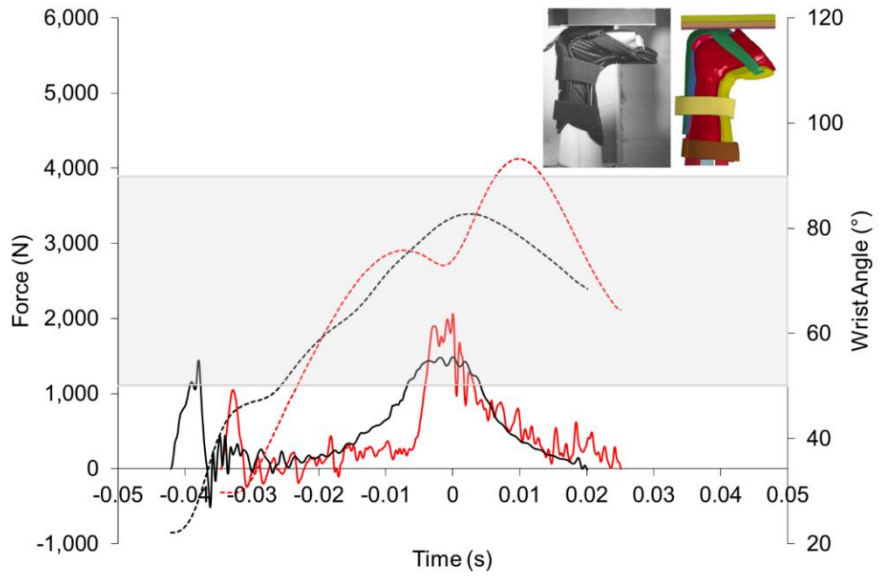
Figure 7-21 Comparison between experimental data and FE model for the short protector at 10 to 50 J in terms of temporal force and temporal wrist angle traces and a high-speed video image vs. model at maximum wrist angle.

7. FE Model of Wrist Protectors Under Impact

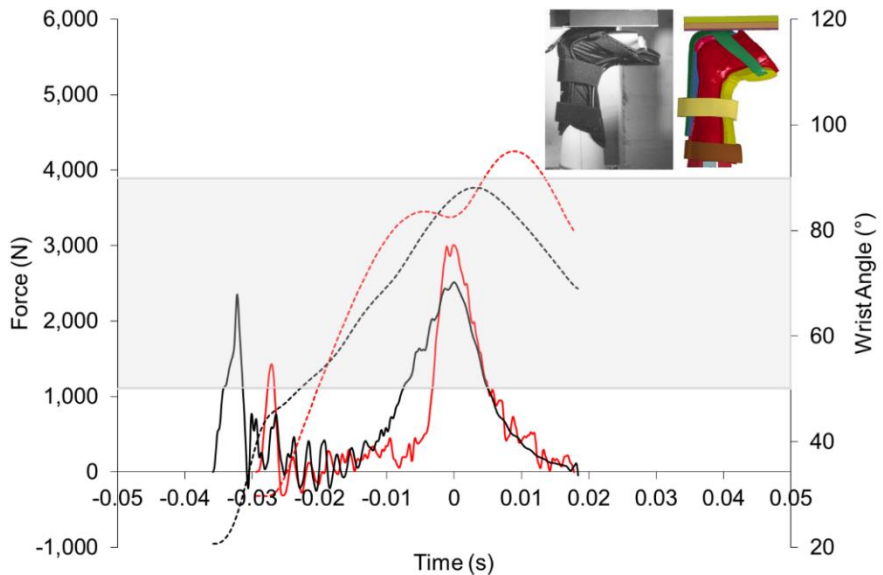
10 J



20 J



30 J



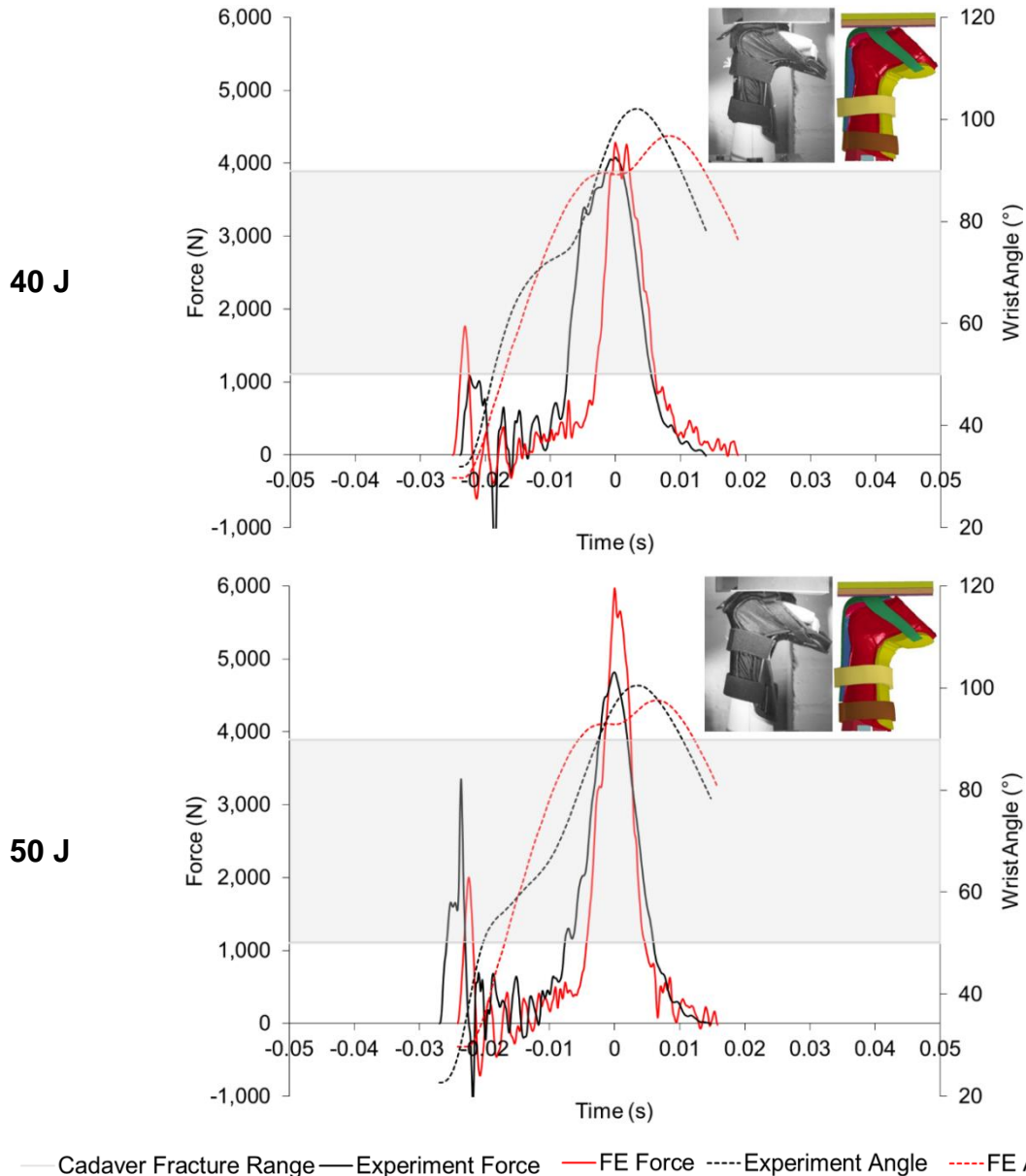


Figure 7-22 Comparison between experimental data and FE model for the long protector at 10 to 50 J in terms of temporal force and temporal wrist angle traces and a high-speed video image vs. model at maximum wrist angle.

7.4.5 Model and Experiment Comparison - Force vs. Wrist Angle

A comparison of the model (red line) against the experimental impact (black line) across five energies (10 to 50 J) as a force vs. wrist angle trace, is shown for the short (Figure 7-23) and long (Figure 7-24) protector. The figure highlights that the force vs. wrist angle trace was not well replicated within the model, unlike the temporal force traces. For the short protector, the experimental force vs. wrist angle trace had a two-part loading curve, a quasi-linear phase up to $\sim 90^\circ$ followed by a rapid increase in force and angle, up to peak. The model, on the other hand, had a three-part loading curve. A sharp increase in force between $\sim 60^\circ$ and 70° , followed by a quasi-linear phase and then a final increase up to peak force and maximum wrist angle. For the long protector, the experimental force vs. wrist angle trace was

a two-part curve. This curve consisted of a gradual increase in force with angle beyond $\sim 60^\circ$ until peak force; maximum wrist angle was then reached as force started to decrease. In the model, however there was a sharp increase in force at ~ 70 to 90° up to peak followed by a decrease in force where maximum angle was reached. The discrepancies are likely to be due to the temporal wrist angle traces showing a poor match in Figure 7-21 and Figure 7-22.

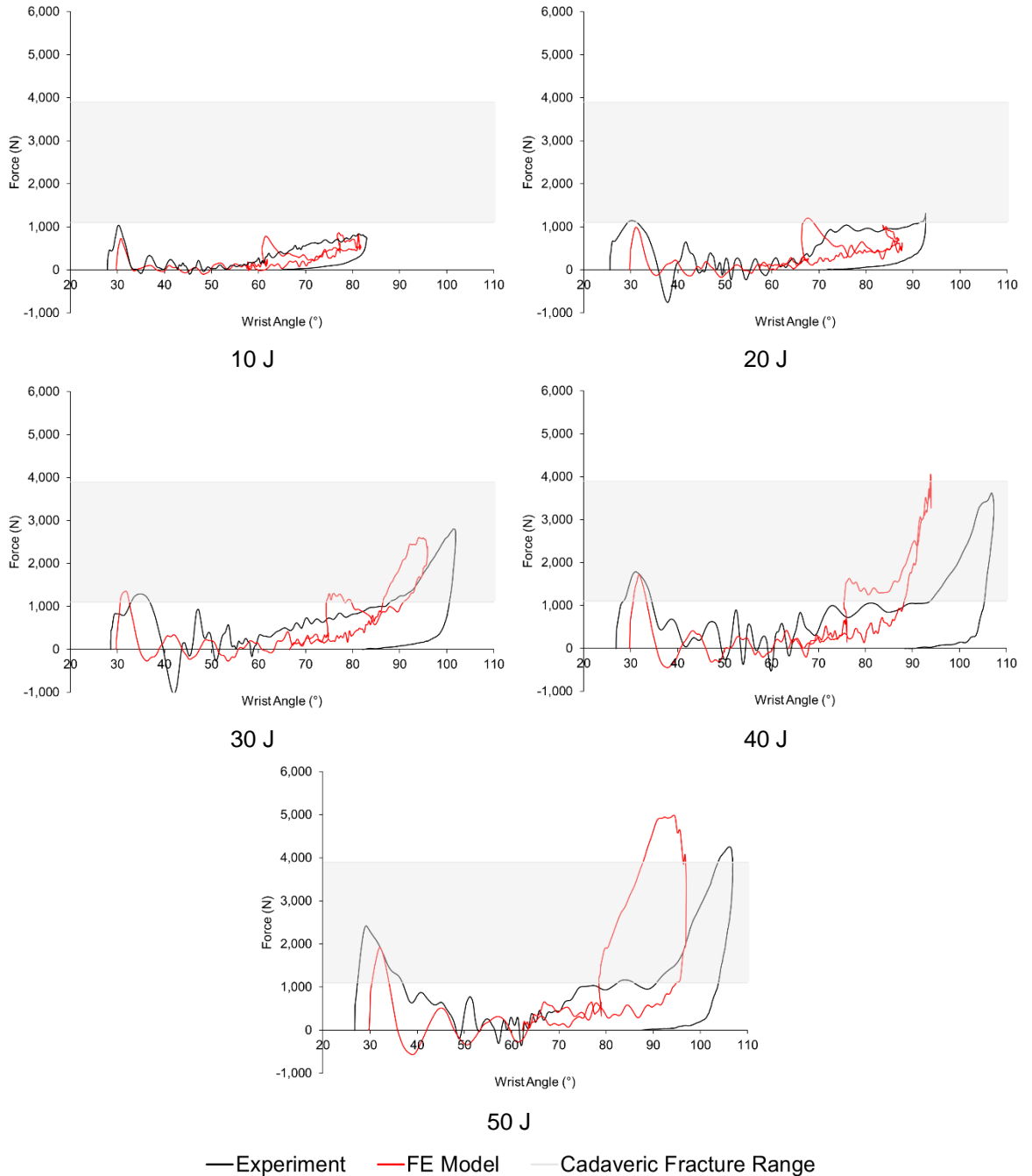


Figure 7-23 Comparison between experimental data and FE model for the short protector at 10 to 50 J in terms of a force vs. wrist angle trace.

7. FE Model of Wrist Protectors Under Impact

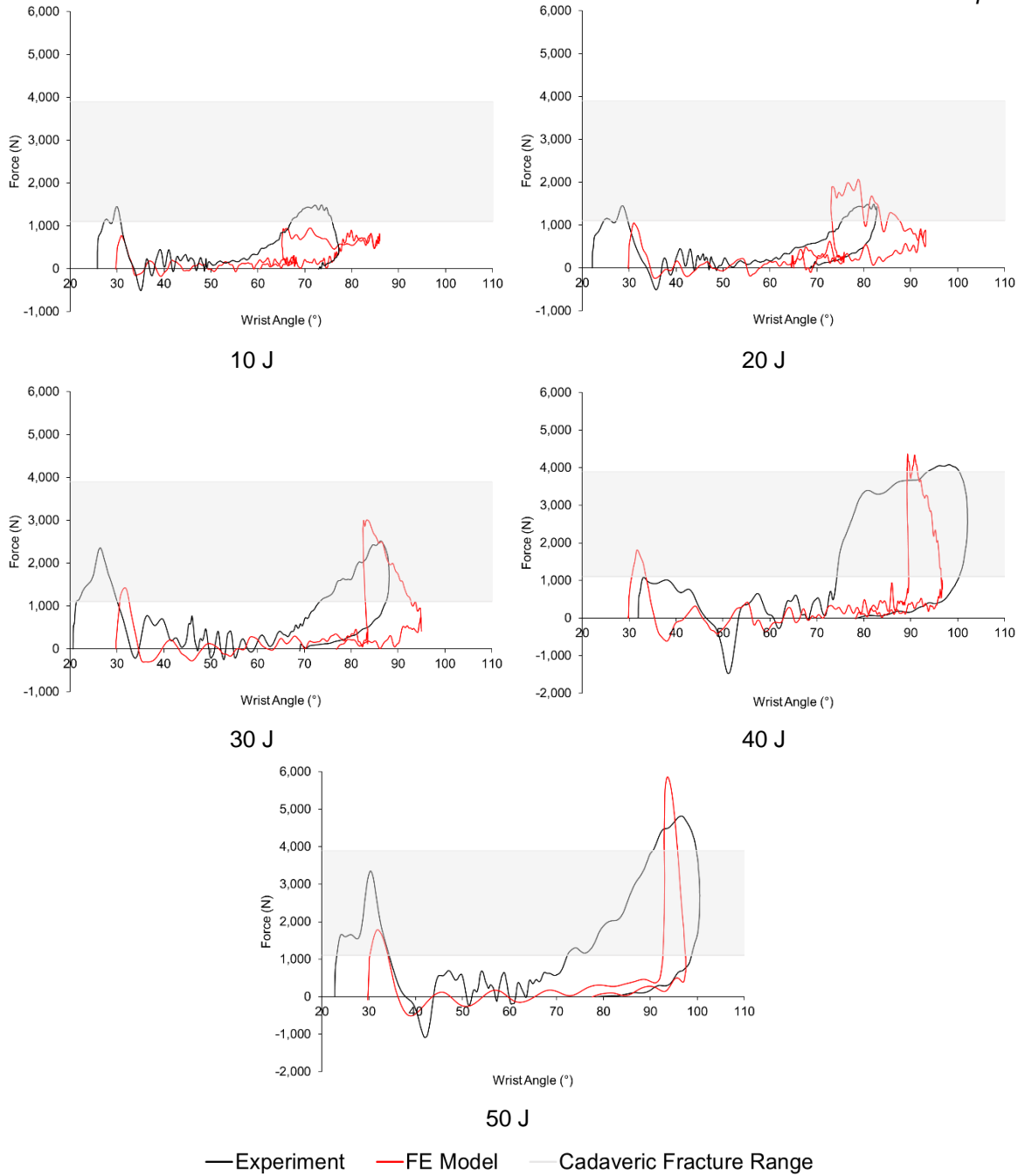
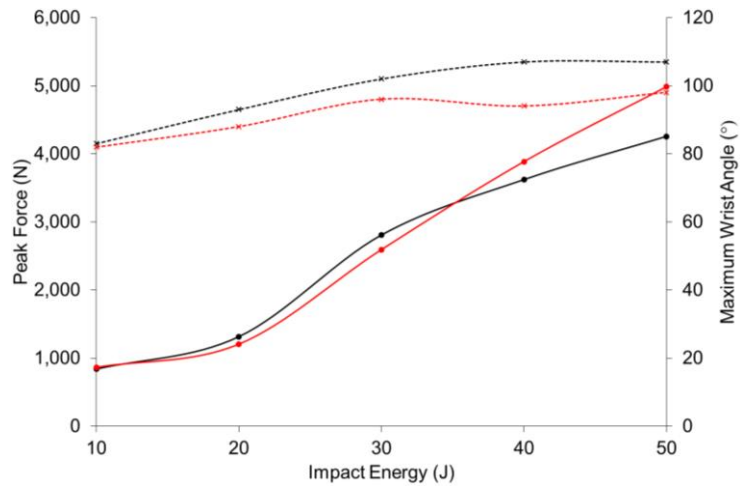


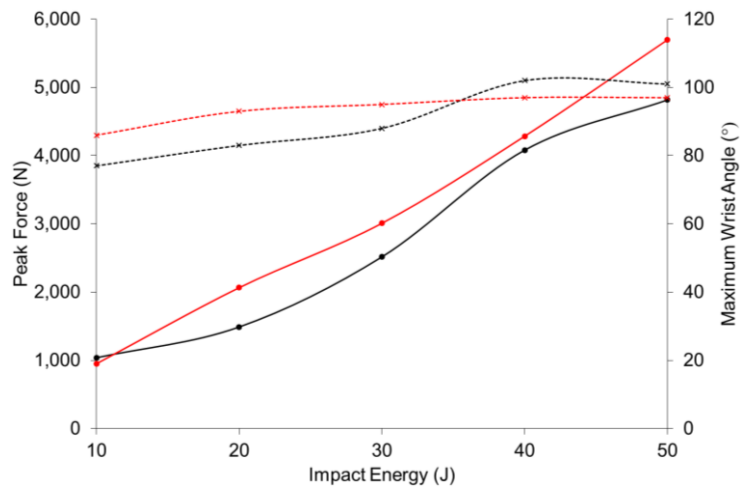
Figure 7-24 Comparison between experimental data and FE model for the long protector at 10 to 50 J in terms of a force vs. wrist angle trace.

7.4.6 Comparative Overview

The difference between the experiment (black line) and model (red line) for peak force and maximum wrist angle is shown in Figure 7-25a for the short protector and Figure 7-25b for the long protector. The overall mean difference across all energies was 9 and 18% for peak force, and 7 and 8% for maximum wrist angle (short and long protector respectively).



(a)



(b)

• Exp - Force • FE - Force x Exp - Angle x FE - Angle

Figure 7-25 Comparison of peak forces and maximum wrist angles for both the experiment and FE model at 10 to 50 J, (a) short protector and (b) long protector.

7.4.7 Sensitivity of the Model

Chapter 5 (Figure 5-10) showed the effect of the variance in stress vs. strain response on the material models and in turn the FE model response of the individual palmar components under impact. The softest and stiffest material models for the short protector palmar pad, long protector D3O® and supporting foam were trialled within the full wrist protector impact at 40 J, to understand the effect of this variability

(Figure 7-26). When modelling the stiffest short protector pad, peak force increased by 19% (740 N) and wrist angle increased by 5% (5°). Using the stiffest long protector D3O® material model increased peak force by 12% (527 N) and decreased maximum wrist angle by 1% (1°), while the stiffest supporting foam material model increased force by 12% (524 N) and decreased wrist angle by 1% (1°). Minimal differences were observed when the softest material models were simulated (1%, ~50 N) compared to the median sample used throughout the thesis, so this data was not presented.

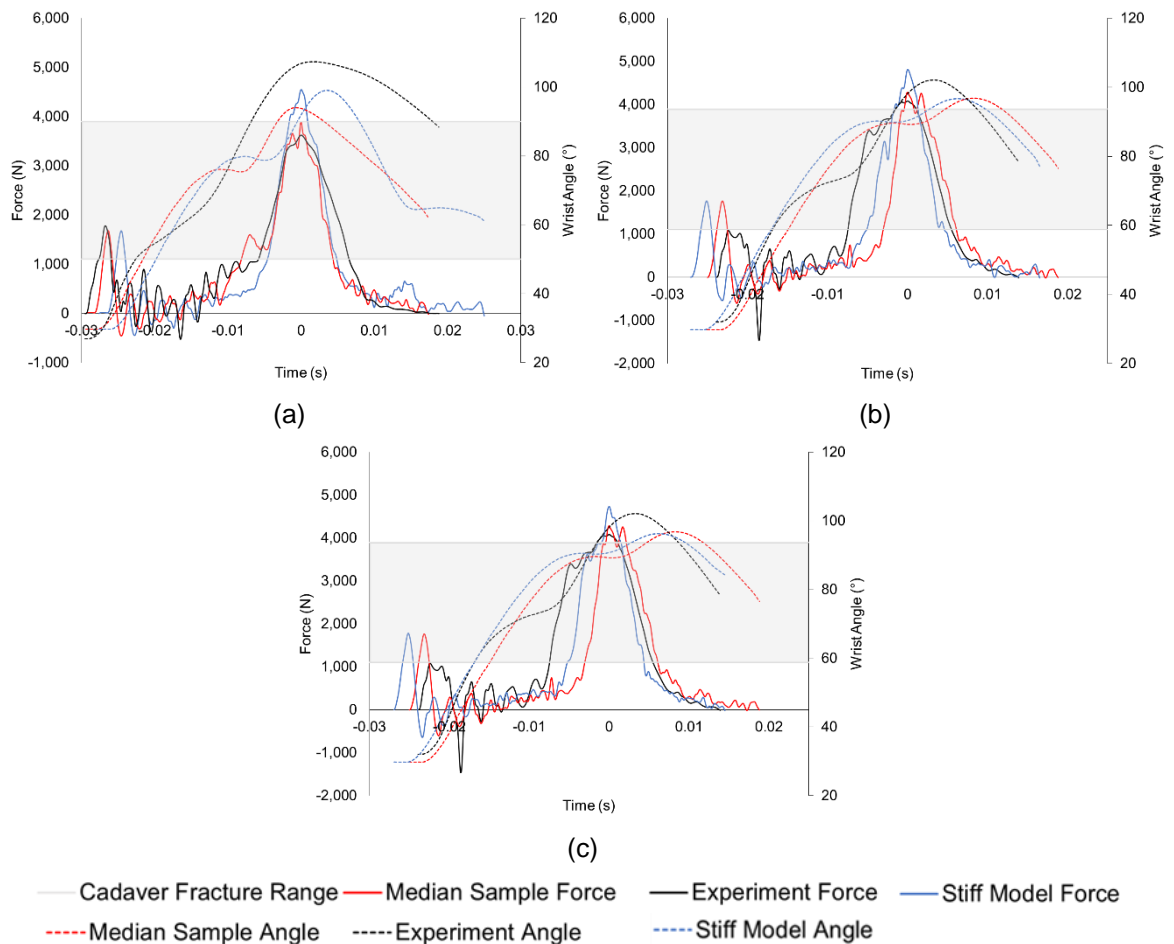


Figure 7-26 Temporal force traces of the full protectors impacted at 40 J, demonstrating the effect of using the stiffest material models from Chapter 5 for (a) short protector palmar pad, long protector (b) D3O® and (c) supporting foam.

The sensitivity of the FE model was also explored by reducing the Young's modulus of the splints by one standard deviation of the three point bend test results (0.12 GPa). This lowering of splint stiffness reduced peak force by 77 N (2%) and increased maximum wrist angle by 1° (1%), demonstrating that the model was not sensitive to small changes in splint material stiffness. The sensitivity of the model to changing the impact velocity of the impactor by $\pm 1\%$ ($0.02 \text{ rad}\cdot\text{s}^{-1}$, $0.03 \text{ m}\cdot\text{s}^{-1}$) was

also assessed. Increasing the impact velocity increased peak force by 150 N (~4%) and maximum wrist angle did not change.

7.5 Discussion

FE models of a bare hand, short protector and long protector impact were developed and compared to the experiment in Chapter 6. In both the experiment and model, peak force and maximum wrist angle (for protector models) increased with impact energy.

The polychloroprene material model established in Section 7.2 was able to replicate the behaviour of the polychloroprene impactor within a bare hand impact set up, across a range of energies in terms of temporal force relationships. Peak force from the model had an overall mean difference of 11% compared to the experiment across all energies, with the percentage difference increasing with the impact energy (5 to 19%). Impact duration was under predicted by an overall mean of 15% compared to the experiment.

When the short protector was modelled, temporal force traces were similar to those of the experiment. This included a small peak force on initial contact with the surrogate, followed by a period of low force as the wrist extended until peak force and maximum wrist angle were achieved. The modelling technique was seen to be transferable to a second wrist protector design (long protector), where the same trends were present, but the overall mean percentage difference between the experiment and model in terms of peak force and maximum wrist angle was higher (9 and 6% for the short protector vs. 18 and 8% for the long). Models for both protectors showed agreement with the experiment in terms of temporal force, as well as peak force and maximum wrist angle. However, there were clear differences in temporal wrist angle and in turn force vs. wrist angle traces.

Differences between the model and experiment could be due to a number of factors. Firstly, simplifications were made to the geometry of the protectors; the exterior fabric and the top strap of the short protector were not modelled as it was presumed that these would not influence the performance of the protectors. For simplification, the supporting foam was modelled as a continuous part, rather than four separate sections. The protector's geometry was created by measuring a physical protector and re-creating the parts in CAD. Using a scanning technique, similar to Mills and Gilchrist (2008) and Thoraval *et al.* (2013), could more accurately capture the

external geometry of the protector on the wrist surrogate, but it would not improve the internal geometry and fit.

Within the experiment, there was evidence that the surrogate deflected laterally under impact (Chapter 6, Figure 6-12). The model replicated this motion, but with less movement than the experiment (± 0.6 mm compared to -9.8 to 8.7 mm at 50 J). The differences seen between the experiment and model in terms of the temporal wrist angle trace could be partly due to the lower lateral deflection within the model.

It was presumed that the material models for the protector components (pad, D3O[®] and supporting foams) created and tested below 10 J on a rigid flat impact (Chapter 5) would be valid for a 50 J impact when modelled on a moving surrogate in new geometric forms. This was not the case for the short protector supporting foam, which required artificially stiffening, and the EVA in the long protector, which could not be characterised and was assigned material properties of the D3O[®], due to negative volume errors occurring. Chapter 4 highlighted that when all palmar components were impacted, there was a 19% variance between short protector samples and a 3% variance for long protector samples. As only one untested protector was impacted at each energy in Chapter 6, the variance in the full wrist protector impact is unknown and along with the material assumptions made, could explain the differences between the model and experiment.

Sensitivity analyses for parameters not measured experimentally were only performed at one impact energy (40 J), and the values selected may not have been applicable at the other energies (10 to 50 J). The extremities of the individual component material properties identified in Chapter 5 were simulated to analyse the variance within the model. The difference in results demonstrated that the material properties of the protector had an effect on the impact performance under impact, and should be further explored (Chapter 8). Future work could further explore the use of dynamic relaxation for applying the strapping pressure within the models, either through using a more powerful PC to reduce run time or alternatively it could be used when fewer protector designs were to be assessed and runtime may not be an issue.

7.6 Chapter Summary

FE models have been developed which replicate the experimental impact scenario from Chapter 6. When compared to the experiment, similar trends in data were seen between the FE models of bare hand impacts and two styles of wrist protectors across five energies. The bare hand was within 11%, the short protector was within 9% and the long protector was within 18% of the experiment, in terms of both peak force and maximum wrist angle. As the models level of accuracy and sensitivity have been quantified, they can now be used as a design tool. Chapter 8 will manipulate the splint designs of the two wrist protector models in terms of dimensions and materials to understand the effect of these changes on the impact performance. The splints were chosen for the design changes as Adams (2018) and Senner *et al.* (2019) both suggested that they had a large influence on impact performance.

8 FE Model Design Case Study

8.1 Introduction

Chapter 7 developed and validated FE models of wrist protector impacts when fitted to a wrist surrogate, replicating the experiment of Chapter 6. In this chapter, the validated models were used to investigate the effect of protector design changes on impact performance (Figure 8-1). The design of the splints were changed for both wrist protectors, in terms of their length, thickness and material. This chapter will address objective four of the thesis; to use the validated models to predict how design parameters influence the protection levels of wrist protectors.

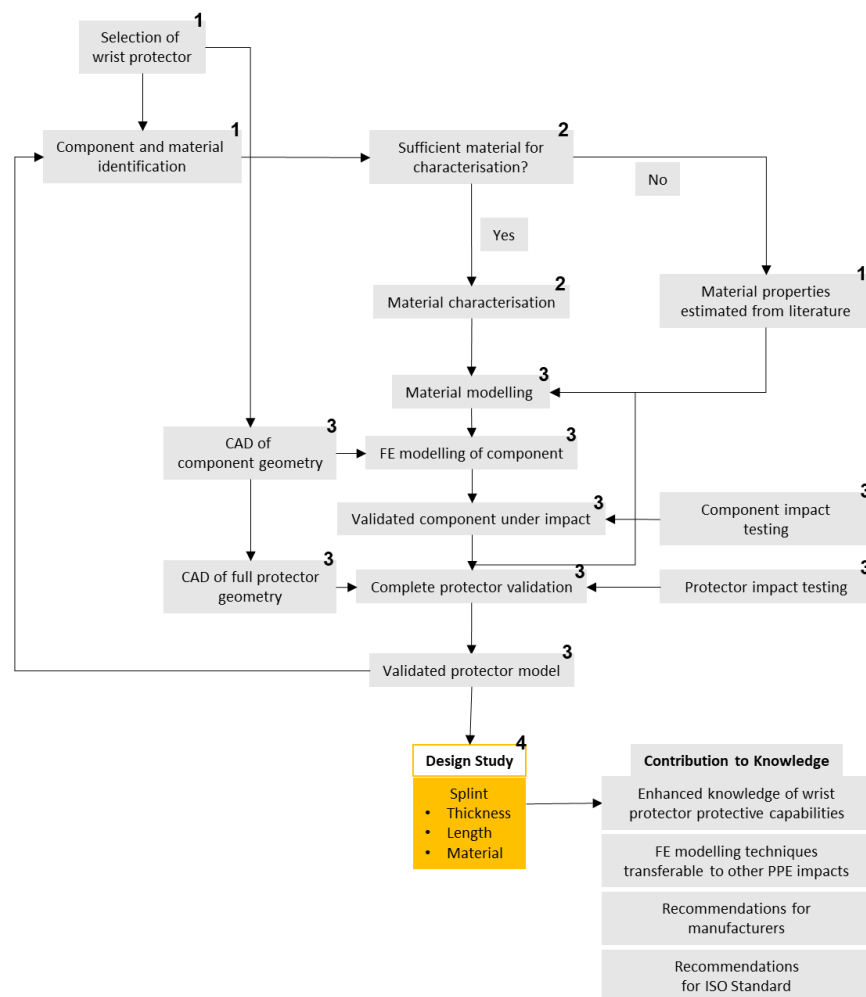


Figure 8-1 Schematic diagram indicating where this chapter (highlighted in yellow) fits within the overall project (numbers correlate to the objectives of the thesis).

8.2 Methodology

The models of the short and long protector were used to investigate the effect of design changes to the splints on impact performance. Protectors on the market (Chapter 3, Table 3-1) informed the design changes in terms of typical splint dimensions and materials. Protector designs were modelled, and simulated at

impact energies of 10 and 40 J. These energies were chosen as they gave the best match for peak force and maximum wrist angle (within a mean of 58 and 210 N and 7 and 9° for 10 and 40 J respectively for the two protectors) between the model and experiment in Chapter 7 (Figure 7-25).

Figure 8-2 and Figure 8-3 show the protector designs modelled, where splints were modified in terms of their length, thickness or material stiffness (Young's modulus). When splints were shortened the splint was cut, a section was removed and the remaining section retained its original form (Figure 8-2, 50 mm dorsal splint). When splints were lengthened, they were scaled along the x-axis (Figure 8-2, 224 mm dorsal splint).

Models had the same boundary conditions, analysis and mesh settings as described in Chapter 7.3. Material model parameters were also the same, except when splint material was assessed by changing Young's modulus. The splint materials explored included injection moulded plastics (0.03 to 1.8 GPa), stiffer polymers such as polyester or polymer-fibre composites (7 GPa) and aluminium (~70 GPa) (MatWeb, 2019b). When changing some parameters within the model, such as making the palmar splint of the short protector thicker or assigning the dorsal splints a Young's modulus of 70 GPa (aluminium), negative volume errors were returned, indicating that high forces were causing parts to "bottom out". Therefore, there are some missing data points in Figure 8-11 and Figure 8-12, corresponding to the models with negative volume errors, potentially limiting the strength of the statistical findings within this study.

The temporal support force (spcforc) in the x-axis was obtained for each simulation and filtered using the method described in Chapter 7.3. Wrist angle was obtained using the 3-node measurement also described in Chapter 7.3. Temporal force, temporal wrist angle and force vs. wrist angle traces were compared to determine the effect of design changes on the impact response of the protectors. Peak force and maximum wrist angle were compared for each design for both impact energies, and stress contour plots were compared at 40 J. The effect of manipulating the two wrist protectors (short and long) was assessed separately with overall findings discussed. A Pearson's coefficient (r) was computed to assess the relationship between the control parameter (e.g. splint length, thickness, and Young's modulus), peak force and maximum wrist angle.

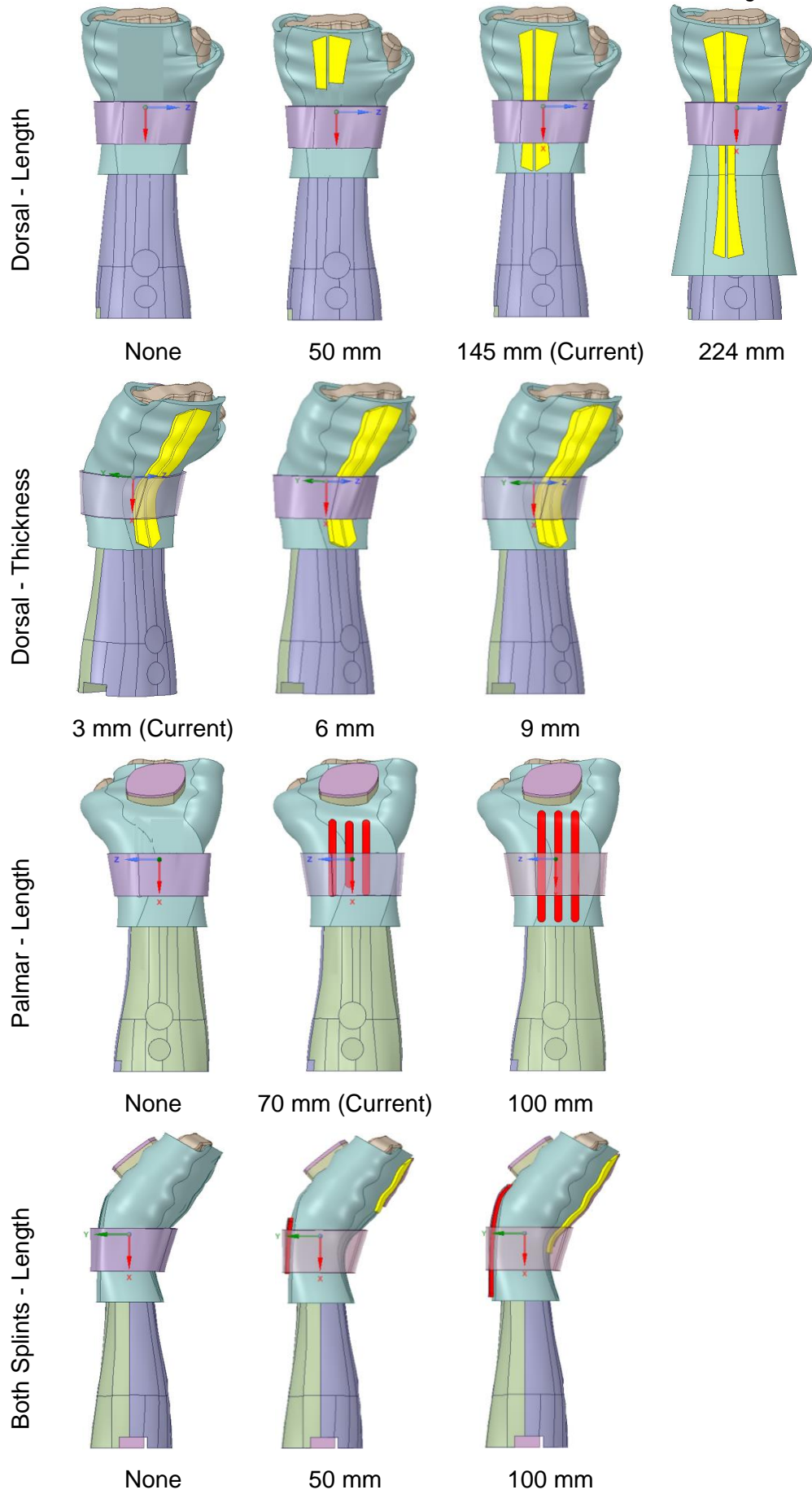


Figure 8-2 Different design iterations of the short protector model, simulated at 10 and 40 J to understand the effect of design changes on impact performance.

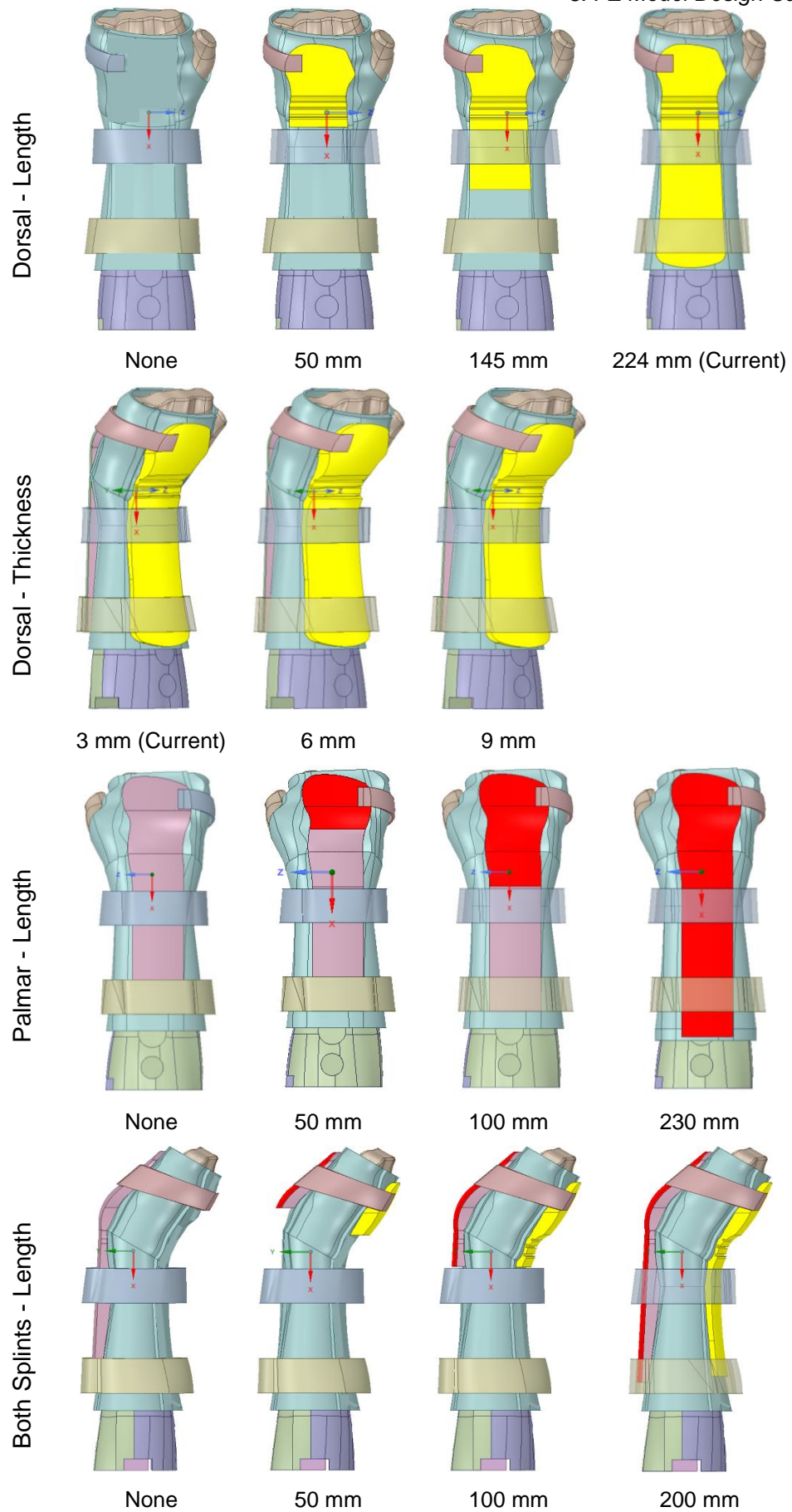


Figure 8-3 Different design iterations of the long protector model, simulated at 10 and 40 J to understand the effect of design changes on impact performance.

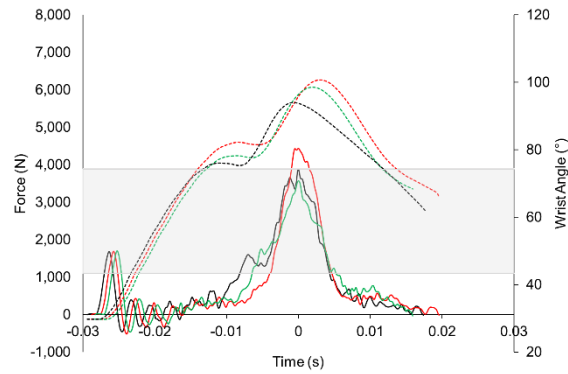
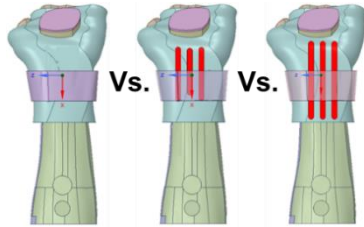
8.3 Results

8.3.1 Changes in Splint Length

Figure 8-4 and Figure 8-5 show the effect of changing splint length on temporal force, temporal wrist angle and force vs. wrist angle traces for both protectors at 40 J. When comparing both protectors with and without a palmar splint, the shapes of the traces did not change considerably (Figure 8-4a and Figure 8-5a), but peak force (~20% and ~44%) was reduced (short and long). For both protectors, changing the length of the dorsal splint had the largest effect on the shape of all the traces (temporal force, temporal wrist angle and force vs. wrist angle) (Figure 8-4b and Figure 8-5b). For the long protector, when modelled without a dorsal splint as compared to with a 224 mm dorsal splint, the temporal force changed from exhibiting two peaks to three; one on initial impact, one as the splint became engaged ($t = -0.0062$ s) and a third at peak force ($t = 0$ s). Increasing the dorsal splint from 0 to 224 mm increased maximum wrist angle by 8%, while peak force decreased by 57%. The equivalent comparison for the long protector showed a reduction in maximum wrist angle by 10% and a reduction in peak force by 25%.

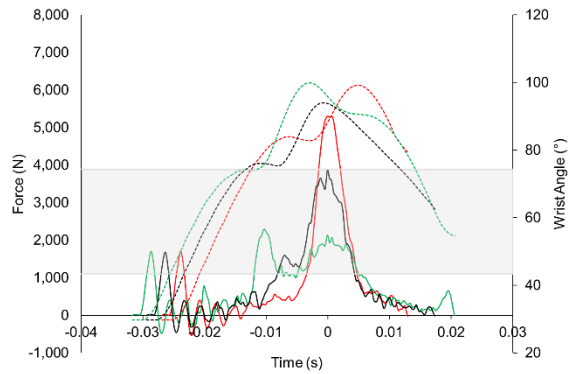
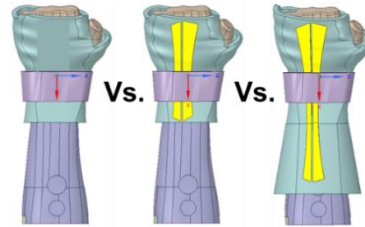
As palmar splint length increased, the angle the wrist extended to following initial impact, prior to the splint becoming engaged, became lower (Figure 8-4d and Figure 8-5d – gold x) (no palmar splint vs. 100 mm splint, ~76° vs. ~83° for the short and ~86° vs. ~94° for the long protector). The same effect was seen when increasing the length of the dorsal splint (Figure 8-4e and Figure 8-5e) (no dorsal splint vs. 224 mm splint, ~84° vs. ~74° for the short and ~105° vs. 85° for the long protector – gold x). Changing the length of both splints produced results akin to those for changing the palmar and dorsal splints individually (Figure 8-4 and Figure 8-5c and f).

No palmar splints vs. Original vs. 100 mm splints



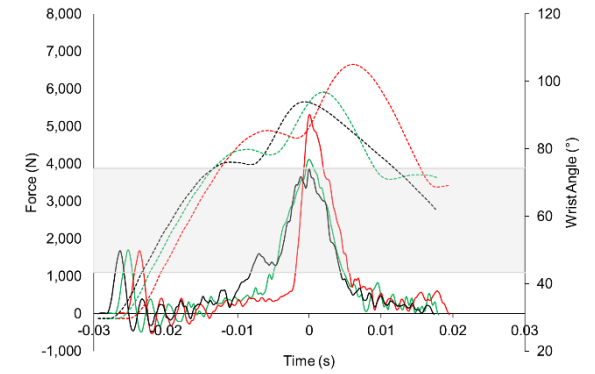
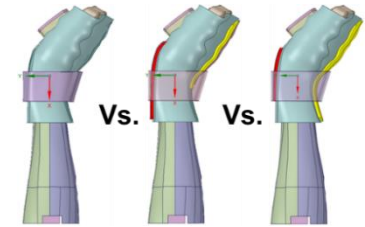
(a)

No dorsal splints vs. Original vs. 224 mm splints

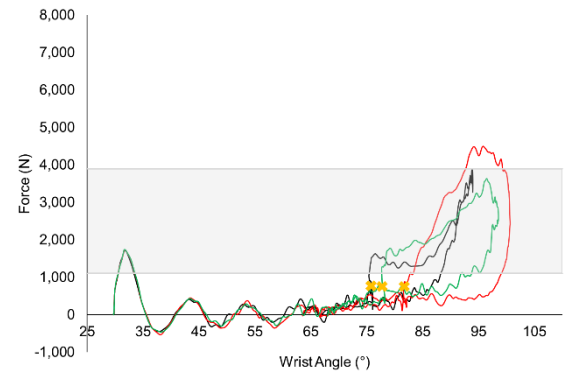


(b)

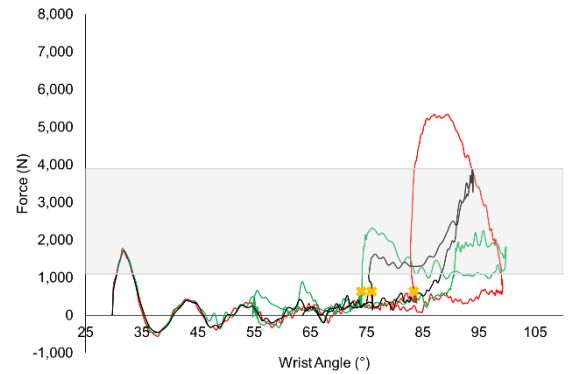
No splints vs. 100 mm splints vs. Original



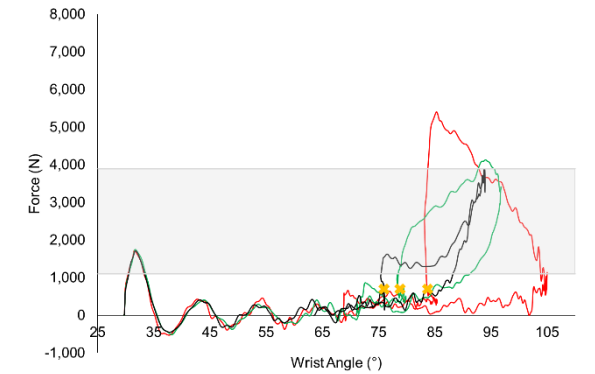
(c)



(d)



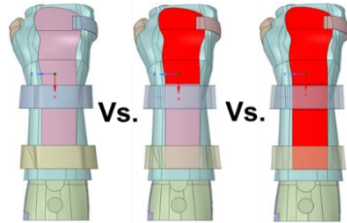
(e)



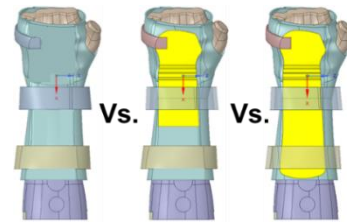
(f)

Figure 8-4 The effect of design changes regarding splint length on temporal force, temporal wrist angle and force vs. wrist angle traces for the short protector at 40 J.

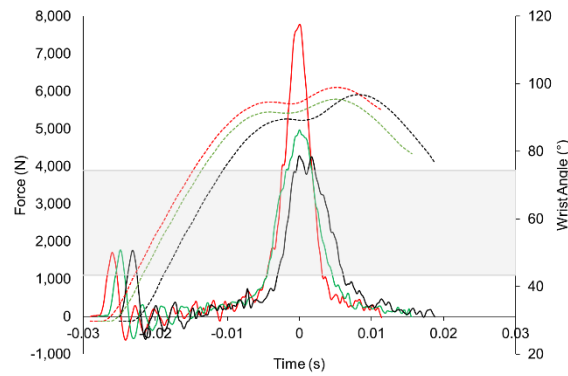
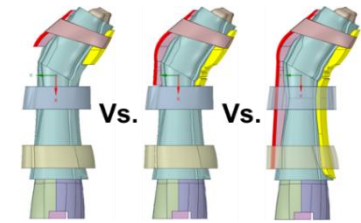
No palmar splint vs. 100 mm palmar vs. Original



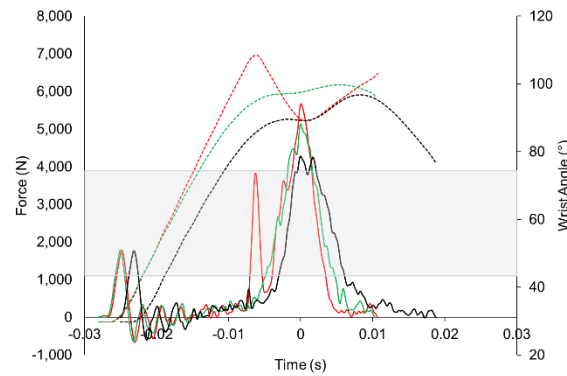
No dorsal splint vs. 145 mm dorsal vs. Original



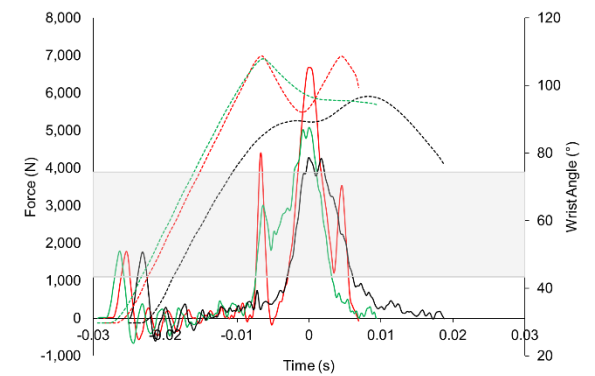
Both 50 mm vs. Both 100 mm vs. Original



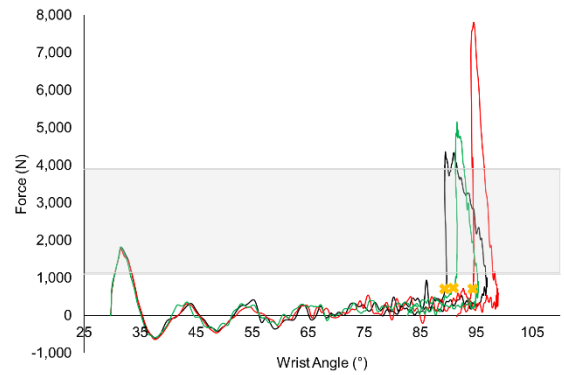
(a)



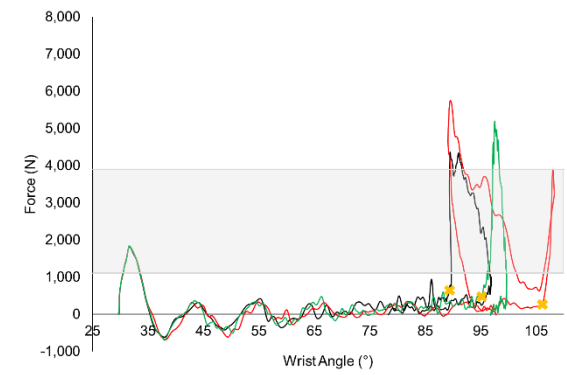
(b)



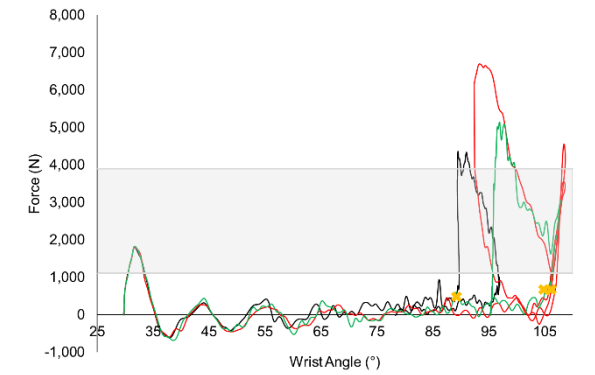
(c)



(d)



(e)



(f)

Figure 8-5 The effect of design changes regarding splint length on temporal force, temporal wrist angle and force vs. wrist angle traces for the long protector at 40 J.

When modelling the short protector with a 224 mm dorsal splint the force vs. wrist angle trace was quite different in shape to those for shorter splints (Figure 8-4e – green line). Figure 8-6 highlights the trace (red is the loading phase up to maximum wrist angle and green is the unloading phase) a sequence of images from the model to help to explain the force vs. wrist angle trace for the short protector with 224 mm dorsal splints. At 74°, the impactor struck the pad of the protector (a) and there was a clear increase in force (~2,350 N, b). The wrist then continued to extend, breaking contact with the impactor (c) with a decrease in force and a continued increase in wrist angle (d), up to maximum (e, 100°). The wrist then started to flex back towards its original position retaining contact with the impactor and generating peak force (f). Following peak force, the wrist continued to flex as the impactor rebounded off the protector (g and h). Similar force vs. wrist angle traces were seen when the short protector was modelled with a polymer-fibre composite (7 GPa) dorsal splint (Figure 8-7e), both splints as aluminium (70 GPa) (Figure 8-7f) and the dorsal splints were 9 mm thick (Figure 8-9a), for the reasons shown in Figure 8-6.

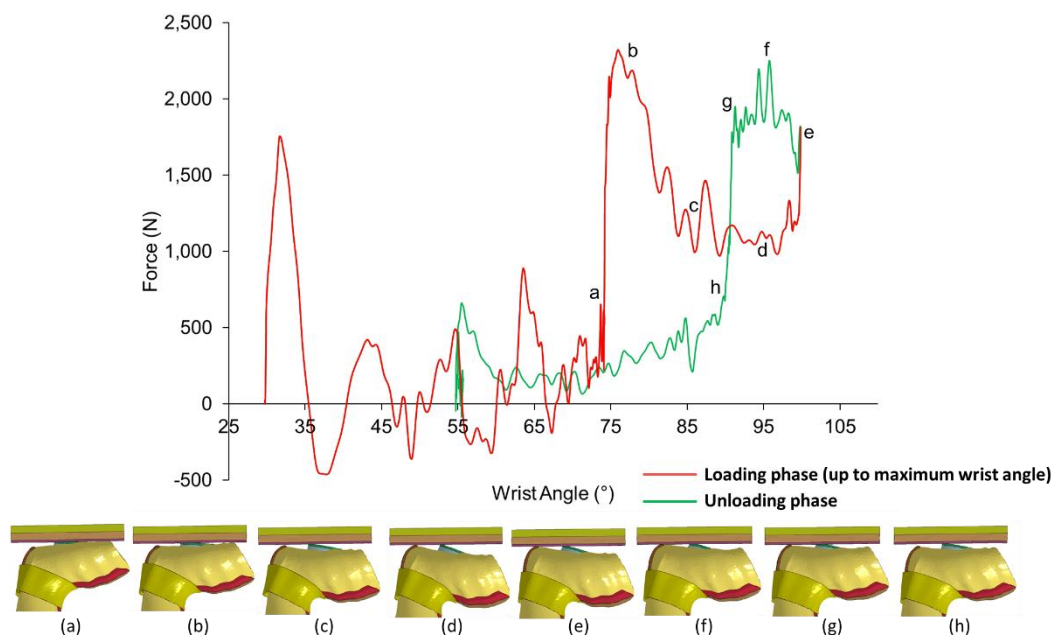


Figure 8-6 Force vs. wrist angle trace for the short protector model with 224 mm dorsal splints at 40 J. Highlighting the reason for the difference in the shape of the trace compared to other impact traces for shorter splints. Images are at 2 ms intervals from $t = -0.012$ to 0.002 s.

8.3.2 Changes in splint material

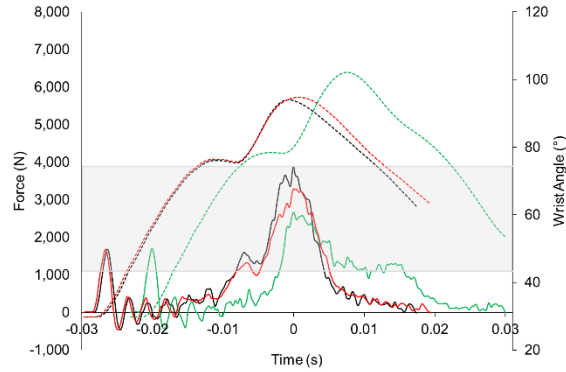
Figure 8-7 and Figure 8-8 show the affect of splint material on temporal force, temporal wrist angle and force vs. wrist angle traces for both protectors at 40 J. Splint material effected the shape of all the traces when the palmar, dorsal or both

splints were changed between a low stiffness injection moulded plastic, to a stiffer polymer-fibre composite or aluminium material.

When palmar splint stiffness was increased to simulate aluminium, peak force occurred at a lower wrist angle than when the palmar splint was an injection moulded plastic (0.03 GPa) (short protector $\sim 76^\circ$ vs. $\sim 95^\circ$, long protector $\sim 85^\circ$ vs. $\sim 88^\circ$) (Figure 8-7 and Figure 8-8a and d – gold x). For both protectors, peak force reduced when a stiffer splint, compared to its original material stiffness, was modelled (short: 0.47 GPa, long: 0.55 GPa), with a larger effect seen for the long protector (short protector 3,885 vs. 2,669 N, long protector 4,284 vs. 2,268 N). A low stiffness (0.03 GPa) dorsal splint for the long protector provided less resistance to wrist extension, meaning motion was continuous from initiation until maximum angle (Figure 8-8b – red line). A stiffer dorsal splint (7 GPa) provided higher resistance, meaning wrist extension was less continuous and more abrupt (Figure 8-8b – green line). The opposite effect was seen when changing the stiffness of the long protector palmar splints, where a stiffer (70 GPa) splint provided less resistance to wrist extension compared to a low stiffness (0.03 GPa) palmar splint (Figure 8-8a).

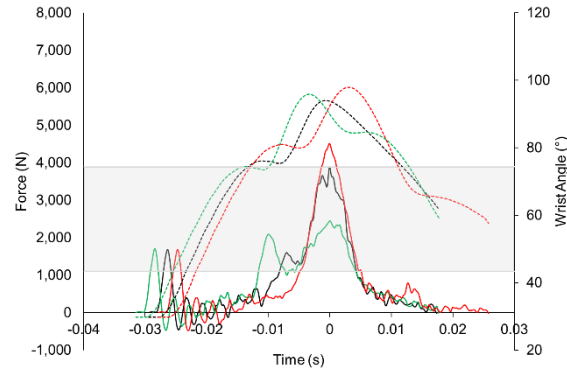
For both protectors, simulating a polymer-fibre composite (7 GPa) dorsal splint reduced peak force compared to their original lower stiffness dorsal splints (short: 0.47 GPa, long: 0.55 GPa) (short protector 3,885 vs. 2,448 N and long protector 4,284 vs. 3,432 N) (Figure 8-7 and Figure 8-8b and e). Increasing the stiffness of the dorsal splint to represent a polymer-fibre composite (7 GPa) for both protectors also reduced the wrist angle at peak force, compared to when modelling the original splint stiffness (short protector $\sim 90^\circ$ vs. 94° , long protector $\sim 80^\circ$ vs. 90°). Increasing the stiffness of both splints (to aluminium for the short and to a polymer-fibre composite for the long protector) from their original stiffness, reduced peak force and maximum wrist angle (short protector 3,885 vs. 2,948 N and 94° vs. 88° , long protector 4,284 vs. 2,585 N and 97° vs. 92°) (Figure 8-7 and Figure 8-8c and f).

Palmar splints 0.03 GPa vs. 0.47 GPa (Original)
vs. 70 GPa



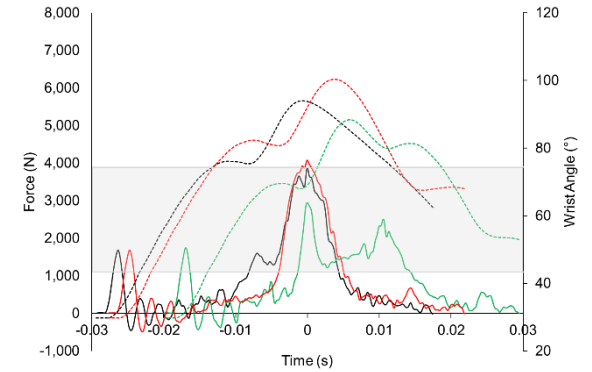
(a)

Dorsal splints 0.03GPa vs. 0.47 GPa (Original)
vs. 7 GPa

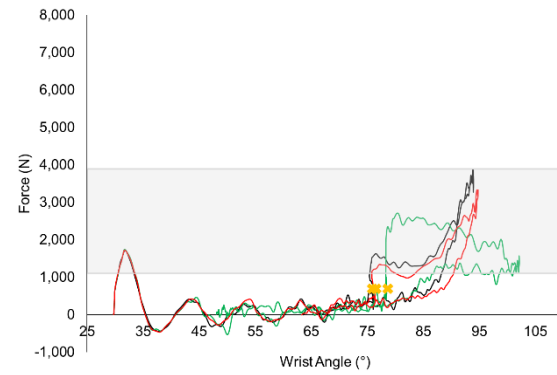


(b)

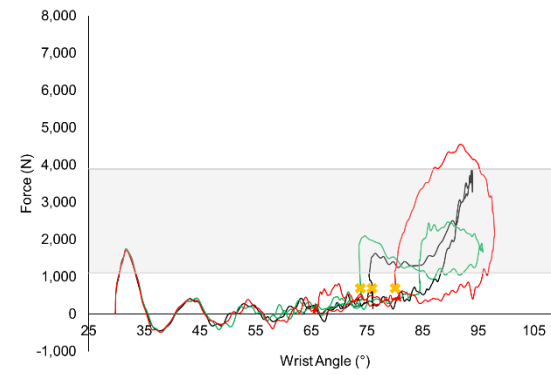
Both splints 0.03 GPa vs. 0.47 GPa (Original)
vs. 70 GPa



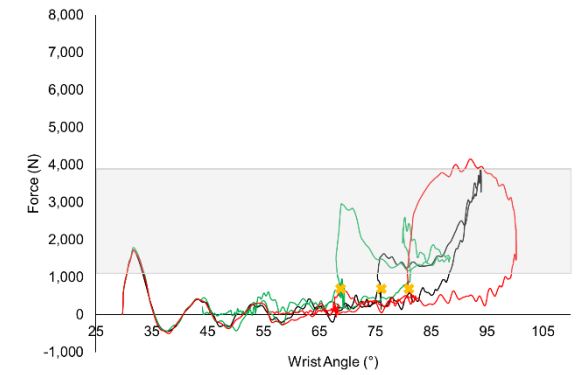
(c)



(d)



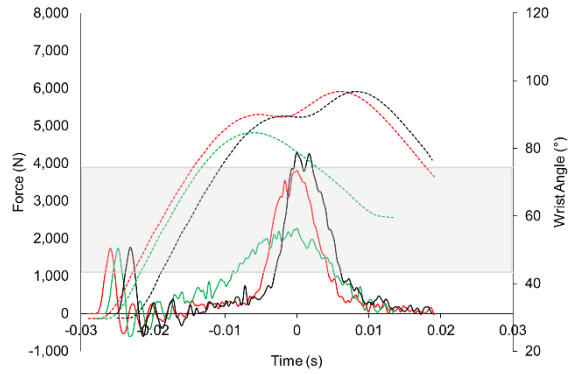
(e)



(f)

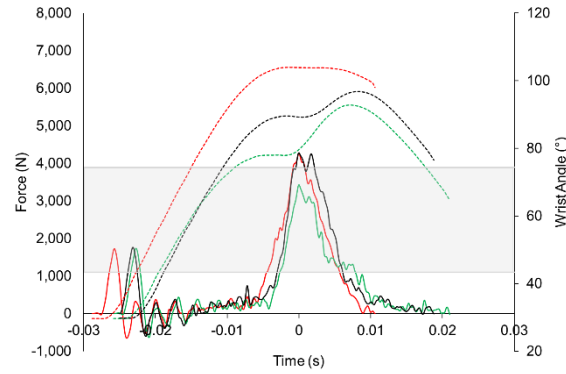
Figure 8-7 The effect of design changes regarding splint material on temporal force, temporal wrist angle and force vs. wrist angle traces for the short protector at 40 J.

**Palmar splints 0.03 GPa vs. 0.55 GPa
(Original) vs. 70 GPa**



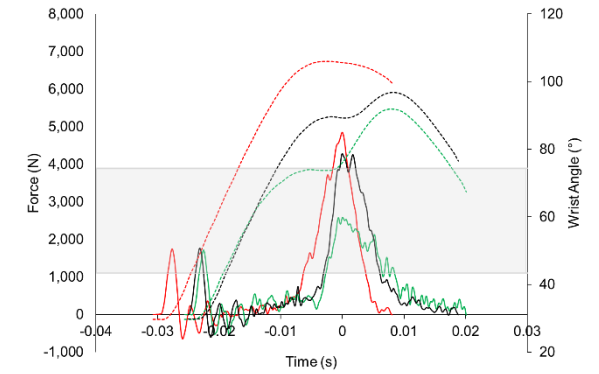
(a)

**Dorsal splints 0.03 GPa vs. 0.55 GPa (Original)
vs. 7 GPa**

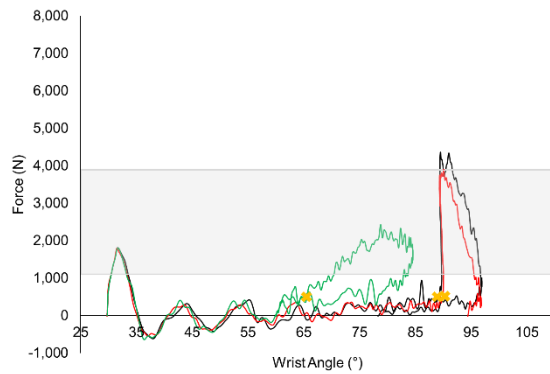


(b)

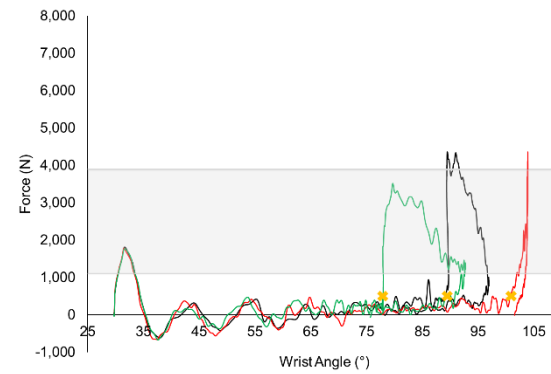
**Both splints 0.03 GPa vs. 0.55 GPa (Original)
vs. 7 GPa**



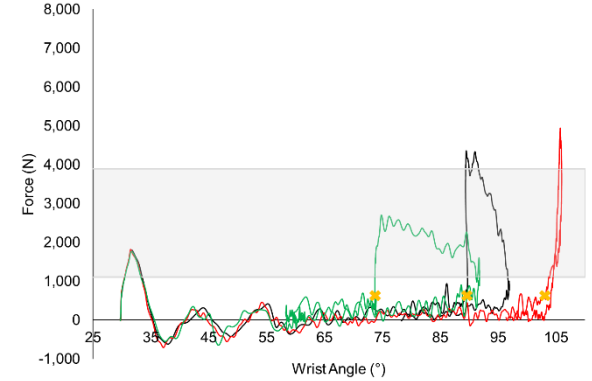
(c)



(d)



(e)



(f)

Figure 8-8 The effect of design changes regarding splint material on temporal force, temporal wrist angle and force vs. wrist angle traces for the long protector at 40 J.

8.3.3 Changes in Splint Thickness

Figure 8-9 shows the effect of changing dorsal splint thickness on temporal force, temporal wrist angle and force vs. wrist angle traces for both protectors at 40 J. Increasing splint thickness had a similar effect to changing the stiffness of the splint material, where a thicker splint reduced peak force and maximum wrist angle. For both protectors, peak force was reduced with a thicker dorsal splint particularly for the short protector (short protector 5,303 vs. 2,270 N, long protector 5,674 vs. 3,313 N) (Figure 8-9a and b). Increasing the thickness of the dorsal splint changed the shape of all traces. When the thickness of the dorsal splint was increased from 3 to 9 mm, peak force occurred at a reduced angle (short protector $\sim 88^\circ$ vs. $\sim 86^\circ$, long protector $\sim 89^\circ$ vs. $\sim 78^\circ$) (Figure 8-9c and d, gold x).

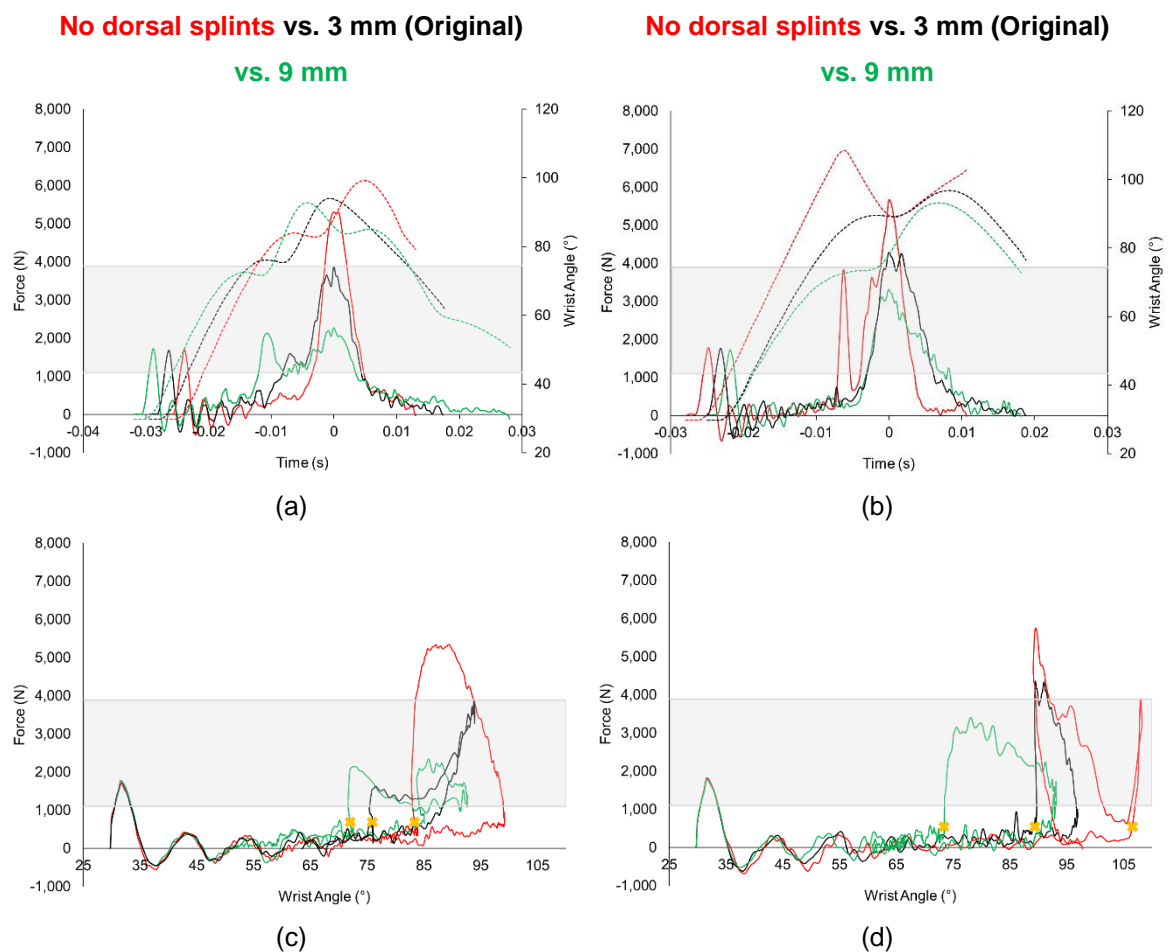


Figure 8-9 The effect of design changes regarding dorsal splint thickness on temporal force, temporal wrist angle traces (a) short and (b) long protector and force vs. wrist angle traces (c) short and (d) long protector concept at 40 J.

8.3.4 Summary of Results

As splint length or stiffness increased (through either increased thickness or material stiffness), peak force and maximum wrist angle tended to decrease (Figure 8-11 and Figure 8-12), with some exceptions. When the length of the short protector splints were changed for a 10 J impact peak force barely changed (Figure 8-11a), and maximum wrist angle increased with the palmar splint material stiffness for the short protector at 40 J (Figure 8-11g). There were relationships seen in Figure 8-11 and Figure 8-12 that were significant when analysed by a Pearson's correlation, as highlighted in Table 8-1. Stress contour plots (effective von Mises stress) for the surrogate wrist were obtained from the models at peak force to further investigate the results at 40 J (Figure 8-10). Stress contours could not be obtained for the hand as it was modelled as a rigid material (*MAT_RIGID), (hence the 0 Pa stress in Figure 8-10), so stress at the top of the central support was investigated and shown in Figure 8-11 and Figure 8-12.

The region of stress at the top of the central support tended to reduce as splint length and material stiffness increased, for both protectors. Small and low areas of stress were particularly seen for the short protector when the dorsal splint was modelled as 224 mm or with a polymer-fibre composite splint (7 GPa) or the palmar splint was aluminium (70 GPa). For the long protector, small and low areas of stress were also seen when modelling the dorsal splint or both splints as a polymer-fibre composite (7 GPa) or the dorsal splint with 9 mm of thickness.

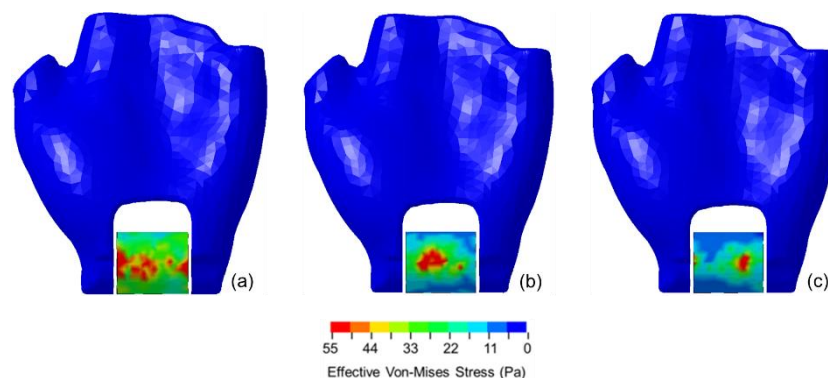


Figure 8-10 Example stress contour plots for the long protector at 40 J when changing the length of the palmar splint (a) no splint, (b) 100 mm and (c) 230 mm.

Table 8-1 Pearson's *r* matrix for all the relationships shown in Figure 8-11 and Figure 8-12, with significant relationships denoted by bold and * ($p < 0.05$).

40 J					
Control Parameter		Peak Force		Maximum Wrist Angle	
		Short	Long	Short	Long
Dorsal	Length	-0.98*	-0.94	0.29	-0.99*
	Stiffness (Y.M.)	-0.97*	-0.63	-0.09	-0.66
Palmar	Length	-1.00*	-0.66	-0.49	-0.50
	Stiffness (Y.M.)	-0.84	-0.95*	0.89*	-0.97*
Both	Length	0.78	0.37	-0.87	-0.97
	Stiffness (Y.M.)	-0.88	-0.93	-0.87	-0.69
10 J					
Dorsal	Length	0.90	-0.99*	-0.78	-0.98*
	Stiffness (Y.M.)	0.61	-0.43	-0.80	-0.65
Palmar	Length	0.99	0.01	-0.91	-0.47
	Stiffness (Y.M.)	0.99*	-0.25	-0.72	-0.84
Both	Length	0.78	0.37	-0.87	-0.97
	Stiffness (Y.M.)	0.37	-0.37	-0.78	-0.68

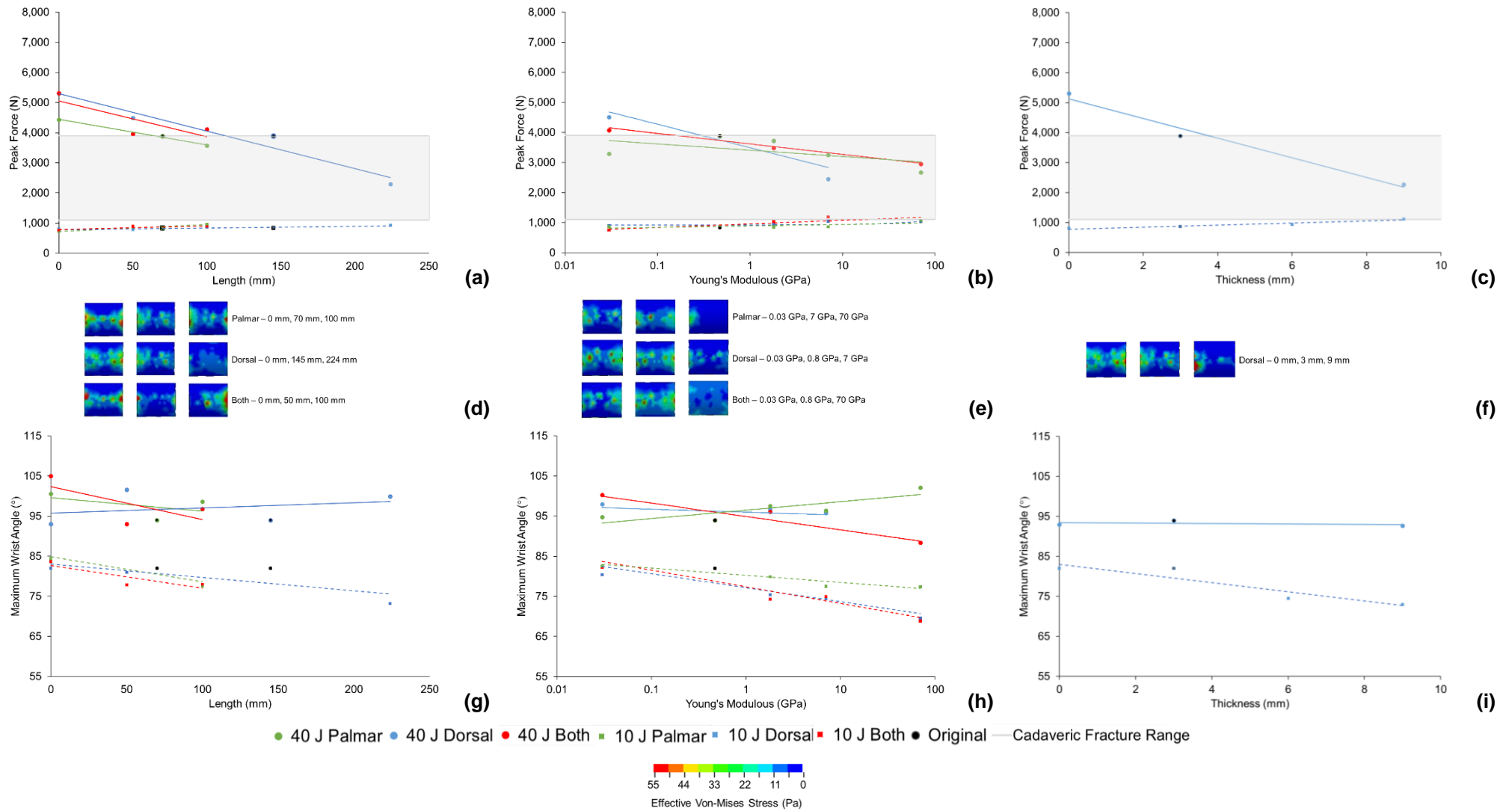


Figure 8-11 Effect of changing the splint (a) length, (b) material and (c) thickness on peak force for the short protector with respective stress contour plots at 40 J (d, e and f). The effect of changing the same three parameters on maximum wrist angle in (g), (h) and (i).

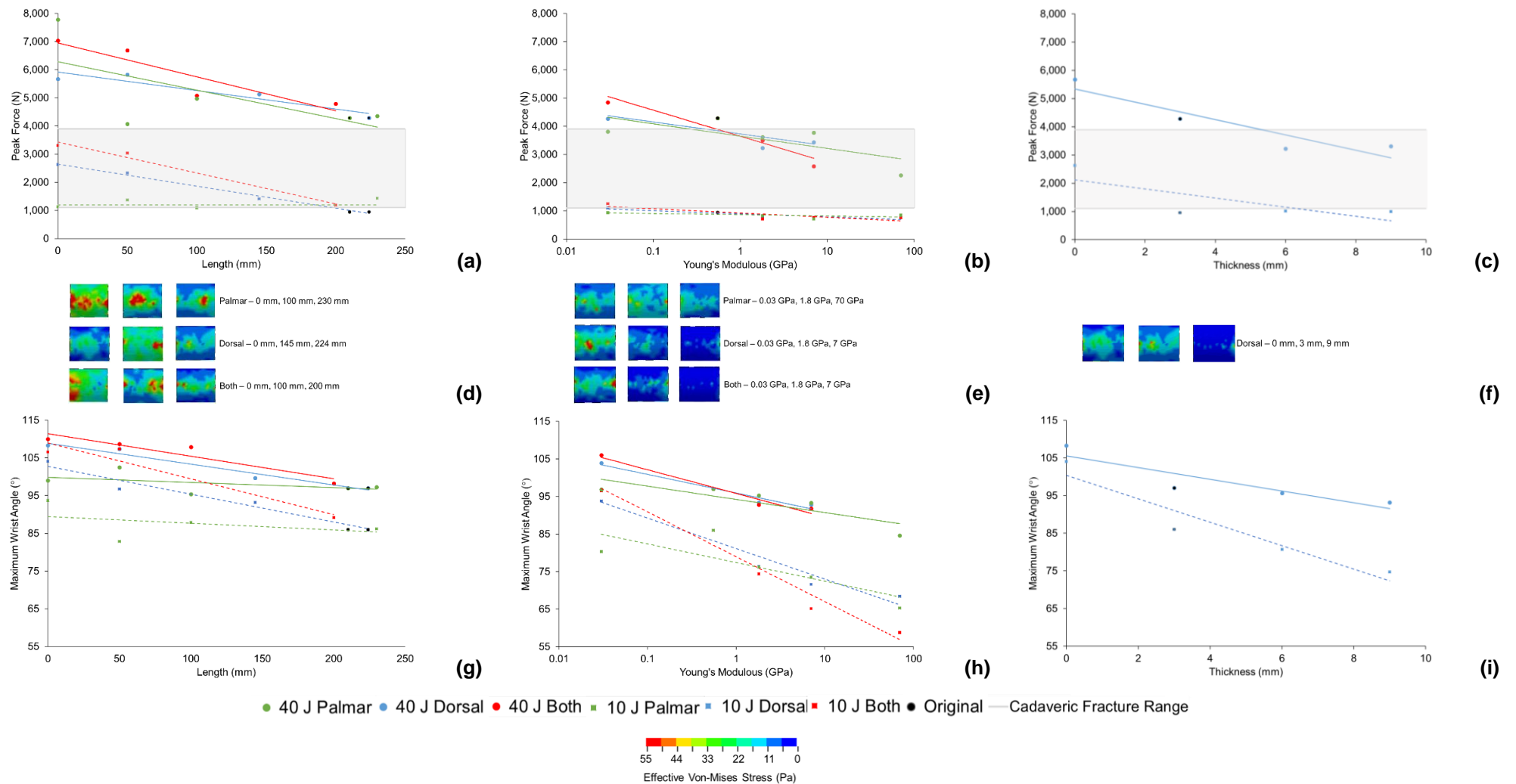


Figure 8-12 Effect of changing the splint (a) length, (b) material and (c) thickness on peak force for the long protector with respective stress contour plots at 40 J (d, e and f). The effect of changing the same three parameters on maximum wrist angle in (g), (h) and (i).

8.4 Discussion

Geometric and material composition of splints was found to affect the impact performance of the wrist protectors. As splint length or stiffness increased (through either increased thickness or material stiffness), peak force and maximum wrist angle decreased. In terms of correlations between protector input parameters and peak force, some trends were significant, including dorsal and palmar splint length and material at 40 J (total of 6), while maximum wrist angle saw fewer significant relationships (total of 4). The lack of significance in the maximum wrist angle trends could be due to the model not accurately capturing this parameter, as clear differences were seen between the experiment and the model in Chapter 7.

Ronning *et al.* (2001) suggested that splint position in wrist protectors can affect impact performance, which is supported by the findings from this study. When no splints were modelled, peak force was reduced by a mean of 25% compared to an unprotected scenario, indicating that the other components of the protector offered some cushioning of impact (37% short and 16% long protector). When either the dorsal or palmar splint were modelled in isolation (100 mm in length), peak force was reduced more by having a palmar splint (mean of 35% vs. 27%). These findings support the suggestion by Michel *et al.* (2013) that the primary role of the dorsal splint is to provide stability to the wrist and prevent hyperextension, while the palmar splint distributes impact forces. It also supports the findings of Hwang and Kim (2004) who found that the dorsal splint had a secondary role in absorbing impact energy in addition to preventing hyperextension.

As dorsal splint length increased there was a significant decrease in peak force at 40 J, complementing the findings of Wadsworth *et al.* (2012), Adams (2018) and Senner *et al.* (2019). Dickson and Terwiel (2011) found that the likelihood of sustaining a wrist fracture was greater when a short palm-side only protector was worn compared to a long dorsal or both sided protector, in agreement with findings presented here. Increasing the length of the palmar or both splints to 100 mm had the largest effect on reducing peak force compared to changing the length of the dorsal splints to 100 mm (18% dorsal, 28% palmar, 25% both). Maximum wrist angle was reduced furthest when the length of the dorsal, or both, splints were increased, compared to when increasing the length of the palmar splint (4% dorsal, 3% palmar, 5% both).

Previous studies have not isolated the splint material within a protector to determine the effect of changing this parameter, so the results of this design study cannot be compared to the literature. The study showed that increasing the stiffness of the splint material to 7 GPa (polymer-fibre composite or stiff plastic) from 0.03 GPa (plastic) decreased peak force and maximum wrist angle. Changing the material of the dorsal or both splints to 7 GPa had the greatest effect on reducing peak force compared to changing the dorsal splint length (33% dorsal, 1% palmar, 37% both) and maximum wrist angle (6% dorsal, 3% palmar, 12% both). The minimal effect of changing the palmar splint material stiffness on peak force could be due to it primarily acting to compress the palmar padding to spread impact force rather than bending to resist wrist extension, a similar effect to when the HDPE shell was added on top of the palmar pad in Chapter 4.

When impact testing wrist protectors, Adams (2018) found that those with thicker dorsal splints had lower peak force with a longer time to peak. This study returned similar findings for splint thickness, in terms of a reduction in peak force but not time to peak. Due to the low range of splint thicknesses on the market and hence investigated (2 to 8 mm – dorsal and 2 to 4 mm – palmar) relationships between splint thickness and peak force or maximum wrist angle were inconclusive. However, changing the thickness of the splints appeared to have a similar effect to changing the material stiffness.

From the results in this study and the previous experimental chapter (6), it could be suggested that between the two commercially available protectors tested, the long protector provides a better impact performance. The reasons being that, experimentally there was less degradation, greater energy absorption and through the model it is suggested that longer splints reduce peak force and maximum wrist angle. It could also be suggested based on this study, that to improve the short protector concept, longer splints could be trialled, or stiffer splint materials could also be another alternative to increase the impact performance.

A limitation of the design study was the range of parameters chosen being narrow as they were based on a pool of protectors currently on the market (Chapter 3, Table 3-1). In turn, this meant the effect of some changes, such as splint thickness, were not fully understood. Also, the design changes were only based on the two wrist protector models from Chapter 7. While the original models of the two protectors

were validated (Chapter 6), the predicted results for the design changes were not validated experimentally.

Following the study presented in this chapter, the splints material properties within the two protectors modelled in Chapter 7 could have been optimised to give results that better match those of the experiment, especially in terms of temporal angles and consequently the force vs. wrist angle traces. Proposals for modifications include the short protector being modelled with lower stiffness dorsal splints and the long protector with both splints stiffer, through changes to the Young's modulus.

8.5 Chapter Summary

Validated FE models from Chapter 7 have been used to investigate changes to the splints, in terms of length, thickness and material. The effect of changing splint parameters was explored by comparing temporal force, temporal wrist angle and force vs. wrist angle traces, as well as peak forces and maximum wrist angles. It was found that the roles of the dorsal splint are to prevent hyperextension and absorb impact energy, and the role of the palmar splint is to distribute impact forces, supporting previous literature. Trends within the data also showed that as splint length or stiffness (thickness or material) increased, peak force and maximum wrist angle decreased. This study showed that the models created could be manipulated in their design to understand the impact performance of snowboard wrist protectors in greater detail. The models have also allowed the effect of individual parameters within a protector concept to be understood. Chapter 9 will reflect on the whole thesis, highlighting the findings and limitations of the PhD, as well as making suggestions for future work.

9 Conclusions and Future Research

9.1 Introduction

The aim of this thesis was to develop an FE model for predicting the impact performance of snowboard wrist protectors. Models were developed and validated by comparison against experimental data. Materials from two protectors were characterised and used to model the components under impact. The models of the components were developed into full protectors fitted to a wrist surrogate and subject to impact (Figure 9-1). The validated models were used to explore the influence of changing the splint length, thickness and material on impact performance. Changes to the splints were compared in terms of temporal force, temporal wrist angle and force vs. wrist angle traces, as well as peak force and maximum wrist angle. This chapter highlights how the objectives of the study have been met, the strengths and limitations to the methods and the novelty of the findings. Recommendations for future work are proposed.

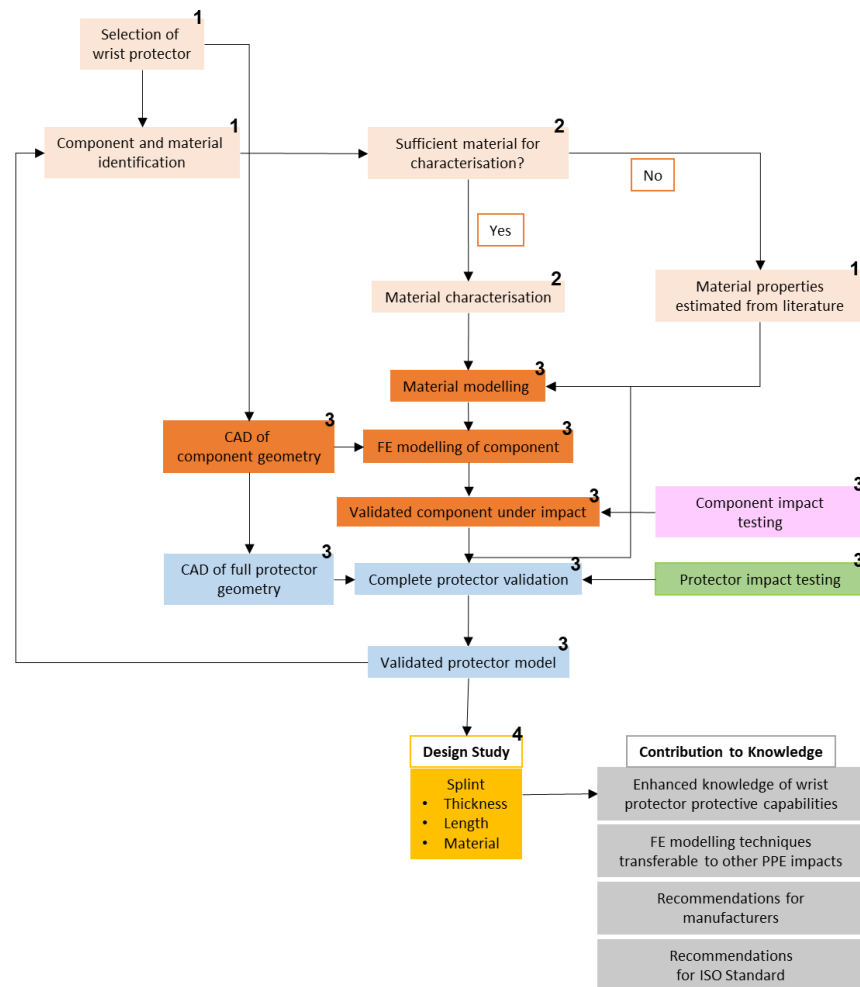


Figure 9-1 Schematic diagram highlighting the content of the thesis (numbers correlate to the objectives of the thesis).

9.2 Summary of Research – Findings, Limitations, Novelty and Future Work

A literature review identified that wrist and forearm injuries are the most prevalent in snowboarding, with beginners and adolescents being the most vulnerable. Wrist injuries are mainly due to a compressive load applied to a hyperextended wrist, resulting in distal radius fractures. To reduce the risk of sustaining wrist injuries while snowboarding, wearing wrist protectors is recommended by snowsport injury experts. Current knowledge on the effectiveness of snowboard wrist protectors is limited, however, and it is unclear as to whether a particular design is more effective, which could be due to the lack of a standard for these products. Wrist protectors reduce the risk and severity of injury by limiting wrist hyperextension and impact forces, spreading them over a longer time to absorb impact energy. Based on current knowledge of wrist injury mechanics and the associated loads, wrist protectors should aim to limit forces transmitted to the wrist below a range of 1,100 to 3,900 N, while preventing wrist extension from exceeding $\sim 70^\circ$.

There has been a large body of research concerning injury rates and severity in snowboarding injury epidemiology, the biomechanics of falls and mechanical testing (using cadavers and surrogates/anvils) identifying the protective capabilities of wrist protectors. There have also been previous studies developing FE models of protectors, however, there are gaps in the research recreating the geometry and materials of wrist protectors, considering all components nor recreating a representative way of fitting the wrist protector to the surrogate. Taking these shortcomings into account the objectives were developed for this thesis.

9.2.1 Objective 1

Objective one was to identify the main components and materials of the contemporary snowboard wrist protectors. A pool of protectors representative of those sold in the UK plus further designs selected in conjunction with the ISO standard working group were chosen. The protective components and materials of the wrist protector were identified from visual inspection and information on websites and product labels. Two wrist protectors were examined in detail through deconstruction and Fourier Transform Infrared Spectroscopy (FT-IR) to help further determine the construction materials.

The two wrist protectors chosen for modelling had palmar and dorsal splints. The long protector had palmar padding consisting of a layer of EVA and D3O[®] under the

palmar splint, which was made of high impact polypropylene and a supporting polybutylene terephthalate foam. For the short protector, the palmar padding was identified as polyurethane foam and the splints were high-density polyethylene. The FT-IR libraries within the university (Thermo Scientific™ Aldrich™ Collection of FT-IR Spectra Edition II and PerkinElmer® Polymers ATR Starter Library), were unable to match three of the materials from the protectors, but they were identified from information on their packaging as D3O®, acrylonitrile butadiene rubber and a soft gel. Future work could repeat the tests on a machine with a larger material library or alternatively seek a different technique such as Raman spectroscopy (Vaskova, 2010). As wrist protectors are used over a wide range of temperatures, Differential Scanning Calorimetry (DSC) based techniques could also be explored to understand the thermal properties of the polymer splints and padding materials (Drzeżdżon *et al.*, 2019). Limitations to this study are that deconstruction and FT-IR was only performed on two protectors and some materials were not identified.

Adams (2018) conducted online market research identifying the types of wrist protectors on the market and their construction, including dimensions of the splints and palmar padding components. However, to the author's knowledge, this is the first study that has identified the materials of components within wrist protectors, both through a combination of market research and FT-IR.

9.2.2 Objective 2

Objective two was to characterise the material properties of the main components of snowboard wrist protectors. The two protectors were deconstructed and where possible compression and tensile test samples were extracted from the component materials. Compression, tensile and stress relaxation testing was performed on the wrist protector materials at strains up to 50% and strain rates up to 2 s^{-1} . Three point bend tests were also conducted on the splints.

All compression samples demonstrated hyperelastic and rate dependent characteristics, reflecting the findings from previous research for similar materials (Cecere *et al.*, 1990; Neilsen *et al.*, 1995; Degrange *et al.*, 2005; Lu, 2014; Mane *et al.*, 2017; D3O, 2019). The experimental 3-point bend test results, when compared to hand calculations for uniform beams, fell within the expected range of elastic modulus. Five samples were tested from the same size/brand protector from the right hand. Intra-sample repeatability was high for the five samples (mean percentage variance $5 \pm 5\%$), but inter-sample repeatability was low (mean

percentage variance $16 \pm 10\%$), with some being significantly different from each other.

There is a lack of knowledge as to the strain and strain rates within wrist protector materials during snowboarding falls, and future work could look to quantify these values. Characterising materials at high strains and strain rates is challenging using the Hounsfield HK10S or Instron® available within the university due to the machine limits in terms of crosshead speed, and future work could explore other material characterisation devices and techniques. For high strain rates, this could be through DMA (Menard and Menard, 2006; Price *et al.*, 2008), a split-Hopkinson pressure bar (Marais *et al.*, 2004) or time-temperature superposition (Schwarzl and Staverman, 1952). Characterising materials at both high strains and strain rates remains a challenge (Burbank and Smith, 2012).

Within this study, materials were only characterised at room temperature. Snowboard wrist protectors may also be required to perform whilst cold, especially those worn on the outside of the glove. Future work could characterise the materials and impact test the protectors at lower temperatures, like Signetti *et al.* (2018) when testing snowsport back protectors. Standards for snow-sport equipment could be a starting point for selecting temperatures at which to characterise the materials, with the draft for wrist protectors (ISO/DIS 20320) and ski goggles (BS EN 174:2001) specifying room temperature and -10°C and helmets for alpine skiers and snowboarders (BS EN 1077:2007) specifying room temperature and -25°C . Future work could also look at the possible effects of the interactions between the materials within the protector and incorporate these into the model, especially as a reductionist approach was taken within this project, so this aspect was not considered.

The techniques used within this study are commonly used in sports engineering, however, to the author's knowledge objective two is novel and contributes to research as the first time materials from snowboard wrist protectors have been characterised. It is also the first time samples of the same brand/size protector have been tested and compared, highlighting inconsistencies and reiterating the need for a standard for these products.

9.2.3 Objective 3

Objective three was to develop and validate FE models of snowboard wrist protectors for simulating hand/surface impacts. The compression samples used for material characterisation were impact tested at energies up to 6.0 J, both individually and combined as a palmar padding unit. FE models replicating the impact tests on the material samples were created and compared to the experimental results to quantify their accuracy. The material characterisation data was used to select appropriate material model algorithms to replicate the different behaviours of the materials. The most common material models chosen were a linear elastic model and a hyperelastic model (Mooney-Rivlin and Ogden) paired with a Prony series.

The FE models were developed into full wrist protectors fitted to a wrist surrogate, with impact simulated for energies between 10 to 50 J. The two styles of protector were impact tested for comparison against the model, using a modified version of the pendulum rig of Adams (2018). Peak force and maximum wrist angle increased with impact energy for the protectors in both the experiment and models. There were clear differences in results for both material and protector impact testing between samples, indicating variability in the products that posed challenges for modelling and validation. There was also evidence of degradation of the short protector from repeated impacts. The models were therefore compared against the first experimental impact at each energy.

There was a significant difference between a bare hand and a protector impact across all energies, no matter the design of protector, complementing the findings of others (Lewis *et al.*, 1997; Kim *et al.*, 2006; Burkhart and Andrews, 2010; Adams, 2018). Peak force was not always lowered below the range of 1,104 to 3,896 N reported for cadaveric fractures when a protector was fitted to the surrogate. Models for both protector impacts showed agreement with the experiment in terms of temporal and peak force (9% difference - short and 18% difference – long, RMSE of 363 N – short and 529 N – long). There were clear differences between the model and experiment for temporal wrist angles and in turn force vs. wrist angle traces, despite maximum wrist angle values falling within 6 and 8% (short and long protector respectively).

Limitations to the experimental aspects of this study include; both the anvil and drop mass being metal plates in the individual component testing and the wrist surrogate being rigid in the wrist protector testing. The wrist surrogate also has zero resistance

which is not very realistic of the human wrist joint. When replicating an impact involving a human, a bio-fidelic anvil/surrogate (including soft tissue, muscle and skin simulants) should ideally be used (Pain *et al.*, 2008; Payne *et al.*, 2015b; Petrone *et al.*, 2019). Future work could explore incorporating more biomechanically reflective motions of the wrist during a fall, as well as increasing the bio-fidelity of the wrist surrogate. The current study used the impact rig of Adams (2018) which incorporated the use of polychloroprene on the impactor for the full protector impact experiment. Future work could develop the rig and explore alternative materials for polychloroprene that may better replicate the impact properties of snow and ice.

The selection of parameters, such as the mass, velocity, energy and orientation of the impactor and surrogate is also a limitation to this study. There is a lack of data and knowledge of injury mechanisms and loads, such as the typical forces and wrist angles causing distal radius fractures during snowboarding falls. Future work could look to further understanding of injury mechanisms and loads for wrist fractures amongst snowboarders. Once wrist injury mechanisms are better understood, experimental protocols (and models) could be developed to be more representative of real fall scenarios.

A limitation to the modelling aspect of this study was the simplifications to the protector geometries within the CAD replica, such as modelling the supporting foam as a continuous part rather than separate meshes and foams. The short protector supporting foam had to be artificially stiffened for the full protector, reinforcing the need to characterise the materials at higher strain rates. To improve the match between the model and experiment other material models could be explored.

The experimental testing conducted was novel by enhancing a previous technique (Adams, 2018) and being one of the first to identify an impact energy where wrist protectors reduced force below a cadaveric wrist fracture threshold (10 J). This is, however, only applicable to the experimental setup used and may not be transferable to all scenarios. In addition, to the author's knowledge this was the first test to compare an untested protector to a previously impacted protector to assess degradation, with implications for certification and product lifespan. There was evidence that repeated impact reduced the performance of the protectors, although this was limited to the set up used and future work could explore this finding further in other scenarios. The largest contribution to scientific knowledge from objective three was the creation of an FE model of a wrist protector fitted to a surrogate that

accurately captures the geometry, materials and fit of the protector, and simulates its performance under impact, however this is still at a hypothesis stage as some parameters needed to be tuned.

9.2.4 Objective 4

Objective four was to use the validated models to predict how design parameters influenced the protection levels of wrist protectors. The models of the short and long protector were modified in terms of splint design (length, thickness and material). By changing one splint parameter within the model at a time, individual design affects were analysed. Splint manipulation was based on protectors on the market (as identified in objective one) and the different designs were simulated at impact energies of 10 and 40 J. The effect of design changes was assessed by comparing the full impact response, as well as peak force and maximum wrist angle.

The geometric and material composition of the splints affected the impact performance of the wrist protectors, trends in data showed that an increase in splint length or stiffness (through either increased thickness or material stiffness) decreased peak force and maximum wrist angle. When either the dorsal or palmar splint were modelled in isolation (100 mm in length), peak force was reduced more by having a palmar splint (mean of 35% vs. 27%). This finding supports the suggestion by Michel *et al.* (2013) that the primary role of the dorsal splint is to provide stability to the wrist by avoiding hyperextension, and the palmar splint, to distribute impact forces.

Limitations of this study include the design changes being limited to the splints of two protectors. The parameters chosen spanned a limited range meaning the influence of some changes were not fully understood, such as splint thickness. Future work could model more iterations of the protectors, or model other protectors. The model could also be developed to incorporate gloves, as they are commonly worn over wrist protectors.

While the models of the two wrist protectors were validated against an experiment, the findings of this design study have not been confirmed experimentally. Future work could prototype the design concepts and test them experimentally to check the model's accuracy, followed by further developments to the model as required. This iterative approach could be developed into a tool for improving the design of wrist protectors. Such a tool could also be adapted to sit alongside the new ISO standard

(once published) to predict whether new wrist protector designs would fulfil certification requirements (International Organisation for Standardisation, 2018).

Many studies have found no association between wrist protector use and an increased risk of other injuries, although some studies claim that wrist protectors transfer the impact from the forearm and wrist to the elbow and shoulder (Chow *et al.*, 1996; Hagel *et al.*, 2005). This study has not considered this force transfer as the wrist surrogate used only included the hand and forearm. Future work could check these claims, developing the experiment and model to include an upper arm and shoulder section.

Future research could focus on increasing the use of wrist protectors amongst snowboarders; with studies highlighting the main reason for low usage was a lack of perceived need (Langran, 2004; Kroncke *et al.*, 2007; Dickson, 2008; Dickson and Terwiel, 2011; Chaudhry *et al.*, 2012). Chaudhry *et al.* (2012) claim that over 75% of snowboarders would wear wrist protectors if provided with strong evidence of a reduced risk of injury. This thesis has provided more evidence to show that wrist protectors reduce the risk of injuries, but more research is needed as outlined above. Along with the implementation of the standard, infographics displayed throughout ski schools and resorts as well as adding wrist protectors to rental packages could increase awareness and usage. Discomfort was the second most common reason for lack of wrist protector usage, which this study has not considered and future work could factor comfort into design studies.

Splint length or palmar padding thickness were investigated by Senner *et al.* (2019), however, before now material changes have not been considered. Objective four has provided scientific evidence to support theories within the literature as to the roles of the palmar and dorsal splints, which could enhance future protector designs.

9.3 Overall Conclusions

This thesis developed an FE model for predicting the impact performance of snowboard wrist protectors, which was compared against experimental data to quantify its accuracy. The validated models have been used to explore the influence of changing splint properties on the impact performance to enhance the understanding of wrist protector design. The findings of this research can provide scientific evidence for both the development of an ISO standard and for manufacturers in terms of wrist protector design. The project has also developed the knowledge of FE modelling techniques that could be applied to other sport equipment, PPE and other types of wrist protectors, such as those for the elderly population.

References

- Adams, C. (2018) *Evaluating the performance of snowboard wrist protectors*. Doctor of Philosophy. Sheffield Hallam University.
- Adams, C., James, D., Senior, T., Allen, T. and Hamilton, N. (2016) 'Development of a new method for measuring quasi-static stiffness of snowboard wrist protectors.' *In ISEA 2016 - The engineering of sport 11*. Delft, Netherlands, 11-14 July.
- Adams, C., James, D., Senior, T., Allen, T. and Hamilton, N. (2018) 'Effect of surrogate design on the measured stiffness of snowboarding wrist protectors.' *Sports Engineering*, pp. 1-9.
- Addison, B. J. and Lieberman, D. E. (2015) 'Tradeoffs between impact loading rate, vertical impulse and effective mass for walkers and heel strike runners wearing footwear of varying stiffness.' *Journal of Biomechanics*, 48 pp. 1318-1324.
- Allen, T., Haake, S. and Goodwill, S. (2009) 'Comparison of a finite element model of a tennis racket to experimental data.' *Sports Engineering*, 12(2) pp. 87-98.
- Andena, L., Aleo, S., Caimmi, F., Briatico-Vangosa, F., Mariani, S., Tagliabue, S. and Pavan, A. (2018) 'Modelling the cushioning properties of athletic tracks.' *Sports Engineering*, 21(4) pp. 453-463.
- Ankrah, S. and Mills, N. J. (2003) 'Performance of football shin guards for direct stud impacts.' *Sports Engineering*, 6 pp. 207-220.
- Ankrah, S. and Mills, N. J. (2004) 'Analysis of ankle protection in Association football.' *Sports Engineering*, 7 pp. 41-52.
- Ansys. (2015) 'ANSYS Mechanical Advanced Nonlinear Materials, Appendix 4A: Hyperelasticity.' [Online] [Accessed on 10th January 2019]
- Ansys. (2018) 'ANSYS Workbench' Version 18.2. [Software] [Accessed on 10th September 2019]
- ASTM. (2016) Standard test methods for flexural properties of Unreinforced and reinforced plastics and electrical insulating materials. Vol. D790 - 15, pp. 1-12.
- Augat, P., Reeb, H. and Claes, L. E. (1996) 'Prediction of fracture load at different skeletal sites by geometric properties of cortical shell.' *Journal of Bone and Mineral Research*, 11 pp. 1356-1363.

- Augat, P., Iida, H., Jiang, Y., Diao, E. and Genant, H. K. (1998) 'Distal Radius Fractures: Mechanisms of Injury and Strength Prediction by Bone Mineral Assessment.' *Journal of Orthopaedic Research*, 16(5) pp. 629-635.
- Balakrishnan, K., Sharma, A. and Ali, R. (2017) 'Comparison of Explicit and Implicit Finite element methods and its effectiveness for drop test of electronic control unit.' *In 11th International Symposium on Plasticity and Impact Mechanics, Implast 2016*. Vol. 173. New Delhi, India, Gupta, N. K. e. a. (ed.): Procedia Engineering, pp. 424-431.
- Basques, B. A., Gardner, E. C., Samuel, A. M., Webb, M. L., Lukasiewicz, A. M., Bohl, D. D. and Grauer, J. N. (2018) 'Injury patterns and risk factors for orthopaedic trauma from snowboarding and skiing: a national perspective.' *Knee surgery, sports traumatology, arthroscopy*, 26(7) pp. 1916-1926.
- Bladin, C., Giddings, P. and Robinson, M. (1993) 'Australian snowboard injury data base study.' *The American Journal of Sports Medicine*, 21(5) pp. 701-704.
- Bladin, C., McCrory, P. and Pogorzelski, A. (2004) 'Snowboarding Injuries Current Trends and Future Directions.' *Sports Med*, 34(2) pp. 133-139.
- Blau, P.J., 2008. Friction science and technology: from concepts to applications. CRC press.
- Boone, D. C. and Azen, S. P. (1979) 'Normal range of motion of joints in male subjects.' *The Journal of Bone and Joint Surgery*, 61 pp. 756-759.
- Boreflex Ltd. (no date) *Technical Data Sheet - Soft Neoprene Rubber WCM123*.
- Bower, A. F. (2009) *Applied Mechanics of Solids*. 1st ed.: CRC Press.
- British Standards Institution. (2003) *BS EN 14120:2003+A1:2007 Protective clothing. Wrist, palm, knee and elbow protectors for users of roller sports equipment. Requirements and test methods*. Milton Keynes: BSI.
- Brizard, D., Ronel, S. and Jacquelin, E. (2017) 'Estimating measurement uncertainty on stress-strain curves from SHPB.' *Experimental Mechanics*, 57(5) pp. 735-742.
- Brolin, K. and Wass, J. (2016) 'Explicit finite element methods for equestrian applications.' *Procedia Engineering*, 147 pp. 275-280.
- Burbank, S. and Smith, L. (2012) 'Dynamic characterisation of rigid foam used in finite element sports ball simulations.' *Proceedings of the Institution of Mechanical Engineers, Part P: Journal of Sports Engineering and Technology*, 226(2) pp. 77-85.

Burkhart, T. and Andrews, D. M. (2010) 'The effectiveness of wrist guards for reducing wrist and elbow accelerations resulting from simulated forward falls.' *Journal of applied Biomechanics*, 26(3) pp. 281-289.

Burkhart, T. A. (2012) *Biomechanics of the Upper Extremity in Response to Dynamic Impact Loading Indicative of a Forward Fall: An Experimental and Numerical Investigation*. PhD. University of Windsor, Ontario, Canada.

Burkhart, T. A., Andrews, D. M. and Dunning, C. E. (2012) 'Failure characteristics of the isolated distal radius in response to dynamic impact loading.' *J Orthop Res*, 30(6), Jun, pp. 885-892.

Burkhart, T. A., Andrews, D. M. and Dunning, C. E. (2013) 'Finite element modeling mesh quality, energy balance and validation methods: a review with recommendations associated with the modeling of bone tissue.' *J Biomech*, 46(9), May 31, pp. 1477-1488.

Cecere, A., Greco, R., Ragosta, G., Scarinzi, G. and Tagliatalatela, A. (1990) 'Rubber toughened polybutylene terephthalate: influence of processing on morphology and impact properties.' *Polymer*, 31(7) pp. 1239-1244.

Celina, M., Wise, J., Ottesen, D. K., Gillen, K. T. and Clough, R. L. (2000) 'Correlation of chemical and mechanical property changes during oxidative degradation of neoprene.' *Polymer Degradation and Stability*, 68(2) pp. 171-184.

Chaudhry, T., Noor, S. and Rajaratnam, V. (2012) 'Factors affecting wrist guard use amongst snowboarders.' *European Orthopaedics and Traumatology*, 3(4) pp. 247-250.

Chow, T. K., Corbett, S. W. and Farstad, D. J. (1996) 'Spectrum of Injuries from Snowboarding.' *The Journal of Trauma: Injury, Infection and Critical Care*, 41(2) pp. 321-325.

Cifuentes, A. O. and Kalbag, A. (1992) 'A performance study of tetrahedral and hexahedral elements in 3-D finite element structural analysis.' *Finite Elements in Analysis and Design*, 12 pp. 313-318.

Coto, N. P., Meira, J. B., Brito e Dias, R., Driemeier, L., de Oliveira Roveri, G. and Noritomi, P. Y. (2012) 'Assessment of nose protector for sport activities: finite element analysis.' *Dent Traumatol*, 28(2), Apr, pp. 108-113.

Coury, T., Napoli, A. M., Wilson, M., Daniels, J., Murray, R. and Milzman, D. (2013) 'Injury patterns in recreational alpine skiing and snowboarding at a mountainside clinic.' *Wilderness & environmental medicine*, 24(4) pp. 417-421.

- Cross, R. (2014) 'Impact of sports balls with striking implements.' *Sports Engineering*, 17(1) pp. 3-22.
- D3O. (2019) *Materials - D3O*. Cogent Elliott. [Online] [Accessed on 2nd July 2019] <https://www.d3o.com/what-is-d3o/materials/>
- Darling, T., Muthuswamy, J. and Rajan, S. D. (2016) 'Finite Element modeling of human brain response to football helmet impacts.' *Computer Methods in Biomechanics and Biomedical Engineering*, 19(13) pp. 1432-1442.
- Davis, J. R. (2004) *Tensile Testing*. 2nd ed.: ASM International.
- de Roulet, A., Inaba, K., Strumwasser, A., Chouliaras, K., Lam, L., Benjamin, E., Grabo, D. and Demetriades, D. (2017) 'Severe injuries associated with skiing and snowboarding: A national trauma data bank study.' *Journal of trauma and acute care surgery*, 82(4) pp. 781-786.
- Deady, L. H. and Salonen, D. (2010) 'Skiing and snowboarding injuries: a review with a focus on mechanism of injury.' *Radiologic Clinics*, 48 pp. 1113-1124.
- DeGoede, K. M. and Ashton-Miller, J. A. (2002) 'Fall arrest strategy affects peak hand impact force in a forward fall. .' *Journal of biomechanics*, 35 pp. 843-848.
- DeGoede, K. M. and Ashton-Miller, J. A. (2003) 'Biomechanical simulations of forward fall arrests: effects of upper extremity arrest strategy, gender and aging-related declines in muscle strength.' *Journal of Biomechanics*, 36(3) pp. 413-420.
- DeGoede, K. M., Ashton-Miller, J. A. and Schultz, A. B. (2003) 'Fall-related upper body injuries in the older adult: a review of the biomechanical issues.' *Journal of Biomechanics*, 36(7) pp. 1043-1053.
- Degrange, J., Thomine, M., Kapsa, P., Pelletier, J., Chazeau, L., Vigier, G., Dudragne, G. and Guerge, L. (2005) 'Influence of viscoelasticity on the tribological behaviour of carbon black filled nitrile rubber (NBR) for lip seal application.' *In Wear*. Vol. 259: Elsevier, pp. 684-692.
- Derler, S., Spierings, A. B. and Schmitt, K.-U. (2005) 'Anatomical hip model for the mechanical testing of hip protectors.' *Medical Engineering & Physics*, 27 pp. 475-485.
- Descartes, R., 2017. *Discourse on the Method of Rightly Conducting one's Reason and Seeking Truth in the Sciences*.
- Diani, J., Fayolle, B. and Gilormini, P. (2009) 'A review on the Mullins effect.' *European Polymer Journal*, 45(3) pp. 601-612.

Dickson, Gray, T., Downey, G., Saunders, J. and Newman, C. (2008) 'Profiling Australian snowsport injuries: A snapshot from the Snowy Mountains.' *Journal of sport and tourism*, 13 pp. 273-295.

Dickson, T. (2008) 'Behaviors and attitudes towards snowsport safety in Australia.' *Journal of ASTM International*, 5(4) pp. 65-72.

Dickson, T. and Terwiel, F. A. (2011) 'Snowboarding injuries in Australia: investigating risk factors in wrist fractures to enhance injury prevention strategies.' *Wilderness and Environmental Medicine*, 22(3) pp. 228-235.

Direct Plastic Ltd. (no date) 'Polypropylene Natural - Material Data Sheet.' *Direct Plastics*. p. 1. [Online] [Accessed 14th January 2018] <https://www.directplastics.co.uk/pub/pdf/datasheets/Polypropylene%20Natural%20Data%20Sheet.pdf>

Drzeżdżon, J., Jacewicz, D., Sielicka, A. and Chmurzynski, L. (2019) 'Characterization of polymers based on differential scanning calorimetry based techniques.' *Trends in Analytical Chemistry*, 110 pp. 51-56.

Duma, S. M., Boggess, B. M., Crandall, J. R. and MacMahon, C. B. (2003) 'Injury risk function for the small female wrist in axial loading.' *Accident Analysis & Prevention*, 35(6) pp. 869-875.

DuPont. (2017) *Material Data - Data Table*. [Online] [Accessed on 10th January 2019] <https://dupont.materialdatacenter.com/profiler/B0Ejv/>

Englander, F., Hodson, T. J. and Terregrossa, R. A. (1996) 'Economic dimensions of slip and fall injuries.' *Journal of Forensic Science*, 41(5) pp. 733-746.

Fasanella, E. L. and Jackson, K. E. (2002) *Best Practices for crash modelling and simulation*. Langley Research Center, Hampton, Virginia.

Frykman, G. (1967) 'Fracture of the Distal Radius Including Sequelae Shoulder-Handfinger Syndrome, Disturbance in the Distal Radio-Ulnar Joint and Impairment of Nerve Function: A Clinical and Experimental Study.' *Acta Orthopaedica Scandinavica*, 38 pp. 1-61.

Gama, N. V., Ferreira, A. and Barros-Timmons, A. (2018) 'Polyurethane Foams: Past, Present, and Future.' *Materials*, 11 p. 1841.

Giacobetti, F. B., Sharkey, P. F., Bos-Giacobetti, M. A., Hume, E. L. and Taras, J. S. (1997) 'Biomechanical analysis of the effectiveness of in-line skating wrist guards for preventing wrist fractures.' *The American journal of sports medicine*, 25 pp. 223-225.

- Gialain, I. O., Coto, N. P., Driemeier, L., Noritomi, P. Y. and Dias, R. B. (2016) 'A three-dimensional finite element analysis of the sports mouthguard.' *Dental Traumatology*, 32(5), pp. 409-415.
- Gibson, L. J. and Ashby, M. F. (1999) *Cellular solids: structure and properties*. Cambridge university press.
- Godderidge, C. (1995) *Pediatric imaging*. Vol. 15. Saunders.
- Greenwald, R., Calabro, S., Thomas, N. and Michel, F. I. (2011) *An instrumented glove to measure wrist biomechanics during snowboarding falls*. Keystone, Colorado, USA, Scher, I. and Greenwald, R. (eds.):
- Greenwald, R. M., Simpson, F. H. and Michel, F. I. (2013) 'Wrist biomechanics during snowboard falls.' *Proceedings of the Institution of Mechanical Engineers, Part P: Journal of Sports Engineering and Technology*, 227(4) pp. 244-254.
- Greenwald, R. M., Janes, P. C., Swanson, S. C. and McDonald, T. R. (1998) 'Dynamic impact Response of human Cadaveric Forearms Using a Wrist Brace.' *The American Journal of Sports Medicine*, 26(6) pp. 825-830.
- Hagel, Pless, I. B. and Goulet, C. (2005) 'The effect of wrist guard use on upper-extremity injuries in snowboarders.' *American Journal of Epidemiology*, 162(2), Jul 15, pp. 149-156.
- Hagel, B. E., Goulet, C., Platt, R. W. and Pless, I. B. (2004) 'Injuries Among Skiers and Snowboarders in Quebec.' *Epidemiology*, 15(3) pp. 279-286.
- Hansen, K., Dau, N., Feist, F., Deck, C., Willinger, R., Madey, S. and Bottlang, M. (2013) 'Angular Impact Mitigation system for bicycle helmets to reduce head acceleration and risk of traumatic brain injury.' *Accident Analysis and Prevention*, 59 pp. 109-117.
- Helelä, T. (1969) 'Age-Dependent variations of the cortical thickness of the clavicle.' *Annals of clinical research*, 1 pp. 140-143.
- Higgins, R. A. (1994) *Properties of Engineering Materials*. Oxford, United Kingdom: Butterworth-Heinemann.
- Hooke, R. (1678) *Lectures de potentia restitutiva, or, Of spring: explaining the power of springing bodies: to which are added some collections*. London: John Martin.
- Horsman, A. and Currey, J. D. (1983) 'Estimation of mechanical properties of the distal radius from bone mineral content and cortical width.' *Clinical orthopaedics and related research*, pp. 298-304.

- Hsiao, E. T. and Robinovitch, S. N. (1997) 'Common protective movements govern unexpected falls from standing height.' *Journal of biomechanics*, 31 pp. 1-9.
- Hunter, R. E. (1999) 'Current Concepts – Skiing Injuries.' *The American Journal of Sports Medicine*, 27(3) pp. 381-389.
- Hwang, I. K. and Kim, K. J. (2004) 'Shock absorbing effects of various padding conditions in improving efficacy of wrist guards.' *Journal of Sports Science and Medicine*, 3(1) pp. 23-29.
- Hwang, I. K., Kim, K. J., Kaufman, K. R., Cooney, W. P. and An, K. N. (2006) 'Biomechanical efficiency of wrist guards as a shock isolator.' *J Biomech Eng*, 128(2), Apr, pp. 229-234.
- Idzikowski, J. R., Janes, P. C. and Abbott, P. J. (2000) 'Upper extremity snowboarding Injuries. Ten-Year Results from the Colorado Snowboard Injury Survey.' *American Orthopaedic Society for Sports Medicine* 28(6) pp. 825-832.
- Instron. (2019) *5 kN Static Load Cell*. [Online] [Accessed on 27th March] <https://www.instron.us/en-us/products/testing-accessories/load-cells/static/2580-series-static/2580-5kn>
- International Boxing Association. (2019) *AIBA Technical & Competition Rules*.
- International Ice Hockey Federation. (2018) *IIHF Official Rule Book 2018-2022*. 1st ed.
- International Olympic Committee, (2018) *Snowboard Equipment and History*. [Online] [Accessed on 26th November 2018] <https://www.olympic.org/snowboard-equipment-and-history>
- International Ski Federation. (2018) *Specifications for competition equipment*. 2018/2019 ed. Switzerland.
- International Standards Organisation (2018) *ISO/DIS 20320: Protective clothing for use in snowboarding — wrist protectors — requirements and test methods*. [draft] Geneva: ISO. [Online] [Accessed on 29th August 2019] <https://bsol-bsigroup-com.mmu.idm.oclc.org/Bibliographic/BibliographicInfoData/00000000030318776>
- Katholieke Universiteit Leuven (2011) *Polychloroprene (CR, unreinforced) datasheet*. Course Hero: [Online] [Accessed on 27th August 2019] <https://www.coursehero.com/file/18781343/CR-Chloroprene-Rubber-Neoprene/>
- Kennedy, J. B. and Neville, A. M. (1986) *Basic Statistical Methods for Engineers and Scientists*. 3rd ed.: Longman Higher Education.

- Kim, B., Beom Lee, S., Lee, J., Cho, S., Park, H., Yeom, S. and Han Park, S. (2012) 'A comparison among Neo-Hookean model, Mooney-Rivlin Model, and Ogden Model for Chloroprene Rubber.' *International journal of precision engineering and manufacturing*, 13 pp. 759-764.
- Kim, K. J., Alian, A. M., Morris, W. S. and Lee, Y. H. (2006) 'Shock attenuation of various protective devices for prevention of fall-related injuries of the forearm/hand complex.' *Am J Sports Med*, 34(4), Apr, pp. 637-643.
- Kim, S. and Lee, S. K. (2011) 'Snowboard wrist guards-use, efficacy, and design: a systematic review.' *Bulletin of the NYU Hospital for Joint Diseases*, 69(2) pp. 149-157.
- Koehle, M. S., Lloyd-Smith, R. and Taunton, J. E. (2002) 'Alpine ski injuries and their prevention.' *Sports Medicine*, 32(12) pp. 785-793.
- Kroncke, E. L., Niedfeldt, M. W. and Young, C. C. (2007) 'Use of protective equipment by adolescents in inline skating, skateboarding & snowboarding.' *Clinical Journal for Sport Medicine*, 18 pp. 38-43.
- Kuptsov, A. H. and Zhizhin, G. N. (1998) *Handbook of fourier transform Raman and infrared spectra of polymers*. p. 529. Elsevier Science.
- Lakes, R. and Lakes, R. S. (2009) *Viscoelastic materials*. Cambridge University Press.
- Lane, B., Sherratt, P., Hu, X. and Harland, A. (2018) 'Measurement of strain and strain rate during impact of tennis ball cores.' *Applied Sciences*, 8(3) p. 371.
- Langran, M. (2004) 'Increased Injury Risk Among First-Day Skiers, Snowboarders, and Skiboarders.' *American Journal of Sports Medicine*, 32(1) pp. 96-103.
- Langran, M. (2013) *Safety and Risk of Snowboarding*. [Online] [Accessed on 20th October] <http://snowboarding-101.weebly.com/safety-and-risk-of-snowboarding.html>
- Langran, M. and Selvaraj, S. (2002) 'Snow sports injuries in Scotland: a case-control study.' *British Journal of Sports Medicine*, 36(2) pp. 135-140.
- Larkin, P. (2011) *Infrared and Raman Spectroscopy: principles and spectral interpretation*. Elsevier.
- Lee, H. H. (2015) *Finite Element Simulations with ANSYS Workbench 16*. Mission, Kansas, USA: SDC Publications.

- Lee, K.-M. and Liu, C.-H. (2012) 'Explicit dynamic finite element analysis of an automated grasping process using highly damped compliant fingers.' *Computers & Mathematics with Applications*, 64(5) pp. 965-977.
- Lehner, S., Geyer, T., Michel, F. I., Schmitt, K.-U. and Senner, V. (2014) 'Wrist Injuries in Snowboarding – Simulation of a Worst Case Scenario of Snowboard Falls.' *Procedia Engineering*, 72 pp. 255-260.
- Levangie, P. K. and Norkin, C. C. (2011) *Joint structure and function: a comprehensive analysis*. 4th ed., Philadelphia, PA: FA Davis Company.
- Lewis, L. M., Clark West, O., Standeven, J. and Jarvis, H. E. (1997) 'Do wrist guards protect against fractures?' *Annals of emergency medicine*, 29(6) pp. 766-769.
- Li, Z. M., Kuxhaus, L., Fisk, J. A. and Christophel, T. H. (2005) 'Coupling between wrist flexion-extension and radial-ulnar deviation.' *Clinical biomechanics*, 20 pp. 177-183.
- Lin, Y., Choi, K. F., Luximon, A., Yao, L., Hu, J. Y. and Li, Y. (2011) 'Finite element modelling of male leg and sportswear: contact pressure and clothing deformation.' *Textile Research Journal*, 81(14) pp. 1470-1476.
- LS-DYNA. (2011) 'Review of Solid Element Formulations in LS-DYNA: Properties, Limits, Advantages, Disadvantages.' *dynamore*. p. 36. [Online] [Accessed on 17th January 2019]
<https://www.dynamore.de/de/download/papers/forum11/entwicklerforum-2011/erhart.pdf>
- LS-DYNA Support. (2019) *Negative volume in soft materials*. [Online] [Accessed on 17th January 2019] <https://www.dynasupport.com/howtos/material/negative-volume-in-soft-materials>
- LSTC. Livermore Software Technology Group (1998) LS-DYNA Examples Manual. In: Reid, J. D., p. 296.
- LSTC. Livermore Software Technology Group (2017a) LS-DYNA Theory Manual. *LS-DYNA Dev*. p. 878.
- LSTC. Livermore Software Technology Group (2017b) 'Volume II: Material Models.' *In LS-DYNA Keyword User's Manual*. Vol. 2. p. 1549.
- LSTC. Livermore Software Technology Group (2011) *Total Human Model for Safety – THUMS*. [Online] [Accessed on 3rd October 2018] <http://www.lstc.com/thums>

- LSTC, (2017) 'Volume II: Material Models.' *In LS-DYNA Keyword User's Manual*. Vol. 2. p. 1549.
- Lu, W. Y. (2014) *Mechanical characterization of rigid polyurethane foams* (No. SAND-2014-20708). Livermore, CA (United States): Sandia National Lab (SNL-CA).
- Lubahn, J., Englund, R., Trinidad, G., Lyons, J., Ivance, D. and Buczek, F. L. (2005) 'Adequacy of laboratory simulation of in-line skater falls.' *The Journal of Hand Surgery*, 30(2) pp. 283-288.
- Luo, Y. and Liang, Z. (2013) 'Sport Helmet Design and Virtual Impact Test by Image-based Finite Element Modeling.' *In 35th Annual International Conference of the IEEE EMBS*. Osaka, Japan, 3-7 July 2013.
- Maeno, T. and Hasegawa, J. (2001) *Development of a finite element model of the total human model for safety (THUMS) and application to car-pedestrian impacts*. (No. 2001-06-0054). SAE Technical Paper.
- Mane, J. V., Chandra, S., Sharma, S., Ali, H., Chavan, V. M., Manjunath, B. S. and Patel, R. J. (2017) 'Mechanical Property Evaluation of Polyurethane Foam under Quasi-static and Dynamic Strain Rates - An Experimental Study.' *In 11th International Symposium on Plasticity and Impact Mechanics, Implast*. Vol. 173: Procedia Engineering, pp. 726-731.
- Mao, H., Cai, Y. and Yang, K. H. (2014) 'Numerical study of a 10-year-old child forearm injury.' *Advances in Biomechanics and Applications*, 1(3) pp. 143-158.
- Marais, S. T., Tait, R. B., Cloete, T. J. and Nurick, G. N. (2004) 'Material testing at high strain rate using the split Hopkinson pressure bar.' *Latin American Journal of Solids and Structures*, 1 pp. 319-339.
- Marshall, M. M., Mozrall, J. R. and Shealy, J. E. (1999) 'The effects of complex wrist and forearm posture on wrist range of motion.' *Human Factors*, 41 pp. 205 - 213.
- Mascia, L. (1982) *Thermoplastics: Materials Engineering*. London, United Kingdom: Applied Science Publishers Ltd.
- Materialise. (2018) *PA 12 (SLS)*. [Online] [Accessed on 8th February] <https://www.materialise.com/en/manufacturing/materials/pa-12-sls>
- Matsumoto, K., Sumi, H., Sumi, Y. and Shimizu, K. (2004) 'Wrist Fractures From Snowboarding: A Prospective Study for 3 seasons from 1998 to 2001.' *Clinical Journal of Sport Medicine*, 14(2) pp. 64-71.

- Matweb. (2018) *Overview of materials for High Density Polyethylene (HDPE), Injection Molded.* [Online] [Accessed on 10th January] <http://www.matweb.com/search/DataSheet.aspx?MatGUID=fce23f90005d4fbe8e12a1bce53ebdc8&ckck=1>
- Matweb. (2019a) *Overview of materials for 6000 series Aluminium Alloy.* [Online] [Accessed on 12th March 2019] <http://www.matweb.com/search/datasheet.aspx?MatGUID=26d19f2d20654a489aefc0d9c247cebf&ckck=1>
- MatWeb, L. (2019b) *Material Property Data.* [Online] [Accessed on 18th April 2019] <http://www.matweb.com/>
- Maurel, M. L., Fitzgerald, L. G., Miles, A. W. and Giddins, G. E. (2013) 'Biomechanical study of the efficacy of a new design of wrist guard.' *Clin Biomech (Bristol, Avon)*, 28(5), Jun, pp. 509-513.
- McCann, A. (2013) Protective Gear For Snowboarding. *Snowboard Addiction*. Vol. 2019.
- McGrady, L. M., Hoepfner, P., Young, C. C., Raasch, W. G., Lim, T. and Han, J. S. (2001) 'Biomechanical effect of in-line skating wrist guards on the prevention of wrist fracture.' *KSME International Journal*, 15(7) pp. 1072-1076.
- Meade Spratley, E. (2013) *Patient-Specific Modeling of an Adult Acquired Flatfoot Deformity Cohort Before & After Surgery.* Doctor of Philosophy. Virginia Commonwealth University.
- Menard, K. P. and Menard, N. (2006) 'Dynamic mechanical analysis.' *Encyclopedia of Analytical Chemistry: Applications, Theory and Instrumentation*, pp. 1-25.
- Michel, F. I., Schmitt, K.-U., Greenwald, R. M., Russell, K., Simpson, F. I., Schulz, D. and Langran, M. (2013) 'White Paper: functionality and efficacy of wrist protectors in snowboarding—towards a harmonized international standard.' *Sports Engineering*, 16(4) pp. 197-210.
- Michigan Tech. (2019) *Mechanical Properties Data.* Properties of Selected Fibres. [Online] [Accessed on 18th April 2019] <http://www.mse.mtu.edu/~drjohn/my4150/props.html>
- Mills, N. J. and Gilchrist, A. (2008) 'Finite-element analysis of bicycle helmet oblique impacts.' *International Journal of Impact Engineering*, 35(9) pp. 1087-1101.
- Mooney, M. (1940) 'A theory of Large Elastic Deformation.' *Journal of applied Physics*, 11(9) pp. 582-592.

- Moore, M. S., Popovic, N. A., Daniel, J. N., Boyea, S. R. and Polly, D. W. (1997) 'the effect of a wrist brace on injury patterns in experimentally produced distal radius fractures in a cadaveric model.' *The American Journal of Sports Medicine*, 25(3) pp. 394-401.
- Mullins, L. (1969) 'Softening of rubber by deformation.' *Rubber chemistry and technology*, 42(1) pp. 339-362.
- Myers, E. R., Hecker, A. T., Rooks, D. S., Hipp, J. A. and Hayes, W. C. (1993) 'Geometric variables from DXA of the radius predict forearm fracture load in vitro.' *Calcified Tissue International*, 52 pp. 199-204.
- Myers, E. R., Sebeny, E. A., Hecker, A. T., Corcoran, T. A., Hipp, J. A., Greenspan, S. L. and Hayes, W. C. (1991) 'Correlations between photon absorptions properties and failure load of the distal radius vitro.' *Calcified Tissue International*, 49 pp. 292 - 297.
- Nagaoka, T., Matsuda, A., Shimana, T. and Omori, K. (2012) 'A proposal of Material Modeling for Swimwear Considering Anisotropy and Viscosity.' *Procedia Engineering*, 34 pp. 700-705.
- Nate. (2019) What Snowboarding Safety Equipment Do I Need. *The Right Gear for the Perfect Ride*. Vol. 2019. Snowboarding Profiles.
- Neilsen, M. K., Krieg, R. D. and Schreyer, H. L. (1995) 'A Constitutive Theory for Rigid Polyurethane Foam.' *Polymer engineering and science*, 35 pp. 387 - 394.
- Nevins, D. and Smith, L. (2013) 'Influence of Ball Properties on Simulated Ball-to-Head Impacts.' *Procedia Engineering*, 60 pp. 4-9.
- Nicotra, M., Moncalero, M., Messori, M., Fabbri, E., Fiorini, M. and Colonna, M. (2014) Thermo-mechanical and impact properties of polymeric foams used for snow sports protective equipment. *Procedia Engineering*, 72, pp.678-683.
- O'Neill, D. F. (2003) 'Wrist injuries in guarded versus unguarded first time snowboarders.' *Clin Orthop Relat Res*, (409), Apr, pp. 91-95.
- Ogawa, H., Sumi, H., Sumi, Y. and Shimizu, K. (2010) 'Skill level-specific differences in snowboarding-related injuries.' *Am J Sports Med*, 38(3), Mar, pp. 532-537.
- Ogden, R. W. (1972) 'Large deformation isotropic elasticity – On the correlation of theory and experiment for incompressible rubberlike solids.' *Proceedings of the royal society A: Mathematical, physical and engineering sciences*, 326(1567) pp. 565-584.

- Pain, M. T., Tsui, F. and Cove, S. (2008) 'In vivo determination of the effect of shoulder pads on tackling forces in rugby.' *Journal of sports sciences*, 26(8)
- Payne, T. (2015) *Improved Human Soft Tissue Thigh Surrogate for Superior Assessment of Sports Personal Protective Equipment*. Doctor of philosophy. Loughborough University.
- Payne, T., Mitchell, S. and Bibb, R. (2013) 'Design of human surrogates for the study of biomechanical injury: a review.' *Biomedical engineering*, 41(1)
- Payne, T., Mitchell, S., Bibb, R. and Waters, M. (2015a) 'Development of novel synthetic muscle tissues for sports impact surrogates.' *Journal of the Mechanical Behaviour of Biomedical Materials*, 41, Jan, pp. 357-374.
- Payne, T., Mitchell, S., Bibb, R. and Waters, M. (2015b) 'The evaluation of new multi-material human soft tissue simulants for sports impact surrogates.' *Journal of the Mechanical Behaviour of Biomedical Materials*, 41, Jan, pp. 336-356.
- Petrone, N., Ceolin, F. and Morandin, T. (2010) 'Full scale impact testing of ski safety barriers using an instrumented anthropometric dummy.' *In The Engineering of Sport 8 - Engineering Emotion*. Vol. 2. Vienna, Austria, Sabo, A., Kafka, P., Litzenberger, S. and Sabo, C. (eds.): Procedia Engineering, pp. 2593-2598.
- Petrone, N., Candiotta, G., Marzella, E., Uriati, F., Carraro, G., Backstrom, M. and Koptug, A. (2019) 'Feasibility of using a novel Instrumented Human Head Surrogate to measure helmet, head & brain kinematics and intracranial pressure during multidirectional impact tests.' *Journal of Science and Medicine in Sport*.
- Price, D. S., Jones, R., Harland, A. R. and Silberschmidt, V. V. (2008) 'Viscoelasticity of multi-layer textile reinforced polymer composites used in soccer balls.' *Journal of Materials Science*, 43(8) pp. 2833-2843.
- Pugh, A. W., Hamilton, R., Nash, D. H. and Otto, S. R. (2010) 'Characterization of the materials in golf ball construction for use in finite element analysis.' *In 8th Conference of the International Sports Engineering Association (ISEA)*. Vol. 2. Vienna, Italy: Elsevier Ltd, pp. 3231-3236.
- Ramos, A. and Simoes, J. A. (2006) 'Tetrahedral versus hexahedral finite elements in numerical modelling of the proximal femur.' *Medical engineering & physics*, 28 pp. 916-924.
- Ranga, D. and Strangwood, M. (2010) 'Finite element modelling of the quasi-static and dynamic behaviour of a solid sports ball based on component material properties.' *Procedia Engineering*, 2(2) pp. 3287-3292.

- Rivlin, R. S. (1948) 'Large elastic deformations of isotropic materials IV. further developments of the general theory.' *Philosophical transactions of the royal society A: Mathematical, physical and engineering sciences*, 241(835)
- Ronning, R., Ronning, I., Gerner, T. and Engebretsen, L. (2001) 'The efficacy of wrist protectors in preventing snowboarding injuries.' *The American journal of sports medicine* 29(5) pp. 581-585.
- Russell, K., Francescutti, L. H. and Hagel, B. (2007) 'The Effect of Wrist Guards on Wrist and Arm Injuries Among Snowboarders: A Systematic Review.' *Clinical Journal of Sport Medicine*, 17 pp. 145-150.
- Russell, K., Hagel, B. and Goulet, C. (2010) 'Snowboarding.' In Caine, DJ, Harmer, P. and Schiff, M. (eds.) *Epidemiology of injuries in Olympic Sports*. Oxford, United Kingdom: Blackwell Publishing, pp. 447-472.
- SAE, S. (2007) 'J211-1 Instrumentation for Impact Test—Part 1—Electronic Instrumentation.' *SAE International*.
- Schmitt, K.-U., Spierings, A. B. and Derler, S. (2004) 'A finite element approach and experiments to assess the effectiveness of hip protectors.' *Technology and Health Care*, 12 pp. 43-49.
- Schmitt, K.-U., Michel, F. I. and Staudigl, F. (2011) *Analysing the impact behaviour of recent snowboarding wrist protectors*. Vol. 39. Krakow, Poland:
- Schmitt, K.-U., Michel, F. I. and Staudigl, F. (2012a) 'Testing damping performance and bending stiffness of snowboarding wrist protectors.' *Journal of ASTM International*, 9(4) pp. 1-12.
- Schmitt, K.-U., Gross, J. and Muser, M. (2018) *Development of a standardised pendulum to impact ice hockey boards*. Bern: bfu - Beratungsstelle für Unfallverhütung.
- Schmitt, K.-U., Wider, D., Michel, F. I., Brugger, O., Gerber, H. and Denoth, J. (2009) *Investigating the wrist load in snowboard backwards falls*. Garmisch-Partenkirchen, Germany, Veit Senner, I. (ed.):
- Schmitt, K.-U., Wider, D., Michel, F. I., Brugger, O., Gerber, H. and Denoth, J. (2012b) 'Characterizing the mechanical parameters of forward and backward falls as experienced in snowboarding.' *Sports Biomechanics*, 11(1), Mar, pp. 57-72.
- Schwarzl, F. and Staverman, A. J. (1952) 'Time-temperature dependence of linear viscoelastic behaviour.' *Journal of Applied Physics*, 23(8) pp. 838-843.

- Senner, V., Lehner, S., Michel, F. I. and Brugger, O. (2019) '11 Modelling and simulation to prevent overloads in snowboarding.' In Baca, A. and Perl, J. (eds.) *Modelling and Simulation in sport and exercise*. Routledge, pp. 211-236.
- Shahzad, M., Kamran, A., Zeeshan Siddiqui, M. and Farhan, M. (2015) 'Mechanical Characterization and FE Modelling of a Hyperelastic Material.' *Materials Research*, 18 pp. 918-924.
- Sharcnet. (2016) *Element Quality*. [Online] [Accessed on 6th February] https://www.sharcnet.ca/Software/Ansys/17.0/en-us/help/wb_msh/msh_Element_Quality_Metric.html
- Shimana, T., Nakashiman, M., Matsuda, A. and Omori, K. (2013) 'A new method for designing sportswear by using three dimensional computer graphic based anisotropic hyperelastic models and musculoskeletal simulations.' *Procedia Engineering*, 60 pp. 331-336.
- Shultz, S., Houglum, P. and Perrin, D. (2015) *Examination of Musculoskeletal Injuries with Web Resource*. 4th ed., Leeds, UK: Human Kinetics.
- Shultz, S. J., Houglum, P. A. and Perrin, D. H. (2010) *Examination of musculoskeletal Injuries*. 3rd ed. ed.: Human Kinetics.
- Shuttleworth, M. (2008) *Scientific Reductionism*. [Online] [Accessed on 26th December 2019] <https://explorable.com/scientific-reductionism>
- SIA research. (2014) 'SIA snow sports market, intelligence report.' [Online]. [Accessed on 6th March 2017] http://cdn2.hubspot.net/hubfs/413130/2014_SIA_Snow_Sports_Intelligence_Report.pdf?utm_campaign=Intelligence%20Report&utm_medium=2014%20Intelligence%20Report&utm_source=Andy%20Shevitz
- Sieglkas, P., Sharp, D. and Ghajari, M. (2019) 'The traumatic brain injury mitigation effects of a new viscoelastic add-on liner.' *Scientific Reports, Nature Publishing Group*, 8
- Signetti, S., Nicotra, M., Colonna, M. and Pugno, N. M. (2018) 'Modeling and simulation of the impact behaviour of soft polymeric-foam-based back protectors for winter sports.' *Journal of science and medicine in sport*,
- Smith, L. and Duris, J. (2009) 'Progress and challenges in numerically modelling solid sports balls with application to softballs.' *Journal of Sports Science*, 27(4) pp. 353-360.
- Smith, L. and Burbank, S. (2013) 'Simulating sport ball impact through material characterisation.' *Procedia Engineering*, 60 pp. 73-78.

- Smith, L., Nevins, D., Dat, N. T. and Fua, P. (2016) 'Measuring the accuracy of softball impact simulations.' *Sports Engineering*, pp. 1-8.
- Sorvari, J. and Malinen, M. (2006) 'Determination of the relaxation modulus of a linearly viscoelastic material.' *Mechanics of Time-Dependent Materials*, 10(2) pp. 125-133.
- SpaceClaim. (2014) *Shared topology in ANSYS*. SpaceClaim Online Help. [Online] [Accessed on 24th January] http://help.spaceclaim.com/2015.0.0/en/Content/ANSYS_SharedTopology.htm
- Staebler, M. P., Moore, D. C., Akelman, E., Weiss, A. P. A., Fadale, P. D. and Crisco, J. J. (1999) 'The effect of wrist guards on bone strain in the distal forearm.' *The American journal of sports medicine*, 27 pp. 500-506.
- Sutherland, A. G., Holmes, J. D. and Myers, S. (1996) 'Difference in injury patterns in snowboarding and alpine skiing.' *Injury*, 27(6) pp. 423-425.
- Tanabe, H., Matsuda, A., Shimana, T. and Omori, K. (2012) 'Numerical analysis of competitive swimwear using finite element method.' *Procedia Engineering*, 34 pp. 718-723.
- Tanaka, K., Teranishi, Y. and Ujihashi, S. (2012) 'Finite element modelling and simulations for golf impact.' *Proceedings of the Institution of Mechanical Engineers, Part P: Journal of Sports Engineering and Technology*, 227(1) pp. 20-30.
- Tanaka, K., Sato, F., Oodaira, H., Teranishi, Y., Sato, F. and Ujihashi, S. (2006) 'Construction of the finite element models of golf balls and simulations of their collisions.' *Proceedings of the Institution of Mechanical Engineers, Part L: Journal of Materials: Design and Applications*, 220(1) pp. 13-22.
- Tang, M., Huang, G., Zhang, H., Liu, Y., Chang, H., Song, H., Xu, D. and Wang, Z., 2017. Dependences of Rheological and Compression Mechanical Properties on Cellular Structures for Impact-Protective Materials. *ACS Omega*, 2(5), pp.2214-2223.
- Thomas Publishing Company. (2018) *Neoprene Traits and Applications*. [Online] [Accessed on 11th December] <https://www.thomasnet.com/articles/plastics-rubber/traits-applications-neoprene>
- Thoraval, C., Hault-Dubrulle, A., Drazetic, P., Morvan, H. and Barla, C. (2013) 'Evaluation of wrist guard effectiveness for snowboarders.' *Computer Methods in Biomechanics and Biomedical Engineering*, 16(1) pp. 187-188.
- Tilley, A. R. (2002) *The measure of man and woman: human factors in design*. Vol. 1. John Wiley & Sons.

- Tinard, V., Deck, C. and Willinger, R. (2012) 'Modelling and validation of motorcyclist helmet with composite shell.' *International Journal of Crashworthiness*, 17(2) pp. 209-215.
- Tsukeman, I. and Plaks, A. (1998) 'Comparison of accuracy criteria for approximation of conservative fields on tetrahedra.' *IEEE Transactions on Magnetism*, 34 pp. 3252-3255.
- Tyler, D. J. (2016) *Impact protection for functional apparel*. Poznan, Poland: The Textile Institute.
- Valentini, P. P., Pennestrì, E. and Quattrociocchi, L. (2015) 'Biomechanical model for simulating impacts against protective padding of sport facility.' *Sports Engineering*, 19(1) pp. 47-57.
- Van den Kroonenberg, A. J., Hayes, W. C. and McMahon, T. A. (1995) 'Dynamic models for sideways falls from standing height.' *Journal of Biomechanical Engineering*, 117 pp. 309-318.
- van Huffelen, R., Zipfel, A. and Baaran, J. (2004) *The determination of the effective mass and moment of inertia of a pendulum impactor*.
- van Mechelen, W., Hlobil, H. and Kemper, H. C. G. (1992) 'Incidence, Severity, Aetiology and Prevention of Sports injuries.' *Sports Medicine*, 14(2) pp. 82-99.
- Vaskova, H. (2010) *Raman Spectroscopy: A modern technique for material properties identification*. Vol. Annals of DAAAM & Proceedings. Vienna, Austria: DAAAM International Vienna.
- Wadsworth, P., Binet, M. H. and Rowlands, A. (2012) *Prospective study to compare efficacy of different designs of wrist protection for snowboarders*. Vol. 19th. Skiing Trauma and Safety. ASTM International.
- Weisang. (2018) *CFC Filter Analysis Object (Digital Filters Option)*. FlexPro Documentation. [Online] [Accessed on 1st May] https://www.weisang.com/en/documentation/cfcfilteranalysis_en/
- Whiting, W. C. and Zernicke, R. F. (2008) *Biomechanics of Musculoskeletal injury*. 2nd ed., Leeds, UK: Human Kinetics.
- Yamauchi, K., Wakahara, K., Fukuta, M., Matsumoto, K., Sumi, H., Shimizu, K. and Miyamoto, K. (2010) 'Characteristics of upper extremity injuries sustained by falling during snowboarding: a study of 1918 cases.' *Am J Sports Med*, 38(7), Jul, pp. 1468-1474.

Zaouk, A. K., Bedewi, N. E., Kan, C. D. and Marzougui, D. (1996) 'Validation of a non-linear finite element vehicle model using multiple impact data.'

Zapata, E., Rongieras, F., Pialat, J. B., Follet, H. and Mitton, D. (2017) 'An ex vivo experiment to reproduce a forward fall leading to fractured and non-fractured radii.' *Journal of biomechanics*, 63 pp. 174-178.

10 Appendices

10.A ISO/DIS 20320 Bend Test Surrogate Engineering Drawing

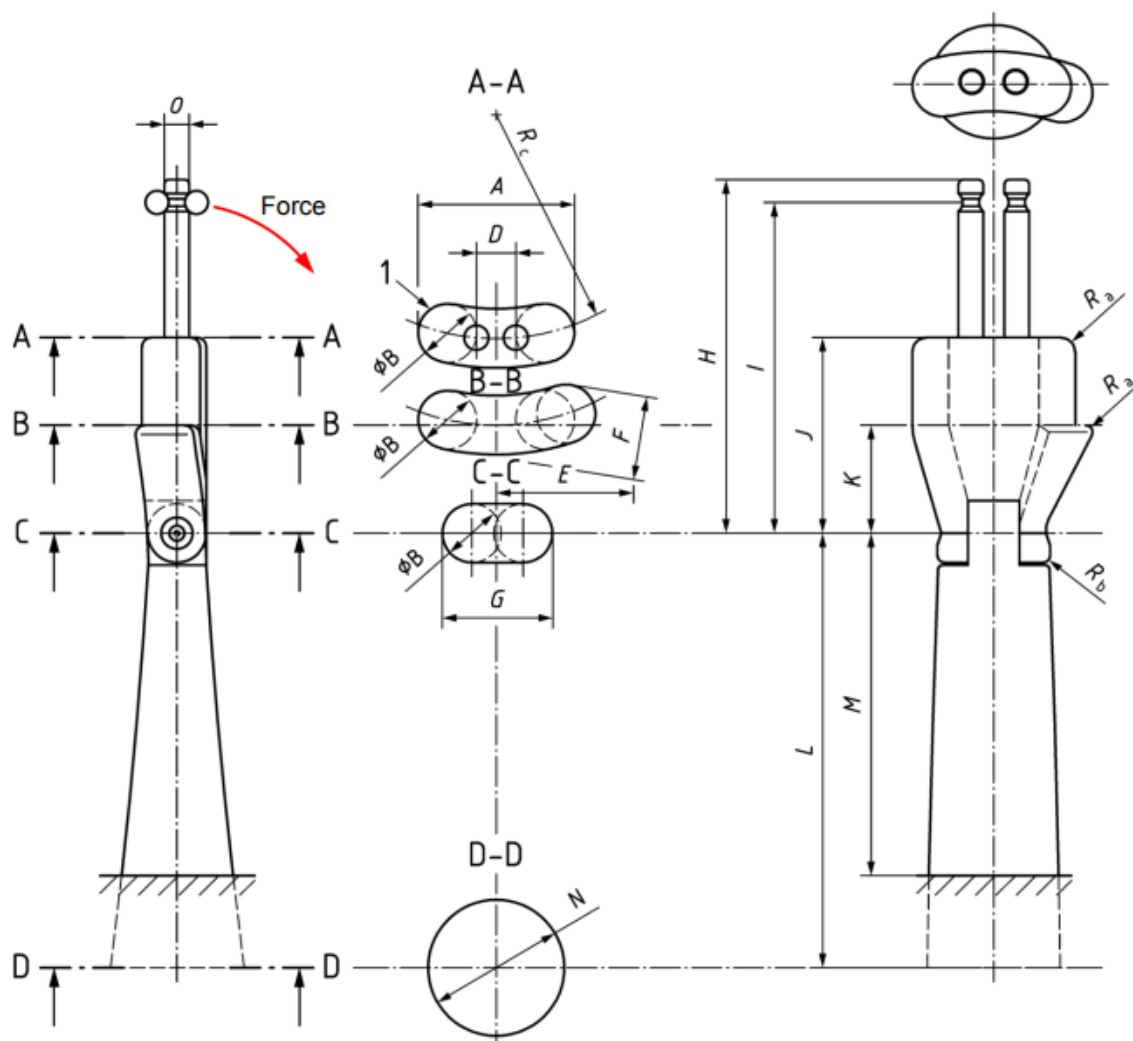


Figure 3 — Hand prosthesis

Table 6 — Dimensions of the hand prosthesis

Prosthesis size	Range	Dimensions of the hand prosthesis (Values in mm)															
		A	B	RC	D	E	F	G	H	I	J	K	L	M	N	O	X
S	A	72	24	120	19	45	39	50	160	148	91	52	245	180	54	12	172
M	B	82	30	115	22	50	47	57	182	170	100	56	273	180	69	12	200
L	C	95	38	110	24	55	58	66	204	192	111	62	312	180	88	12	235

Dimension X: resulting circumference of the Hand.
 Chamfer: RA 2 mm.
 Chamfer RB 10 mm.
 Prosthesis dimensions are based on anthropometric data[5],[6],[2].
 Hand length (Dimension H) of the three prostheses correspond to hand length of ISO 21420:
 — Prosthesis size S corresponds to size 6;
 — Prosthesis size M corresponds to size 8;
 — Prosthesis size L corresponds to size 10.

10.B Monthly Stock Check of Wrist Protectors in the UK

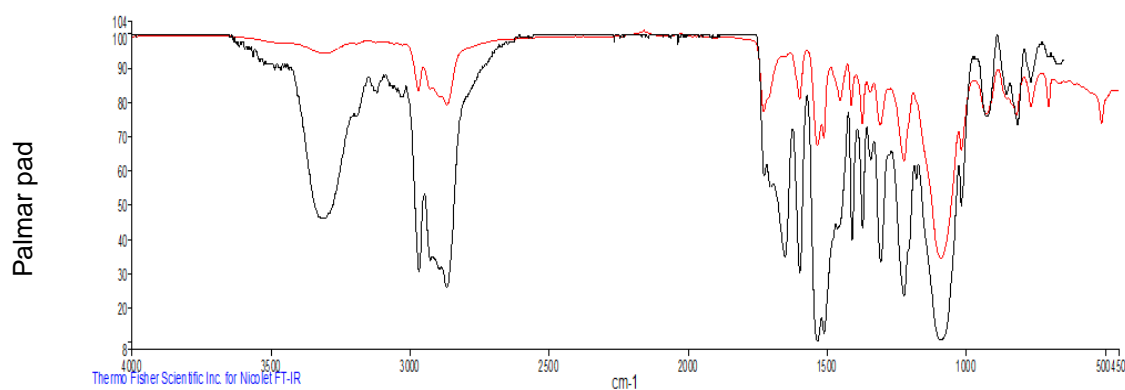
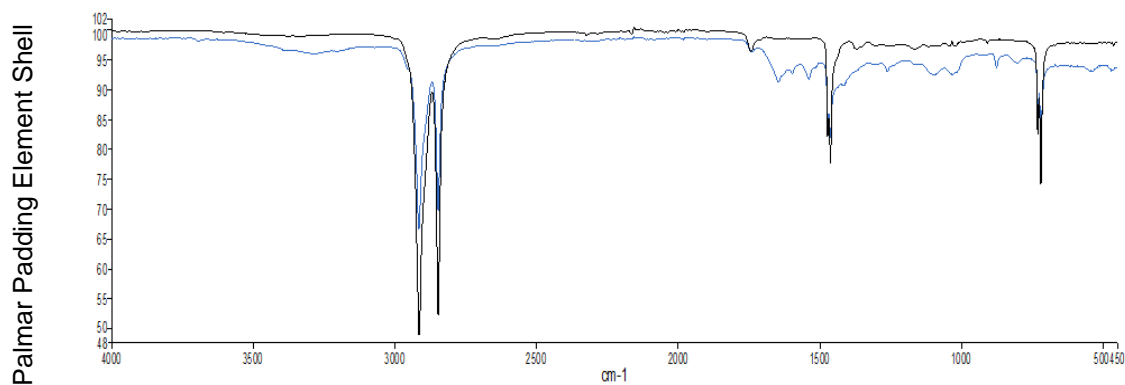
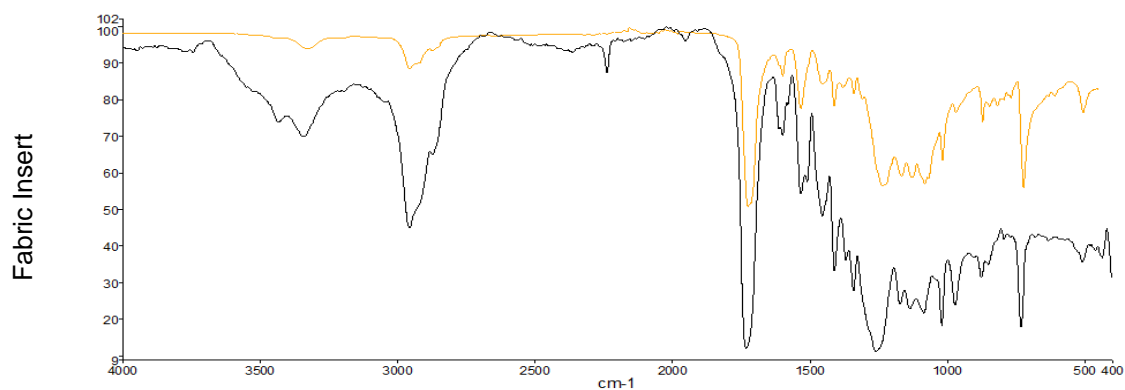
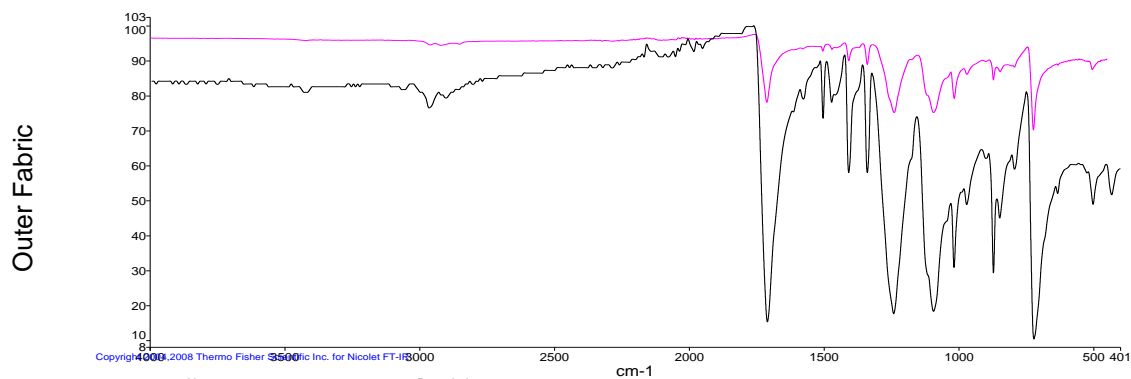
Thirty stores in the UK were identified to stock snowboard wrist protectors in November 2016. A store was included if it was searchable within the first 10 pages of the google search of “snowboard wrist protectors” and the website highlighted that there was a physical store in the UK. On the first Monday of every month, the websites of all thirty stores were checked to see which wrist protectors were available to be purchased and their price. The monthly tracking records for the pool of wrist protectors identified in Chapter 3 (Table 3-1) for modelling are shown in Table 10-1 between November 2016 and March 2019.

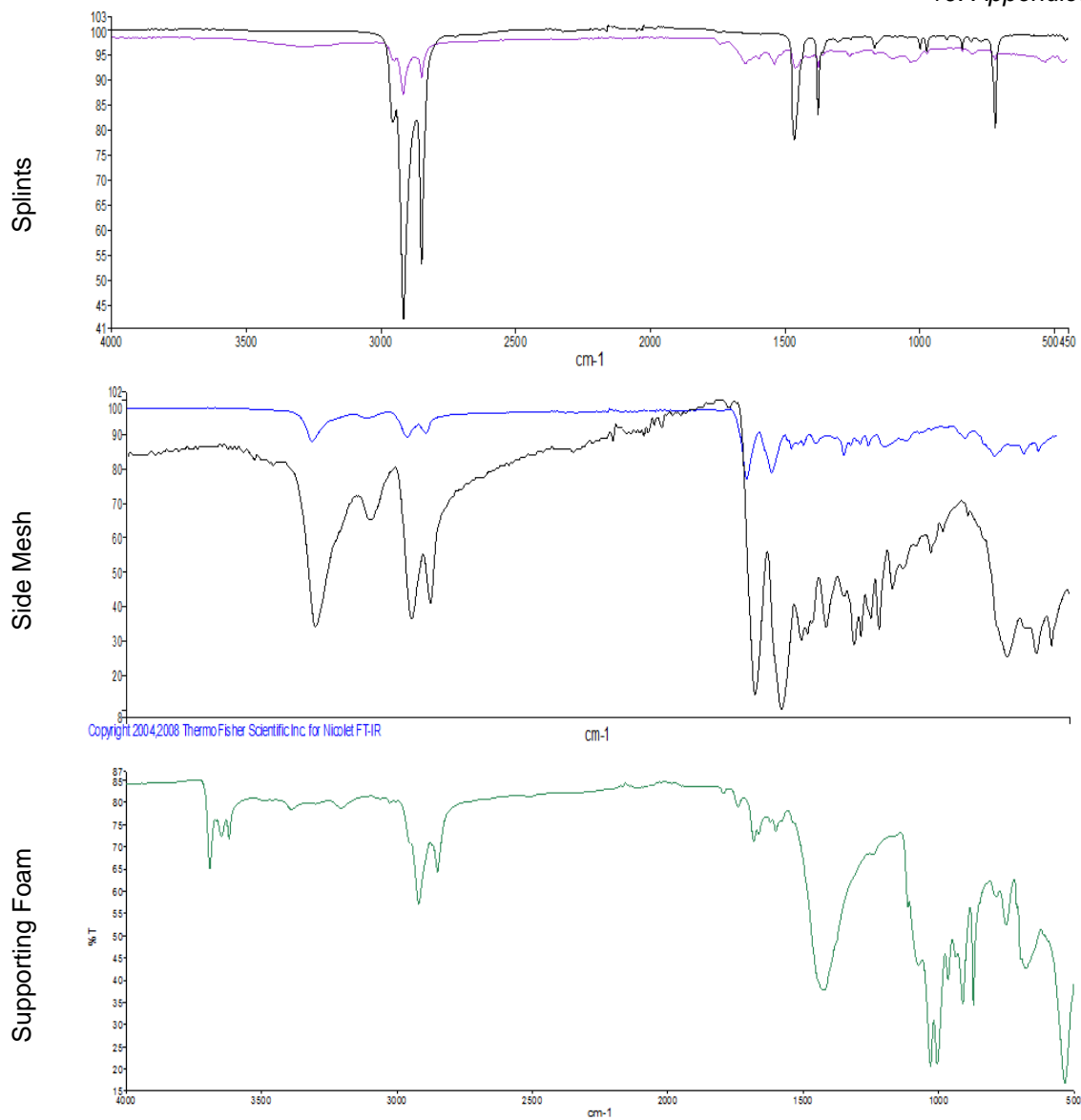
Table 10-1 Monthly tracking record for the pool of wrist protector identified for modelling, highlighting how many stocked each protector and their mean price (£) each month. Protector F and H were not stocked at any stores in the UK.

Wrist Protector	Nov-16		Jan-17		Feb-17		Mar-17		Apr-17		May-17		Jun-17		Jul-17		Aug-17	
	No.	Price	No.	Price	No.	Price	No.	Price	No.	Price	No.	Price	No.	Price	No.	Price	No.	Price
A	1	39.00	1	41.00	1	41.00	1	41.00	1	41.00	1	41.00	1	41.00	1	28.50	1	28.50
B	10	24.97	11	24.98	10	24.60	10	23.98	8	22.79	7	21.94	7	22.83	9	21.64	7	21.76
C	5	40.49	3	38.42	3	38.42	1	50.32	1	52.11	1	50.62	2	41.29	2	42.03	1	52.71
D	17	16.04	17	15.37	14	15.19	13	14.79	14	14.36	13	13.97	14	13.85	16	13.96	16	13.93
E	2	58.98	1	59.00	1	59.00	1	59.00	1	59.00	1	59.00	1	40.99	1	40.99	2	54.97
G	1	9.99	1	9.99	1	9.99	1	9.99	1	9.99	1	9.99	1	9.99	1	9.99	1	9.99
Wrist Protector	Sep-17		Oct-17		Dec-17		Jan-18		Feb-18		Mar-18		May-18		Jun-18		Jul-18	
	No.	Price	No.	Price	No.	Price	No.	Price	No.	Price	No.	Price	No.	Price	No.	Price	No.	Price
A	1	28.50	1	41.00	1	41.00	1	41.00	1	41.00	0	0.00	0	0.00	0	0.00	0	0.00
B	7	24.54	7	26.38	8	26.95	7	28.26	7	28.37	7	27.57	5	22.39	4	22.74	4	22.74
C	1	55.41	2	54.86	3	51.57	3	48.23	3	41.70	3	41.70	2	41.50	3	41.70	3	38.70
D	18	15.74	15	16.10	17	16.91	17	16.95	15	16.78	13	16.59	12	15.60	11	15.89	11	15.63
E	2	54.97	2	69.97	4	64.91	4	69.47	4	69.47	3	66.67	3	66.67	1	51.75	1	68.95
G	1	11.99	1	11.99	1	11.99	1	11.99	1	11.99	1	11.99	1	11.99	1	11.99	1	11.99
Wrist Protector	Aug-18		Sep-18		Oct-18		Nov-18		Dec-18		Jan-19		Feb-19		Mar-19			
	No.	Price	No.	Price	No.	Price	No.	Price	No.	Price	No.	Price	No.	Price	No.	Price		
A	0	0.00	0	0.00	1	41.00	1	41.00	1	41.00	1	41.00	1	41.00	1	41.00		
B	4	22.74	4	25.84	6	28.38	9	28.68	9	29.43	8	28.21	9	27.35	8	26.93		
C	2	32.50	2	32.50	1	57.00	2	42.00	2	50.50	2	42.50	2	33.45	1	32.00		
D	11	15.72	13	21.01	13	22.67	14	17.34	16	16.57	15	16.86	17	16.50	16	15.27		
E	2	61.47	2	55.22	3	59.80	3	59.46	3	62.83	4	64.38	5	60.85	4	59.61		
G	1	11.99	1	11.99	1	11.99	1	11.99	1	11.99	1	11.99	1	12.99	1	12.99		

10.C FT-IR Traces for Wrist Protector Components

Short Protector

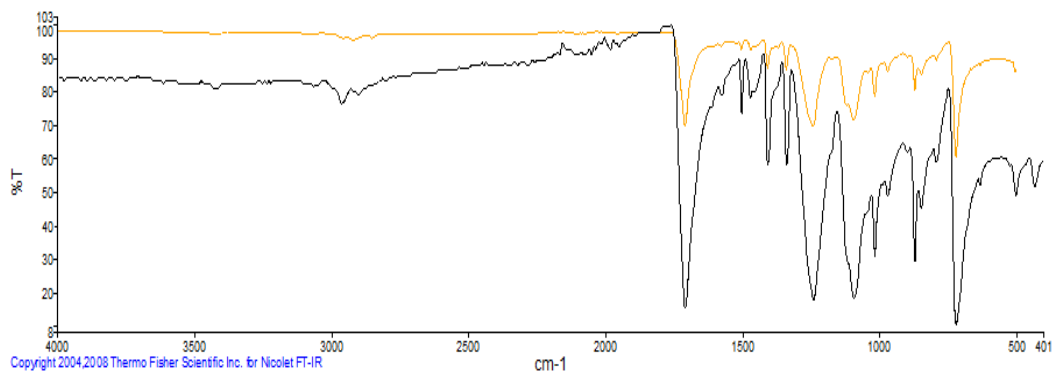




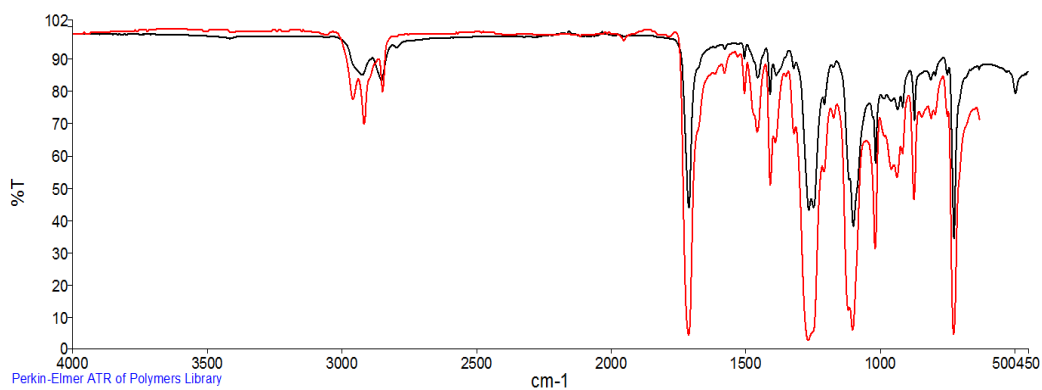
Key – coloured line is the material that was assessed and the black line is the material library match.

Long Protector

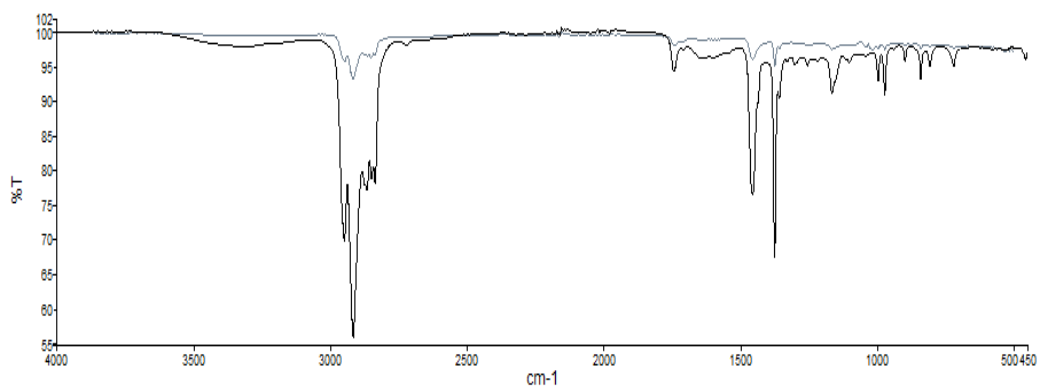
Outer Fabric



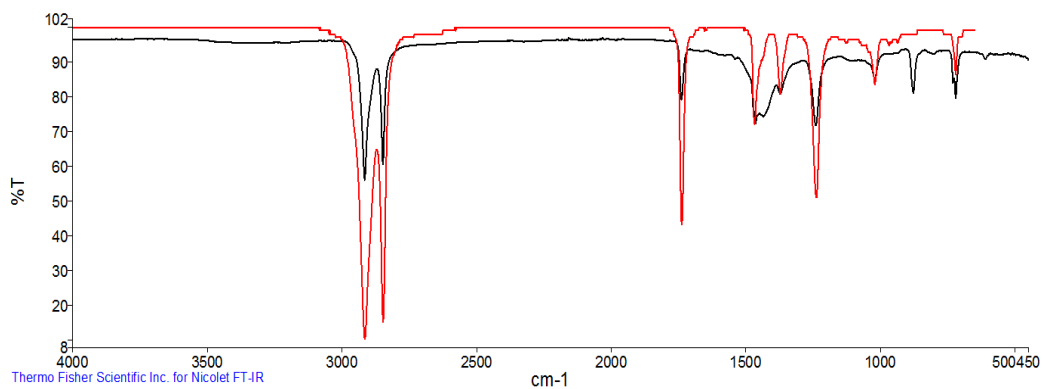
Supporting Foam

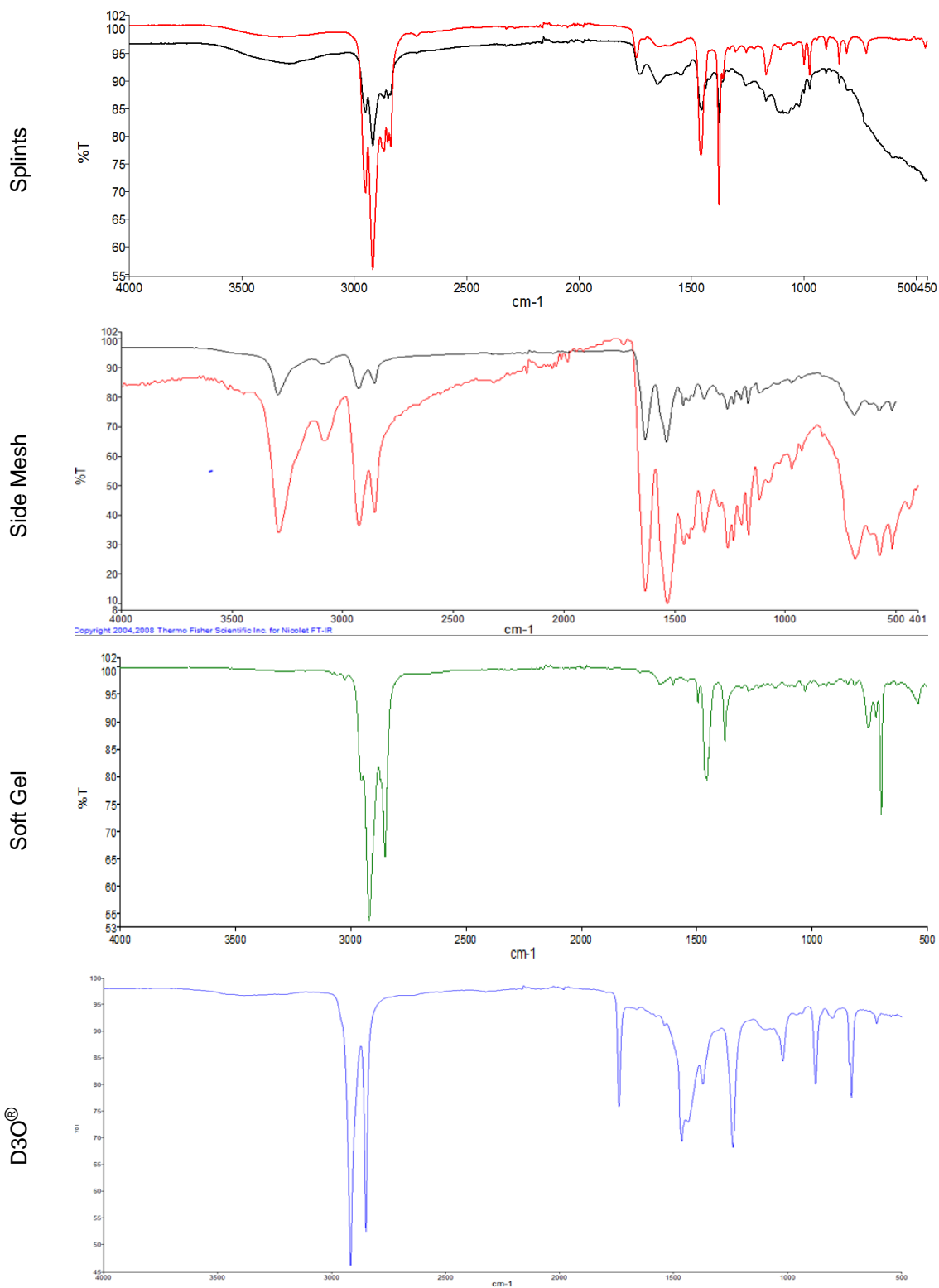


Skid Plate



Foam





Key – coloured line is the material that was assessed and the black line is the material library match.

10.D Statistical Analysis

A one way ANOVA was performed to see whether samples were significantly different from each other. For each sample tested, a descriptive table is presented including the number of samples, mean, standard deviation, confidence intervals for the dependent variable (stress) and the coefficient of variance for each separate group and the groups combined (overall). The outputs of the ANOVA analysis are shown in the second section highlighting whether samples are significantly different (p-value, if significant the value is highlighted in bold text). In the table SS is the sum of the squares, df is the degrees of freedom, MS is the mean of the squares, F is the mean square between divided by the mean square within and p is the significance value. In order to find out which of the specific groups differed a Tukey post hoc test was performed and the p values when comparing each sample individually are presented in the third section of the table.

When only two sets of data were being compared, a two sample t-test was performed to check for significant differences. For each energy and scenario, a descriptive table of statistics is presented highlighting the number of samples, mean, standard deviation and standard error mean. The outputs of the t-test are shown in a second table highlighting whether there was a significant difference between the two scenarios being tested (p value, if significant the value is highlighted in bold text). Also highlighted in this table is the t statistic, the degrees of freedom (df) and the significance value (p value).

10.D.1 Chapter 3

A one way ANOVA was performed comparing the stress for each sample at 50% strain for compression testing and 40% strain for tensile testing. An ANOVA was also used to compare samples in the three-point bend test where the force required to displace the splints of both protectors to 6.4 mm was compared.

Short protector pad - compression testing

Descriptive Statistics

Samples	No.	Mean (Pa)	St Dev (Pa)	95% Confidence Interval for		Coefficient of variance
				Mean (Pa)		
				Lower Bound	Upper Bound	
A	5	407,454	4,268	391,420	4,233,489	1.05
B	5	136,212	3,428	120,177	152,247	2.52
C	5	441,622	26,499	425,587	457,657	6.00
D	5	367,511	26,265	351,476	383,546	7.15
E	5	433,951	7,429	417,916	449,985	1.71
Overall	25	357,350	116,964	345,644	430,181	32.73

ANOVA Results

Source of Variance	SS (Pa)	df	MS (Pa)	F	p
Between groups	3.22E+11	4	8.06E+10	272.83	< 0.001
Within groups	5.91E+09	20	2.95E+08		
Total	3.28E+11	24			

Tukey Post Hoc Results

	B	C	D	E
A	< 0.001	0.037	0.012	0.146
B		< 0.001	< 0.001	< 0.001
C			< 0.001	0.953
D				< 0.001

Short protector supporting foam - compression testing

Descriptive Statistics

Samples	No.	Mean (Pa)	St Dev (Pa)	95% Confidence Interval for Mean (Pa)		Coefficient of variance
				Lower Bound	Upper Bound	
				A	5	
B	5	141,220	1,097	138,873	143,568	0.78
C	5	149,156	4,646	146,808	151,503	3.12
D	5	123,585	1,376	121,238	125,933	1.11
E	5	139,492	1,290	137,145	141,840	0.92
Overall	25	137,122	9,134	130,234	142,225	6.66

ANOVA Results

Source of Variance	SS (Pa)	df	MS (Pa)	F	p
Between groups	1.88E+09	4	4.69E+08	74.05	< 0.001
Within groups	1.27E+08	20	6.33E+06		
Total	2.00E+09	24			

Tukey Post Hoc Results

	B	C	D	E
A	< 0.001	< 0.001	< 0.001	< 0.001
B		< 0.001	< 0.001	0.812
C			< 0.001	< 0.001
D				< 0.001

Short protector strap - tensile testing

Descriptive Statistics

Samples	No.	Mean (Pa)	St Dev (Pa)	95% Confidence Interval for Mean (Pa)		Coefficient of variance
				Lower Bound	Upper Bound	
				A	5	
B	5	14,429,375	338,378	13,655,346	15,203,404	2.35
C	5	14,168,750	938,884	13,394,721	14,942,779	6.63
D	5	12,712,500	1,127,714	11,938,471	13,486,529	8.87
E	5	14,430,000	737,902	13,655,971	15,204,029	5.11
Overall	25	13,998,125	1,007,438	13,509,375	14,681,250	7.20

ANOVA Results

Source of Variance	SS (Pa)	df	MS (Pa)	F	p
Between groups	1.06E+13	4	2.65E+12	3.85	0.018
Within groups	1.38E+13	20	6.88E+11		
Total	2.44E+13	24			

Tukey Post Hoc Results

	B	C	D	E
A	0.997	1.000	0.057	0.997
B		0.987	0.028	1.000
C			0.077	0.987
D				0.028

Short protector splint – three point bend test

Descriptive Statistics

Samples	No.	Mean (N)	St Dev (N)	95% Confidence Interval for		Coefficient of variance
				Mean (N)		
				Lower Bound	Upper Bound	
A	5	19.60	0.11	19.19	20.02	0.58
B	5	35.06	0.35	34.64	35.47	0.98
C	5	21.53	0.27	21.11	21.94	1.24
D	5	31.08	0.69	30.67	31.49	2.22
E	5	31.37	0.55	30.96	31.78	1.74
Overall	25	27.73	6.18	21.26	32.04	22.30

ANOVA Results

Source of Variance	SS (N)	df	MS (N)	F	p
Between groups	913.31	4	228.33	1166.10	< 0.001
Within groups	3.92	20	0.20		
Total	917.22	24			

Tukey Post Hoc Results

	B	C	D	E
A	< 0.001	< 0.001	< 0.001	< 0.001
B		< 0.001	< 0.001	< 0.001
C			< 0.001	< 0.001
D				0.512

Long protector D3O® - compression testing

Descriptive Statistics

Samples	No.	Mean (Pa)	St Dev (Pa)	95% Confidence Interval for		Coefficient of variance
				Mean (Pa)		
				Lower Bound	Upper Bound	
A	5	16,957	182	16,679	17,234	1.07
B	5	27,529	365	27,251	27,806	1.33
C	5	27,710	220	27,432	27,987	0.79
D	5	36,245	362	35,968	36,523	1.00
E	5	23,652	311	23,375	23,930	1.31
Overall	25	26,419	6,406	23,446	27,475	24.25

ANOVA Results

Source of Variance	SS (Pa)	df	MS (Pa)	F	p
Between groups	9.83E+08	4	2.46E+08	2779.25	<0.001
Within groups	1.77E+06	20	8.84E+04		
Total	9.85E+08	24			

Tukey Post Hoc Results

	B	C	D	E
A	< 0.001	< 0.001	< 0.001	< 0.001
B		0.869	< 0.001	< 0.001
C			< 0.001	< 0.001
D				< 0.001

Long protector supporting foam - compression testing

Descriptive Statistics

Samples	No.	Mean (Pa)	St Dev (Pa)	95% Confidence Interval for		Coefficient of variance
				Mean (Pa)		
				Lower Bound	Upper Bound	
A	5	32,545	2,143	30,647	34,444	6.58
B	5	53,751	1,258	51,853	55,650	2.34
C	5	42,703	1,625	40,804	44,602	3.81
D	5	45,710	3,232	43,811	47,608	7.07
E	5	58,446	1,205	56,548	60,345	2.06
Overall	25	46,631	9,371	40,274	46,358	20.10

ANOVA Results

Source of Variance	SS (Pa)	df	MS (Pa)	F	p
Between groups	2.02E+09	4	5.06E+08	122.21	<0.001
Within groups	8.28E+07	20	4.14E+06		
Total	2.11E+09	24			

Tukey Post Hoc Results

	B	C	D	E
A	< 0.001	< 0.001	< 0.001	< 0.001
B		< 0.001	< 0.001	0.012
C			0.175	< 0.001
D				< 0.001

Long protector supporting foam - tensile testing

Descriptive Statistics

Samples	No.	Mean (Pa)	St Dev (Pa)	95% Confidence Interval for Mean (Pa)		Coefficient of variance
				Lower Bound	Upper Bound	
				A	5	
B	5	616,500	91,012	504,721	728,279	14.76
C	5	810,125	167,826	698,346	921,904	20.72
D	5	747,000	119,235	635,221	858,779	15.96
E	5	669,625	76,208	557,846	781,404	11.38
Overall	25	718,925	129,510	613,750	787,500	18.01

ANOVA Results

Source of Variance	SS (Pa)	df	MS (Pa)	F	p
Between groups	1.15E+11	4	2.89E+10	2.01	0.132
Within groups	2.87E+11	20	1.44E+10		
Total	4.03E+11	24			

Tukey Post Hoc Results

	B	C	D	E
A	0.412	0.935	1.000	0.815
B		0.118	0.444	0.954
C			0.917	0.372
D				0.843

Long protector strap - tensile testing

Descriptive Statistics

Samples	No.	Mean (Pa)	St Dev (Pa)	95% Confidence Interval for Mean (Pa)		Coefficient of variance
				Lower Bound	Upper Bound	
				A	5	
B	5	11,800,000	710,634	11,336,158	12,263,842	6.02
C	5	11,540,000	622,227	11,076,158	12,003,842	5.39
D	5	11,910,000	193,506	11,446,158	12,373,842	1.62
E	5	11,493,333	467,499	11,029,491	11,957,176	4.07
Overall	25	11,568,000	537,784	11,200,000	12,000,000	4.65

ANOVA Results

Source of Variance	SS (Pa)	df	MS (Pa)	F	p
Between groups	2.00E+12	4	4.99E+11	2.02	0.130
Within groups	4.94E+12	20	2.47E+11		
Total	6.94E+12	24			

Tukey Post Hoc Results

	B	C	D	E
A	0.207	0.629	0.111	0.717
B		0.919	0.997	0.863
C			0.764	1.000
D				0.680

Long protector splint – three point bend test

Descriptive Statistics

Samples	No.	Mean (N)	St Dev (N)	95% Confidence Interval for		Coefficient of variance
				Mean (N)		
				Lower Bound	Upper Bound	
A	5	155.72	5.89	150.84	160.60	3.78
B	5	121.69	3.45	116.81	126.57	2.83
C	5	156.40	3.44	151.52	161.28	2.20
D	5	155.07	5.25	150.19	159.95	3.38
E	5	152.48	7.13	147.60	157.36	4.67
Overall	25	148.27	2.89	144.90	158.40	9.74

ANOVA Results

Source of Variance	SS (N)	df	MS (N)	F	p
Between groups	4460.30	4	1115.07	40.76	< 0.001
Within groups	547.10	20	27.35		
Total	5007.40	24			

Tukey Post Hoc Results

	B	C	D	E
A	< 0.001	1.000	0.988	0.211
B		< 0.001	< 0.001	< 0.001
C			0.958	0.289
D				0.088

10.D.2 Chapter 4

A one way ANOVA was used to compare all five samples at one impact energy in terms of peak force, maximum compression and impact duration.

Short protector pad – 2.5 J

Descriptive Statistics

Samples	No.	Force					Maximum Compression					Impact duration				
		Mean (N)	St Dev (N)	95% Confidence Interval for Mean (N)		Coefficient of variance	Mean (mm)	St Dev (mm)	95% Confidence Interval for Mean (mm)		Coefficient of variance	Mean (ms)	St Dev (ms)	95% Confidence Interval for Mean (ms)		Coefficient of variance
				Lower	Upper				Lower	Upper				Lower	Upper	
A	5	3,099	13	3,073	3,125	0.42	0.60	0.05	0.54	0.66	8.39	1.94	0.04	1.90	1.99	2.31
B	5	2,204	37	2,178	2,230	1.67	0.91	0.08	0.85	0.97	9.19	2.71	0.09	2.67	2.76	3.26
C	5	3,922	35	3,896	3,948	0.90	0.60	0.05	0.55	0.66	7.91	1.62	0.01	1.57	1.66	0.52
D	5	2,897	29	2,872	2,923	0.99	0.65	0.07	0.59	0.70	10.27	2.37	0.01	2.32	2.41	0.38
E	5	3,791	16	3,765	3,816	0.41	0.65	0.05	0.60	0.71	7.50	1.66	0.03	1.61	1.70	1.94
Overall	25	3,183	640	3,094	3,954	20.11	0.68	0.13	0.58	0.70	19.11	2.06	0.43	1.64	2.38	21.06

ANOVA Results

Source of Variance	Force					Maximum Compression					Impact duration				
	SS (N)	df	MS (N)	F	p	SS (mm)	df	MS (mm)	F	p	SS (ms)	df	MS (ms)	F	p
Between groups	9.81E+06	4	2.45E+06	3,211	< 0.001	0.33	4	0.084	22.43	< 0.001	4.47	4	1.117	506.49	< 0.001
Within groups	15,274	20	746			0.07	20	0.004			0.04	20	0.002		
Total	9.83E+06	24				0.41	24				4.51	24			

Tukey Post Hoc Results

	Force					Maximum Compression					Impact Duration			
	B	C	D	E		B	C	D	E		B	C	D	E
A	< 0.001	< 0.001	< 0.001	< 0.001	A	< 0.001	1.000	0.735	0.623	A	< 0.001	< 0.001	< 0.001	< 0.001
B		< 0.001	< 0.001	< 0.001	B		< 0.001	< 0.001	< 0.001	B		< 0.001	< 0.001	< 0.001
C			< 0.001	< 0.001	C			0.799	0.694	C			< 0.001	0.706
D				< 0.001	D				1.000	D				< 0.001

Short protector pad + shell – 2.5 J

Descriptive Statistics

Samples	No.	Force					Maximum Compression					Impact duration				
		Mean (N)	St Dev (N)	95% Confidence Interval for Mean (N)		Coefficient of variance	Mean (mm)	St Dev (mm)	95% Confidence Interval for Mean (mm)		Coefficient of variance	Mean (ms)	St Dev (ms)	95% Confidence Interval for Mean (ms)		Coefficient of variance
				Lower	Upper				Lower	Upper				Lower	Upper	
A	5	2,830	10	2,795	2,866	0.36	0.65	0.06	0.58	0.72	8.75	2.80	0.04	2.77	2.82	1.44
B	5	2,073	57	2,038	2,108	2.75	0.94	0.08	0.87	1.01	8.94	2.86	0.02	2.84	2.89	0.87
C	5	3,669	41	3,634	3,704	1.13	0.63	0.07	0.56	0.70	10.57	2.00	0.02	1.98	2.02	0.79
D	5	2,614	40	2,579	2,649	1.54	0.81	0.10	0.74	0.88	12.76	2.64	0.02	2.62	2.66	0.71
E	5	3,496	20	3,461	3,531	0.57	0.84	0.05	0.77	0.91	5.83	2.00	0.02	1.98	2.02	0.79
Overall	25	2,936	598	2,576	3,512	20.36	0.77	0.14	0.69	0.92	18.04	2.46	0.39	2.01	2.81	15.88

ANOVA Results

Source of Variance	Force					Maximum Compression					Impact duration				
	SS (N)	df	MS (N)	F	p	SS (mm)	df	MS (mm)	F	p	SS (ms)	df	MS (ms)	F	p
Between groups	8.55E+06	4	2.14E+06	1512	< 0.001	0.36	4	0.089	15.96	< 0.001	3.65	4	0.913	1471.97	< 0.001
Within groups	28,290	20	1,414			0.11	20	0.006			0.01	20	0.001		
Total	8.58E+06	24				0.47	24				3.66	24			

Tukey Post Hoc Results

	Force					Maximum Compression					Impact Duration			
	B	C	D	E		B	C	D	E		B	C	D	E
A	< 0.001	< 0.001	< 0.001	< 0.001	A	< 0.001	0.990	0.017	0.006	A	0.004	< 0.001	< 0.001	< 0.001
B		< 0.001	< 0.001	< 0.001	B		< 0.001	0.087	0.201	B		< 0.001	< 0.001	< 0.001
C			< 0.001	< 0.001	C			0.006	0.002	C			< 0.001	1.000
D				< 0.001	D				0.990	D				< 0.001

Scenario	Peak force			Maximum Compression			Impact Duration		
	t	df	P value	t	df	P value	t	df	P value
Pad vs. Pad + Shell	1.00	45	0.322	3.20	45	0.003	3.40	47	0.001

Short protector supporting foam – 2.5 J

Descriptive Statistics

		Force					Maximum Compression					Impact duration				
Samples	No.	Mean (N)	St Dev (N)	95% Confidence Interval for Mean (N)		Coefficient of variance	Mean (mm)	St Dev (mm)	95% Confidence Interval for Mean (mm)		Coefficient of variance	Mean (ms)	St Dev (ms)	95% Confidence Interval for Mean (ms)		Coefficient of variance
				Lower	Upper				Lower	Upper				Lower	Upper	
				A	4				3,043	125				2,943	3,143	
B	4	2,644	80	2,544	2,744	3.01	6.17	0.15	6.00	6.34	2.43	8.70	0.27	8.55	8.85	3.07
C	4	2,902	102	2,802	3,002	3.50	5.67	0.10	5.49	5.84	1.81	8.33	0.07	8.18	8.48	0.86
D	4	2,932	85	2,832	3,032	2.88	5.99	0.18	5.81	6.16	3.04	8.33	0.06	8.17	8.48	0.74
E	4	2,986	68	2,886	3,086	2.29	5.99	0.18	5.81	6.16	3.04	8.29	0.05	8.14	8.44	0.57
Overall	20	2,901	164	2,788	3,023	5.65	5.77	0.44	5.56	6.07	7.61	8.41	0.20	8.29	8.44	2.36

ANOVA Results

Source of Variance	Force						Maximum Compression						Impact duration					
	SS (N)	df	MS (N)	F	p		SS (mm)	df	MS (mm)	F	p	SS (ms)	df	MS (ms)	F	p		
Between groups	3.78E+05	4	94,461	10.72	< 0.001		3.27	4	0.816	30.85	< 0.001	0.45	4	0.111	5.49	0.006		
Within groups	1.32E+05	15	8,814				0.40	15	0.026			0.30	15	0.020				
Total	5.10E+05	19					3.66	19				0.75	19					

Tukey Post Hoc Results

Force						Maximum Compression						Impact Duration					
	B	C	D	E		B	C	D	E		B	C	D	E			
A	< 0.001	0.260	0.474	0.908	A	< 0.001	< 0.001	< 0.001	< 0.001	A	0.054	0.970	0.965	0.855			
B		0.011	0.005	< 0.001	B		0.004	0.513	0.516	B		0.016	0.016	0.008			
C			0.991	0.714	C			0.088	0.087	C			1.000	0.995			
D				0.920	D				1.000	D				0.997			

Short protector all palmar components (pad, shell + supporting foam) – 5 J

Descriptive Statistics

		Force					Maximum Compression					Impact duration				
Samples	No.	Mean (N)	St Dev (N)	95% Confidence Interval for Mean (N)		Coefficient of variance	Mean (mm)	St Dev (mm)	95% Confidence Interval for Mean (mm)		Coefficient of variance	Mean (ms)	St Dev (ms)	95% Confidence Interval for Mean (ms)		Coefficient of variance
				Lower	Upper				Lower	Upper				Lower	Upper	
				A	4				1,915	71				1,860	1,970	
B	4	1,454	34	1,400	1,509	2.33	8.00	0.46	7.70	8.29	5.78	11.67	0.14	11.45	11.90	1.16
C	4	2,534	52	2,479	2,588	2.06	6.43	0.18	6.14	6.73	2.85	8.62	0.05	8.39	8.84	0.54
D	4	1,906	48	1,851	1,961	2.53	7.47	0.16	7.17	7.76	2.15	9.43	0.06	9.20	9.66	0.65
E	4	2,311	45	2,256	2,366	1.93	6.75	0.18	6.45	7.05	2.73	8.69	0.08	8.46	8.91	0.87
Overall	20	2,024	385	1,860	2,355	19.00	7.23	0.63	6.64	7.63	8.68	9.81	1.23	8.65	11.01	12.50

ANOVA Results

Source of Variance	Force					Maximum Compression					Impact duration				
	SS (N)	df	MS (N)	F	p	SS (mm)	df	MS (mm)	F	p	SS (ms)	df	MS (ms)	F	p
Between groups	2.77E+06	4	6.92E+05	261.68	< 0.001	6.33	4	1.582	20.53	< 0.001	27.88	4	6.969	155.35	< 0.001
Within groups	3.97E+04	15	2,645			1.16	15	0.077			0.67	15	0.045		
Total	2.81E+06	19				7.49	19				28.55	19			

Tukey Post Hoc Results

Force					Maximum Compression					Impact Duration				
	B	C	D	E		B	C	D	E		B	C	D	E
A	< 0.001	< 0.001	0.999	< 0.001	A	0.127	< 0.001	1.000	0.013	A	< 0.001	< 0.001	< 0.001	< 0.001
B		< 0.001	< 0.001	< 0.001	B		< 0.001	0.100	< 0.001	B		< 0.001	< 0.001	< 0.001
C			< 0.001	< 0.001	C			< 0.001	0.512	C			< 0.001	0.991
D				< 0.001	D				0.017	D				< 0.001

Long protector D3O® – 0.5 J

Descriptive Statistics

Samples	No.	Force					Maximum Compression					Impact duration				
		Mean (N)	St Dev (N)	95% Confidence Interval for Mean (N)		Coefficient of variance	Mean (mm)	St Dev (mm)	95% Confidence Interval for Mean (mm)		Coefficient of variance	Mean (ms)	St Dev (ms)	95% Confidence Interval for Mean (ms)		Coefficient of variance
				Lower	Upper				Lower	Upper				Lower	Upper	
A	4	571	5	565	577	0.83	2.99	0.07	2.87	3.10	2.35	10.66	0.02	10.58	10.73	0.22
B	4	551	3	545	558	0.53	2.93	0.17	2.81	3.04	5.89	10.41	0.08	10.33	10.48	0.74
C	4	569	2	563	576	0.29	2.87	0.07	2.75	2.98	2.46	10.09	0.07	10.02	10.16	0.73
D	4	547	10	541	554	1.75	3.14	0.12	3.03	3.25	3.72	10.56	0.10	10.49	10.63	0.91
E	4	573	7	567	580	1.21	2.83	0.06	2.72	2.95	2.15	10.43	0.03	10.35	10.50	0.28
Overall	20	562	12	552	571	2.19	2.95	0.15	2.80	3.05	4.95	10.43	0.21	10.34	10.63	1.98

ANOVA Results

Source of Variance	Force					Maximum Compression					Impact duration				
	SS (N)	df	MS (N)	F	p	SS (mm)	df	MS (mm)	F	p	SS (ms)	df	MS (ms)	F	p
Between groups	2,354	4	588	16.93	< 0.001	0.23	4	0.058	5.13	0.008	0.74	4	0.185	42.16	< 0.001
Within groups	521	15	35			0.17	15	0.011			0.07	15	0.004		
Total	2,875	19				0.40	19				0.81	19			

Tukey Post Hoc Results

	Force				Maximum Compression				Impact Duration					
	B	C	D	E	B	C	D	E	B	C	D	E		
A	0.002	0.995	< 0.001	0.970	A	0.919	0.501	0.311	0.297	A	< 0.001	< 0.001	0.301	0.002
B		0.005	0.891	< 0.001	B		0.924	0.081	0.745	B		< 0.001	0.033	0.992
C			< 0.001	0.851	C			0.018	0.994	C			< 0.001	< 0.001
D				< 0.001	D				0.008	D				0.073

Long protector supporting foam – 0.5 J

Descriptive Statistics

Samples	No.	Force					Maximum Compression					Impact duration				
		Mean (N)	St Dev (N)	95% Confidence Interval for Mean (N)		Coefficient of variance	Mean (mm)	St Dev (mm)	95% Confidence Interval for Mean (mm)		Coefficient of variance	Mean (ms)	St Dev (ms)	95% Confidence Interval for Mean (ms)		Coefficient of variance
				Lower	Upper				Lower	Upper				Lower	Upper	
A	4	1,019	14	1,003	1,034	1.36	3.48	0.21	3.30	3.65	6.08	8.18	0.05	7.94	8.43	0.66
B	4	966	16	950	981	1.70	3.75	0.12	3.58	3.92	3.11	9.12	0.02	8.87	9.36	0.21
C	4	1,016	23	1,000	1,032	2.22	3.32	0.21	3.15	3.49	6.27	8.22	0.02	7.97	8.46	0.29
D	4	1,017	3	1,002	1,033	0.25	3.51	0.12	3.33	3.68	3.31	8.25	0.04	8.00	8.50	0.49
E	4	980	10	965	996	1.01	3.47	0.12	3.30	3.65	3.51	8.67	0.51	8.43	8.92	5.90
Overall	20	1,000	26	983	1,023	2.63	3.51	0.20	3.41	3.66	5.74	8.49	0.42	8.20	8.93	4.99

ANOVA Results

Source of Variance	Force					Maximum Compression					Impact duration				
	SS (N)	df	MS (N)	F	p	SS (mm)	df	MS (mm)	F	p	SS (ms)	df	MS (ms)	F	p
Between groups	9,872	4	2,468	11.47	< 0.001	0.38	4	0.095	3.65	0.029	2.60	4	0.650	12.16	< 0.001
Within groups	3,228	15	215			0.39	15	0.026			0.80	15	0.053		
Total	13,101	19				0.77	19				3.40	19			

Tukey Post Hoc Results

	Force					Maximum Compression					Impact Duration			
	B	C	D	E		B	C	D	E		B	C	D	E
A	< 0.001	0.999	1.000	0.016	A	0.167	0.674	0.999	1.000	A	< 0.001	0.999	0.993	0.059
B		0.002	< 0.001	0.635	B		0.014	0.256	0.167	B		< 0.001	< 0.001	0.100
C			1.000	0.025	C			0.514	0.674	C			1.000	0.087
D				0.019	D				0.999	D				0.124

Long protector all palmar components (D3O® + supporting foam) – 2.5 J

Descriptive Statistics

Samples	No.	Force					Maximum Compression					Impact duration				
		Mean (N)	St Dev (N)	95% Confidence Interval for Mean (N)		Coefficient of variance	Mean (mm)	St Dev (mm)	95% Confidence Interval for Mean (mm)		Coefficient of variance	Mean (ms)	St Dev (ms)	95% Confidence Interval for Mean (ms)		Coefficient of variance
				Lower	Upper				Lower	Upper				Lower	Upper	
A	4	2,992	41	2,939	3,045	1.37	7.22	0.34	7.02	7.41	4.76	9.01	0.03	8.97	9.05	0.32
B	4	2,810	54	2,757	2,864	1.93	7.06	0.13	6.86	7.25	1.86	9.05	0.06	9.01	9.09	0.65
C	4	2,868	57	2,815	2,922	1.99	6.90	0.10	6.71	7.09	1.44	8.99	0.03	8.95	9.02	0.32
D	4	2,847	39	2,794	2,900	1.39	7.16	0.10	6.97	7.36	1.42	8.94	0.04	8.90	8.98	0.39
E	4	2,890	55	2,837	2,943	1.92	7.06	0.10	6.86	7.25	1.41	8.96	0.02	8.92	9.00	0.23
Overall	20	2,882	77	2,827	2,937	2.67	7.08	0.30	6.98	7.19	2.77	8.99	0.05	8.95	9.02	0.58

ANOVA Results

Source of Variance	Force					Maximum Compression					Impact duration				
	SS (N)	df	MS (N)	F	p	SS (mm)	df	MS (mm)	F	p	SS (ms)	df	MS (ms)	F	p
Between groups	74,881	4	18,720	7.48	0.002	0.23	4	0.058	1.77	0.188	0.03	4	0.008	5.85	0.005
Within groups	37,553	15	2,504			0.50	15	0.033			0.02	15	0.001		
Total	112,435	19				0.73	19				0.05	19			

Tukey Post Hoc Results

	Force				Maximum Compression				Impact Duration					
	B	C	D	E	B	C	D	E	B	C	D	E		
A	< 0.001	0.023	0.007	0.073	A	0.737	0.156	0.994	0.738	A	0.558	0.826	0.074	0.350
B		0.498	0.838	0.214	B		0.739	0.921	1.000	B		0.123	0.004	0.025
C			0.972	0.971	C			0.294	0.738	C			0.398	0.906
D				0.740	D				0.922	D				0.896

10.D.3Chapter 6

A two-sample t-test was performed to understand whether there was a significant difference between an unprotected and protected impact in terms of peak force. A t-test was also used to see whether there was a difference between the two styles of protectors (short and long) in terms of peak force, wrist angle and energy absorbed. A brand new protector was compared to a protector that had been previously impacted (denoted by protector A in the tables) to see if there was a significant difference in peak force, wrist angle and energy absorbed, across all five impact energies (10 to 50 J). Finally, bare hand impacts at the start of an impact energy were compared to bare hand impacts at the end of each energy to check for degradation of the polychloroprene.

Bare Hand – Descriptive statistics					
Energy (J)		N	Mean (N)	St. Dev (N)	St. Error Mean
10	Before	3	3,094	63	37
	After	3	3,283	15	8
	Overall	6	3,189	111	45
20	Before	3	5,041	69	40
	After	3	4,770	50	29
	Overall	6	4,906	158	64
30	Before	3	6,923	223	129
	After	3	6,952	132	76
	Overall	6	6,938	165	67
40	Before	3	9,487	365	211
	After	3	9,152	100	58
	Overall	6	9,320	301	123
50	Before	3	10,692	126	72
	After	3	10,595	394	227
	Overall	6	10,644	267	109
Overall	Before	15	7,053	2,891	747
	After	15	6,945	2,796	722
	Overall	30	6,999	2,795	510

Short Protector - Descriptive statistics

	Energy (J)	N	Mean (N)	St. Dev (N)	St. Error Mean
10	Overall - Force	5	1,035	46	20
	Overall – Wrist Angle	5	88.31	3.11	1.39
	Overall – Energy absorption	5	23.20	2.59	1.16
20	Protector A - Force	5	2,227	351	157
	New protector - Force	5	1,929	376	168
	Overall - Force	10	2,078	377	119
	Protector A – Wrist angle	5	94.75	0.83	0.37
	New protector – Wrist Angle	5	95.17	1.74	0.78
	Overall – Wrist Angle	10	94.96	1.31	0.41
	Protector A – Energy absorption	5	19.70	1.40	0.62
30	New protector – Energy absorption	5	20.10	1.29	0.58
	Overall – Energy absorption	10	19.90	1.29	0.41
	Protector A - Force	5	3,990	66	29
	New protector - Force	5	3,072	331	148
	Overall - Force	10	3,531	533	169
	Protector A – Wrist angle	5	97.33	0.68	0.30
	New protector – Wrist Angle	5	99.84	2.15	0.96
40	Overall – Wrist Angle	10	98.59	2.00	0.63
	Protector A – Energy absorption	5	14.60	0.49	0.22
	New protector – Energy absorption	5	21.20	3.19	1.40
	Overall – Energy absorption	10	17.90	4.09	1.29
	Protector A - Force	5	5,667	386	173
	New protector - Force	5	4,372	732	327
	Overall - Force	10	5,020	878	277
50	Protector A – Wrist angle	5	98.97	1.39	0.62
	New protector – Wrist Angle	5	107.71	4.33	1.90
	Overall – Wrist Angle	10	103.34	5.51	1.74
	Protector A – Energy absorption	5	14.30	1.05	0.47
	New protector – Energy absorption	5	24.55	4.51	2.00
	Overall – Energy absorption	10	19.43	6.22	1.97
	All	Protector A - Force	5	7,669	522
New protector - Force		5	5,549	1294	579
Overall - Force		10	6,609	1454	460
Protector A – Wrist angle		5	100.88	0.50	0.22
New protector – Wrist Angle		5	110.89	2.62	1.20
Overall – Wrist Angle		10	105.88	5.57	1.76
Protector A – Energy absorption		5	13.96	0.62	0.28
All	New protector – Energy absorption	5	24.78	2.86	1.30
	Overall – Energy absorption	10	19.37	6.03	1.91
	Protector A - Force	20	4,888	2,095	468
	New protector - Force	20	3,730	1,570	351
	Overall - Force	40	4,309	1,919	303
	Protector A – Wrist angle	20	97.98	2.45	0.55
	New protector – Wrist Angle	20	103.41	6.91	1.50
All	Overall – Wrist Angle	40	100.69	5.81	0.92
	Protector A – Energy absorption	20	15.64	2.57	0.58
	New protector – Energy absorption	20	22.66	3.59	0.80
Overall – Energy absorption	40	19.15	4.71	0.74	

Long Protector - Descriptive statistics

	Energy (J)	N	Mean (N)	St. Dev (N)	St. Error Mean
10	Overall - Force	5	1245	155	69
	Overall – Wrist Angle	5	82.84	4.52	2.02
	Overall – Energy absorption	5	20.00	6.04	2.70
20	Protector A - Force	5	1988	96	43
	New protector - Force	5	1877	230	103
	Overall - Force	10	1933	176	56
	Protector A – Wrist angle	5	85.79	2.91	1.30
	New protector – Wrist Angle	5	84.89	2.05	0.92
	Overall – Wrist Angle	10	85.34	2.42	0.77
	Protector A – Energy absorption	5	15.40	3.70	1.70
	New protector – Energy absorption	5	19.57	1.67	0.75
	Overall – Energy absorption	10	17.48	3.49	1.10
30	Protector A - Force	5	3362	579	259
	New protector - Force	5	3272	356	159
	Overall - Force	10	3317	456	144
	Protector A – Wrist angle	5	94.23	1.02	0.45
	New protector – Wrist Angle	5	93.36	3.08	1.40
	Overall – Wrist Angle	10	93.80	2.21	0.70
	Protector A – Energy absorption	5	25.33	1.35	0.61
	New protector – Energy absorption	5	31.29	5.11	2.30
	Overall – Energy absorption	10	28.31	4.72	1.49
40	Protector A - Force	5	4607	188	84
	New protector - Force	5	4498	409	183
	Overall - Force	10	4553	306	97
	Protector A – Wrist angle	5	103.93	0.56	0.25
	New protector – Wrist Angle	5	101.25	2.14	0.96
	Overall – Wrist Angle	10	102.59	2.04	0.65
	Protector A – Energy absorption	5	44.79	3.18	1.40
	New protector – Energy absorption	5	43.44	3.10	1.40
	Overall – Energy absorption	10	44.12	3.05	0.96
50	Protector A - Force	5	4763	79	35
	New protector - Force	5	4689	111	50
	Overall - Force	10	4726	99	31
	Protector A – Wrist angle	5	110.45	1.26	0.56
	New protector – Wrist Angle	5	106.79	3.80	1.70
	Overall – Wrist Angle	10	108.62	3.29	1.04
	Protector A – Energy absorption	5	50.64	1.97	0.88
	New protector – Energy absorption	5	44.07	6.11	2.70
	Overall – Energy absorption	10	47.36	5.51	1.74
All	Protector A - Force	20	3680	1181	264
	New protector - Force	20	3584	1187	265
	Overall - Force	40	3632	1170	185
	Protector A – Wrist angle	20	98.60	9.75	2.20
	New protector – Wrist Angle	20	96.57	8.87	2.00
	Overall – Wrist Angle	40	97.59	9.26	1.46
	Protector A – Energy absorption	20	34.00	14.90	3.30
	New protector – Energy absorption	20	34.60	11.10	2.50
	Overall – Energy absorption	40	34.32	12.93	2.04

Paired samples tests

Pair	t-test scenario	Energy (J)	t	df	P value
1	Bare Hand Vs. Protector	10	30.71	13	< 0.001
		20	31.39	16	< 0.001
		30	27.60	23	< 0.001
		40	20.64	22	< 0.001
		50	15.08	22	< 0.001
		Overall	6.18	37	< 0.001
2	Protector A vs. fresh protector (force – short)	20	1.30	7	0.236
		30	6.08	4	0.004
		40	3.50	6	0.013
		50	3.40	5	0.019
		Overall	1.98	35	0.056
3	Protector A vs. fresh protector (wrist angle – short)	20	0.49	5	0.643
		30	2.49	4	0.067
		40	4.30	4	0.013
		50	8.39	4	0.001
		Overall	3.31	23	0.003
4	Protector A vs. fresh protector (energy absorption – short)	20	-0.47	7	0.653
		30	-4.57	4	0.010
		40	-4.95	4	0.008
		50	-8.27	4	0.001
		Overall	-7.10	34	<0.001
5	Protector A vs. fresh protector (force – long)	20	1.00	5	0.364
		30	0.30	6	0.777
		40	0.54	5	0.613
		50	1.22	7	0.262
		Overall	0.26	37	0.799
6	Protector A vs. fresh protector (wrist angle – long)	20	0.56	7	0.592
		30	0.60	4	0.582
		40	2.72	4	0.053
		50	2.05	4	0.110
		Overall	0.69	37	0.496
7	Protector A vs. fresh protector (energy absorption – long)	20	-2.30	5	0.070
		30	-2.52	4	0.065
		40	0.68	7	0.519
		50	2.29	4	0.084
		Overall	-0.13	35	0.895

Pair	t-test scenario	Energy (J)	t	df	P value
8	Short vs. long protector (force)	10	2.92	4	0.043
		20	1.10	12	0.292
		30	0.96	17	0.349
		40	1.59	11	0.140
		50	4.09	9	0.003
		Overall	1.57	74	0.121
9	Short vs. long protector (wrist angle)	10	2.23	7	0.061
		20	11.07	13	< 0.001
		30	5.08	17	< 0.001
		40	0.40	11	0.696
		50	1.34	14	0.203
		Overall	1.87	77	0.065
10	Short vs. long protector (energy absorption)	10	1.09	5	0.326
		20	2.06	11	0.064
		30	-5.27	17	< 0.001
		40	-11.27	13	< 0.001
		50	-10.84	17	< 0.001
		Overall	-6.97	49	< 0.001
11	Bare hand before vs. after	10	5.03	2	0.037
		20	5.52	3	0.012
		30	0.20	3	0.856
		40	1.53	2	0.265
		50	0.41	2	0.723
		Overall	0.10	27	0.917

10.D.4 Chapter 7

A one way ANOVA was performed to compare the stress for each sample at 50% strain for compression testing. A one way ANOVA was also used to compare all five samples at a 5 J impact in terms of peak force, maximum compression and impact duration.

Polychloroprene – compression test**Descriptive Statistics**

Samples	No.	Mean (N)	St Dev (N)	95% Confidence Interval for		Coefficient of variance
				Mean (N)		
				Lower Bound	Upper Bound	
A	5	2,559,882	12,569	2,517,124	2,602,640	0.49
B	5	2,181,525	50,929	2,138,767	2,224,283	2.33
C	5	2,363,782	73,069	2,321,024	2,406,540	3.09
D	5	2,425,857	30,687	2,383,099	2,468,615	1.26
E	5	2,226,935	38,362	2,184,177	2,269,693	1.72
Overall	25	2,351,596	145,712	2,218,470	2,363,076	6.20

ANOVA Results

Source of Variance	SS (N)	df	MS (N)	F	p
Between groups	4.68E+11	4	1.17E+11	55.64	< 0.001
Within groups	4.20E+10	20	2.10E+09		
Total	5.10E+11	24			

Tukey Post Hoc Results

	B	C	D	E
A	< 0.001	< 0.001	0.001	< 0.001
B		< 0.001	< 0.001	0.534
C			0.242	0.001
D				< 0.001

Polychloroprene Impact – 5 J

Descriptive Statistics

Samples	No.	Force					Maximum Compression					Impact duration				
		Mean (N)	St Dev (N)	95% Confidence Interval for Mean (N)		Coefficient of variance	Mean (mm)	St Dev (mm)	95% Confidence Interval for Mean (mm)		Coefficient of variance	Mean (ms)	St Dev (ms)	95% Confidence Interval for Mean (ms)		Coefficient of variance
				Lower	Upper				Lower	Upper				Lower	Upper	
A	5	1,649	159	1,401	1,898	9.65	5.17	0.18	5.03	5.30	3.56	14.10	0.64	13.63	14.57	4.51
B	5	1,779	308	1,531	2,028	17.29	5.08	0.12	4.95	5.21	2.37	14.82	0.48	14.35	15.29	3.21
C	5	1,745	77	1,497	1,993	4.41	5.17	0.10	5.03	5.30	1.90	13.76	0.51	13.29	14.23	3.73
D	5	1,873	456	1,624	2,121	24.37	5.25	0.10	5.12	5.39	1.87	13.88	0.44	13.41	14.35	3.20
E	5	1,589	142	1,340	1,837	8.91	5.03	0.18	4.90	5.17	3.66	14.48	0.40	14.01	14.95	2.74
Overall	25	1,727	263	1,583	1,805	15.25	5.14	0.15	4.99	5.21	2.96	14.21	0.61	13.70	14.60	4.27

ANOVA Results

Source of Variance	Force						Maximum Compression					Impact duration				
	SS (N)	df	MS (N)	F	p		SS (mm)	df	MS (mm)	F	p	SS (ms)	df	MS (ms)	F	p
Between groups	247,598	4	61,899	0.87	0.497		0.15	4	0.037	1.81	0.167	3.84	4	0.961	3.85	0.018
Within groups	1,417,273	20	70,864				0.41	20	0.020			5.00	20	0.250		
Total	1,664,870	24					0.55	24				8.84	24			

Tukey Post Hoc Results

	Force				Maximum Compression					Impact Duration				
	B	C	D	E	A	B	C	D	E	A	B	C	D	E
A	0.936	0.978	0.678	0.996	A	0.863	1.000	0.863	0.596	A	0.193	0.817	0.955	0.750
B		1.000	0.980	0.787	B		0.863	0.324	0.988	B		0.023	0.052	0.817
C			0.939	0.883	C			0.863	0.596	C			0.995	0.193
D				0.463	D				0.145	D				0.350

10.D.5 Chapter 8

A Pearson's coefficient (r) was computed to assess the relationship between the control parameter (e.g. splint length, thickness, Young's modulus), peak force and maximum wrist angle. A Pearson's r gives an indication as to the strength of the relationship between the two variables, with a larger absolute value indicating a stronger relationship (values between 0 and 1). It can also indicate whether the relationship is significant denoted by a * and bold text in the table ($p < 0.05$).

Splint Length – 40 J					
	Splint Changed (Control)	Statistics	Peak Force	Maximum Wrist Angle	
Short	Both	Pearson's r	-0.81	-0.65	
		P value	0.403	0.546	
		N		3	
	Dorsal	Pearson's r	-0.98		0.29
		P value	0.024*		0.711
		N		4	
	Palmar	Pearson's r	-1		-0.49
		P value	0.044*		0.677
		N		3	
Long	Both	Pearson's r	-0.84	-0.97	
		P value	0.364	0.160	
		N		3	
	Dorsal	Pearson's r	-0.94		-0.99
		P value	0.060		0.014*
		N		4	
	Palmar	Pearson's r	-0.66		-0.50
		P value	0.230		0.389
		N		5	
Both	Both	Pearson's r	-0.25	-0.28	
		P value	0.630	0.587	
		N		6	
	Dorsal	Pearson's r	-0.76		-0.34
		P value	0.029*		0.414
		N		8	
	Palmar	Pearson's r	-0.4		-0.42
		P value	0.329		0.297
		N		8	
All	Pearson's r	-0.52		-0.32	
	P value	0.013*		0.152	
	N		22		

Splint Length – 10 J				
	Splint Changed (Control)	Statistics	Peak Force	Maximum Wrist Angle
Short	Both	Pearson's <i>r</i>	0.78	-0.87
		P value	0.430	0.333
		N		3
	Dorsal	Pearson's <i>r</i>	0.90	-0.78
		P value	0.100	0.219
		N		4
	Palmar	Pearson's <i>r</i>	0.99	-0.91
		P value	0.081	0.266
		N		3
Long	Both	Pearson's <i>r</i>	0.37	-0.97
		P value	0.762	0.154
		N		3
	Dorsal	Pearson's <i>r</i>	-0.99	-0.98
		P value	0.005*	0.020*
		N		4
	Palmar	Pearson's <i>r</i>	0.01	-0.47
		P value	0.983	0.420
		N		5
Both	Both	Pearson's <i>r</i>	0.37	-0.27
		P value	0.473	0.609
		N		6
	Dorsal	Pearson's <i>r</i>	-0.45	-0.50
		P value	0.258	0.211
		N		8
	Palmar	Pearson's <i>r</i>	0.36	-0.13
		P value	0.383	0.762
		N		8
All	Pearson's <i>r</i>	-0.12	-0.33	
	P value	0.596	0.130	
	N		22	

Splint Material – 40 J				
	Splint Changed (Control)	Statistics	Peak Force	Maximum Wrist Angle
Short	Both	Pearson's <i>r</i>	-0.88	-0.87
		P value	0.119	0.129
		N		4
	Dorsal	Pearson's <i>r</i>	-0.97	-0.09
		P value	0.030*	0.914
		N		4
	Palmar	Pearson's <i>r</i>	-0.84	0.89
		P value	0.073	0.041*
		N		5
Long	Both	Pearson's <i>r</i>	-0.93	-0.69
		P value	0.065	0.313
		N		4
	Dorsal	Pearson's <i>r</i>	-0.63	-0.66
		P value	0.365	0.343
		N		4
	Palmar	Pearson's <i>r</i>	-0.95	-0.97
		P value	0.013*	0.007*
		N		5
Both	Both	Pearson's <i>r</i>	Quadratic	-0.62
		P value	0.012*	0.104
		N		8
	Dorsal	Pearson's <i>r</i>	-0.81	-0.46
		P value	0.014*	0.254
		N		8
	Palmar	Pearson's <i>r</i>	-0.87	-0.22
		P value	<0.001*	0.550
		N		10
All	Pearson's <i>r</i>	Quadratic	-0.38	
	P value	<0.001*	0.055	
	N		26	

Splint Material – 10 J				
	Splint Changed (Control)	Statistics	Peak Force	Maximum Wrist Angle
Short	Both	Pearson's <i>r</i>	0.37	-0.78
		P value	0.538	0.121
		N		5
	Dorsal	Pearson's <i>r</i>	0.61	-0.80
		P value	0.196	0.106
		N		5
	Palmar	Pearson's <i>r</i>	0.99	-0.72
		P value	<0.001*	0.171
		N		5
Long	Both	Pearson's <i>r</i>	-0.37	-0.68
		P value	0.541	0.205
		N		5
	Dorsal	Pearson's <i>r</i>	-0.43	-0.65
		P value	0.471	0.238
		N		5
	Palmar	Pearson's <i>r</i>	-0.25	-0.84
		P value	0.636	0.073
		N		5
Both	Both	Pearson's <i>r</i>	-0.04	Quadratic
		P value	0.906	0.020*
		N		10
	Dorsal	Pearson's <i>r</i>	-0.06	-0.64
		P value	0.0871	0.049*
		N		10
	Palmar	Pearson's <i>r</i>	0.42	-0.68
		P value	0.232	0.03*
		N		10
	All	Pearson's <i>r</i>	0.05	Quadratic
		P value	0.791	<0.001*
		N		30

Splint Thickness – 40 J				
	Splint Changed (Control)	Statistics	Peak Force	Maximum Wrist Angle
Short	Dorsal	Pearson's <i>r</i>	-0.99	-0.19
		P value	0.097	0.879
		N		3
	Palmar	Pearson's <i>r</i>	N/A	N/A
		P value	N/A	N/A
		N		2
Long	Dorsal	Pearson's <i>r</i>	-0.92	-0.91
		P value	0.077	0.094
		N		4
	Palmar	Pearson's <i>r</i>	-0.87	-0.87
		P value	0.333	0.333
		N		3
Both	Dorsal	Pearson's <i>r</i>	-0.93	-0.53
		P value	0.002*	0.222
		N		7
	Palmar	Pearson's <i>r</i>	-0.56	-0.63
		P value	0.328	0.257
		N		5
All	Pearson's <i>r</i>	-0.77	-0.57	
	P value	0.003*	0.055	
	N		12	
Splint Thickness – 10 J				
	Splint Changed (Control)	Statistics	Peak Force	Maximum Wrist Angle
Short	Dorsal	Pearson's <i>r</i>	0.95	-0.94
		P value	0.045*	0.064
		N		4
	Palmar	Pearson's <i>r</i>	N/A	N/A
		P value	N/A	N/A
		N		2
Long	Dorsal	Pearson's <i>r</i>	-0.76	-0.95
		P value	0.241	0.050
		N		4
	Palmar	Pearson's <i>r</i>	0.35	-0.80
		P value	0.773	0.407
		N		3
Both	Dorsal	Pearson's <i>r</i>	-0.38	-0.76
		P value	0.354	0.027*
		N		8
	Palmar	Pearson's <i>r</i>	0.52	-0.41
		P value	0.367	0.491
		N		5
All	Pearson's <i>r</i>	-0.18	-0.73	
	P value	0.550	0.005*	
	N		13	

10.E Experimental Testing

10.E.1 Instrumentation Calibration

The Hounsfield HK10S was last calibrated in July 2016 with all load cells, where it was certified that the accuracy of the load cells was to within 1% of its capacity.

Tinius Olsen Limited
6 Perrywood Business Park Redhill, Surrey RH1 5DZ UK
Tel: 01737 765001 Fax: 01737 764768
FIELD SERVICE REPORT

Date: 28th July, 2016 **Service Order Number:** 300756
Customer: Manchester Metropolitan University **Customer Order Number:** 82045442
Chemistry Laboratories 5th Floor
John Dalton Main Building, Chester Street
Manchester, M1 5GD

EQUIPMENT
S/N 500LC-0146 - LASER EXTENSOMETER - w/ Dell Latitude E5530 - No Adjustments - Good Condition

SCHEDULED WORK COMPLETED, OR DAILY PROGRESS REPORT
SERVICE AND CALIBRATION ON THE EQUIPMENT LISTED ABOVE. NO PRE-CALIBRATION ADJUSTMENTS MADE. LOWER LOADCELL CALIBRATION LIMITS AS FOLLOWS - 10KN L/C = 100N (1%) - 1KN L/C = 10N (1%) 100N L/C = 1N (1%)..
UNABLE TO CALIBRATE 100SC DUE TO PROBLEMS WITH LVDT - UNABLE TO ZERO.

NEW PARTS USED

Work Done By: Keith Flanagan
Calibration Technician

Time Arrived: 09:30 AM **Time Left:** 12:00 PM **Witnessed By:** MIKE GREEN

10.E.2 Impact Rig Validation & Calculations

Once estimated, the actual effective mass of a range of setups was measured by placing a weighing scale (Mettler Toledo PM16) under the end of the impactor (Figure 10-1). A reading from the scales was taken after 30 s, and compared against the hand calculations to assess accuracy. As expected calculations for effective mass gave a strong correlation to the experimentally measured values with a linear regression of 1.05 and r^2 value of 0.998 (Figure 10-1).

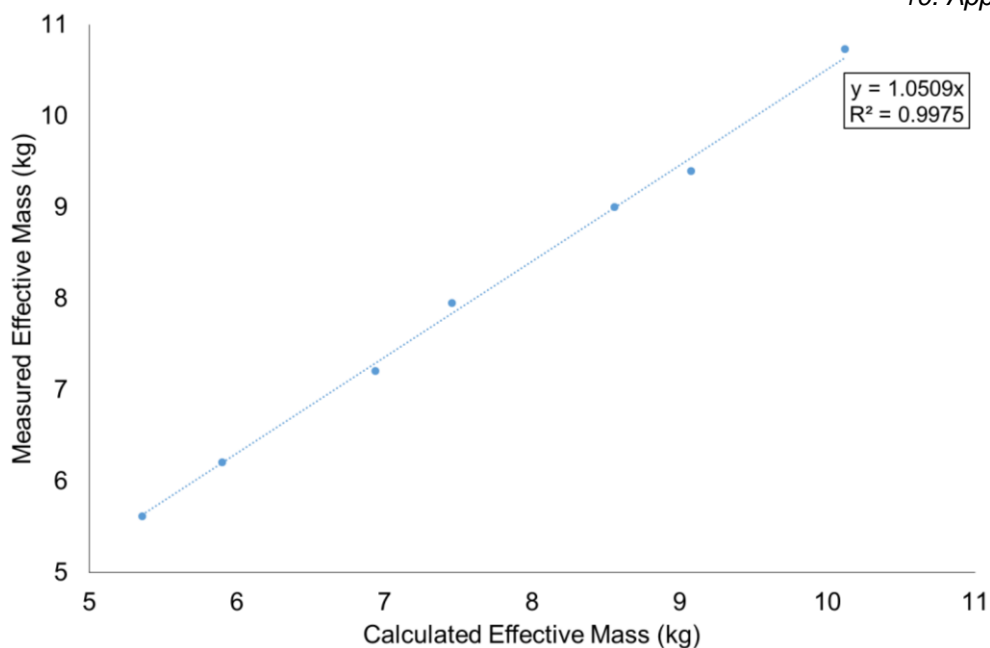


Figure 10-1 Hand calculated effective mass vs. the measured effective mass of the impact rig with a linear regression.

Figure 10-2 shows the results of the calibration check performed for the wrist and pendulum potentiometers. Adams (2018) had calibration factors of $-14.13x + 98.26$ and $13.55x - 4.12$, which are less than 1% different from the factors found in this study. Therefore, the coefficients used by Adams (2018) were used. The accuracy of the calculated forces and angles were quantified to be ± 0.01 N and $\pm 0.01^\circ$ due to the DAQ quoting voltage to 0.00001 V.

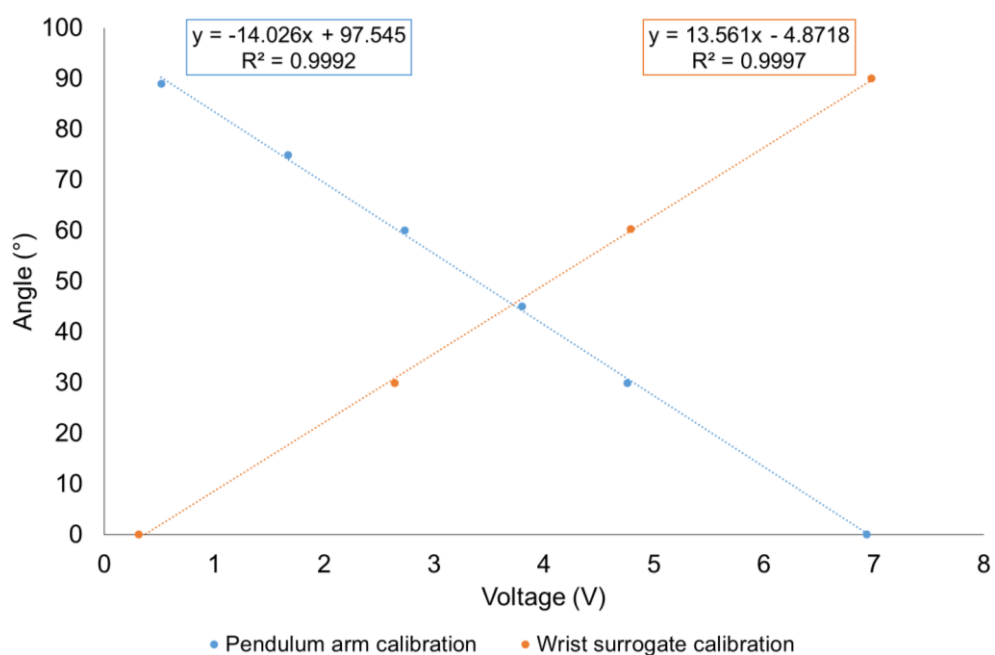


Figure 10-2 Calibration data for the pendulum and wrist potentiometers

10.E.3 Material Data Sheets


The polychloroprene attached to the pendulum arm of the full wrist protector impact rig was sourced from Boreflex Ltd, Rotherham. The data sheet for this material was provided upon ordering however is not available online, so has therefore being included here.

ELASTOMERS

Technical Data Sheet

Soft Neoprene Rubber WCM123

<u>CHEMICAL DESCRIPTION:</u>	Polychloroprene, Chloroprene (CR)
<u>PHYSICAL PROPERTIES</u>	
TENSILE STRENGTH:	40 KG/CM ²
DENSITY:	1.45
ELONGATION AT BREAK:	200%
ABRASION RESISTANCE:	Good
TEMPERATURE RANGE:	-30° - +80° C
OZONE RESISTANCE:	Good
HARDNESS RANGE:	50° Sh. A +/- 5° Sh.
RESILIENCE:	Fair
<u>CHEMICAL RESISTANCE</u>	
WATER:	Good especially Salt Water
ACIDS:	Fair – Suitable to PH 4 – Otherwise use a higher grade.
ALKALIS:	Fair to Good
OILS:	Good
FUELS AND PETROLEUM SOLVENTS:	Fair
KETONES:	Poor
ACTIVE POLYMER CONTENT	10%



Chloroprene is one of the original synthetic rubbers and it has the most balanced range of desirable properties. The chlorine atom gives it a good level of resistance to oils, which is somewhere between natural rubber and nitrile, and this mid-range is often sufficient for many general applications.

CR is resistant to many inorganic chemical products except oxidising acids and halogens.

It has moderate resistance to aliphatic hydrocarbons. (paraffin, grease, vegetable oils, animal fats etc.)

10.E.4 Rigid and Dynamic Model Calculations

Impact velocity was calculated by Adams (2018) using the body position at impact during a backwards fall in a study by Schmitt *et al.* (2012b) and anthropometric data (Tilley, 2002). Within an experimental fall scenario from a drop height of ~0.125 m, a shoulder angle of 56° was found (Schmitt *et al.*, 2012b). By simplifying the fall scenario and assuming the arm configuration is constant throughout the entire fall

(Figure 10-3), the fall can be replicated as a pendulum. Using trigonometry, the conservation of energy (Equation 10-1 to Equation 10-5) and the assumption the body is rigid, inbound velocity was predicted based on a range of anthropometric data (Table 10-2).



Figure 10-3 Experimental set up from Schmitt et al. (2012b) with the shoulder angle highlighted and a rigid body diagram highlighting the parameters used within the trigonometry calculations by Adams (2018). Image from Adams (2018).

$$L = \sqrt{(Al^2 + Sh^2 - (2 \times Al \times Sh \times \cos \phi))} \quad \text{Equation 10-1}$$

$$\theta = \sin^{-1} \left(\frac{Al \times \sin \phi}{L} \right) \quad \text{Equation 10-2}$$

$$\delta = 90 - \theta \quad \text{Equation 10-3}$$

$$h = L \times \sin \delta \quad \text{Equation 10-4}$$

$$v = \sqrt{2 \times g \times h} \quad \text{Equation 10-5}$$

$\phi = 56^\circ$ (Schmitt et al., 2012b), h is fall height, Al is arm length, L is distance from heel to the wrist and Sh is shoulder height (Figure 10-3).

Van den Kroonenberg et al. (1995) developed a two-link dynamic model in order to predict impact velocity and effective mass during a sideways fall from standing (Equation 10-6 to Equation 10-9). Within the model, it is presumed that there is no energy loss during the fall. The body is represented as a chain of two rigid links connected by a frictionless hinge; a leg connected to the floor by a hinge and a trunk (Figure 10-4). The angles recommended within the study for a vertical fall were used ($\alpha_1 = 0.087$, $\alpha_2 = 0.087$, $\omega_1 = 0$ and $\omega_2 = 0.205$) along with anthropometric parameters for height (floor to the fingers at standing) and mass, in order to calculate a range of inbound velocities (Table 10-2).

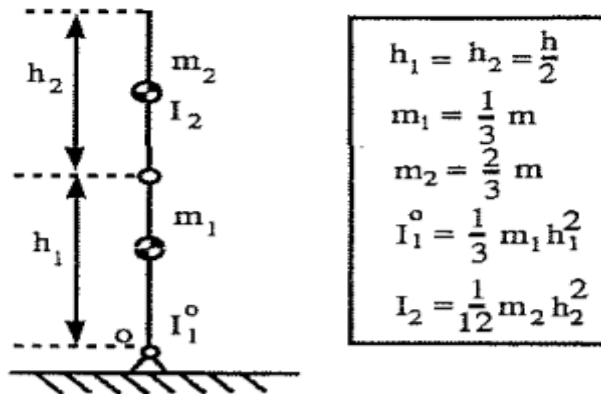


Figure 10-4 Schematic of the two-link dynamic model used by Van den Kroonenberg et al. (1995).

$$E = m_1 g h_1^{cg} + m_2 g h_2^{cg} + \frac{1}{2} m_2 v_2^2 + \frac{1}{2} I_2 \omega_2^2 \quad \text{Equation 10-6}$$

$$h_1^{cg} = \frac{h}{4} \cos \alpha_1 \quad \text{Equation 10-7}$$

$$h_2^{cg} = \frac{h}{2} \cos \alpha_1 + \frac{h}{4} \cos \alpha_2 \quad \text{Equation 10-8}$$

$$v_2 = \omega_2 \frac{h}{4} \quad \text{Equation 10-9}$$

E is the total available energy, m_i are the point masses of the links, g is acceleration due to gravity, h_i^{cg} are the initial heights of the centres of gravity of the links, I is the moment of inertia about the pivot, ω is angular velocity and v is linear velocity

Table 10-2 Estimated fall velocities using the rigid body model (Adams, 2018) and dynamic model (Van den Kroonenberg et al., 1995) from the literature, for a range of anthropometric parameters (Tilley, 2002).

Age (yrs)	Sex	Percentile	Body Mass (Kg)	Body Height (m)	Shoulder height (m)	Arm length (m)	Heel to wrist height (m)	Rigid Body Model estimated velocity (ms ⁻¹)	Dynamic Body Model estimated velocity (ms ⁻¹)
12	F/M	50	39.1	1.49	1.16	0.62	0.96	4.00	3.32
13	F/M	50	44.2	1.55	1.21	0.65	1.01	4.09	3.39
14	F/M	50	50.0	1.59	1.24	0.67	1.03	4.13	3.43
15	F/M	50	54.2	1.64	1.28	0.69	1.06	4.19	3.48
16	F/M	50	58.9	1.69	1.32	0.70	1.10	4.27	3.54
17	F/M	50	60.1	1.68	1.32	0.69	1.09	4.27	3.53
20 to 65	F	50	62.5	1.63	1.33	0.67	1.10	4.32	3.54
20 to 65	M	50	78.4	1.76	1.44	0.73	1.20	4.50*	3.69

*Shows the same estimated velocity as calculated by Adams (2018)

10.E.5 Loading Rate

Adams (2018) tuned the stiffness of the impact rig to match the loading case of Greenwald *et al.* (1998) by attaching five polychloroprene blocks to the end of the pendulum arm, via an aluminium plate. As the impact rig was modified to accommodate high velocities for 10 to 50 J impacts, the modified setup loading rate was compared (Figure 10-5). At 10 J, the loading case is seen to be similar to Greenwald *et al.* (1998) and Adams (2018), however, as impact energy increases, loading rate increases meaning the system becomes stiffer.

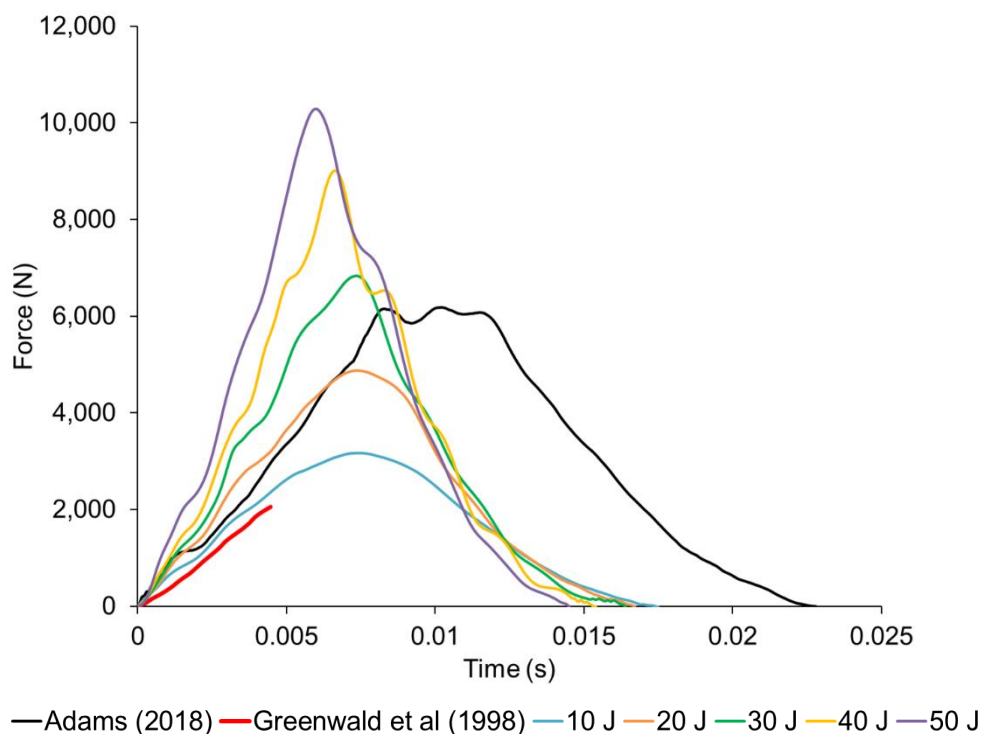
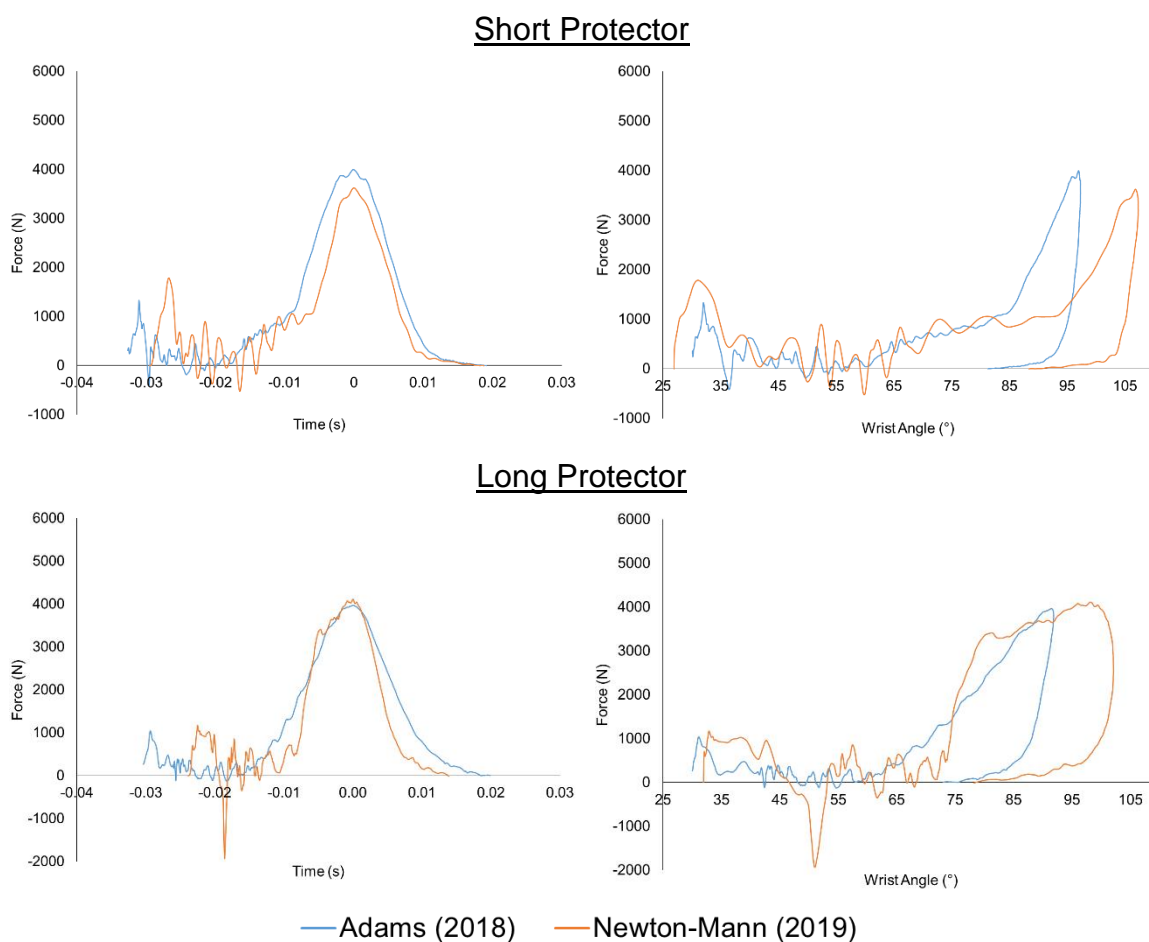


Figure 10-5 Temporal force plot showing the impact traces for this study at 10 to 50 J, an impact using the unmodified rig in Adams (2018) and the loading curve from the cadaveric study by Greenwald *et al.* (1998).

10.E.6 Comparison of Data to Adams (2018)

A comparison of the data collected in this study was compared to the results presented by Adams (2018) in terms of temporal force and force vs. wrist angle traces for the short and long protector at 40 J.



10.F Material Models

The hyperelastic material models used within the wrist protector FE models are shown below in the k file format. A snippet from the k file manual for the *MAT_HYPERELASTIC_RUBBER and *MAT_OGDEN_RUBBER are also shown for reference (LSTC, 2017a).

*MAT_OGDEN_RUBBER

This is also Material Type 77. This material model provides the Ogden [1984] rubber model combined optionally with linear viscoelasticity as outlined by Christensen [1980].

Card 1	1	2	3	4	5	6	7	8
Variable	MID	RO	PR	N	NV	G	SIGF	REF
Type	A8	F	F	I	I	F	F	F

Card 3 for N = 0. Set the material parameters directly.

Card 3	1	2	3	4	5	6	7	8
Variable	MU1	MU2	MU3	MU4	MU5	MU6	MU7	MU8
Type	F	F	F	F	F	F	F	F

Card 4 for N = 0. Set the material parameters directly.

Card 4	1	2	3	4	5	6	7	8
Variable	ALPHA1	ALPHA2	ALPHA3	ALPHA4	ALPHA5	ALPHA6	ALPHA7	ALPHA8
Type	F	F	F	F	F	F	F	F

Optional Viscoelastic Constants Cards. Up to 12 cards may be input. A keyword card (with a "*" in column 1) terminates this input if less than 12 cards are used.

Card 5	1	2	3	4	5	6	7	8
Variable	GI	BETA1	VFLAG					
Type	F	F	I					
Default			0					

***MAT_HYPERELASTIC_RUBBER**

This is Material Type 77. This material model provides a general hyperelastic rubber model combined optionally with linear viscoelasticity as outlined by Christensen [1980].

Card 1	1	2	3	4	5	6	7	8
Variable	MID	RO	PR	N	NV	G	SIGF	REF
Type	A8	F	F	I	I	F	F	F

Card 3 for N = 0. Set the material parameters directly.

Card 3	1	2	3	4	5	6	7	8
Variable	C10	C01	C11	C20	C02	C30	THERML	
Type	F	F	F	F	F	F	F	

Optional Viscoelastic Constants & Frictional Damping Constant Cards. Up to 12 cards may be input. A keyword card (with a "*" in column 1) terminates this input if less than 12 cards are used.

Card 4	1	2	3	4	5	6	7	8
Variable	Gi	BETAi	Gj	SIGFj				
Type	F	F	F	F				

Variable	Description
MID	Material identification
RO	Mass density
PR	Poisson's ratio
N	Number of constants to solve for: EQ.1: Solve for C10 and C01; EQ.2: Solve for C10, C01, C11, C20, and C02; EQ.3: Solve for C10, C01, C11, C20, C02, and C30
NV	Number of Prony series terms in fit.
G	Shear modulus for frequency independent damping.
SIGF	Limit stress for frequency independent frictional damping.
REF	Use reference geometry to initialize the stress tensor.
MU _i	Material constant
ALPHA _i	Material constant
C _i	Material constant
G _i	Optional shear relaxation modulus for the <i>i</i> th term
BETA _i	Optional decay constant if <i>i</i> th term
G _j	Optional shear modulus for frequency independent damping represented as the <i>j</i> th spring and slider in series in parallel to the rest of the stress contributions.
SIGF _j	Limit stress for frequency independent, frictional, damping represented as the <i>j</i> th spring and slider in series in parallel to the rest of the stress contributions.

Short protector:

Pad

```
*MAT_HYPERELASTIC_RUBBER
      3  3.12E-10  0.31  0  0  0  0  0
-28.97  31.7  -170.2  58.13  139.2  0
0.00414  7.0639
0.97587  0.057908
0.013306  0.8332
```

Supporting Foam – raw (individual impact)

```
*MAT_OGDEN_RUBBER
      3  1.84E-10  0.48  0  0  0  0  0
0.0301  0  0  0  0  0  0
7.244  0  0  0  0  0  0
0.47069  0.10983
0.071044  1.188
0.063283  15.817
```

Supporting Foam – artificially stiffened (full protector impact)

```
*MAT_HYPERELASTIC_RUBBER
      4  1.84E-10  0.495  0  0  0  0  0
0.0208869  0.2329215  0.4538302  0  0  0
0.47069  0.10983
0.071044  1.188
0.063283  15.817
```

Long protector:

D30®

```
*MAT_HYPERELASTIC_RUBBER
      2  1.54E-10  0.497  0  0  0  0  0
-0.072146  0.097125  0.035551  0  0  0
0.04940  14.602
0.27338  0.087829
0.064056  1.153
```

Supporting Foam

```
*MAT_OGDEN_RUBBER
      1  2.94E-10  0.499  0  0  0  0  0
0.0034872  0  0  0  0  0
11.028  0  0  0  0  0
0.08372  9.7815
0.09747  0.37418
4.75E-05  1.7591
```

10.G Mesh Convergence Studies

Fundamentally, finite element modelling consists of dividing a geometry into multiple simple shapes (mesh), in order to compute different selected parameters (e.g. stress or strain), at multiple locations throughout a part. The accuracy of the results obtained from the FE model is therefore related to the mesh used. The finer the mesh, the more elements created, meaning the computed parameters are being processed over more points, in turn, meaning a more accurate solution is being processed. However, the more elements there are the higher the computational power needed and hence the longer the solution time. Therefore, a mesh convergence study allows the user to see when the change between the measured outputs is small enough to suggest that the solution has become independent of the mesh. Meaning that a finer mesh will not produce any more accurate results, however, will increase run time exponentially.

10.G.1 Individual Component Impacts

A mesh convergence study took place for a 6.4 mm pad sample that was 38 mm in diameter and was impacted at 2.5 J as described in Chapter 5.3 FE Model Methodology. A quadrilateral mesh was applied to the cylinder ensuring there were at least three elements across the thickness. Minimum element size was then incrementally changed and the associated peak force and maximum compression were plotted against the total number of elements to assess convergence (Figure 10-6). After 18,000 elements (element size 1 mm) both peak force and maximum compression converge. Therefore, as all samples had the same size diameter, an element size of 1 mm was selected for meshing of all the cylinder samples and the resulting number of nodes and elements is shown in Table 10-3. After this point, refining the mesh only increased run time (an increase of 45 minutes for half the element size) and no longer effected the peak force or maximum compression outputs.

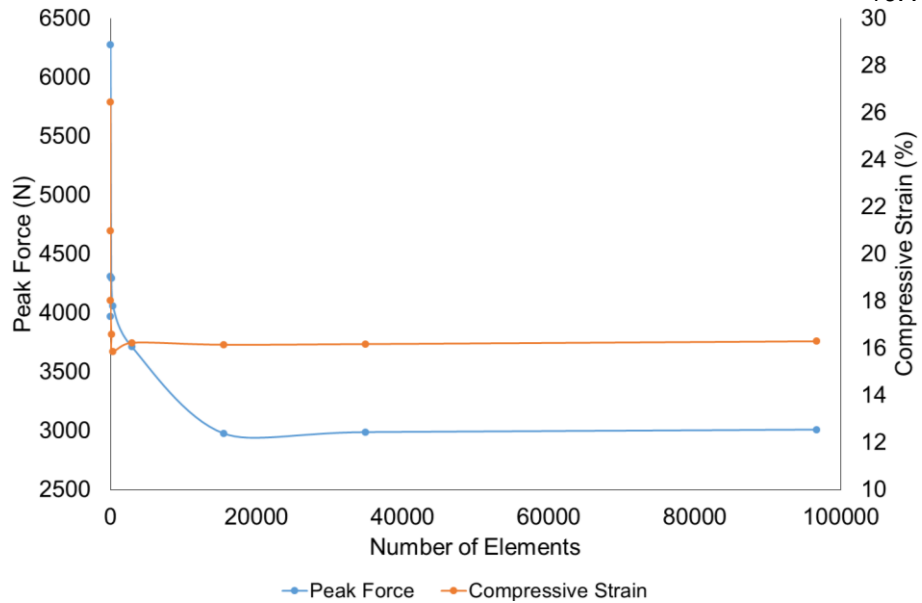


Figure 10-6 Mesh convergence study showing the total number of elements and the effect on peak force and maximum compression of a pad sample being impacted at 2.5 J.

Table 10-3 Parts within the FE model and the number of elements and nodes they were meshed with, following a mesh convergence study (Figure 10-6).

Protector	Part	Thickness (mm)	Elements	Nodes	No. of elements through thickness
Short	Pad	6.2	15,547	18,168	7
	Shell	3.0	23,596	5,686	3
	Supporting Foam	7.4	17,768	20,439	8
Long	D30®	4.5	10,255	12,636	5
	Supporting Foam	4.5	10,255	12,636	5
Impactor	Polychloroprene	20.0	46,641	49,962	21
	Drop mass	2.0	22,737	30,740	3
	Base plate	2.0	12,800	19,683	2

10.G.2 Bare Hand Impact

A mesh convergence study took place for a 40 J impact on to a surrogate (bare hand scenario), as described in Chapter 7.3. All parts of the impactor were meshed with solid brick elements (ELFORM 1) and all parts of the surrogate were meshed with solid tetrahedral elements (ELFORM 10). Minimum element size was incrementally changed and the associated peak force was plotted against the total number of elements to assess convergence (Figure 10-7). As the wrist was not extending in this scenario and deformation of the polychloroprene impactor was not able to be identified, only peak force was assessed for convergence. An element size of 4 mm (corresponding to a total element number of ~93,500) was used for the impactor and wrist surrogate in all FE impacts in Chapter 7.3, and Chapter 8.2.

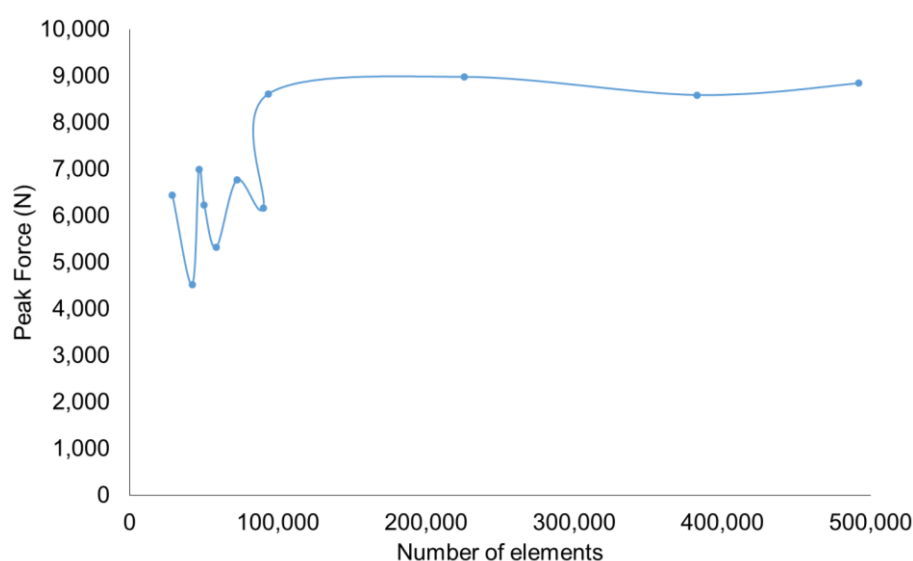


Figure 10-7 Mesh convergence study showing the total number of elements and the effect on peak force of the bare hand set up being impacted at 40 J.

Within pilot testing, the pad of the short protector with a similar geometry to that used in the full wrist protector models, was subject to a 2.5 J impact and a mesh convergence study. The pad was meshed with solid tetrahedral elements (ELFORM 10), the minimum element size was incrementally changed and the associated peak force and maximum compressive strain were plotted against the total number of elements to assess convergence (Figure 10-8). An element size of 2 mm (~13,000 elements) was chosen and used for the pad and shell in all FE impacts in Chapter 7.3, and Chapter 8.2.

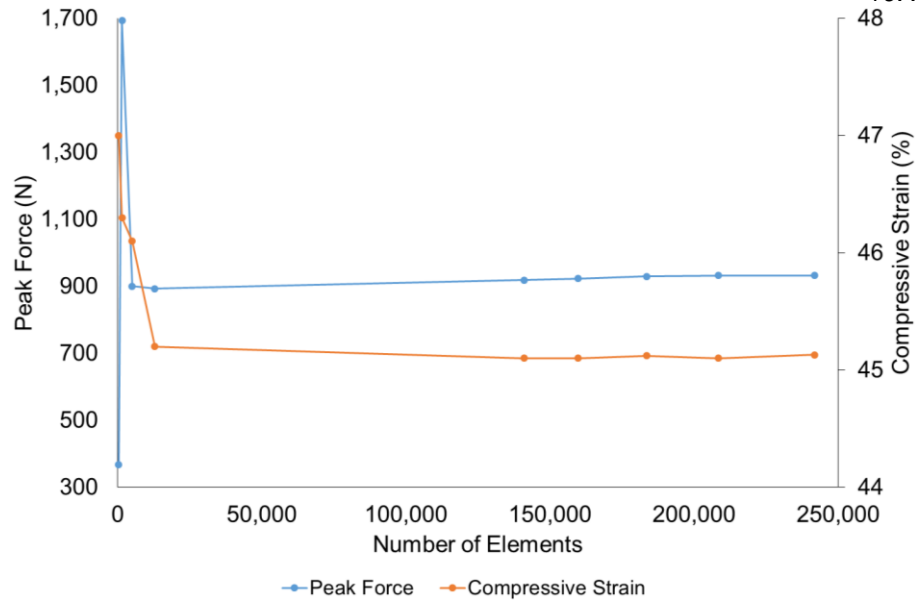


Figure 10-8 Mesh convergence study showing the total number of elements and the effect on peak force and maximum compressive strain of the palmar pad being impacted at 2.5 J.

Also within pilot testing one of the short protector dorsal splints, with similar geometry to that used in the full wrist protector models, was subject to a three-point bend test in ANSYS® Mechanical Static structural, where a mesh convergence study was undertaken. The splint was meshed with solid tetrahedral elements (ELFORM 10), the minimum element size was incrementally changed and the associated peak force to displace the splint by 7 mm at a support span of 90 mm, was plotted against the total number of elements to assess convergence (Figure 10-9). An element size of 2 mm (~7,000 elements) was chosen and used for the splints in all FE impacts in Chapter 7.3, and Chapter 8.2.

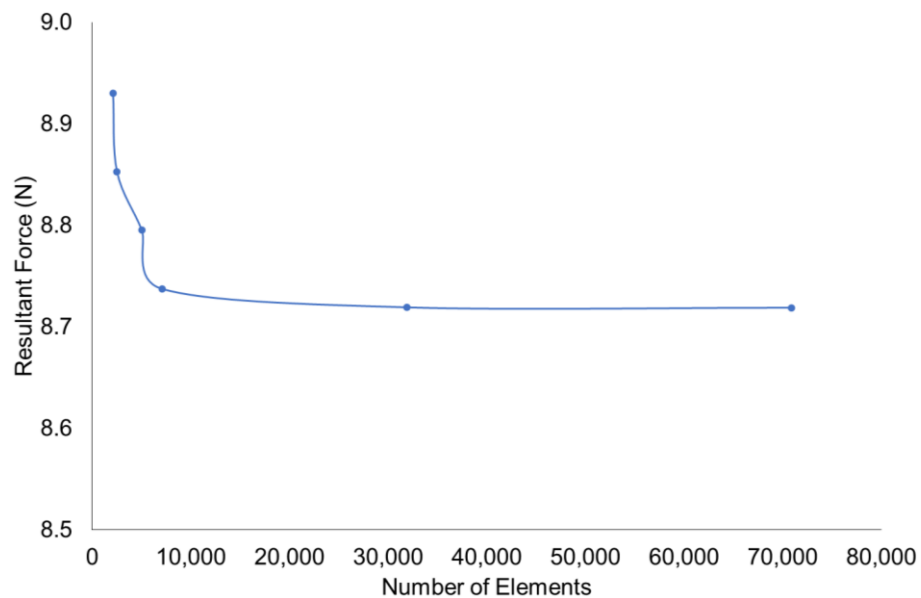


Figure 10-9 Mesh convergence study showing the total number of elements and the effect on the resultant force needed to displace the short protector dorsal splint by 7 mm within a three-point bend test.